PULSAR DISCOVERIES AND THEIR EXPLOITATION

Dissertation
zur
Erlangung des Doktorgrades (*Dr. rer. nat.*)
der
Mathematisch-Naturwissenschaftlichen Fakultät
der
Rheinischen Friedrich–Wilhelms–Universität, Bonn

vorgelegt von

Patrick Lazarus
aus
Montreal, Canada

Bonn, 10, Sept. 2015

Angefertigt mit Genehmigung der Mathematisch-Naturwissenschaftlichen Fakultät
der Rheinischen Friedrich-Wilhelms-Universität Bonn

1. Referent: Prof. Dr. Michael Kramer
2. Referent: Prof. Dr. Norbert Langer
Tag der Promotion: 9 März, 2016
Erscheinungsjahr: 2016

לחן

CONTENTS

LIST OF FIGURES

List of Tables

ABSTRACT

Pulsars are the rapidly-rotating, highly-magnetized, neutron star remnants of the supernova explosions of massive stars. Pulsars have been used in a wide variety of studies of astronomy and physics. Of the >2500 pulsars now known, most were found in blind, large-scale searches at radio frequencies. The PALFA survey at the Arecibo Observatory is an example of this type of search. I present details of the PALFA data analysis software that I designed, which has already been used to discover 40 pulsars, bringing the total number of discoveries in the survey to 144 pulsars. Additionally, I implemented a novel technique for reliably measuring the survey's sensitivity in the presence of terrestrial interference and red noise. The sensitivity determined with my technique agrees with theoretical predictions for millisecond-period pulsars (MSPs), but is reduced for long-period ($P \gtrsim 100\,\mathrm{ms}$) pulsars. Simulations suggest that this reduction in sensitivity should result in $33 \pm 3\%$ fewer detections than expected, which corresponds to 224 ± 16 pulsars detected, given the observations to date. This result is consistent with the 241 pulsars actually detected.

In general, pulsar timing analyses based on long-term monitoring campaigns are extremely productive scientifically. My collaborators and I conducted such an analysis for PSR J1952+2630, a 20.7-ms pulsar in a binary system with a massive white dwarf companion, found in the PALFA survey. Our analysis made it possible to constrain the evolutionary history of the binary system and the composition of the pulsar's companion. Furthermore, our simulations of future observations of PSR J1952+2630 indicate that this system will be useful in constraining theories of relativistic gravity in the next ~10 years.

To maximize the scientific potential of MSPs, Pulsar Timing Array (PTA) projects conduct long-term, large-scale observing campaigns with many of the world's largest radio telescopes. For example, as part of the European Pulsar Timing Array (EPTA), the Effelsberg 100-m radio telescope regularly observes ~50 MSPs with PSRIX, a new data recording instrument installed in 2011. The first four years of these data have been reduced with the automated software that I developed. By comparing the PSRIX data with results from the previous instrument, the Effelsberg-Berkeley Pulsar Processor, I found that PSRIX provides significantly greater sensitivity. With this increased sensitivity, I estimated the improvement in our chances of detecting the low-frequency gravitational wave background (GWB) with MSPs, one of the main goals of PTAs. A major obstacle to this detection is the effect of interstellar medium variations. With this in mind, I conducted observations at 5 and 9 GHz with PSRIX and showed that by pushing PTA observations to higher frequencies, it may be possible to mitigate this source of noise and further enhance the sensitivity to the GWB.

Observations from the EPTA have been combined with data from the International Pulsar Timing Array (IPTA) community to form the largest, most sensitive pulsar timing data set ever assembled. This unique data set has many diverse applications. For instance, I am using it to measure the masses of the Solar System planets. My ongoing analysis already provides results consistent with previous studies, and thus can be used to verify the quality of the IPTA data set, a key first step towards exploiting its unrivalled sensitivity.

ACKNOWLEDGMENTS

I would like to thank David, Paulo, and Michael for their guidance and patience over the past four years. They gave me the freedom to take my time to explore new ideas and to focus on problems that suit me, but also gave me the support I needed when I needed it.

The encouragement I received from my family despite being so far away has been immense. So many thanks to Mom, Dad, Nana, Rocky, Riel, Stephanie, and especially Wren. The unconditional support I got from Chen throughout my entire PhD has been an amazingly beautiful source of motivation. I would also like to thank Mor for constantly reminding me that the real world is vastly different from the one I live in.

I very much appreciate the help of my mother, Ralph, Greg, Seb, and most of all Chen, who proofread parts of my thesis. Their attention to detail and advice helped greatly improve the clarity of this work.

Being surrounded by so many smart and passionate people during my PhD has made the environment at the MPIfR an interesting and exciting place to work. The diversity of perspectives, personalities, skills, and interests of the MPIfR Pulsar Group has enriched my experience. I particularly want to acknowledge my various office mates over the years: Nicolas, Pablo, John, Ewan, Alessandro, and Pablo (again).

My friends[1] have made Bonn a fun place to hang out. Thanks!

Also, a big thank you to Kira for helping translate the many submission-related forms and regulations I've encountered.

The work presented in this thesis would not be possible if it weren't for my many co-authors and colleagues in the PALFA, EPTA, and IPTA collaborations. A big thank you to Vicky, Scott, Adam, Paul, Ryan, Erik, Chitrang, Chen, Weiwei, and Maura for the extremely helpful discussions we've had during PALFA pipeline working group telecons. Also, it's been amazing getting to collaborate with friends, and make friends with collaborators. It's been especially nice being able to work, travel, and hang out with Jason, Gemma, Cees, Maggie, and Rene. It's hard for me to believe that we've known each other for almost 10 years now.

I acknowledge the fantastic technical support of Alex Kraus and the Effelsberg operators for making the telescope so easy to use, as well as the RZ group in Bonn, especially Jan, who have been great for helping me stay focused on research instead of getting frustrated with computer issues. I also want to acknowledge the support of the system administrators who keep Guillimin running, merp, and Adam – all of who assisted me despite being so far away. Also, Ramesh, though not a system administrator, has been unbelievably helpful at making observations work, troubleshooting computer issues, and finding work-arounds to various computer-related issues, some of which I caused.

---

[1] I don't dare list names. In any case, you know who you are.

1

Introduction

1.1 A Brief History of Pulsars

The first pulsar discovered, CP1919 (later designated PSR B1919+21, and now also known as PSR J1921+2153), was found in 1967 by Hewish et al. (1968) with the Mullard Radio Astronomy Observatory. The "unusual signal" they detected showed a repetition rate of $P \simeq 1.337\,\mathrm{s}$. The same periodic signal was detected on multiple days and was found to always come from a specific celestial location, indicating it was not of terrestrial origin. Furthermore, early observations showed no evidence of parallax, leading Hewish et al. (1968) to suggest that the source of the periodicity was beyond the Solar System.

Hewish et al. (1968) originally hypothesized that the observed radio emission was produced by the radial pulsations of a neutron star (NS) or white dwarf (WD). However, it was not long before alternative explanations were suggested. Proposed theories needed to explain both the origin of the radio emission as well as its astounding clock-like regularity of 1 part in $\sim 10^5$–10^7 (e.g. Hewish et al., 1968; Pilkington et al., 1968). Broadly speaking, theories for the clock mechanism fell into three categories: orbital motion, pulsations, and rotation.

For a short time following the announcement of the discovery of pulsars, the number of proposed theoretical explanations dwarfed the number of pulsars known. However, by 1970 more than 40 pulsars had been discovered. The diversity in the observed properties of the growing pulsar population became increasingly difficult to reconcile with most of the proposed theories, causing these theories to be abandoned. I will now examine several hypotheses put forth to explain the pulsar phenomenon. A graphical summary and timeline of the main theories can be found in Figure 1.1.

Orbital Motion

Several theories proposed the pulsar clock mechanism stems from orbital motion. For example, one suggestion was that the interaction of a small satellite around a magnetized star could give rise to periodic radio pulses, similar to the emission of Jupiter and Io (Burbidge & Strittmatter, 1968). An alternative hypothesis was that gravitational lensing occurring in a double neutron star system could produce regular radio pulses (Saslaw et al., 1968).

Difficulties with orbital-motion-based theories for the clock mechanism were outlined by Pacini & Salpeter (1968). Specifically, it was known that a binary system will emit gravitational waves, causing the orbit to shrink and thus the observed pulsation rate to increase. However, even as early as 1968, the lack of such an observed increase could already be used to put tight constraints on the emission of GWs from the supposed binary systems, making it extremely unlikely that the observed pulsations were due to orbital motion. The death-blow to this family of theories finally came from the observed slow-down of pulsation rates (e.g. Davies et al., 1969; Cole, 1969, and so many more since).

Binary orbits speed up over time, whereas pulsar pulsation rates are observed to slow down; pulsars are not the result of orbital motion.[1]

Pulsating White Dwarfs

One of the models proposed by Hewish et al. (1968) for the origin of the regular radio pulses they observed was radial pulsations of a WD. This model was initially disfavoured because the fundamental modes of oscillation of WDs were thought to be too long ($\gtrsim$8 s) to explain the observed pulse period ($P \simeq 1.337$ s). Explaining pulsation rates of $\sim$1 s would require a mechanism that could excite higher-order modes without exciting the fundamental. It was not long before updated theories of WD oscillations explained that under certain conditions, fundamental modes with shorter periods could exist (e.g. Faulkner & Gribbin, 1968; Durney et al., 1968). Moreover, mechanisms for exciting harmonic modes were outlined a short time later (Thorne & Ipser, 1968). The flurry of progress by theoreticians on pulsation modes of WDs led to explanations for pulsation periods as short as 100 ms. However, the discoveries of the Vela pulsar ($P \simeq 89$ ms, Large et al., 1968) and the Crab pulsar ($P \simeq 33$ ms, Staelin & Reifenstein, 1968; Comella et al., 1969) stymied even the furthest-reaching pulsating WD theories.

Periods of $\lesssim$100 ms (e.g. of the Crab and Vela pulsars) are inconsistent with radial pulsations of white dwarfs; pulsars are not pulsating white dwarfs.

Pulsating Neutron Stars

Hewish et al. (1968) also suggested the pulsar phenomenon could arise from the radial pulsations of NSs. However, the pulsation rates of NSs are too fast. To explain observed periods of $P \sim 1$ s, the central densities of the NSs must be so low that the pulsations are unstable (Thorne & Ipser, 1968).

Periods of $\sim$1 s are too long to be consistent with radial pulsations of neutron stars; pulsars are not pulsating neutron stars.

Rotating White Dwarfs

The hypothesis that the pulsar phenomenon was due to rotating WDs with hot spots on their surface was advanced by Ostriker (1968). However, WDs are not able to sustain the rotation rates required to explain the sub-second pulsations observed without breaking apart, or being significantly more dense, which would preclude them from being WDs.

Furthermore, as knowledge of pulsar positions improved, the lack of optical counterparts became a burden for all WD-based models (e.g. MacKay et al., 1968; Turtle & Vaughan, 1968).

White dwarfs rotating with periods $\lesssim$1 s would be torn apart by centrifugal forces; pulsars are not rotating white dwarfs.

---

[1] Some pulsars *are* observed to be in binary systems. The orbital motion modulates the observed pulsation periods due to Doppler shifts (see § 2.4), and the variable time-of-flight across the pulsar's orbit delays or advances when pulses arrive at the Earth (see § 4.3).

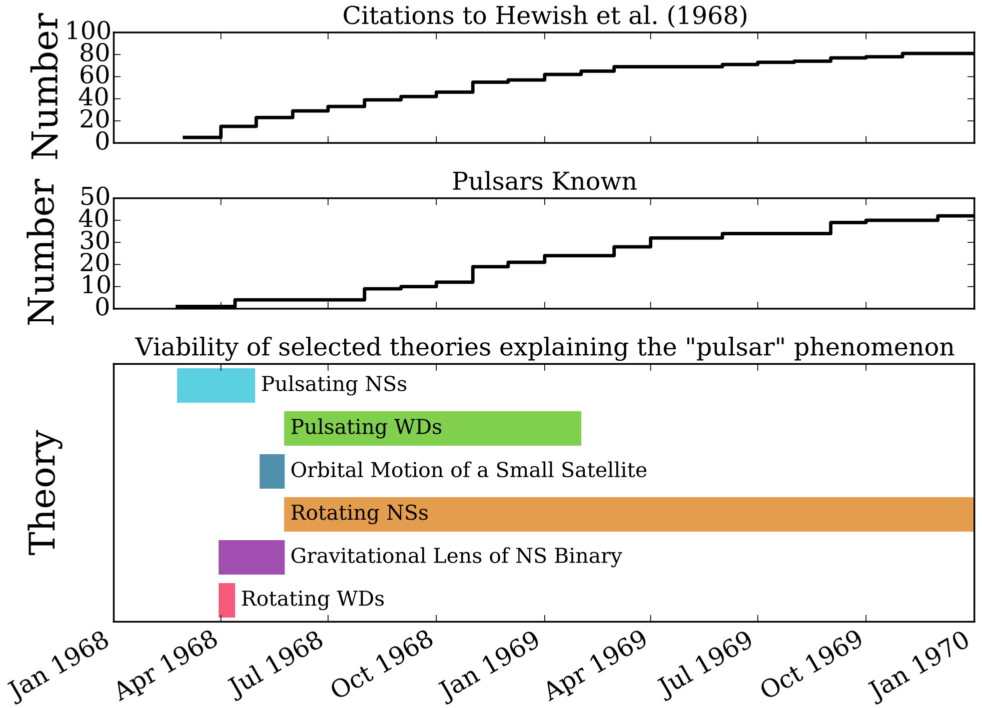

Figure 1.1: *Top* – The number of citations to Hewish et al. (1968), who reported the discovery of CP1919, the first known pulsar, between 1968 and 1970. Today there are >550 citations to Hewish et al. (1968).
Middle – The number of pulsars published in the first two years following the publication of the discovery of CP1919 by Hewish et al. (1968).
Bottom – The time between selected theories of the "pulsar" phenomenon being initially proposed and finally being shown to be inconsistent with observations. Today the preferred explanation is rotating NSs. See § 1.1 for details.

Rotating Neutron Stars

The hypothesis that the pulsar phenomenon is produced by rotating NSs was originally proposed by Gold (1968). This model gives an excellent explanation for the regularity of pulses, as well as qualitative predictions for rotational slowing, the existence of faster pulsars, and the association between supernova remnants and pulsars (Gold, 1968, 1969).

The original sketch of how the radio emission is generated (Gold, 1968) has long since been discarded in favour of more sophisticated models of the pulsar magnetosphere (Goldreich & Julian, 1969; Ruderman & Sutherland, 1975). Nevertheless, the rotating NS model of pulsars has proven to be remarkably consistent with observations.

The observed properties of pulsars are entirely consistent with originating from rotating neutron stars.

The next section provides a brief introduction to NSs. This is followed by a simple pulsar model useful for describing their general behaviour.

1.2 Neutron Stars and Pulsars

When a massive main sequence star ($\sim 8-15\,M_\odot$;[1] see e.g. Woosley & Weaver, 1986; Carroll & Ostlie, 2006; Lyne & Graham-Smith, 2012, and references therein) exhausts the hydrogen in its core, it contracts because the radiation pressure from nuclear fusion is no longer present to balance the gravitational force pulling on its outer layers. The star heats as it contracts; eventually the core is hot enough to fuse helium. At this point, the star expands into a giant. This process of exhausting nuclear fuel in the core, contracting, heating, and re-igniting repeats several more times, involving the fusion of progressively heavier atoms at each stage. Eventually, the core consists largely of iron since nuclei more massive than ^{56}Fe do not release energy as they undergo nuclear fusion. At this point, the core of the star can truly no longer support its own weight and it dramatically collapses in a so-called "core-collapse supernova" event. As the core collapses, the strong nuclear force causes it to rebound, resulting in an outward shock wave that expels a large amount of mass. This supernova event is many orders of magnitude more luminous than the Sun ($L \sim 10^{10} L_\odot$;[2] Arnett, 1996). The core that remains[3] after the explosion is a NS (see e.g. Woosley & Weaver, 1986), a stellar object containing a mass of roughly $\sim 1-2\,M_\odot$ within a radius of ~ 10 km. Pulsars form a sub-class of NSs. Pulsars are characterized by rapid rotation rates ($\sim 0.1-1000$ Hz) and strong magnetic fields ($\sim 10^9-10^{15}$ G). The strong rotating magnetic field accelerates charges in the magnetosphere surrounding the pulsar. These accelerating charges give rise to collimated beams of emission that are oriented along the magnetic axis of the star. Because the magnetic axis is misaligned from the star's spin axis, as the pulsar rotates, its emission beams sweep across the celestial sphere. If this emission impinges upon the Earth, we can detect the NS as a pulsar.

As of yet, there is no complete model of the mechanism by which pulsar emission is created. The rich diversity observed in pulsars has challenged both detailed descriptions and empirical models of the origin of their emission. Despite this, it is possible to summarize the basic behaviour of pulsars with the aid of a simple model.

1.3 The Simplified Pulsar Model

Many elementary properties of pulsars can be estimated from a small number of observed parameters by assuming a simplified model. In this model, the pulsar has a purely dipolar magnetic field oriented along the magnetic axis, $\vec{\mu}$, which is misaligned from the rotation axis, $\vec{\Omega}$, and is assumed to be in a vacuum (see Figure 1.2). I will examine some of the implications of this simple pulsar model by following the discussion of Lorimer & Kramer (2004).

The rotation rates of pulsars are observed to decrease with time. This loss of rotational energy is referred to as the *spin-down luminosity* and is given by

$$\dot{E} = 4\pi^2 I \dot{P} P^{-3}\,, \tag{1.1}$$

---

[1] The solar mass unit is $M_\odot \approx 2 \times 10^{30}$ kg.

[2] The luminosity of the Sun is $L_\odot \approx 3.86 \times 10^{33}$ ergs/s.

[3] The supernova of stars more massive than $\sim 15-25\,M_\odot$ may result in a black hole (see e.g. Woosley & Weaver, 1986).

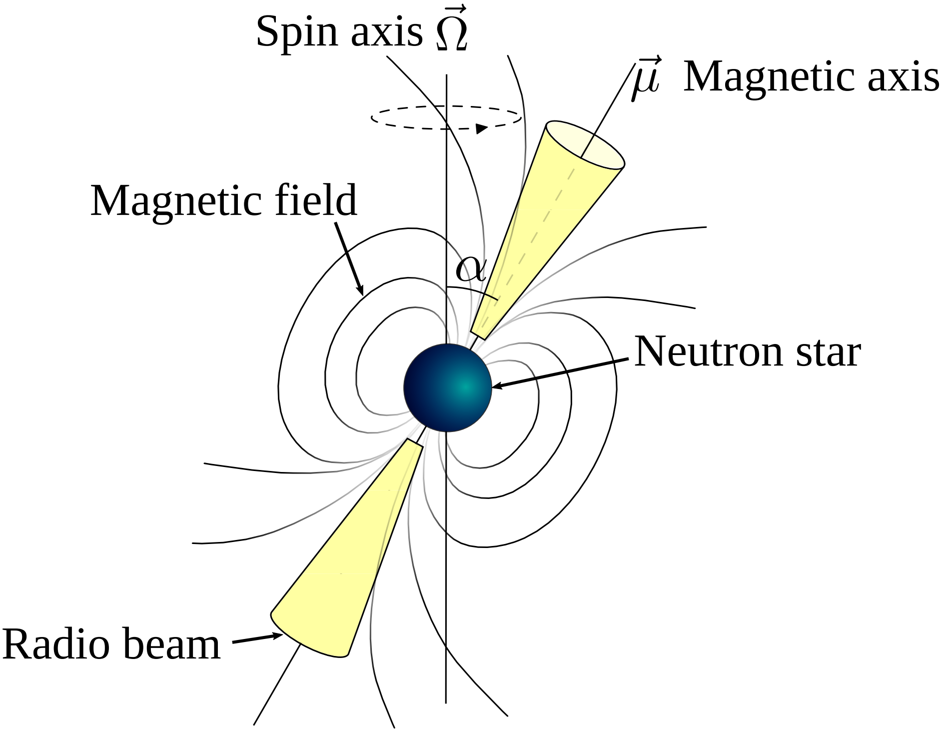

Figure 1.2: The simplified pulsar model. The neutron star at the centre rotates about its spin axis, $\vec{\Omega}$. This causes the collimated beams of radio emission to sweep across the celestial sphere since they are oriented along the pulsar's magnetic axis, $\vec{\mu}$, which is misaligned by an angle α with respect to $\vec{\Omega}$. This figure is closely based on Figure 3.1 from Lorimer & Kramer (2004).

where I is the moment of inertia of the pulsar, P is the rotational period, and $\dot{P}$ is the rate of change of the rotational period. To estimate $\dot{E}$, the canonical value of $I = 10^{45}\,\mathrm{g\,cm^2}$ is typically used.

As the pulsar rotates, its dipolar magnetic field radiates. Assuming the pulsar is in a vacuum and that this magnetic dipole radiation is the only source of rotational energy loss, the strength of the magnetic field at the surface of the star can be estimated by equating the power radiated by a rotating magnetic dipole with Eq. 1.1, and subsequently solving for the magnetic field strength,

$$B = \sqrt{\frac{3c^3}{8\pi^2}\frac{I}{R^6 \sin^2\alpha} P\dot{P}}, \tag{1.2}$$

where c is the speed of light in vacuum, R is the radius of the pulsar, and α is the angle between the magnetic axis and rotation axis. Characteristic values of B are generally estimated using $I = 10^{45}\,\mathrm{g\,cm^2}$, $R = 10^6\,\mathrm{cm}$, and $\alpha = 90°$.

It is also possible to estimate the age of the pulsar by integrating the power-law relation between the spin-down rate and the spin period suggested by equating Eq. 1.1 with the power radiated by a magnetic dipole. The power-law spin-evolution can be generalized slightly as

$$\dot{\nu} = -K\nu^{n} \,, \tag{1.3}$$

where $\nu = P^{-1}$ is the spin frequency of the pulsar, $\dot{\nu} = -P^{-2}\dot{P}$ is the spin frequency derivative, n characterizes the spin evolution of the pulsar and is known as the *braking index*, and K is a general multiplicative factor. By integrating Eq. 1.3 assuming K and n are constants, the age of the pulsar is estimated to be

$$T = \frac{P}{(n-1)\dot{P}}\left[1 - \left(\frac{P_0}{P}\right)^{n-1}\right] . \tag{1.4}$$

It is common to estimate the *characteristic age* of a pulsar using Eq. 1.4 assuming the pulsar rotation is slowed only by dipolar magnetic field braking (that is, $n = 3$) and that the birth period of the pulsar, P_0, is significantly smaller than the current period. Under these assumptions the characteristic age is given by the simplified expression

$$\tau_c = \frac{P}{2\dot{P}} \,. \tag{1.5}$$

In summary: the spin-down luminosity, $\dot{E}$, the inferred surface magnetic field strength, B, and the characteristic age, τ_c, can be computed from the observed spin period, P, and slow-down, $\dot{P}$, of the pulsar by making the following assumptions:

- *The magnetic field of the pulsar is purely dipolar.*
- *The pulsar is in a vacuum.*
- *The slow down of the pulsar rotation is exclusively due to magnetic braking.*
- *The birth period of the pulsar is significantly smaller than its current spin period.*

In addition to enabling basic estimates of pulsar parameters, the simplified pulsar model is also a good starting point to identify and understand common traits in various sub-classes of pulsars.

1.4 The Pulsar Population

Including radio-quiet sources, there are 2524 pulsars known according the the ATNF on-line pulsar catalogue[1] (Manchester et al., 2005). The vast majority (∼97 %) of the known pulsars can be detected in the radio band. The pulsar population can be summarized in the period/period-derivative (P–$\dot{P}$) diagram (see Figure 1.3).

1.4.1 Pulsars: A Population that Embraces Diversity

Based on radiative and spin properties, there is a large amount of diversity in the sample of known pulsars. Several clusters are evident in the P–$\dot{P}$ diagram. Focusing on sources detected at radio frequencies, I will now summarize the main groups of pulsars in the P–$\dot{P}$ diagram.

Canonical Pulsars

The canonical pulsars make up a large proportion (∼65 %) of the overall population. They are characterized by spin periods between ∼0.1 s and ∼5 s, and period-derivatives between $\sim10^{-17}\,\mathrm{s\,s^{-1}}$ and $\sim10^{-13}\,\mathrm{s\,s^{-1}}$.

---

[1] Version 1.53, accessed on Aug. 24, 2015 (http://www.atnf.csiro.au/people/pulsar/psrcat/)

Young Pulsars

Pulsars are born with small spin periods and large slow-down rates. Therefore, in the P–$\dot{P}$ diagram, young pulsars are located along the upper-left edge of the cluster of canonical pulsars. As pulsars age, they follow tracks according to their braking index, n (see Eq. 1.3).

Many pulsars thought to be young based on their spin properties (i.e. small characteristic age, τ_c) are found to be associated with supernova remnants (SNRs; see Figure 1.3), giving credence to the notion that the characteristic age of a pulsar is, at least qualitatively, related to its true age. Furthermore, this instills some confidence that the general features of the simplified model described in § 1.3 are reasonable.

Millisecond Pulsars (MSPs)

The millisecond pulsars (MSPs) are characterized by the fastest rotational periods and the smallest spin-down rates of any pulsar sub-class, typically $P \sim 1 - 10\,\mathrm{ms}$ and $\dot{P} \sim 10^{-21} - 10^{-18}\,\mathrm{s\,s^{-1}}$, respectively. MSPs are located in the bottom-left corner of the P–$\dot{P}$ diagram.

MSPs are believed to be spun up to their short periods by accreting matter and angular momentum from a binary companion (e.g. Alpar et al., 1982). This accretion process, commonly known as *recycling*, takes $\sim 10^7 - 10^9$ yr and results in a pulsar with a $\lesssim 10\,\mathrm{ms}$ spin period (e.g. Tauris & van den Heuvel, 2006). Recent observations of systems that appear to be transitioning between LMXBs and MSPs support this recycling formation hypothesis (e.g. Archibald et al., 2009; Papitto et al., 2013; Stappers et al., 2014). Because the inferred magnetic field strengths of MSPs are significantly lower than those of the canonical pulsars ($\sim 10^8$ G vs. $\sim 10^{12}$ G), it is believed the accretion also quenches the magnetic field of the pulsar. A binary system in which accretion is actively recycling a NS into a MSP would be observed as a low-mass X-ray binary (LMXB).[1]

Because the formation mechanism of MSPs requires a binary companion, it is expected that MSPs would be observed to be in binary systems. This is indeed the case; MSPs are predominately found to be in binaries. In the P–$\dot{P}$ diagram (Figure 1.3) I have marked binary pulsars with circles to clearly show the prevalence of MSPs in binary systems.

MSPs exhibit the most stable rotation of all known pulsars (e.g. Verbiest et al., 2009). Their extreme clock-like stability makes them useful in a broad range of applications (see § 1.6 for applications of MSPs and other pulsars).

Mildly Recycled Pulsars

The accretion process involving a LMXB resulting in a MSP is a stable, long-lived process. However, this is not the case when the donor star is too heavy. When the donor star is more massive, such as in an intermediate-mass X-ray binary ($M_{\mathrm{donor}} \sim 1 - 10\,M_\odot$) or a high-mass X-ray binary ($M_{\mathrm{donor}} \gtrsim 10\,M_\odot$), the accretion phase is unstable and thus short-lived. These factors make the mass-transfer onto the pulsar less efficient. In the case of accretion via an IMXB or HMXB phase, the pulsar is only

---

[1] In LMXBs, a low-mass ($M \lesssim 2\,M_\odot$) star expands as it evolves, eventually becoming so large that its outer layers are more strongly attracted to its NS companion. It is this matter that is accreted onto the NS. The X-ray emission of LMXB is due to radiation from hot matter which is heated as it falls towards the NS. X-ray emission also arises from thermal radiation from the hot NS and from occasional thermonuclear bursts on its surface (see e.g. Lewin et al., 1997, and references therein).

mildly recycled to a period of $\sim 10-100$ ms. The aborted accretion still appears to quench pulsar magnetic fields, but to a lesser degree than the MSPs. The inferred magnetic field strengths of mildly recycled pulsars ($B \sim 10^{9}-10^{11}$ G) are appropriately between those of the canonical pulsars and the fully recycled MSPs.

Most of the mildly recycled pulsars known are in binary systems with a massive WD companion ($\sim 1\,M_{\odot}$; either a CO or ONeMg WD), or another NS. The detailed case study of PSR J1952+2630, a mildly recycled pulsar with a massive WD companion, can be found in Chapter 5.

Magnetars

The archetypal magnetar is a X-ray pulsar whose luminosity is larger than can be explained by its spin-down luminosity, suggesting an additional power source, which is generally thought to be the decay of its extremely strong magnetic field (Thompson & Duncan, 1995, 1996). Owing to their long spin periods ($\gtrsim 1$ s) and large spin-down rates ($\gtrsim 10^{-12}\,\mathrm{s\,s^{-1}}$), magnetars are located in the top-right corner of the P–$\dot{P}$ diagram.

Predominantly X-ray sources, most magnetars have not been detected at radio frequencies despite sensitive observations (e.g. Burgay et al., 2006; Crawford et al., 2007; Lazarus et al., 2012). However, some magnetars have been observed to also emit at radio frequencies (see Olausen & Kaspi, 2014, and references therein). The radio emission of magnetars is transient, commonly appearing following a radiative event in X-rays or gamma-rays (e.g. Halpern et al., 2005; Shannon & Johnston, 2013), and either slowly fades over time like XTE J1810−197 (Camilo et al., 2007b), or shows deep amplitude modulations on timescales of days like 1E 1547.0−5408 (Camilo et al., 2008).

The radio emission of magnetars has peculiar properties not shared by the majority of pulsars. For instance, magnetars have flat radio spectra, and thus are much brighter at high radio frequencies than common radio pulsars (see e.g. Camilo et al., 2007c; Torne et al., 2015). Also, the luminosities of radio magnetars show large intensity variations (see e.g. Camilo et al., 2006). Furthermore, the radio profiles of magnetars vary substantially more than those of the canonical pulsars (e.g. Camilo et al., 2007a), and are extremely highly polarized (e.g. Camilo et al., 2008; Eatough et al., 2013b).

Rotating Radio Transients (RRATs)

The intrinsic emission intensity of most pulsars is constant when averaging over 1000s of pulses. However, some pulsars display variability. For instance, nulling pulsars have brief time intervals where emission is absent (e.g. Burke-Spolaor & Bailes, 2010). The *nulling fraction*, that is, the fraction of rotations without emission, can range from $\sim 1-95\,\%$, depending on the source (e.g. Wang et al., 2007). The most extreme transient pulsars are the rotating radio transients (RRATs), which only exhibit sporadic pulses. The burst rates of RRATs are commonly between $\sim 1-500\,\mathrm{hr}^{-1}$. The spin periods of RRATs are typically longer than those of the canonical pulsars. However, this may be due to biases in search techniques rather than differences in the underlying period distributions (see the discussions in Deneva et al., 2009; Keane, 2010; Karako-Argaman et al., 2015).

It is still unclear how the RRATs are related to other types of NSs (e.g. Weltevrede et al., 2006b; Zhang et al., 2007; Lyne et al., 2009). Some theories for an evolutionary link between RRATs and other NS sub-classes have been proposed to help reconcile

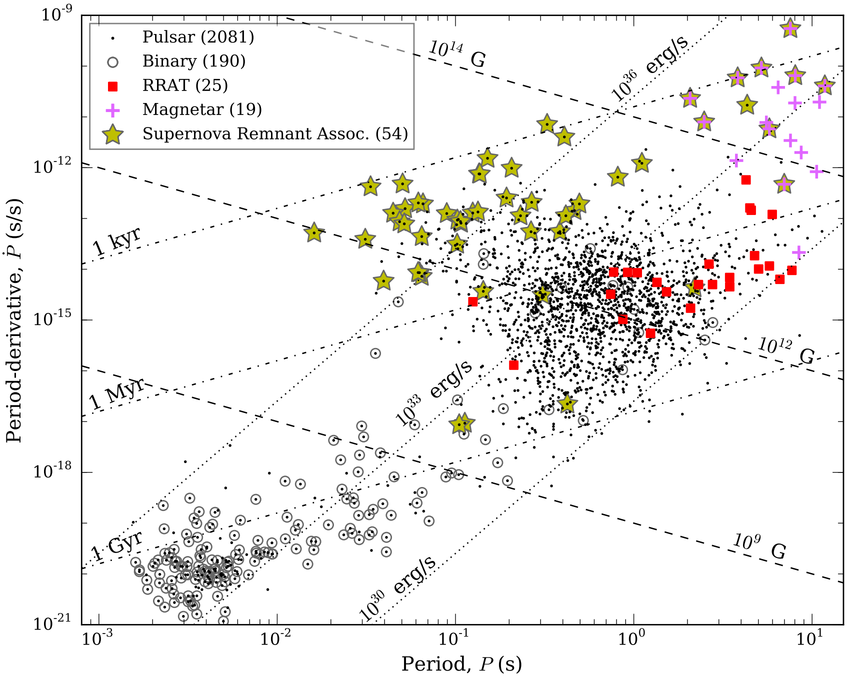

Figure 1.3: Period vs. period derivative (P–$\dot{P}$) diagram summarizing the known sample of pulsars. Lines of constant characteristic age (τ_c; dot-dashed) highlight the correlation between young pulsars (small τ_c) and supernova remnant associations (yellow stars). The lines of constant inferred magnetic field strength (B; dashed) clearly differentiate the magnetars (magenta crosses) in the top-right corner as highly magnetized sources from the bulk of the canonical pulsars. The fast-spinning MSPs in the bottom-left corner are old, weakly magnetized pulsars, and predominantly found in binary systems (circles). The high rate of occurrence of MSPs in binary systems is consistent with the matter-accretion phase that is believed to spin-up these pulsars to their rapid rotation rates. The RRATs (red squares) tend to be found at the old, high-B edge of the canonical pulsar population, leading to speculation of an evolutionary link to either the canonical pulsars or the magnetars (see text for details).

the Galactic population of NSs and the rate of core-collapse supernovae (Keane & Kramer, 2008).

1.4.2 Demographics

Radio emission has been observed from all but 71 of the 2524 known pulsars.[1] The known sample of radio pulsars makes up only a small fraction of the estimated ∼30000 active radio pulsars in the Galaxy that are beamed towards the Earth and are brighter than 0.1 mJy (Lorimer et al., 2006b). Estimates of this sort are the result of *population synthesis analyses*, in which simulated versions of the Milky Way are populated with pulsars, and subsequently "searched" by simulated surveys. The distributions

---

[1] From the ATNF Pulsar Catalogue v1.53.

of various pulsar properties, such as luminosity, period, and position, are tuned to provide the best match against the sample of known pulsars. Thus, these analyses provide insight on the underlying properties of the real population of pulsars in the Milky Way.

1.5 Observational Properties of Pulsar Radio Emission

Radio-detected pulsars exhibit a diverse collection of radiative behaviour (e.g. Lyne & Manchester, 1988; Wang et al., 2007; Tiburzi et al., 2013). Nonetheless, it is possible to summarize the basic observational properties shared by the vast majority of radio pulsars.

Some radio pulsars have been detected at frequencies as low as $\sim$20 MHz (Bruck & Ustimenko, 1973), whereas others have been detected at frequencies as high as 225 GHz (Torne et al., 2015). Most current searches for radio pulsars and follow-up studies are conducted between 200 MHz and 3 GHz (e.g. Manchester et al., 2001; Manchester, 2013; Coenen et al., 2014; Kondratiev et al., 2015; Verbiest et al., 2016).

1.5.1 Individual Pulses and Profile Stability

As described earlier, as pulsars rotate, pulses are observed due to their emission beams crossing the line-of-sight. In many cases, the individual pulses are not sufficiently bright to be detected. However, some pulsars are so bright that individual pulses can be detected. The pulses of these pulsars have been studied extensively, revealing a huge variety of behaviour including amplitude fluctuations, shape modulation, random phase jitter, and systematic phase drifts (e.g. Weltevrede et al., 2006a; Lyne et al., 2010; Burke-Spolaor et al., 2012; Shannon et al., 2014). Despite this pulse-to-pulse variability, the average of a large number of pulses (typically $\gtrsim 10^4$) results in a pulse shape that is found to be remarkably stable (e.g. Helfand et al., 1975; Liu et al., 2012). The stability of the integrated *pulse profile* formed by coherently summing the pulses of an observation is essential to long-term pulsar monitoring (see Chapter 4). Pulse profiles are also an important diagnostic used in pulsar searches (see Chapter 2).

The shape of a pulsar's profile is determined by the particular slice of the emission beam that passes through the line-of-sight to the Earth. This is dictated by details of its emission beam and the geometry of the pulsar. The profiles of some binary pulsars have been observed to vary systematically over time due to geodetic precession[1] slowly altering these pulsars' orientation with respect to the Earth (e.g. Kramer, 1998; Breton et al., 2008). This precession enables the emission region of these precessing pulsars to be mapped.

The integrated pulse profiles of most pulsars are found to be extremely stable. In fact, the lack of profile variability in some pulsars over many years has been used to constrain theories of General Relativity (Shao et al., 2013). Also, slight secular trends in the profile of the Crab pulsar observed over decades have been used to provide evidence for the realignment of the star's magnetic field (Lyne et al., 2013).

In contrast, a relatively small number of pulsars exhibit switches between a small number of quasi-stable emission states with different pulse profiles (referred to as *moding*; see e.g. Lyne et al., 2010).

---

[1] A relativistic effect caused by the coupling between the spin and orbital angular momentum.

1.5.2 Luminosities and Flux Densities

Pulsars are faint radio sources. In most cases many ($10^2 - 10^3$) individual pulses must be integrated to make a significant detection. The strength of a pulsar signal as detected by a radio telescope is measured as a *flux density* (denoted by S), which is the energy per time per unit of collecting area per unit bandwidth. The *Jansky*[1] (Jy) is commonly used as the unit of radio pulsar flux densities.

The distribution of published flux densities of pulsars at 1.4 GHz is shown in the top panel of Figure 1.4. The median flux density of the known pulsar population is 0.47 mJy.

Pulsar luminosities (denoted by L) are typically reported as the product of the source's flux density in mJy and the square of the distance to the pulsar in thousands of *parsecs*[2] (i.e. in mJy kpc^2). Reliably determining the intrinsic luminosity of a pulsar is significantly more challenging than measuring its flux density because in most cases the distance to the source is not known. However, the distances to some pulsars can be precisely determined from parallax measurements (Verbiest et al., 2012, and references therein). The distances of pulsars for which no parallax can be measured are often estimated from the effect of the interstellar medium along the line-of-sight by using a model of the Galactic free electron density (e.g. the `NE2001` model of Cordes & Lazio, 2002). Figure 1.4 shows the distribution of luminosities at 1.4 GHz calculated using published flux densities and the best available distance estimates.

The underlying distribution of luminosities of the Galactic population of pulsars can be estimated with population synthesis analyses. Lorimer et al. (2006b) performed such an analysis and estimated the luminosity distribution to be $\log N = -0.77 \log L + 3.5$, where N is the number of pulsars with luminosity L in the Milky Way. The luminosity distribution determined by Lorimer et al. (2006b) is also shown in the bottom panel of Figure 1.4. Our knowledge of the low-luminosity end of the distribution is increasingly uncertain due to the small number of faint pulsars known. Furthermore, the large discrepancy between the measured luminosities and the predictions of the underlying distribution is due to the fact that radio pulsar surveys are flux density limited; that is, they are not capable of detecting the faintest pulsars. However, this is constantly being improved upon by conducting ever more sensitive searches for radio pulsars such as the PALFA survey described in Chapter 3. Survey sensitivity is affected by many factors, some of which will be quantified and discussed in Chapters 2 and 3.

1.5.3 Radio Spectra

Pulsars have steep radio spectra, meaning they are strong at low frequencies and become fainter with increasing frequency. Most pulsars are found to be well modelled by a single power law spectrum,

$$S_f \propto f^{\alpha}, \tag{1.6}$$

where f is the observing frequency, and α is the spectral index, which is nearly always negative.

---

[1] One Jansky, 1 Jy, is $10^{-26} \frac{\mathrm{W}}{\mathrm{m}^2 \cdot \mathrm{Hz}}$.

[2] One parsec, 1 pc, is approximately 3.26 light years $\simeq 3.1 \times 10^{16}$ m.

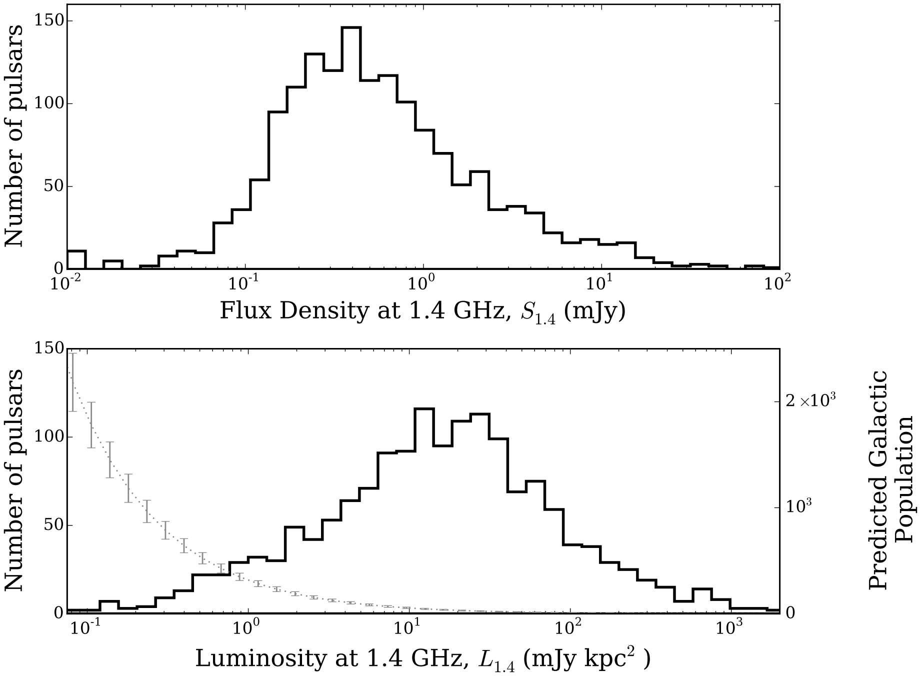

Figure 1.4: *Top* – Distribution of published 1.4 GHz flux densities. The flux densities are taken from the ATNF catalogue (Manchester et al., 2005).
Bottom – Distribution of 1.4 GHz luminosities, estimated from published flux densities and the best available distance, $L_{1.4} = S_{1.4}d^2$ (black histogram). The luminosity distribution derived by Lorimer et al. (2006b) using population synthesis techniques is shown for comparison (grey curve). The known sample of pulsars are a small fraction of the ~30000 potentially detectable pulsars in the Galaxy with $L_{1.4} > 0.1\,\mathrm{mJy\,kpc}^2$. The distances are also taken from the ATNF catalogue.

Maron et al. (2000) used observations at multiple frequencies, predominantly between ~400 MHz and ~5 GHz, to measure the spectral indices of 281 pulsars, finding an average spectral index of $\langle\alpha\rangle = -1.8\pm0.2$. Only a small number of sources, ~10 %, required a two-component, broken power law spectrum.

Measuring spectral indices using the method of Maron et al. (2000) requires calibrated detections of each pulsar at multiple frequencies. This often necessitates dedicated observations. An alternative approach devised by Bates et al. (2013) can be used to estimate the distribution of pulsar spectral indices by simply considering the yields of pulsar surveys conducted at different radio frequencies and applying population synthesis techniques. By using their population synthesis-based method, Bates et al. (2013) found an average spectral index of $\langle\alpha\rangle = -1.4 \pm 1.0$, in agreement with the results of Maron et al. (2000), albeit with a larger variance.

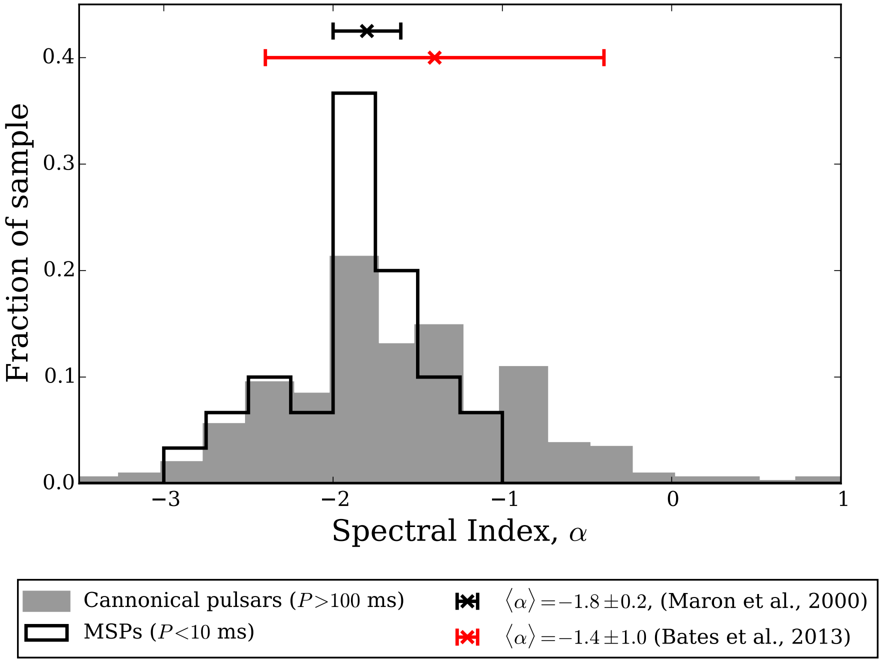

Figure 1.5: Published radio spectral indices for 280 canonical pulsars and 30 MSPs (from the ATNF catalogue; Manchester et al., 2005). Based on the careful analysis of the spectra of 281 pulsars, Maron et al. (2000) reported a mean spectral index of $\langle\alpha\rangle = -1.8 \pm 0.2$. Bates et al. (2013) used a population synthesis approach to estimate the mean spectral index to be $\langle\alpha\rangle = -1.4 \pm 1.0$.

1.6 The Many Applications of Pulsars

Pulsars have been used to great effect as tools to study a wide variety of topics. Many of these applications require long-term (generally multi-year) monitoring campaigns. These observations are used to derive precise models of pulsars' spin phase that are capable of predicting *every* rotation of the star. This type of monitoring, and the related analysis, is referred to as *pulsar timing*. An overview of the topic is presented in Chapter 4, and Chapters 5 through 7 provide examples of pulsar timing in practice and its applications.

In the following sections, I will highlight several applications of pulsar studies, both timing-based and not, to give a sense of breadth of the field and to provide an overview of how scientific studies are conducted with pulsars. In each case, I specify the type of pulsar generally used in the analyses.

Measuring Neutron Star Masses

Type of pulsar: Binary (MSP or mildly recycled)
Type of analysis: Timing

Knowing the mass of a pulsar makes it far more useful for a range of applications. For example, pulsar masses help improve our understanding of the nature of ultra-dense matter. Mass measurements also help constrain theories of relativistic gravity. Furthermore, knowing the masses of binary pulsars provides insight into stellar evolution, as well as the evolution of binary systems.

Masses can be determined for pulsars in binary systems. It is possible to constrain the mass of a binary pulsar by measuring the mass function (e.g. Lorimer & Kramer, 2004),

$$f_m\left(m_p, m_c\right) = \frac{\left(m_c \sin i\right)^3}{\left(m_p + m_c\right)^2} = \frac{4\pi^2}{T_\odot}\frac{x^3}{P_b^2}\ , \tag{1.7}$$

where m_c and m_p are the masses of the companion and pulsar (both measured in $M_\odot$), respectively, i is the inclination angle of the orbit with respect to the line of sight,[1] x, is the semi-major axis of the orbit projected onto the plane of the sky, measured in light-seconds (i.e. $x = \left(a \sin i\right)/c$, where a is the orbit's semi-major axis), P_b is the orbital period, and $T_\odot \equiv \frac{GM_\odot}{c^3} = 4.925490947\,\mu\text{s}$ is a solar mass expressed in time units.

If the mass function of the companion can also be determined (e.g. by measuring the motion of the companion), or if the mass of the companion can be estimated from other means (e.g. by modelling spectra features), then the mass of the pulsar can be further constrained. Unfortunately, this may not uniquely determine the mass of the two stars.

The most precise mass determinations come from measuring the signatures of relativistic effects on the orbital motion of pulsars (see e.g. Damour & Taylor, 1992). These relativistic effects, and other non-relativistic effects, cause the motion of the pulsar to deviate from a Keplerian orbit. Fortunately, these deviations can be parameterized in terms of *post-Keplerian parameters*. The post-Keplerian parameters can be expressed in terms of the masses of the binary components and the Keplerian orbital parameters for a broad range of theories of gravity (Damour & Taylor, 1992). Thus, by measuring at least two post-Keplerian corrections and attributing them entirely to a particular theory of gravity, it is possible to uniquely determine the masses of the two stars in the binary system.

The measured masses of pulsars range from ~1.2 to $2\,M_\odot$ (e.g. Stairs, 2004; Demorest et al., 2010; Antoniadis et al., 2013, and references therein).

Studying Ultra-Dense Matter

Type of pulsar: Binary (MSP or mildly recycled)
Type of analysis: Timing

Pulsars are being used to constrain, and hopefully eventually determine, the behaviour of matter at ultra-high densities. The internal structure of NSs is determined by the *equation-of-state* (EOS) of matter at high densities. The EOS can be defined as $\mathcal{P}(\rho)$, where $\mathcal{P}$ is the pressure as a function of density, ρ (e.g. Shapiro & Teukolsky, 1986). At their cores, the densities of NSs are thought to be greater than that of the atomic nucleus (Lattimer & Prakash, 2004). Thus, it is possible to link the properties of observed NSs to the behaviour of matter at densities inaccessible in terrestrial experiments.

---

[1] An orbit viewed edge-on has $i = 90°$.

For a given model of the EOS it is possible to calculate the dependence of the radius of a NS on its mass, as well as a maximum mass for NSs. If a NS mass is above this maximum mass, it will rule out the EOS. This, in turn, applies constraints on the behaviour of matter at super-nuclear densities. Two massive pulsars have recently excluded many EOS models (Demorest et al., 2010; Antoniadis et al., 2013).

Additional constraints on the nature of ultra-dense matter can be imposed from the maximum known NS spin frequency. Each EOS model predicts a maximal rotation rate. A NS rotating faster than this limit will be torn apart by centrifugal forces (Cook et al., 1994). Therefore, each time a record-breaking fast pulsar is discovered, the constraints on the EOS are further tightened, possibly ruling out some models (e.g. Hessels et al., 2006).

Testing Relativistic Gravity

Type of pulsar: Binary (MSP or mildly recycled), isolated MSPs
Type of analysis: Timing, profile stability

Radio pulsars are stable, predictable objects, so much so that some sources can be used to test Einstein's theory of General Relativity (GR) and alternative theories of relativistic gravity. Some of the latter predict observable effects on pulsar timing, orbital parameters, and pulse profiles. To date, the lack of detection of these effects have been used to impose some of the most stringent constraints on these alternative theories.

Relativistic corrections to Keplerian orbital motion are required to accurately model the dynamics of some binary pulsars. As described above, by measuring two such relativistic terms and assuming a specific theory of gravity, it is possible to measure the mass of a pulsar and its companion. In cases where more than two relativistic corrections are measured, the consistency of these parameters enables tests of relativistic gravity. In the case of the double pulsar system, PSR J0737−3039 A/B, a total of 6 relativistic parameters are measured (Kramer et al., 2006b; Breton et al., 2008). Together with the measured mass ratio, these relativistic terms allow for 5 tests of GR. The most stringent such test is consistent with GR within 0.05 %. Similar tests have been possible with other double NS systems (e.g. Taylor & Weisberg, 1989).

Even studies that do not impose strong constraints on GR have been used to challenge alternative theories of relativistic gravity. For example, studies of the binary pulsar PSR J1738+0333 and its low-mass WD companion have been used to place stringent limits on the emission of dipolar gravitational waves, which have subsequently been used to restrict entire families of alternative theories of gravity (Freire et al., 2012). Also, Gonzalez et al. (2011) used observations of 27 wide-orbit binary MSPs and statistical arguments to set limits on the degree of violation of the strong equivalence principle, which is predicted by some alternatives to GR. Furthermore, tests of relativistic gravity are not limited to binary pulsars: Shao et al. (2013) obtained the most constraining limits on violation of isotropic local Lorentz invariance, which would result in a preferred inertial reference frame, by studying two solitary pulsars, PSRs B1937+21 and J1744−1134.

All of these examples show that a wide variety of pulsars (NS–NS binaries, NS–WD binaries, and isolated pulsars) can be used to study relativistic gravity, so long as the system parameters lie in a fortuitous regime for constructing tests and sufficiently precise measurements are possible.

Probing the Interstellar Medium

Type of pulsar: All
Type of analysis: Wide bandwidth or multi-frequency observations

Radio pulsar signals are influenced by the interstellar medium (ISM). For example, free electrons in the ISM along the line-of-sight cause frequency-dependent delays of radio pulses as they propagate to the Earth. The magnitude of the delay is related to the free-electron density integrated along the line-of-sight, that is, the *dispersion measure* (DM),

$$\mathrm{DM} = \int_0^d n_e \mathrm{d}l, \tag{1.8}$$

where d is the distance to the pulsar, and n_e is the electron number density. The DM of a pulsar is typically reported in units of $\mathrm{pc\,cm^{-3}}$. Additional details about the frequency-dependent dispersion delay are provided in § 2.3.

Also, inhomogeneities in the distribution of free electrons in the Galaxy cause radio waves to be scattered. This causes the emission making up a pulse to follow multiple paths as it propagates towards the Earth, thus broadening the observed shape of the pulse by introducing an exponential tail. These same inhomogeneities also give rise to interstellar scintillation, constructive and deconstructive interference patterns (see e.g. Lorimer & Kramer, 2004). Furthermore, the polarization of radio pulsar signals are rotated by the local Galactic magnetic field along the line-of-sight (i.e. Faraday Rotation).

It is possible to model the ISM by studying the imprint of the ISM on a large collection of pulsar observations. For example, radio pulsars have been used calibrate models of the free-electron content in the Milky Way (e.g. Cordes & Lazio, 2002), as well as improve understanding of large-scale structures of the Galactic magnetic field (e.g. Noutsos et al., 2008; Eatough et al., 2013b).

Studying individual pulsars has proven to be successful at probing specific features of the ISM. For instance, the strength of the ambient magnetic field close to the Galactic Centre has been measured using radio emission from a pulsar (Eatough et al., 2013b). Also, clouds of free electrons migrating through the Galaxy can be detected and studied as they pass in front of a radio pulsar (e.g Maitia et al., 2003).

Building a Gravitational Wave Detector

Type of pulsar: MSPs (extremely stable rotators)
Type of analysis: Timing

The passage of gravitational waves (GWs) over the Earth modulates the arrival times of pulses (Detweiler, 1979). Because the residual effect on pulsars is minuscule, pulse arrival times need to be measured with precisions $\lesssim$100 ns (e.g. Jenet et al., 2005). Fortunately, the high rotational stability of MSPs can be exploited to detect such a small signal. That is, pulsars are sensitive to individual GW sources, as well as to the gravitational wave background (GWB) formed by the superposition of many individual sources of GWs. The cosmological population of super-massive black hole binaries is most likely the strongest contribution to the GWB (see e.g. Sesana, 2013a, and references therein). In addition to super-massive black hole binaries, cosmic strings and relic gravitational waves from inflation may also have a measurable effect on the GWB (e.g. Maggiore, 2000).

An isotropic, stochastic GWB would show correlated deviations in the pulse arrival times of a collection of highly stable MSPs, a so-called *Pulsar Timing Array* (PTA). The magnitude of correlations between different pairs of pulsars only depends on their angular separation (Hellings & Downs, 1983). To measure such a GWB signal, regular observations over ∼10 yr of ∼20 − 40 stable MSPs distributed roughly uniformly over the celestial sphere must be analyzed with specialized algorithms (Jenet et al., 2005).

At present, there are three large PTA collaborations striving to detect gravitational waves: the European Pulsar Timing Array (EPTA; Kramer & Champion, 2013), the North American Nanohertz Observatory for Gravitational Waves (NANOGrav; McLaughlin, 2013), and the Parkes Pulsar Timing Array (PPTA; Hobbs, 2013b). Together, these three collaborations form the broader International Pulsar Timing Array community (IPTA; Manchester, 2013). Data collected by the individual PTA projects are combined for joint IPTA projects (Verbiest et al., 2016, and Chapter 7 for an example of such a project).

To date, none of the individual PTA projects have detected gravitational waves (Demorest et al., 2013; Shannon et al., 2013; Lentati et al., 2015). However, the upper limits derived already constrain some models of structure formation in the Universe (Shannon et al., 2013). Also, the lack of any discernible GW-induced signal was used to argue against the claim of a nearby super-massive black-hole binary system (Jenet et al., 2004).

The unprecedented length and precision of the data set being assembled by the IPTA community is especially well suited to other projects. For instance, in Chapter 7 I use these data to measure the masses of Solar System planets and describe how the available Solar System ephemerides may be validated.

Investigating Binary Stellar Evolution

Type of pulsar: Binary (MSP or mildly recycled)
Type of analysis: Timing, modelling

More than 150 Galactic pulsars exhibit orbital motion[1] (ATNF Pulsar Catalogue, Manchester et al., 2005, and references therein). There is a strong synergy between studying binary pulsars and modelling binary stellar evolution. That is, by combining the observed orbital parameters with knowledge about stellar evolution, accretion physics, and supernova explosions, it is possible to deduce the history of some of these systems, as well as validate the assumptions made when modelling the past evolution of the systems.

The standard models of binary and stellar evolution are capable of explaining the origin of many known pulsar binary systems. However, as more pulsars have been discovered, the number of binary systems not conforming to the standard theories has increased. New discoveries have also uncovered new sub-classes of binary systems (also triple systems! – Ransom et al., 2014), which have led to the suggestion of new formation mechanisms for MSPs (e.g Freire & Tauris, 2014). New studies of binary pulsars have also helped clarify the details of accretion physics. Additionally, the number of pulsars in various types of binary systems helps explain the relative

---

[1] We have excluded binary pulsars in globular clusters because their dense environments increase the chances of stellar interactions, influencing the formation and properties of binary systems.

number of progenitor systems, as well as improve understanding of how these systems evolve. Furthermore, some information can be gleaned about the X-ray binary phases leading to the currently observed binary pulsar systems.

Modelling the Underlying Pulsar Population

Type of pulsar: All
Type of analysis: Pulsar surveys (i.e. discoveries), modelling

It is possible to model the underlying distributions of various pulsar properties by considering the known sample of pulsars, the selection effects of the surveys in which they were found, and the density distribution of free electrons within the Milky Way.

In particular, the >1000 pulsars detected in the Parkes Multibeam Pulsar Survey (PMPS) have been used to calibrate population synthesis analyses: one such analysis was used to predict that there are $(30.0 \pm 1.1) \times 10^3$ pulsars in the Galaxy with a luminosity $>0.1\,\mathrm{mJy\,kpc^2}$ at 1.4 GHz beamed towards the Earth (Lorimer et al., 2006b). Faucher-Giguère & Kaspi (2006) used the same data set to estimate the total number of active pulsars (i.e. without considering a luminosity cut-off) in the Galaxy beamed towards the Earth to be $(1.2 \pm 0.2) \times 10^5$. Faucher-Giguère & Kaspi (2006) also used population synthesis techniques to predict the birth rate of pulsars.

Performing population analyses requires a large sample of pulsars and an accurate understanding of the biases of the surveys in which they were discovered. The severe biases against finding MSPs in the PMPS were taken into account by Lorimer et al. (2015). However, the biases against finding slow canonical pulsars due to long-timescale fluctuations (i.e. red noise) and radio frequency interference have only now been quantified (see Chapter 3). Future population analyses will need to take into account the biases presented in Chapter 3 to make more accurate predictions.

1.7 Organization of this Thesis

The remainder of this thesis is organized into two parts: *Searching for Pulsars* and *Timing Pulsars.*

Part I: Searching for Pulsars begins in Chapter 2 with an overview of how radio observations are analyzed to detect the signals of unknown pulsars. Chapter 3 examines how these techniques are used to analyze data from the PALFA survey for radio pulsars in the Galactic plane being conducted at the Arecibo Observatory in Puerto Rico. Chapter 3 also describes the discovery of 40 pulsars, presents a detailed analysis of the survey's sensitivity and provides a discussion of the implications of these findings on population synthesis analyses.

Part II: Timing Pulsars begins in Chapter 4, where a summary of the principles and techniques underlying pulsar timing is provided. Chapter 5 provides details on the timing analysis of PSR J1952+2630, a mildly recycled pulsar with a massive white dwarf companion discovered in the PALFA survey. Then in Chapter 6, the first four years of pulsar timing with the new wider-bandwidth, higher-precision PSRIX data recorder of the Effelsberg 100-m Radio telescope is presented. Chapter 7 highlights one of the many non-gravitational-wave-related applications of high-precision pulsar timing array data from the IPTA, by using this data set to study the Solar System.

PART I

SEARCHING FOR PULSARS

2

SEARCHING FOR AND DISCOVERING PULSARS

Most known pulsars were discovered from their radio emission. Searches for radio pulsars generally fall into one of two categories: *blind searches* and *targeted searches.*

Blind searches are the basis of large-scale pulsar surveys, which search a wide patch of the sky for radio pulsars, and are responsible for many scientifically interesting pulsars. Recent notable discoveries found in blind radio pulsar searches include the double pulsar system, PSRs J0737−3739A/B (Lyne et al., 2004), PSR J1023+0038, a pulsar transitioning from a LMXB to a MSP (Archibald et al., 2009), the MSP PSR J0337+1715, which is in a triple system (Ransom et al., 2014), and the first magnetar found by its radio emission, PSR J1622−4950 (Levin et al., 2010), among many others. Examples of large-scale pulsar surveys include the PALFA survey, a search of the Galactic plane for radio pulsars with the Arecibo Observatory (see Chapter 3 for details), the Parkes Multibeam Pulsar Survey (PMPS), which is responsible for discovering nearly half of all known radio pulsars (e.g. Manchester et al., 2001; Lorimer et al., 2006b), and the High Time Resolution Universe North/South (HTRU-N/S) surveys, which are using the Parkes Radio Telescope in Australia and the Effelsberg Radio Telescope in Germany to search the entire sky for radio pulsars (Keith et al., 2010a; Barr et al., 2013b). Because the positions and parameters (e.g. period, DM, acceleration) of the undiscovered pulsars in the survey region are not known, a large number of observations must be made. The data from each of these observations must be searched for a broad range of possible parameter values. These searches are computationally expensive, but have discovered the vast majority of all known pulsars, roughly 80 %.

Targeted searches, on the other hand, consist of searching for pulsar signals in observations of specific sky positions thought to likely contain radio pulsars. These might include globular clusters (GCs; e.g. Lyne et al., 1988; Manchester et al., 1991; Ransom et al., 2005), supernova remnants (e.g. Manchester, 1988; Kaspi et al., 1996; Lorimer et al., 1998), the positions of gamma-ray point sources (e.g Ransom et al., 2011; Cognard et al., 2011; Keith et al., 2011; Barr et al., 2013a), or the positions of NSs found in other bands (e.g. Kondratiev et al., 2009; Lazarus et al., 2012). Furthermore, targeted searches may be *informed* if some additional knowledge about the source is available. For example, in the case of GC searches, previously discovered radio pulsars in the GC provide a determination of its dispersion measure (DM). In the case of searching for radio emission from magnetars monitored in the X-ray band, the spin period of the source is already known. Also, in some cases, estimates of binary orbital parameters may be available from optical/gamma-ray observations of a gamma-ray source (e.g. Romani, 2012; Pletsch et al., 2012; Ray et al., 2013). By reducing the number and/or viable range of search parameters, informed searches greatly cut the computational cost of searching for pulsar signals. Despite finding only a relatively modest number of pulsars, targeted searches are responsible for several important discoveries, including the fastest-spinning pulsar known, PSR J1748−2446ad, in the globular cluster Terzan 5 (Hessels et al., 2006), the radio emission from the magnetars XTE J1810−197, 1E 1547.0−5408 and SGR J1745−2900 (Camilo et al., 2006, 2007a; Shannon & Johnston, 2013, , respectively), and many MSPs found coincident with gamma-ray point sources (e.g. Ransom et al., 2011; Cognard et al., 2011; Keith et al., 2011; Barr et al., 2013a).

The basic steps of both blind and targeted searches for radio pulsars are the same. In this chapter, I will provide a general overview of the search process. The next chapter describes the analysis of data from the PALFA survey as a case study in blind, large-scale searches for radio pulsars.

2.1 Overview

Searching for radio pulsars can be divided into five fundamental steps: 1) removing radio frequency interference, 2) removing the effect of the interstellar medium, 3) searching for periodic signals, 4) searching for impulsive signals, and 5) identifying the most promising signal candidates. Diagnostic plots are made for each of these candidates. By inspecting the plots, the candidates most likely to be pulsars are selected to be re-observed in the hopes of confirming the discovery of a pulsar. I will cover the basic principles of each of the five steps and explain its place within the complete search process.

Pulsar Search Software

There exist software packages that implement the algorithms necessary to search radio observations for pulsars. The two main packages are `PRESTO`[1] (Ransom, 2001) and `SIGPROC`[2] (Lorimer, 2011). Both packages are capable of reading various data file formats, and are sufficient to conduct a complete blind pulsar search. In practice, the basic algorithms implemented in these two packages are augmented with site-specific experience and custom methods catered to the individual project. Details of how a search can be customized are presented in Chapter 3, in which the `PRESTO`-based pipeline used to analyze PALFA survey data is thoroughly described. In contrast, the discussion in this chapter focuses on the general methods used in pulsar searches.

Search-Mode Observations

The data from search-mode observations are a sequence of rapidly and uniformly sampled spectra. Modern pulsar surveys (e.g. Cordes et al., 2006; Keith et al., 2010a; Barr et al., 2013b; Stovall et al., 2014; Coenen et al., 2014) have high time and frequency resolution ($\sim 50-100\,\mu$s and $\sim 10-600\,$kHz, respectively), as well as wide bandwidths ($\sim 50-500\,$MHz): high time resolution is required to resolve the pulses of fast pulsars, high frequency resolution is necessary to better correct for the dispersive smearing effect of the interstellar medium, helping to detect distant pulsars, and wide bandwidths make it possible to detect fainter signals, as well as make it easier to differentiate between interference and astrophysical sources. Furthermore, to increase sensitivity to faint pulsars, long integration times are employed. However, longer observations are more computationally challenging to search, especially when performing thorough searches for pulsars in binary systems (see § 2.4).

More details about the various factors that affect the sensitivity of radio observations to pulsars are presented in § 2.6 and re-visited in Chapter 3.

---

[1] https://github.com/scottransom/presto

[2] http://sigproc.sourceforge.net/

2.2 Mitigating Radio Frequency Interference

Radio telescopes inadvertently receive a wide variety of unwanted, non-astrophysical signals. These *radio frequency interference* (RFI) signals are often quite bright and make it difficult to detect the much fainter pulsar signals. Because RFI is of terrestrial origin, it is not dispersed by the interstellar medium, thus it has a DM of $0\,\mathrm{pc\,cm^{-3}}$. RFI is manifested in a variety of ways, impacting various stages of the search process, and thus necessitating a suite of mitigation strategies. A summary of the diversity of RFI signals is shown in Figures 2.1 and 2.2.

The top panel of Figure 2.1 shows a segment of time-domain data from a PALFA survey observation. In this time series, there are clear airport radar signals recurring every $\sim$12 s (at $t \simeq 71$, 83, and 95 s). Each of these radar bursts are made up of many sub-pulses separated by $\sim$3 ms. Also evident is a bright, impulsive signal at $t \sim 94$ s. Additionally, the long-timescale undulations throughout the time span are the result of red noise, possibly caused by gain variations in the receiver or the superposition of many RFI sources.

The bottom panel of Figure 2.1 shows the power spectrum of the entire 181 s of the PALFA observation shown in the top panel of the figure. The power spectrum emphasizes the RFI signals with underlying periodicities. For example, the red noise is manifested as a rising trend towards lower frequencies and the radar sub-pulse structure gives rise to a forest of peaks around $\nu \sim 300$ Hz. These peaks correspond to the various repetition rates of the radar. Furthermore, by inspecting the power spectrum it is possible to discern sources of RFI that are not apparent in the time domain, such as the peak at $\nu = 60$ Hz which is due to the electrical mains.

As in the time domain and the modulation-frequency domain (i.e. power spectrum), there is significant diversity of the properties of RFI in the radio-frequency domain. Broadly speaking, RFI signals are characterized as having broad or narrow bandwidths. Some narrow-band RFI signals are persistent, whereas others are impulsive. Other impulsive RFI signals are broad-band. Examples of broad and narrow-band RFI are shown in Figure 2.2.

RFI must be excised from radio observations to maximize sensitivity to pulsars. Various algorithms are used to identify the offending signals and remove or suppress them at multiple stages of the data analysis. Section 3.3.4 provides a detailed description of the RFI mitigation strategy used by the primary search pipeline of the PALFA survey.

2.3 Removing the Effect of the Interstellar Medium

Free electrons in the interstellar medium (ISM) along the line-of-sight to the pulsar distort its radio emission. Lower frequencies are delayed with respect to high frequencies according to (e.g. Lorimer & Kramer, 2004)

$$\Delta t\left(f; f_{\mathrm{ref}}\right) \simeq 4.15 \times 10^{6} \left(f^{-2} - f_{\mathrm{ref}}^{-2}\right) \mathrm{DM}, \tag{2.1}$$

where Δt is the relative time delay (in ms) between some frequency f and a reference frequency f_{ref} (both in MHz), commonly taken to be the top of the observing band, and DM is the dispersion measure (in $\mathrm{pc\,cm^{-3}}$; recall Eq. 1.8).

Fortunately, because the frequency dependence of this DM delay is well understood, the majority of this effect can be removed, given the DM, by advancing (in time) the

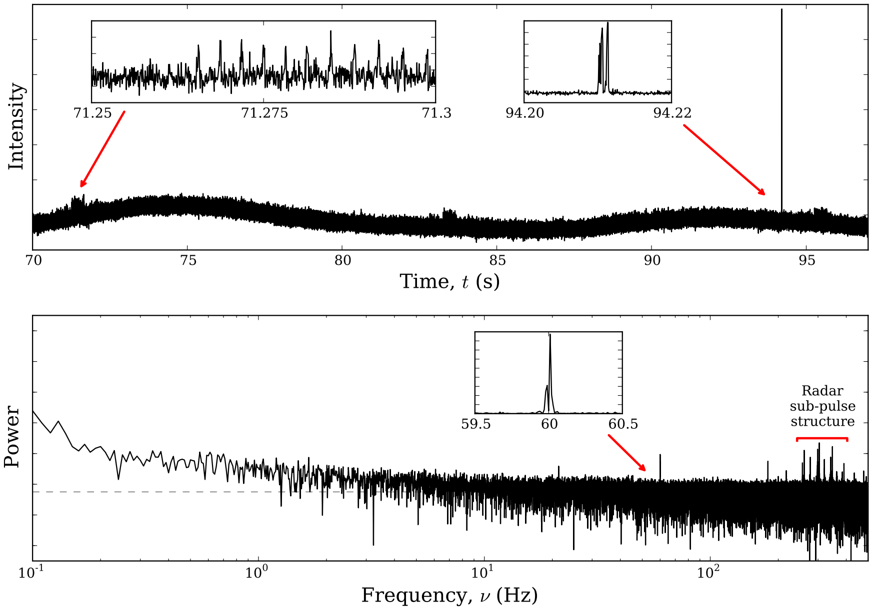

Figure 2.1: Examples of RFI in a 181-s long PALFA survey observation from Nov. 13, 2014. *Top* – A 27-s segment of the observation's DM $= 0\,\mathrm{pc\,cm^{-3}}$ time series. The undulating baseline is due to low-frequency noise (i.e. red noise). The three visible bursts of airport radar at $t \simeq 71$, 83, and 95 s highlight the periodic nature of some sources of RFI, both with its ∼12-s repetition rate, and its ∼3-ms sub-pulse structure (*left inset*). At $t \sim 94$ s there is a short, bright burst of RFI (*right inset*).
Bottom – The power spectrum of this observation also shows the effect of RFI. For instance, red noise is apparent as an excess of power in the low-frequency part of the spectrum. This is especially obvious when comparing against the mean value of the high-frequency part of the spectrum (grey dashed line). Also, the radar sub-pulse structure gives rise to a forest of peaks at around $\nu \sim 300$ Hz, which corresponds to the various sub-pulse repetition rates. The 60-Hz electrical mains of Puerto Rico results in a large peak in the power spectrum at that frequency (*inset*) despite not being obvious in the time series.

individual frequency channels of the data file according to Eq. 2.1.

If the dispersive delay across the observing band is not corrected for, a pulsar signal will be broadened, and thus have lower S/N. As the un-corrected DM delay approaches the period of the pulsar, its pulsations are almost entirely smeared out, rendering them virtually undetectable. Figure 2.3 shows corrected and uncorrected pulse profiles for the 4.57-ms pulsar PSR J1713+0747, as well as the DM delay across the observing band.

When conducting a blind search, because the DMs of pulsars cannot be predicted a priori,[1] many (often thousands) of trial DM values, typically ranging from 0 to $\sim 5000\,\mathrm{pc\,cm^{-3}}$, must be used to retain sensitivity to unknown pulsar signals that may be present in the data. For each DM trial, the frequency channels of an observation are shifted according to Eq. 2.1 and then summed to produce a *dedispersed time series*.

---

[1] When conducting targeted searches, it may be possible to predict the DM of a pulsar due to an association with other objects, such as other pulsars in the same globular cluster.

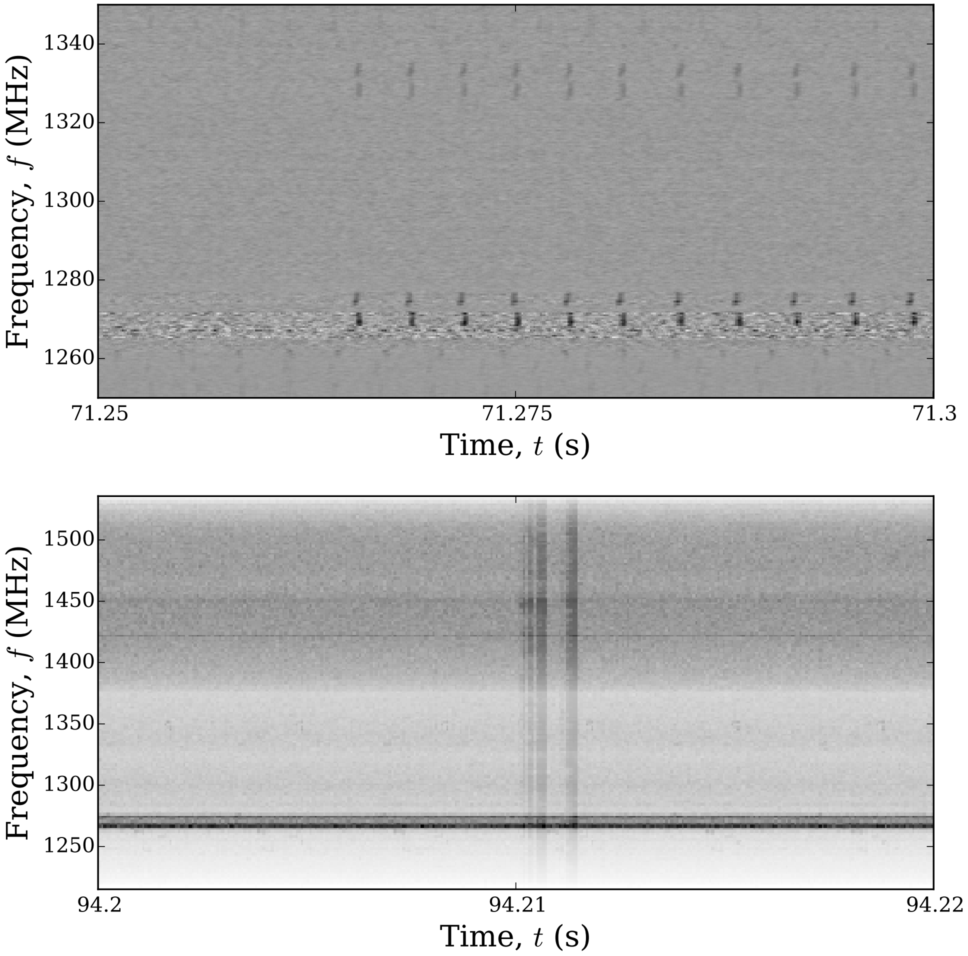

Figure 2.2: Examples of the intensity of RFI over the observing band from the same PALFA survey scan shown in Fig 2.1.
Top – The airport radar pulses are concentrated in narrow bands around $f \simeq 1270$ and 1330 MHz. The data in this panel are from a sub-set of the observation's 322-MHz band. The mean bandpass shape has been subtracted to emphasize the radar pulses at $f \simeq 1270$ MHz and $f \simeq 1330$ MHz.
Bottom – Some interference signals have broad bandwidths, for instance the burst at $t \sim 94.21$ s, whereas others are narrow-band, such as the persistent excess noise at $f \simeq 1270$ MHz.

Each time series is then individually searched for periodic and impulsive signals (see §§ 2.4 and 2.5). The details of how trial DM values are chosen for the analysis of PALFA survey data are provided in § 3.3.3.

In addition to the DM delay across the observing band, there are two effects of the ISM that cannot be corrected for in search-mode observations: the DM smearing within each frequency channel,[1] and the multi-path scattering, which introduces an exponential tail to pulse profiles (recall § 1.6). Both of these effects reduce the S/N of pulse profiles by broadening them (see § 3.5.4 for more details).

2.4 Searching for Periodic Signals

The majority of known pulsars are most significantly detected by using Fourier transforms to uncover the underlying periodicity of their emission. Various techniques have been devised to maximize the sensitivity of Fourier-domain-based searches.

Fourier Transforms

The Fourier Transform (FT) decomposes functions of time into constituent sinusoidal functions of different frequencies. The dedispersed time series generated in pulsar searches are discretely and uniformly sampled, thus the discrete Fourier transform (DFT) is used. The DFT of a time series is (e.g. Press et al., 2007)

$$A_k = \sum_{j=0}^{N-1} n_j \mathrm{e}^{-2\pi i j k / N_{\mathrm{samp}}}, \tag{2.2}$$

where A_k is the Fourier amplitude corresponding to frequency bin k, the n_j are the N_{samp} time series samples indexed by j, and $i = \sqrt{-1}$. The A_k are complex-valued numbers, encoding the amplitude and phase of a sinusoid of frequency $\nu = k/(N_{\mathrm{samp}}\Delta t)$ where Δt is the duration of each time series bin. The duration of the time series, $t_{\mathrm{obs}} = N\Delta t$, determines frequency resolution of the FT as $\Delta\nu = 1/t_{\mathrm{obs}}$. The highest frequency of the FT is given by the *Nyquist frequency*, $\nu_{\mathrm{max}} = 1/(2\Delta t)$. The power spectrum of the FT is related to the A_k according to

$$P_k = |A_k|^2 \,. \tag{2.3}$$

A periodic signal will result in peaks in the power spectrum at the signal's repetition rate and harmonically related frequencies. A pure sinusoid contains a single frequency, and thus results in a single peak. Pulsars typically have profiles that are narrower than a sinusoid and/or have complex shapes. Thus, the power spectrum of data containing a pulsar signal will include multiple peaks corresponding to sinusoids at related frequencies that when summed will reconstruct the signal. Figure 2.4 shows examples of the power spectrum and profiles for a sinusoidal pulse and a Gaussian pulse.

Harmonic Summing

The power of most pulsars is spread over multiple harmonically related peaks in the Fourier spectrum. To maximize sensitivity to a pulsar, the power from all significant

---

[1] The DM smearing within the channels can be lessened by using finer frequency resolution. However, once an observation is made, this cannot be changed.

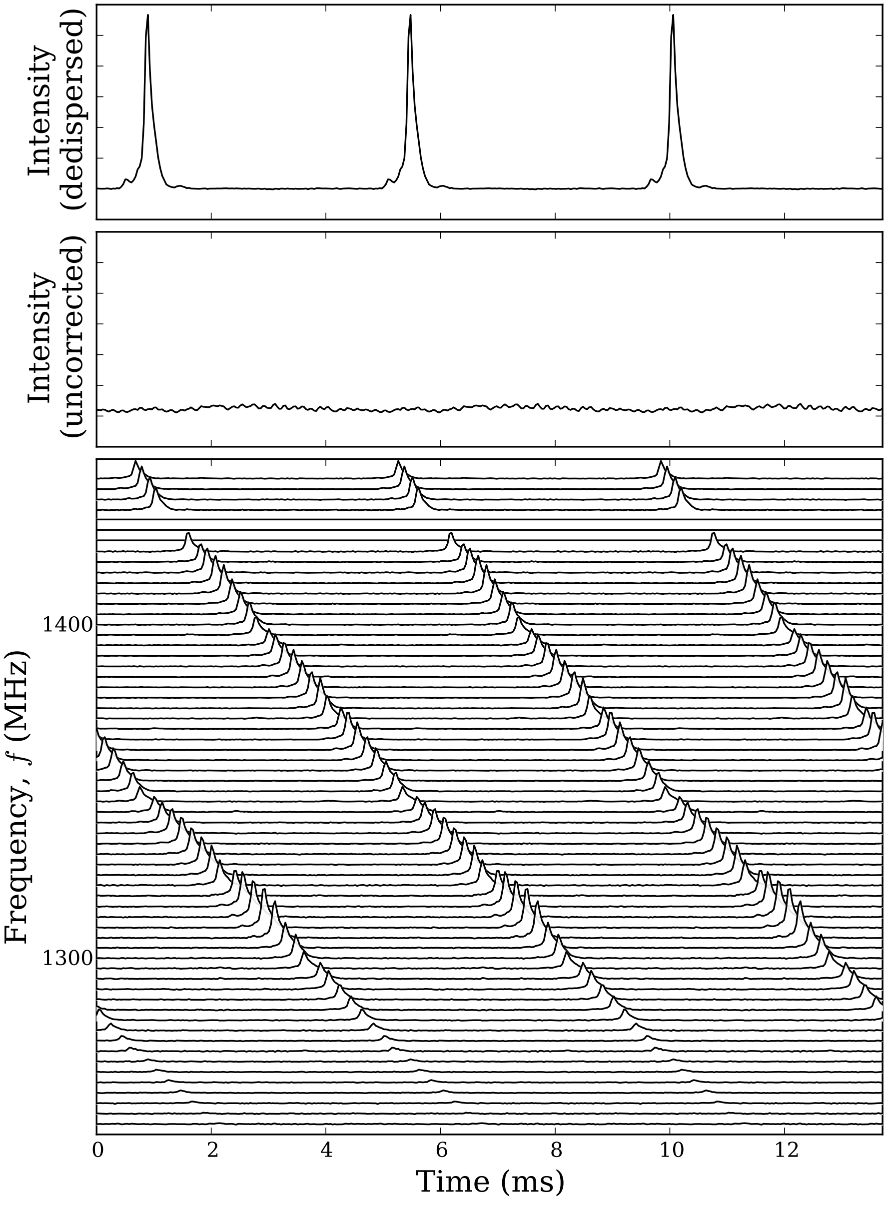

Figure 2.3: *Top* – The dedispersed, frequency-integrated profile for an observation of PSR J1713+0747 ($P \simeq 4.57\,\mathrm{ms}$, $\mathrm{DM} \simeq 16\,\mathrm{pc\,cm^{-3}}$). The profile is repeated 3 times to show the full delay across the frequency band.
Middle – The resulting integrated profile when the effect of dispersion by the ISM is not first removed. The bright pulsar signal is completely washed out.
Bottom – The frequency vs. phase plot of the observation clearly showing the frequency-dependence of the delay affecting the pulse.

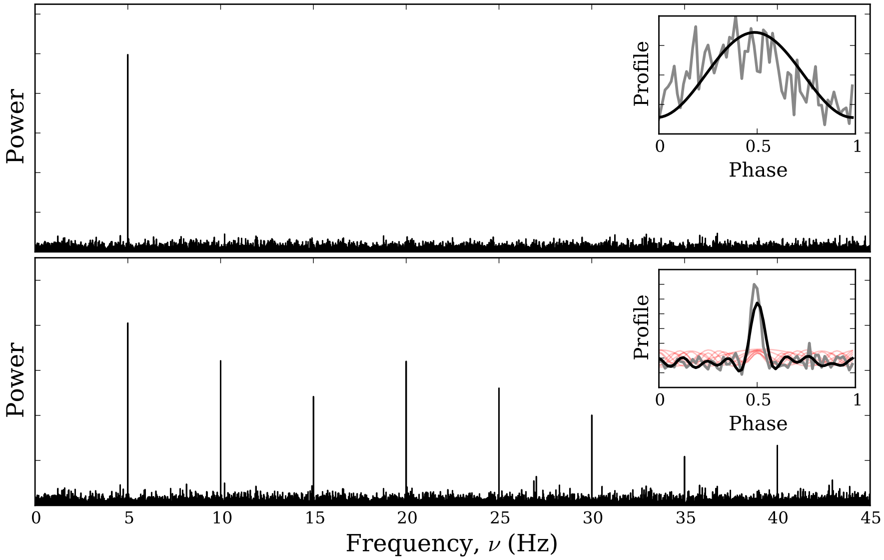

Figure 2.4: *Top* – The power spectrum of a simulated 5-min observation containing a pure sinusoidal signal with a frequency of $\nu = 5\,\mathrm{Hz}$. The Fourier transform of a pure sinusoid contains a single harmonic at the frequency of the sine wave. The inset shows the profile produced when folding the data at $\nu = 5\,\mathrm{Hz}$ (in grey), and the reconstructed profile from the single significant harmonic (in black). See the text for a description of folding.
Bottom – The power spectrum of another simulated 5-min observation, this time containing a train of Gaussian pulses with a repetition rate of $\nu = 5\,\mathrm{Hz}$. The power spectrum contains several peaks at related frequencies. The inset again shows the folded profile (in grey) and the reconstructed profile (in black). The sinusoids corresponding to the individual harmonics are shown (the red curves).

harmonics should be summed. The number of significant harmonics depends on the shape of the pulse profile, scaling roughly as $N_{\mathrm{harm}} \sim P/W$, where P is the pulsar's period and W is the width of the profile. That is, pulsars with wider profiles have their Fourier power concentrated in a small number of harmonics, whereas pulsars with narrower profiles have more significant harmonics and a flatter distribution of powers. See examples of the distribution of harmonic power in Figure 2.4.

When searching data for unknown pulsar signals, neither the fundamental frequency nor the number of significant harmonics are known. Therefore, harmonically summed spectra are computed for all frequency bins. For example, a spectrum consisting of the sum of the fundamental and second harmonic can be computed by stretching the power spectrum by a factor of two and adding it to the original spectrum. This stretch-and-sum technique is repeated to compute high-order harmonic spectra. Periodic signals in the observation are found by searching these harmonically summed spectra for peaks. In practice, it is common to search summed spectra consisting of 1, 2, 4, 8, and 16 harmonics.

Figure 2.5 shows an example of how the significance of a pulsar signal grows as more harmonics are summed. Harmonic summing of FTs is essential to maximize sensitivity to pulsars with narrow profiles.

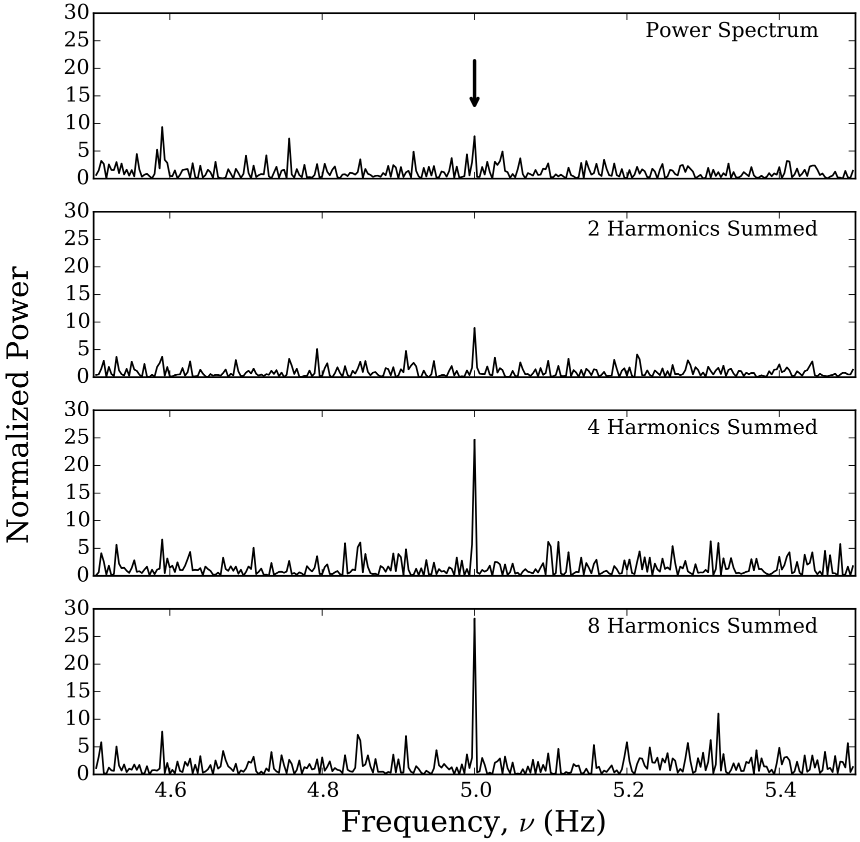

Figure 2.5: The dependence of a simulated pulsar signal's significance on the number of harmonics summed. The profile of this pulsar is relatively narrow (5 % of the pulse phase), thus the power in the Fourier domain is spread over multiple harmonically related peaks (see the bottom panel of Figure 2.4). Harmonic summing is necessary to collect the signal power of these harmonics and increase the detection significance.

Improving Sensitivity to Binary Pulsars

The motion of a binary pulsar about its companion causes the observed periodicity of the pulsar's signal to vary over time due to Doppler shifts. If the resulting line-of-sight velocity is not sufficiently constant over the course of an observation, the pulsar signal is spread over multiple adjacent bins in the power spectrum and its significance is reduced (see Figure 2.6). In the time domain, the pulse profile is smeared out, and thus is also less significant.

Fortunately, it is possible to recover some sensitivity to binary pulsars by conducting *acceleration searches*. In these searches, the acceleration of the pulsar along the line-of-sight is assumed to be constant throughout the observation. This assumption can be incorporated into the analysis in the time domain by appropriately stretching or compressing the time series to remove the effect of the constant acceleration (see e.g. Johnston & Kulkarni, 1991). Alternatively, the assumed acceleration can be accounted for in the Fourier domain by correlating the FTs with templates of how pulsar signals are smeared out by the assumed acceleration in order to recover the distorted signals (Ransom et al., 2002). This Fourier-domain technique is employed in the analysis of PALFA survey data (see § 3.3.3). Both the time and frequency-domain acceleration searches are best suited when the observation duration is $\lesssim 10\,\%$ of the orbital period (i.e. $t_{\mathrm{obs}} \lesssim 0.1\,P_{\mathrm{orb}}$; Ransom et al., 2003; Ng et al., 2015).

Acceleration searching is one of the most computationally expensive steps of radio pulsar searching. This is, in part, because each dedispersed time series must be searched with many trial acceleration values to maintain sensitivity to a broad range of possible binary pulsars at all DMs searched (see e.g. Eatough et al., 2013a). Also, the computational requirements for acceleration searches scale strongly with observation length, roughly as t_{obs}^2.

Because of the potential scientific return from studying pulsars in tight binary systems (e.g. Liu et al., 2014a), even more computationally intensive search algorithms have been devised to improve sensitivity to binary pulsars in tight orbits and/or long observations. One strategy involves including the effect of the first derivative of the acceleration (called "jerk"; Eatough et al., 2013a). Another strategy involves demodulating the dedispersed time series according to a comprehensive set of circular binary orbits (Allen et al., 2013). In contrast to the single parameter used in the conventional acceleration searches described above, this latter algorithm requires three search parameters: the period, phase, and size of the assumed orbit, making this search strategy significantly more computationally demanding. The advantage of this circular orbital demodulation technique is that it is significantly more sensitive to binary pulsars in tight orbits than conventional acceleration searches (Allen et al., 2013). Thus, despite the high computational expense, the technique has been used by the Einstein@Home analysis pipeline, and has found many binary and isolated pulsars (e.g. Knispel et al., 2010, 2011, 2013). So far, none of these discoveries are so extreme that they could not have been found with the conventional search algorithms described earlier.

Sifting

Searching a single observation for periodic signals over a wide range of DMs can produce large numbers ($\gtrsim 10^4$) of candidates.[1] To identify the most promising of

---

[1] Each candidate corresponds to a period-DM pair at which a significant signal was found.

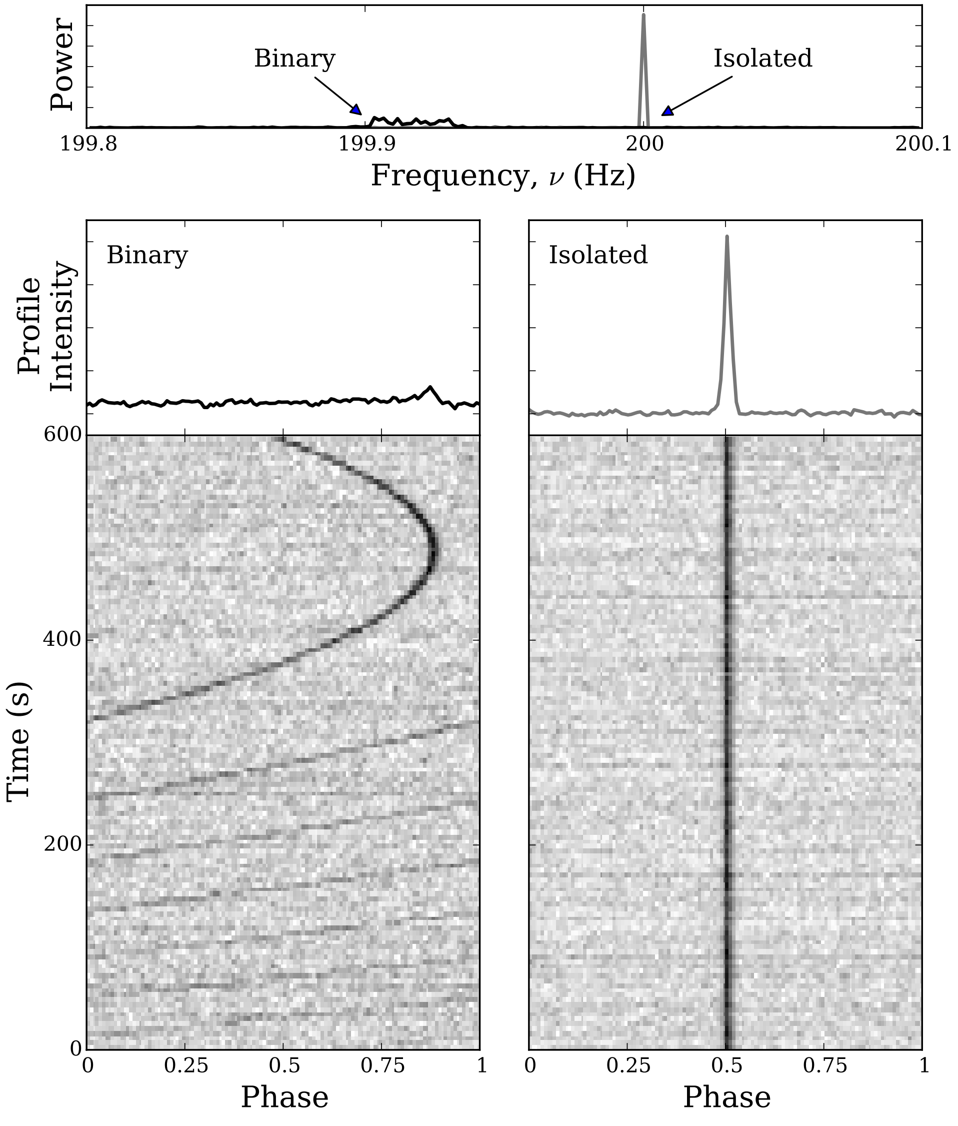

Figure 2.6: *Top* – The power spectra of two simulated 10-min long observations of two $\nu = 200$-Hz pulsars. The grey spectrum corresponds to an isolated pulsar, and the black spectrum corresponds to a pulsar in a 3-hr binary. The properties of the two signals are otherwise identical. Binary motion causes time-dependent Doppler shifts over the course of the observation that vary the apparent frequency of the pulsar, smearing its intrinsically well-defined frequency over many Fourier bins.
Bottom left – The time vs. phase plot and summed profile of the binary pulsar signal aligned assuming a spin frequency of $\nu = 200\,\mathrm{Hz}$. The signal drifts with time as a result of the binary motion.
Bottom right – The time vs. phase plot and summed profile of the isolated pulsar signal, again aligned assuming a spin frequency of $\nu = 200\,\mathrm{Hz}$. The periodicities of isolated pulsars are exceptionally stable over the course of a single observation.

these candidates, several sifting algorithms are used to: 1) reject signals likely caused by RFI, 2) combine candidates due to the same signal but found with slightly different parameters, 3) combine harmonically related candidates, and 4) sort the candidates by significance. The most significant signal candidates are then folded (see below). Details about the sifting process used in the analysis of PALFA survey data can be found in § 3.3.3.

Folding

The observation data are *folded* for each of the most significant candidates output by sifting. The best estimate of a candidate's period and acceleration are used to slice the input data into individual pulses and aligning them in phase. The aligned data are then dedispersed according to the best estimate of the DM, and then averaged together to compute the integrated folded profile. An example of folding a short time series is shown in Figure 2.7.

Averaging together all the pulses in an observation increases the S/N of the detected profile. This is because the individual pulses are aligned in phase, and thus are averaged coherently, whereas the noise is uncorrelated. The S/N of N pulses averaged together typically scales as $S/N \sim \sqrt{N}$. This assumes that the noise is Gaussian distributed and its properties are the same at all frequencies and throughout the entire observation. This scaling also assumes that on average all pulses have the same amplitude and shape. These assumptions are reasonable for most pulsars, especially for observations where the bandwidth is sufficiently small that the pulsar's spectrum is effectively flat and the frequency-evolution of its profile shape is unimportant. Improving the S/N of observed profiles is especially important for pulsar timing (see Chapter 4).

Another advantage of folding pulsar candidates is that the process effectively sums all harmonics coherently (i.e. taking into account the phase of each harmonic). This yields a higher S/N detection than what is possible with Fourier-domain searches alone, where typically only up to 16 harmonics are (incoherently) summed.

In practice, the folded data are only partially integrated, leaving some time and frequency resolution. This remaining time and frequency information make it possible to further optimize the S/N of the candidate by adjusting its period, period-derivative,[1] and DM. The end result is a data cube consisting of pulse phase, observation time, and radio frequency along its axes.

The folded data are used to make diagnostic plots. An example of a diagnostic plot for a periodicity candidate identified in the PALFA survey is shown in Figure 2.8.

The optimized data cube is used to compute the candidate's S/N and various heuristics. These metrics are used to quantify the pulsar-likeness of the candidate (see e.g. § 3.3.5).

Candidate Selection

Millions of optimized, folded candidates are generated over the course of a large-scale pulsar survey. Despite the thorough RFI mitigation and sophisticated searching strategies employed, the overwhelming majority of candidates are not of astrophysical origin. Finding the relatively small number of pulsars, especially the faint, previously undiscovered ones, is exceptionally challenging. Attempting to manually select the

---

[1] Optimizing the period-derivative of a candidate is equivalent to optimizing its acceleration.

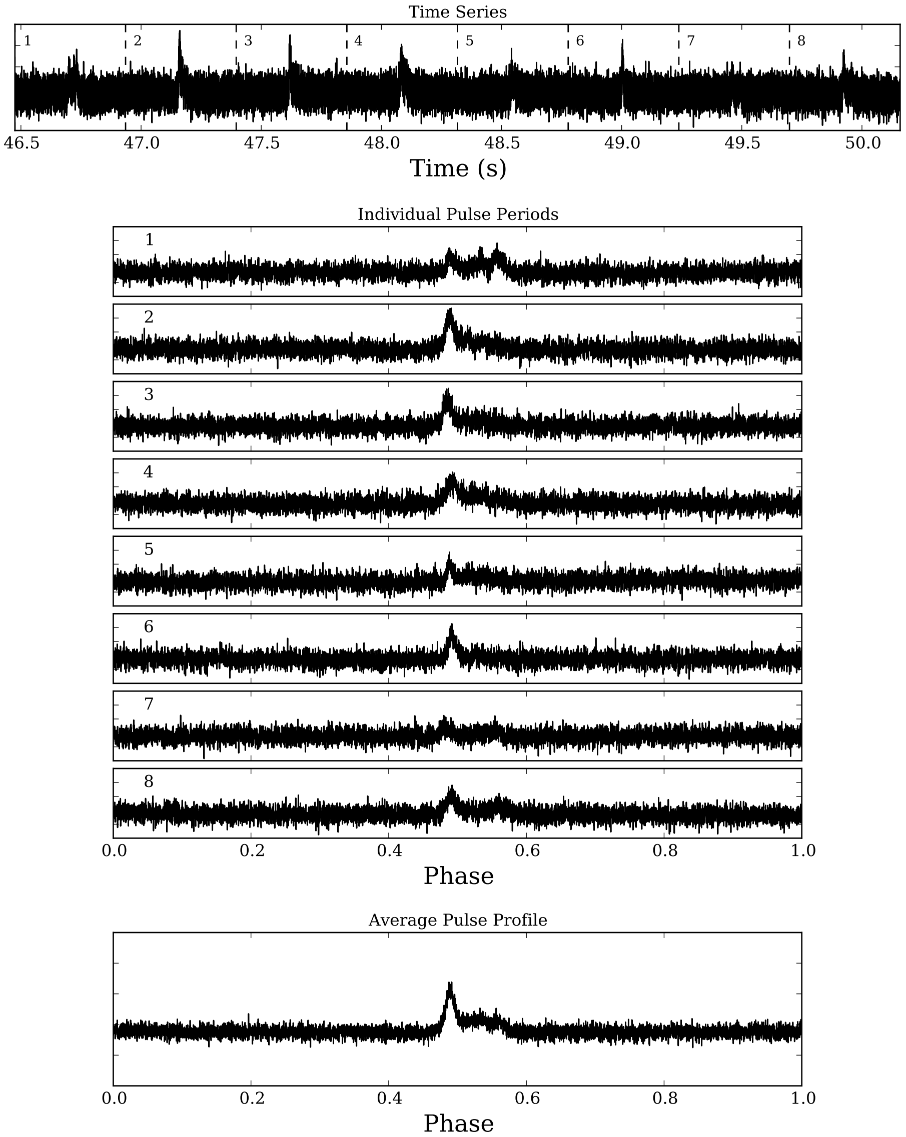

Figure 2.7: *Top* – A time series sliced into segments, each with a duration that equals one rotation of the pulsar.
Middle – The individual pulses are aligned in phase. The pulse appears in the same phase bins in all slices.
Bottom – The aligned individual pulses are averaged together. When folding N pulses, the significance of the detection grows as $S/N \sim \sqrt{N}$.

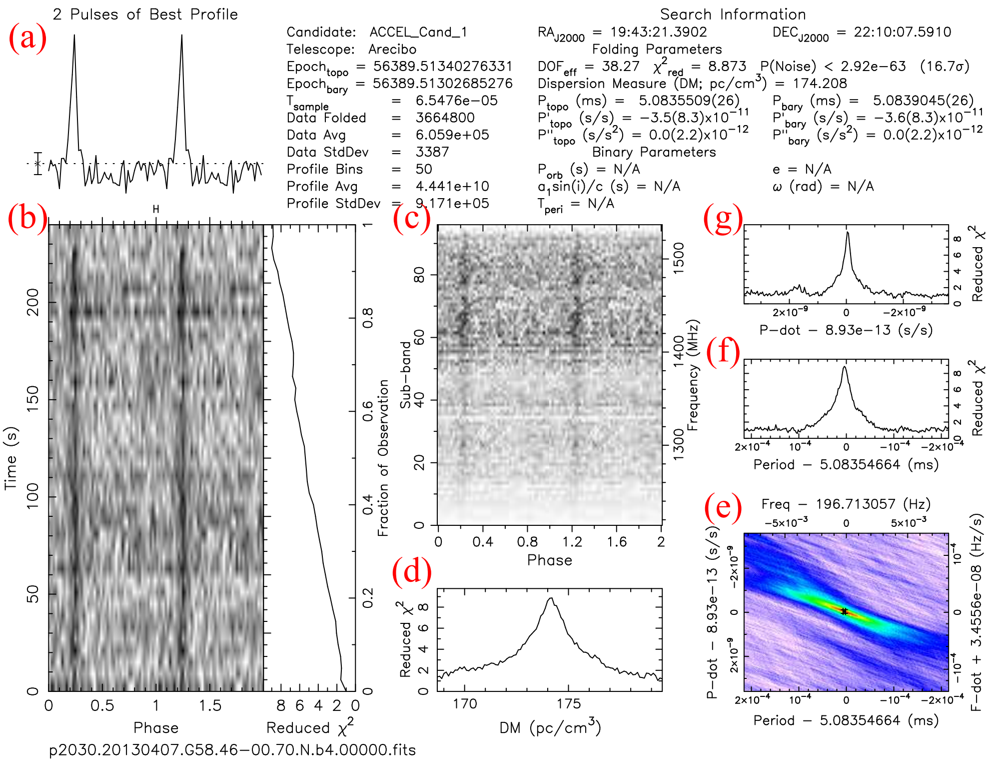

Search Information

Candidate: ACCEL_Cand_1

Telescope: Arecibo

$\mathrm{Epoch_{topo}}$ = 56389.51340276331

$\mathrm{Epoch_{bary}}$ = 56389.51302685276

$\mathrm{T_{sample}}$ = 6.5476e−05

Data Folded = 3664800

Data Avg = 6.059e+05

Data StdDev = 3387

Profile Bins = 50

Profile Avg = 4.441e+10

Profile StdDev = 9.171e+05

$\mathrm{RA_{J2000}}$ = 19:43:21.3902

$\mathrm{DEC_{J2000}}$ = 22:10:07.5910

Folding Parameters

$\mathrm{DOF_{eff}}$ = 38.27 χ^2_{red} = 8.873 P(Noise) < 2.92e−63 (16.7σ)

Dispersion Measure (DM; pc/cm^3) = 174.208

$\mathrm{P_{topo}}$ (ms) = 5.0835509(26)

$\mathrm{P_{bary}}$ (ms) = 5.0839045(26)

$\mathrm{P'_{topo}}$ (s/s) = $-3.5(8.3)\times10^{-11}$

$\mathrm{P'_{bary}}$ (s/s) = $-3.6(8.3)\times10^{-11}$

$\mathrm{P''_{topo}}$ (s/s^2) = $0.0(2.2)\times10^{-12}$

$\mathrm{P''_{bary}}$ (s/s^2) = $0.0(2.2)\times10^{-12}$

Binary Parameters

$\mathrm{P_{orb}}$ (s) = N/A

e = N/A

$a_1\sin(i)/c$ (s) = N/A

ω (rad) = N/A

$\mathrm{T_{peri}}$ = N/A

Figure 2.8: An example of a diagnostic plot of a periodicity candidate (actually a newly discovered pulsar!) found in a PALFA survey observation from April 7, 2013. The panels are: *(a)* – The integrated pulse profile; *(b)* – A time vs. phase plot, to help determine the persistence of the signal. The attached panel to the right shows the reduced χ^2 of the cumulative integrated profile vs. integration time; *(c)* – A frequency vs. phase plot, to gauge the broadbandedness of the signal; *(d)* – The reduced χ^2 of the integrated pulse profile re-dedispersed at trial DMs round the discovery DM; *(e)* – The reduced χ^2 of the integrated pulse profile re-folded according to similar combinations of (P, $\dot{P}$). The small black point indicates the values P and $\dot{P}$ used to align the data in panels (a)–(c); *(f)* – A horizontal slice through the reduced χ^2 map of panel (e). The slice passes through the $\dot{P}$ value indicated by the point in panel (e); *(g)* – A vertical slice through the reduced χ^2 map of panel (e). The slice passes through the P value indicated by the point in panel (e). This diagnostic plot was created with `PRESTO`'s `prepfold`. A plot like this is created for each folded periodicity candidate found in a PALFA observation. Similar plots are generated in other radio pulsar surveys.

relatively few pulsars lurking among the noise and RFI candidates by inspecting all of the candidates produced in a survey is infeasible. The amount of time it would take to complete this task is far too large. Unfortunately, simple selection criteria, such as applying S/N and DM thresholds, do little to distinguish pulsars from both strong RFI and weak noise-like signals in the database of candidates.

To make candidate selection tractable several ranking and machine learning algorithms have been developed (e.g. Eatough et al., 2010; Lee et al., 2013; Zhu et al., 2014). Some of the algorithms make use of the heuristics distilled from the folded data cube (e.g. Keith et al., 2009, and Chapter 3), whereas others use the data cube itself to select the most pulsar-like candidates. In § 3.3.5, I describe details of how heuristics and machine learning algorithms are used to winnow the millions of candidates produced thus far in the PALFA survey and have successfully led to the discovery of several new pulsars.

The most promising candidates identified are eventually re-observed. Successfully re-detecting a signal with the same period and DM at the same celestial position is the most convincing way to confirm a suspected new discovery.

2.5 *Searching for Impulsive Signals*

In addition to searching for periodic signals, all modern pulsar surveys also search for dispersed impulsive signals, such as those from RRATs and apparently extragalactic fast radio bursts (FRBs; e.g. Thornton et al., 2013). Matched-filtering algorithms are used to improve sensitivity to RRAT pulses, which are often considerably wider (McLaughlin et al., 2006; Burke-Spolaor & Bailes, 2010) than the sample times of survey observations (pulses are typically $\sim 1-50\,\mathrm{ms}$ in duration, compared to sample times of $\sim 50-100\,\mu\mathrm{s}$). Thus, dedispersed time series are convolved with boxcars of various widths. These convolved time series are then searched for significant peaks. Relatively high detection thresholds of $S/N \gtrsim 5$ are required to compensate for the high false alarm rate stemming from the large number of trials in DM, time, and pulse width, as well as non-Gaussian noise in the time series due to RFI. The significance of a pulse is maximized when the width of the boxcar used matches the width of the pulse (Cordes & McLaughlin, 2003). Figure 2.9 provides an example of how this smoothing improves the detectability of a single pulse. Sufficiently bright single pulse events can be found with multiple boxcar widths. Events that have the same DM and overlap in time are combined, leaving only the most significant detection.

Summary diagnostic plots are produced for each observation (see Figure 2.10 for an example). Diagnostic plots for individual events may also be generated to help evaluate the broadbandedness and DM-induced frequency sweep of the pulse. Algorithms are then used to cluster together single pulse events from similar times and DMs that originate from the same impulsive signal (Karako-Argaman et al., 2015). Each cluster may then be classified or scored. This clustering and scoring stage is analogous to the sifting and candidate selection stages of the periodicity search described above.

2.6 *Survey Sensitivity*

The minimum detectable flux density of a pulsar survey can be estimated using the modified radiometer equation (Dewey et al., 1985),

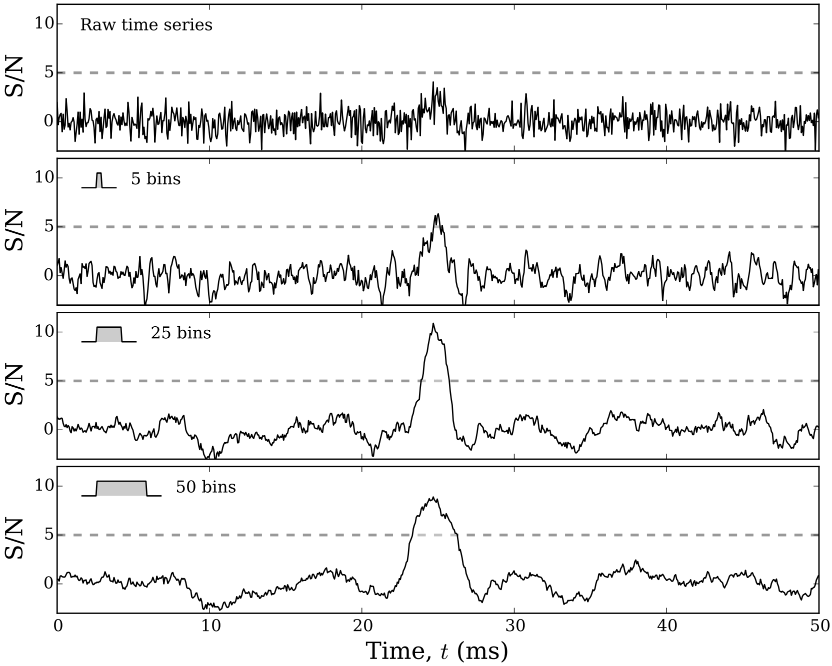

Figure 2.9: *Top* – A short interval of a simulated time series containing a wide single pulse at $t = 25\,\text{ms}$.
Bottom 3 panels – The same time series convolved with boxcars 5, 25, and 50 bins wide. All four cases have been normalized by the standard deviation of the data in the intervals $t < 20\,\text{ms}$ and $t > 30\,\text{ms}$ to estimate the S/N of each bin. The commonly-used detection threshold of $S/N = 5$ is shown in all four panels (grey dashed lines). The pulse is below the detection threshold in the raw time series, but smoothing increases the significance of the pulse, allowing it to be detected. The strongest detection ($S/N \sim 10$) is achieved when smoothing with a boxcar 25 bins wide, roughly the width of the pulse.

$$S_{\text{min}} = \frac{S/N_{\text{min}}\,(T_{\text{sys}} + T_{\text{sky}})}{G\sqrt{n_p t_{\text{obs}} \Delta f}} \left[\sqrt{\frac{W}{P - W}}\right], \tag{2.4}$$

where S/N_{min} is the signal-to-noise ratio threshold, T_{sys} is the temperature (in K) of the observing system (receiver, electronics, etc.), and T_{sky} is the sky temperature (in K). The sky temperature is usually estimated from maps of the Haslam et al. (1982) all-sky survey at 408-MHz scaled to the survey observation's frequency using a spectral index of -2.76 for the Galactic synchrotron emission (Platania et al., 1998). The parameters G, n_p, t_{obs} and Δf are the telescope gain (in K/Jy), number of polarizations summed, observation integration time (in s), and observing bandwidth (in MHz), respectively. The term in square brackets roughly describes the pulse shape, where W and P are the pulse width and pulsar's spin period, respectively.

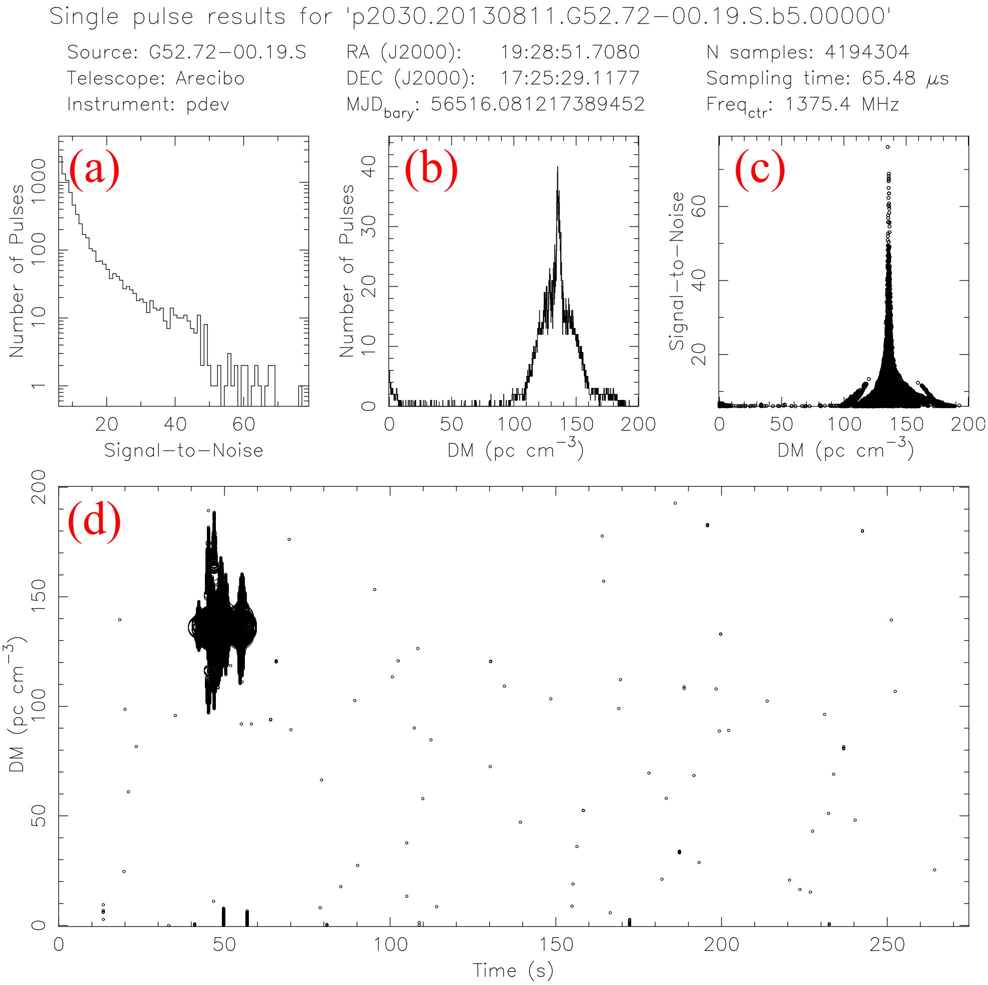

Figure 2.10: An example of a diagnostic plot summarizing single pulse events in a PALFA survey observation from August 11, 2013. The panels are: *(a)* – A histogram of the S/Ns of the single pulse events; *(b)* – A histogram of the DMs of the single pulse events; *(c)* – A plot of S/N vs. DM showing each single pulse event; *(d)* – A plot of DM vs. time of all single pulse events. In this panel, the sizes of the points correspond to the S/Ns of the events. The clusters of events at $t \sim 50\,\mathrm{s}$ and DM $\sim 140\,\mathrm{pc\,cm^{-3}}$ are from the RRAT J1928+1725 which was discovered in this observation. The slight excess of single pulse events at low DMs evident in the left-hand side of panel (b) is due to RFI. This diagnostic plot was created with `PRESTO`'s `single_pulse_search.py`. Several plots like this are generated for different DM ranges for each PALFA observation. Other radio pulsar surveys generate similar plots.

The pulse width, W, is the *observed* width, which includes the broadening effects of dispersive smearing, interstellar scattering, sampling time, etc. Figure 2.11 shows such a comparison of three on-going radio pulsar surveys and the immensely successful Parkes Multibeam Pulsar Survey.

The minimum detectable flux density determined from Eq. 2.4 is only a rough measure of survey sensitivity. A more complete description of survey sensitivity must take into account the shape of the pulse and not only its width, as well as the number of harmonics summed in Fourier-domain searches. Nonetheless, Eq. 2.4 is sufficient for order-of-magnitude estimates and for comparing the sensitivity of different surveys. The more accurate formulation of the radiometer equation by Cordes & Chernoff (1997) incorporates full information about the observed pulse shape. However, Eq. 2.4 is more commonly used due to its simplicity. Both of these versions of the radiometer equation assume the noise is Gaussian distributed. Unfortunately, this assumption does not hold in practice, survey data are affected by RFI and red noise. In Chapter 3, I describe a new, more accurate method for determining the sensitivity of a pulsar survey that I developed to include the effect of RFI and red noise in estimates of the sensitivity of PALFA survey observations to pulsars.

2.7 Summary

The algorithms described in this chapter enable the data from large-scale surveys to be searched for radio pulsars while maximizing sensitivity to a wide range of parameters and marginalizing the effect of RFI. These techniques have been successfully used in many projects to discover $\gtrsim$2000 pulsars (Manchester et al., 2005). In most cases, the procedures described above can be augmented by taking advantage of experience with a specific telescope, and/or by making assumptions about the pulsar signals in the data. Because pulsar searching has a significant computational cost, a balance must be struck between the total processing time and the thoroughness of the search. In Chapter 3, using the analysis of PALFA survey data as a case study, I will show how site-specific knowledge and processing-time considerations are incorporated into the design of a pulsar search pipeline.

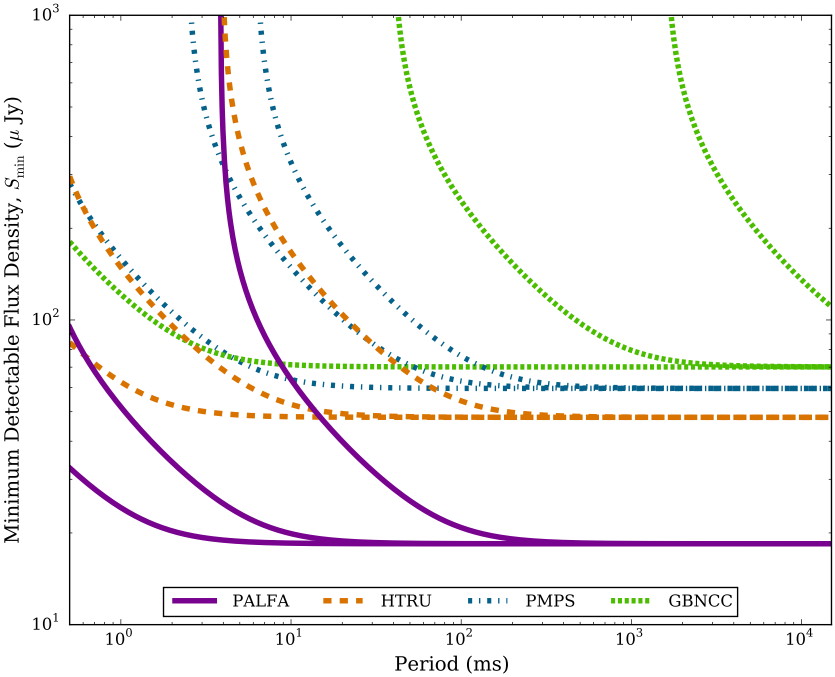

Figure 2.11: The minimum detectable flux densities, S_{min}, for three on-going pulsar surveys (the PALFA survey, the Deep South portion of the High Time Resolution survey, HTRU, and the Green Bank North Celestial Cap survey, GBNCC) and the past, but extremely successful, Parkes Multibeam Pulsar Survey (PMPS). For each survey, S_{min} is estimated using the radiometer equation (Eq. 2.4) assuming a pulse width of 5 % and DMs of 10, 250, and 500 pc cm^{-3} (from bottom to top). The degradation of sensitivity as DM increases is the result of pulse broadening due to dispersive smearing and multi-path scattering. The three on-going surveys are complementary. They focus on different portions of the sky and have different observing frequencies. In particular, the GBNCC has a centre frequency of 350 MHz, whereas the observing bands of PALFA and HTRU are centred around ∼1400 MHz.

3

ARECIBO PULSAR SURVEY USING ALFA. IV. MOCK SPECTROMETER DATA ANALYSIS, SURVEY SENSITIVITY, AND THE DISCOVERY OF 40 PULSARS

This chapter is based on an article published in the Astrophysical Journal (Lazarus et al., 2015). Information about the article can be found online at:
http://adsabs.harvard.edu/abs/2015ApJ...812...81L

The text, figures, and tables have only been modified to match the style, spelling and format of the rest of this thesis.

I am the lead author of the article. My main contributions include developing large parts of the data analysis pipeline, as well as several of the RFI-mitigation algorithms. I also discovered some of the pulsars, and tabulated the discoveries and re-detections. Furthermore, I devised and performed the sensitivity analysis, and integrated it into the population synthesis study.

The full list of authors is:
P. Lazarus, A. Brazier, J. W. T. Hessels, C. Karako-Argaman, V. M. Kaspi, R. Lynch, E. Madsen, C. Patel, S. M. Ransom, P. Scholz, J. Swiggum, W. W. Zhu, B. Allen, S. Bogdanov, F. Camilo, F. Cardoso, S. Chatterjee, J. M. Cordes, F. Crawford, J. S. Deneva, R. Ferdman, P. C. C. Freire, F. A. Jenet, B. Knispel, K. J. Lee, J. van Leeuwen, D. R. Lorimer, A. G. Lyne, M. A. McLaughlin, X. Siemens, L. G. Spitler, I. H. Stairs, K. Stovall, and A. Venkataraman

Abstract

The on-going Arecibo PALFA survey began in 2004 and is searching for radio pulsars in the Galactic plane at 1.4 GHz. Here we present a comprehensive description of one of its main data reduction pipelines that is based on the PRESTO software and includes new interference-excision algorithms and candidate selection heuristics. This pipeline has been used to discover 40 pulsars, bringing the survey's discovery total to 144 pulsars. Of the new discoveries, eight are millisecond pulsars (MSPs; $P < 10\,\mathrm{ms}$) and one is a Fast Radio Burst (FRB). This pipeline has also re-detected 188 previously known pulsars, 60 of them previously discovered by the other PALFA pipelines. We present a novel method for determining the survey sensitivity that accurately takes into account the effects of interference and red noise: we inject synthetic pulsar signals with various parameters into real survey observations and then attempt to recover them with our pipeline. We find that the PALFA survey achieves the sensitivity to MSPs predicted by theoretical models but suffers a degradation for $P \gtrsim 100\,\mathrm{ms}$ that gradually becomes up to ~10 times worse for $P > 4\,\mathrm{s}$ at $\mathrm{DM} < 150\,\mathrm{pc\,cm^{-3}}$. We estimate $33 \pm 3\,\%$ of the slower pulsars are missed, largely due to red noise. A population synthesis analysis using the sensitivity limits we measured suggests the PALFA survey should have found 224 ± 16 un-recycled pulsars in the data set

analyzed, in agreement with the 241 actually detected. The reduced sensitivity could have implications on estimates of the number of long-period pulsars in the Galaxy.

3.1 Introduction

Pulsars are rapidly rotating, highly magnetized neutron stars, the remnants of massive stars after their death in supernova explosions. They are extremely valuable astronomical tools with many physical applications that have been used to, for example, constrain the equation of state of ultra-dense matter (e.g. Hessels et al., 2006; Demorest et al., 2010), test relativistic gravity (e.g Kramer et al., 2006b; Antoniadis et al., 2013), probe plasma physics within the magnetosphere (e.g. Hankins et al., 2003; Kramer et al., 2006a; Lyne et al., 2010; Hermsen et al., 2013), and gain a better understanding of the complete radio pulsar population (e.g. Faucher-Giguère & Kaspi, 2006). Certain individual pulsar systems are especially well suited to studying these areas of astrophysics, and thus continued pulsar surveys to find these rare objects remain an important step of scientific discovery in the field.

Radio pulsars are found primarily in non-targeted, wide-area surveys such as the Pulsar-ALFA (PALFA) survey at 1.4 GHz, which began in 2004 (Cordes et al., 2006). PALFA observations use the 7-beam Arecibo L-band Feed Array (ALFA) receiver of the Arecibo Observatory William E. Gordon 305-m Telescope and focus on the Galactic plane ($|b| < 5^\circ$) in the two regions visible with Arecibo, namely the "inner Galaxy" region ($32^\circ \lesssim l \lesssim 77^\circ$), and the "outer Galaxy" region ($168^\circ \lesssim l \lesssim 214^\circ$).

For the first five years, PALFA survey observations were made using the Wideband Arecibo Pulsar Processor (WAPP), a 3-level auto-correlation spectrometer with 100 MHz of bandwidth (Dowd et al., 2000). Since 2009, the Mock spectrometer,[1] a 16-bit poly-phase filterbank, has replaced the WAPP spectrometer as the data-recorder of the PALFA survey. The Mock spectrometer records two critically sampled, overlapping 172 MHz bands that fully cover the 322 MHz ALFA band. The increased bandwidth, poly-phase filterbank design, and increased bit-depth of the Mock spectrometer have increased the sensitivity and robustness to interference of the PALFA survey. For this reason, we are re-observing regions of the sky previously observed with the WAPP spectrometers.

The PALFA consortium currently employs two independent full-resolution data analysis pipelines. The Einstein@Home-based pipeline (E@H)[2] has already been described by Allen et al. (2013): this pipeline derives its computational power by aggregating the spare cycles of a global network of PCs and mobile devices using the BOINC platform,[3] and is also searching data from the PALFA survey for pulsars. In this work we describe the pipeline based on the `PRESTO` suite of pulsar search programs[4] (Ransom, 2001). In addition to these pipelines, we also employ a reduced-resolution "Quicklook" pipeline, which is run on-site at Arecibo shortly after observing sessions are complete and which enables a more rapid discovery and confirmation of strong pulsars (Stovall, 2013).

As of March 2015, there have been 144 pulsars discovered in WAPP and Mock spectrometer observations with the various PALFA data analysis pipelines. This is

---

[1] http://www.naic.edu/∼astro/mock.shtml

[2] http://einstein.phys.uwm.edu/

[3] http://boinc.berkeley.edu/

[4] http://www.cv.nrao.edu/∼sransom/presto/

already a sizable increase on the previously known sample[1] of 169 Galactic radio pulsars in the survey region out to $|b| < 2°$, the Galactic latitude range we have focused on with the Mock spectrometers.

The relatively high observing frequency and unparallelled sensitivity of Arecibo, coupled with the high time and frequency resolution of PALFA ($\tau_{\rm samp} \simeq 65.5\,\mu$s and $\Delta f_{\rm chan} \simeq 336$ kHz, respectively) make it particularly well suited for detecting millisecond pulsars (MSPs) deep in the plane of the Galaxy, such as the distant MSPs reported by Crawford et al. (2012) and Scholz et al. (2015), the highly eccentric MSP PSR J1903+0327 (Champion et al., 2008), and faint, young pulsars (e.g. Hessels et al., 2008). The huge instantaneous sensitivity of Arecibo enables short integration times, which has been helpful in detecting relativistic binaries (e.g. PSR J1906+0746; Lorimer et al., 2006a) by reducing the deleterious effect of time-varying Doppler shifts of binary pulsars. The PALFA survey has also proven successful at detecting transient astronomical signals. For example, the survey has led to the discovery of several Rotating Radio Transient pulsars (RRATs; Deneva et al., 2009), as well as FRB 121102, the first Fast Radio Burst (FRB) detected with a telescope other than the Parkes Radio Telescope (Spitler et al., 2014).

While PALFA is the most sensitive large-scale survey for radio pulsars ever conducted, it is not the only on-going radio pulsar survey. Other major surveys are the HTRU-S (Keith et al., 2010b), HTRU-N (Barr et al., 2013b), and SPAN512 (Desvignes et al., 2013) surveys at ~1.4 GHz, the GBNCC (Stovall et al., 2014) and AO327 drift (Deneva et al., 2013) surveys at ~350 MHz, and the LOFAR surveys (Coenen et al., 2014) at ~150 MHz.

The underlying distributions of the pulsar population can be estimated using simulation techniques (e.g. Faucher-Giguère & Kaspi, 2006; Lorimer et al., 2006b; Bates et al., 2014). The large sample of pulsars found in non-targeted surveys are essential for these simulations. However, for population analyses to be done accurately, the selection biases of each survey must be taken into account. While the sensitivity of pulsar search algorithms is reasonably well understood, the effect of radio frequency interference (RFI) on pulsar detectability has not been previously studied in detail.

This chapter reports on the current state of PALFA's primary search pipeline, its discoveries, and its sensitivity. The rest of the chapter is organized as follows: the observing set-up is summarized in § 3.2. The details of the PALFA `PRESTO`-based pipeline are described in § 3.3. § 3.4 reports basic parameters of the pulsars found with the pipeline, and § 3.5 details how the survey sensitivity is determined, including a technique involving injecting synthetic pulsars into the data. These accurate sensitivity limits are used to improve upon population synthesis analyses in §3.6. The broader implications of the accurate determination of the survey sensitivity are presented in § 3.7 before the chapter is summarized in § 3.8.

3.2 Observations

The PALFA survey observations have been restricted to the two regions of the Galactic plane ($|b| < 5°$) visible from the Arecibo observatory, the inner Galaxy ($32° \lesssim l \lesssim 77°$), and the outer Galaxy ($168° \lesssim l \lesssim 214°$). Integration times are 268 s and 180 s for

---

[1] As listed in the ATNF Pulsar Catalogue: http://www.atnf.csiro.au/research/pulsar/psrcat (Manchester et al., 2005)

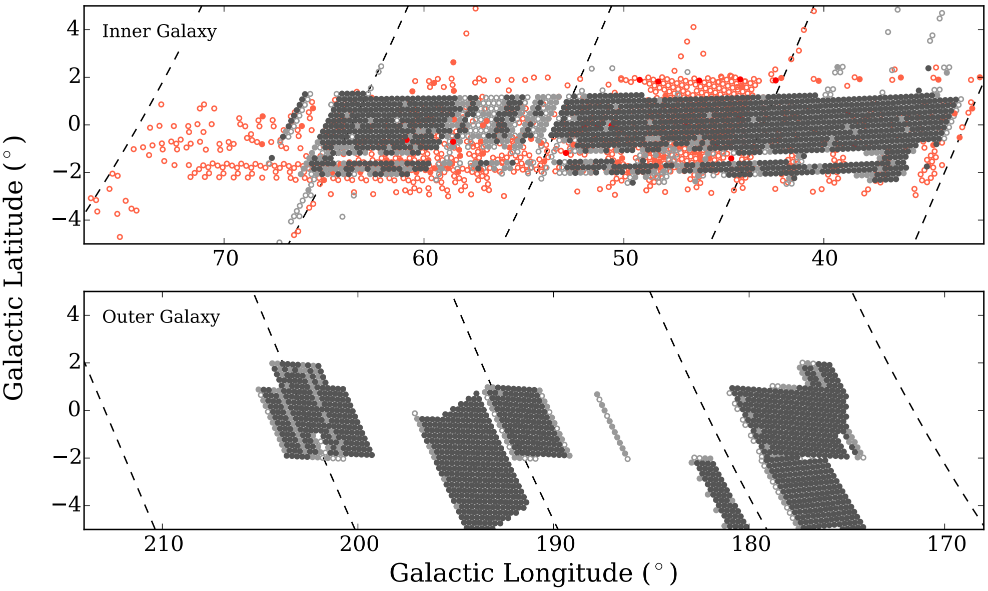

Figure 3.1: Sky map showing the locations of PALFA observations with the Mock spectrometers, which began in 2009, for the inner and outer Galaxy regions. Observations up until December 2014 are included. Each position plotted represents the centre of the 3-pointing set required to densely sample the area. Positions that have been only sparsely observed (i.e. 1 of 3 pointing positions observed) are indicated with un-filled circles. Positions with 2 of 3 pointings observed are indicated with a light-coloured filled circle. Positions that have been densely observed (i.e. all 3 pointing positions observed) are indicated with dark-coloured filled circles. Red indicates observations made prior to adjusting our pointing grid at the request of our commensal partners. As a result, some of the sky area covered in early Mock observations has not been re-observed using the Mocks and the current commensal pointing grid.

inner and outer Galaxy observations, respectively.

To optimize the use of telescope resources, the PALFA survey operates in tandem with other compatible projects using the ALFA 7-beam receiver. In particular, we have reciprocal data-sharing agreements with collaborations that search for galaxies in the optically obscured (“zone of avoidance”) directions through the Milky Way (Henning et al., 2010) and recombination-line studies of ionized gas in the Milky Way (Liu et al., 2013). The PALFA project leads inner Galaxy observing sessions, whereas our partners lead outer Galaxy sessions.

For the inner Galaxy region, the pointing strategy has prioritized observations of the $|b| < 2°$ region before moving on to the Galactic plane at larger Galactic latitudes. Our pointing grid densely samples patches of sky out to the ALFA beam FWHM by interleaving three ALFA pointings (see Cordes et al., 2006, for more details). In contrast, our commensal partners have focused outer Galaxy observations in order to densely sample particular Galactic longitude/latitude ranges. A sky map showing the pointing positions observed with the Mock spectrometers can be found in Figure 3.1.

Observations conducted with ALFA have a bandwidth of 322 MHz centred at 1375 MHz. Each of the seven ALFA beams is split into two overlapping 172-MHz sub-

Table 3.1: PALFA Mock Spectrometer Observing Set-up Parameters

Parameter	Value
General	
Sample Time, $\tau_{\rm samp}$ (μs)	65.476
Integration Time,[a] $t_{\rm obs}$ (s)	268[b] 180[c]
High Sub-Band	
Number of Channels	512
Low Frequency (MHz)	1364.290
High Frequency (MHz)	1536.016
Low Sub-Band	
Number of Channels	512
Low Frequency (MHz)	1214.290
High Frequency (MHz)	1386.016
Merged Band	
Number of Channels	960
Low Frequency (MHz)	1214.290
Centre Frequency (MHz)	1375.489
High Frequency (MHz)	1536.688
Bandwidth, Δf (MHz)	322.398
Channel Bandwidth, $\Delta f_{\rm chan}$ (kHz)	335.831

[a] This is the integration time remaining after the ~5 − 10 s calibration diode signal is removed (see § 3.3.2).

[b] Observations in the Inner Galaxy region ($32° \lesssim l \lesssim 77°$)

[c] Observations in the Anti-Centre region ($168° \lesssim l \lesssim 214°$)

bands and processed independently by the Mock spectrometers.[1] The sub-bands are divided into 512 channels. The data are recorded with a time resolution of ~65.5 μs. The observing parameters are summarized in Table 3.1. The data are recorded to disk in 16-bit search-mode `PSRFITS` format (Hotan et al., 2004a).

PALFA survey data have been recorded with the Mock spectrometers since 2009. However, note that in 2011 our pointing grid was altered slightly to accommodate our commensal partners. This required some sky positions to be re-observed. Prior to 2009, survey observations were recorded with the WAPPs (see Dowd et al., 2000; Cordes et al., 2006). The two data recording systems were run in parallel during 2009 to check the consistency and quality of the Mock spectrometer data.

An un-pulsed calibration diode is fired during the first (or sometimes last) 5 − 10 s of our integration. While this is primarily used by our partners, we have found the diode signals useful in calibrating observations for our sensitivity analysis (see § 3.5.4). The calibration signal is removed from the data prior to searching (see § 3.3.2).

The original 16-bit Mock data files are compressed to have 4 bits per sample. These smaller data files are more efficient to ship and analyze thanks to reduced disk-space requirements. The 4-bit data files utilize the *scales* and *offsets* fields of the `PSRFITS` format to retain information about the bandpass shape despite the reduced dynamic range. The scales and offsets are computed and stored for every 1-s sub-integration. This reduction of bit-depth results in a total loss of only a few percent in the signal-to-noise ratio (S/N) of pulsar signals (see e.g. Kouwenhoven & Voûte, 2001).

---

[1] http://www.naic.edu/~astro/mock.shtml

Table 3.2: Breakdown of PALFA Mock Spectrometer Data

	No. Beams [a]	No. Unique Sky Positions	Sky Coverage (sq. deg.)	Completeness [b] $\vert b\vert < 2^\circ$ (%)	Completeness [b] $\vert b\vert < 5^\circ$ (%)
		Inner Galaxy ($32^\circ \lesssim l \lesssim 77^\circ$)			
Observed	40705	38479	94	69	32
Archived	35030	33243	81	60	27
Analyzed	33888	32499	80	58	27
		Anti-Centre ($168^\circ \lesssim l \lesssim 214^\circ$)			
Observed	60305	26194	64	30	18
Archived	52659	21990	54	23	15
Analyzed	51445	21899	54	23	15

Note. — Including observations up until 2014 December.

[a] There are 7 beams per pointing.

[b] The completeness percentages are relative to the number of pointings we aim to eventually cover with the Mock spectrometers.

The converted 4-bit `PSRFITS` data files are copied to hard disks, and couriered from Arecibo to Cornell University where they are archived at the Cornell University Center for Advanced Computing (CAC). Metadata about each observation, parsed from the telescope logs and the file headers, are stored in a dedicated database.

As of 2014 November, a total of 87689 beams of Mock spectrometer data have been archived. The break-down of observed, archived and analyzed sky positions for the two survey regions is shown in Table 3.2.

PALFA observations more than one year old are publicly available. Small quantities of data can be requested via the web.[1] Access to larger amounts of data is also possible, but must be coordinated with the collaboration because of the logistics involved.

Additional details about the data management logistics and data preparation are in §§ 3.3.1 and 3.3.2.

3.3 Pulsar and Transient Search Pipeline

The `PRESTO`-based pipeline has been used to search PALFA observations taken with the Mock spectrometers since mid-2011 for radio pulsars and transients. All processing is done using the Guillimin supercomputer of McGill University's High Performance Computing centre.[2]

While the pipeline described here was designed specifically for the PALFA survey, it is sufficiently flexible to serve as a base for the data reduction pipeline of other surveys. For example, the SPAN512 survey being undertaken at the Nançay Radio Telescope uses a version of the PALFA `PRESTO` pipeline described here tuned to their specific needs (Desvignes et al., 2013). The PALFA pipeline source code is publicly available online.[3]

Since the analysis began with the pipeline, there have been several major improvements, primarily focusing on ameliorating its robustness in the presence of RFI

---

[1] http://arecibo.tc.cornell.edu/PalfaDataPublic

[2] http://www.hpc.mcgill.ca/

[3] https://github.com/plazar/pipeline2.0

(§ 3.3.4), as well as post-processing algorithms for identifying the best pulsar candidates (§ 3.3.5). The PALFA consortium is constantly monitoring the performance of the pipeline and the RFI environment at Arecibo (as described later, RFI is one of the major challenges), and looking for ways to further improve the analysis. Here we report on the state of the software as of early-2015.

The pipeline overview presented here is grouped into logical components. In § 3.3.1 we outline the significant data tracking and processing logistics required to automate the analysis. In § 3.3.2 we detail the data file preparation required before searching an observation. In § 3.3.3 we describe the techniques used to search for periodic and impulsive pulsar signals. In § 3.3.4 we summarize the various complementary stages of RFI identification and mitigation. Finally, in §§ 3.3.5 and 3.3.6 we outline the tools used to help select and view pulsar candidates, as well as other on-line collaborative facilities used by the PALFA consortium.

Figure 3.2 shows a flowchart summarizing the stages of the pipeline.

3.3.1 Logistics

The PALFA search pipeline is designed to be almost entirely automated. This includes the logistics of data management required to maintain the analysis of $\sim$1000 beams on the Guillimin supercomputer at any given time. This is accomplished with a *job-tracker* database that maintains the status of processes that are downloading raw data, reducing data, and uploading results.

The pipeline is configured to continually request and download raw data that have not been processed and delete the local copies of files that have been successfully analyzed. Data files are copied to McGill via FTP from the Cornell University CAC. The multi-threaded data transfers from the CAC to McGill are sufficiently fast to maintain $1000-2000$ jobs running simultaneously.

When the transfer of an observation is complete, job entries are created in the pipeline's job-tracker database. As compute resources become available, jobs are automatically submitted to the supercomputer's queue.

When jobs terminate, the pipeline checks for results and errors. Failed jobs are automatically re-submitted up to three times to allow for occasional hiccups of the Guillimin task management system, or processing node glitches. If all three processing attempts result in failure, the observation is flagged to be dealt with manually. Observations that are salvageable are re-processed after fixes are applied. The positions of un-salvageable observations are re-inserted into the observing schedule, along with those from observations severely contaminated with RFI. Observations may be un-salvageable if they are aborted scans, contain malformed metadata, or their files have become corrupted. Only $\sim$0.15 % of all observations have data files that cannot be searched, and only $\sim$4.5 % of all observations are flagged to be re-observed due to excessive RFI.

The results from successfully processed jobs are parsed and uploaded to a database at the CAC, and the local copies of the data files are removed to free disk space enabling more observations to be requested, downloaded, and analyzed.

The inspection of uploaded results is done with the aid of a web-application (see § 3.3.6).

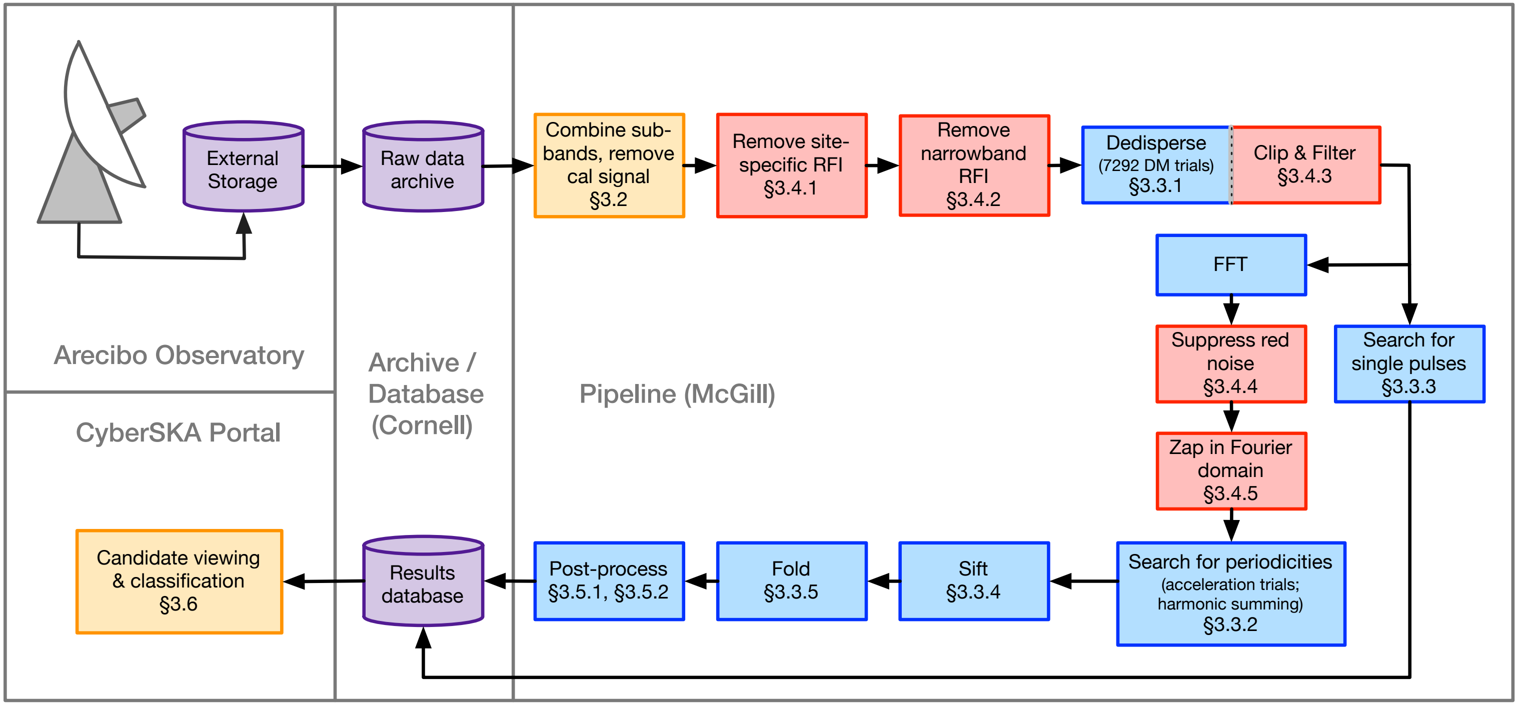

Figure 3.2: An overview of the PALFA survey's `PRESTO`-based pipeline. The colour of each element reflects the category of the step: searching is blue; RFI mitigation is red; data storage and databases are purple; miscellaneous processes are yellow. Additional details about each pipeline stage can be found in the sections listed in each box.

3.3.2 Pre-processing

Before analyzing the data for astrophysical signals, the two Mock sub-bands must be combined into a single `PSRFITS` file. Each of the two Mock data files have 512 frequency channels, 66 of which are overlapping with the other file. For each sub-integration of the observation, the 478 low-frequency channels from the bottom sub-band and the 480 high-frequency channels from the top sub-band are extracted, concatenated together – along with two extra, empty frequency channels – for each sample, and written into a new full-band data file, consisting of 960 channels. The choice to discard part of both bands was made in order to mitigate the effect of the reduced sensitivity at the extremities of the Mock sub-bands, which causes a slight reduction of sensitivity where they are joined together.

The `PSRFITS` scales and offsets of the Mock sub-bands are adjusted such that the data value levels of top and bottom bands are appropriately weighted with respect to each other.

The combining of the two Mock sub-bands is performed using `combine_mocks` of `psrfits_utils`.[1]

Next, the sub-integrations containing the calibration diode signal are deleted from the observation. The start time and length of the observation are updated accordingly.

At this stage, prior to searching for periodic and impulsive signals, `PRESTO`'s `rfifind` is run on the merged observation to generate an RFI mask. See § 3.3.4 for details.

3.3.3 Searching Components

We will now cover the various steps required to search for pulsars and transients.

Dedispersion

Because the DMs of yet-undiscovered pulsars and transients are not known in advance, a wide range of trial DMs must be used to maintain sensitivity to pulsars. For each trial DM value a dedispersed time series is produced by shifting the frequency channels according to the assumed DM value and then summing over frequency. When generating these time series, the motion of the Earth around the Sun is removed so that the arrival times of each sample are referenced to the Solar System barycentre, assuming the coordinates of the beam centre.

The PALFA `PRESTO` pipeline searches observations for periodic and impulsive signals up to a DM of $\sim$10000 pc cm^{-3}. We search to such high DMs despite the maximum DM in our survey region predicted by the `NE2001` model being $\sim$1350 pc cm^{-3} (Cordes & Lazio, 2002) to ensure sensitivity to highly dispersed, potentially extragalactic FRBs (e.g. Thornton et al., 2013; Spitler et al., 2014).

A dedispersion plan is determined by balancing the various contributions to pulse broadening that can be controlled: the duration of each sample (including downsampling), $\tau_{\rm samp}$; the dispersive smearing within a single channel, $\tau_{\rm chan}$; the dispersive smearing within a single sub-band due to approximating the DM, $\tau_{\rm sub}$; and the dispersive smearing across the entire observing band due to the finite DM step size (i.e. if the DM of the pulsar is half-way between two DM trials), $\tau_{\rm BW}$. Additionally, pulses are broadened by interstellar scattering, $\tau_{\rm scatt}$, which cannot be removed. The

---

[1] https://github.com/scottransom/psrfits_utils

Table 3.3: Dedispersion Plan for Mock Spectrometer Data

DM range ($\mathrm{pc\,cm^{-3}}$)	DM step size ($\mathrm{pc\,cm^{-3}}$)	No. DMs	Sub-band DM spacing [a] ($\mathrm{pc\,cm^{-3}}$)	Down-sample factor	Approx. Computing (%)
0−212.8	0.1	2128	7.6	1	73.19
212.8−443.2	0.3	768	19.2	2	12.20
443.2−534.4	0.3	304	22.8	3	8.13
534.4−876.4	0.5	684	38.0	5	2.93
876.4−990.4	0.5	228	38.0	6	2.44
990.4−1826.4	1.0	836	76.0	10	0.73
1826.4−3266.4	2.0	720	144.0	15	0.24
3266.4−5546.4	3.0	760	228.0	30	0.08
5546.4−9866.4	5.0	864	360.0	30	0.05

Note. — See also Figure 3.3 for the pulse broadening as a function of DM due to dispersive smearing and this dedispersion plan.

[a] In all cases 96 sub-bands are used.

amount of scatter-broadening scales with the DM, observing frequency and line of sight. Bhat et al. (2004) empirically determined the relationship as

$$\begin{aligned}\log \tau_{\mathrm{scatt}} = & -6.46 + 0.154 \log \mathrm{DM} \\ & + 1.07 \left(\log \mathrm{DM}\right)^2 - 3.86 \log f,\end{aligned} \tag{3.1}$$

where τ_{scatt} is given in ms, and f is the observing frequency in GHz. Even for the same DM, $\log \tau_{\mathrm{scatt}}$ are different for pulsars in different locations with a scatter of up to $2-3$ orders of magnitude (Bhat et al., 2004). Because τ_{scatt} cannot (in practice) be corrected, we ignore it when determining our dedispersion plan.

The total correctable pulse broadening, τ_{tot}, is estimated by summing the first four contributions in quadrature,

$$\tau_{\mathrm{tot}} = \sqrt{\tau_{\mathrm{samp}}^2 + \tau_{\mathrm{chan}}^2 + \tau_{\mathrm{sub}}^2 + \tau_{\mathrm{BW}}^2}. \tag{3.2}$$

All of these broadening terms vary with DM. The dedispersion plan is chosen to equate these four broadening effects roughly by adjusting the DM step-size and down-sampling factor as a function of DM. To reduce the number of DM trials, the minimum step-size is determined by $\tau_{\mathrm{BW}} > 0.1\,\mathrm{ms}$.

The PALFA survey dedispersion plan for Mock spectrometer data was determined with a version of `PRESTO`'s `DDplan.py` modified to allow for non-power-of-two down-sampling factors, and is shown in Table 3.3. The down-sampling factors are selected to be divisors of the number of spectra per sub-integration, 15270. The amount of dispersive smearing incurred at the middle of the observing band, ~1375 MHz, when using the dedispersion plan in Table 3.3, ranges from ~0.1 ms for the lowest DMs, to ~1 ms for DMs of a few $100\,\mathrm{pc\,cm^{-3}}$, increasing to ~10 ms for a DM of $\sim 10000\,\mathrm{pc\,cm^{-3}}$. Above a DM of $\sim 500\,\mathrm{pc\,cm^{-3}}$ scattering begins to dominate (see Figure 3.3).

The more aggressive down-sampling at higher DMs has the advantage of reducing the data size, making the analysis more efficient. Also, at higher DMs the step-size between successive DM trials is increased, further reducing the amount of processing. Therefore, the extra computing required to go to high DMs is relatively small compared to what is required to search for pulsars and transients at low DMs. Searching DMs between 1000 and $10000\,\mathrm{pc\,cm^{-3}}$ adds only ~5 % the total data analysis time.

Dedispersion is done with `PRESTO`'s `prepsubband`, passing through the raw data 99 times, and resulting in 7292 dedispersed time series. In all cases `prepsubband` internally uses 96 sub-bands, each of 10 MHz, for its two-stage sub-band dedispersion process. Time intervals containing strong impulsive RFI are removed by `prepsubband`, as prescribed by a RFI mask (see § 3.3.4).

A second set of dedispersed time series are created as before, but also applying a version of the zero-DM filtering technique described by Eatough et al. (2009) that has been augmented to use the bandpass shape when removing the zero-DM signal from each channel. These zero-DM filtered time series are especially useful for single-pulse searching, which is described in § 3.3.3. See § 3.3.4 for details on time-domain RFI mitigation strategies used.

Dedispersion makes up roughly 15-20 % of the processing time.

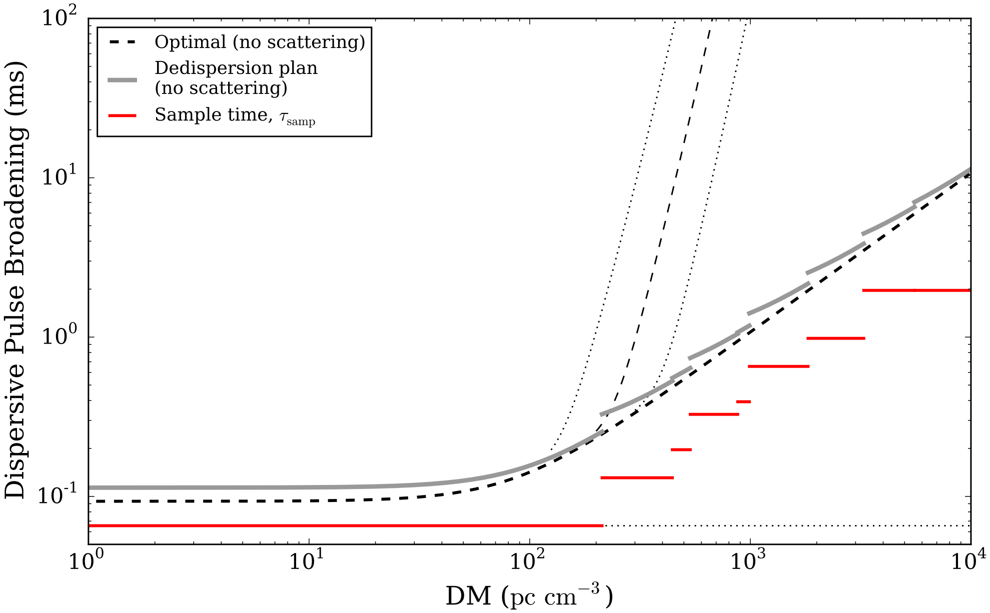

Figure 3.3: Pulse broadening from down-sampling, and dispersive DM smearing for the dedispersion plan generated by `DDplan.py` shown in Table 3.3 (grey), as well as the optimal case (dashed black) where neither down-sampling nor smearing from DM errors are included. The optimal case including interstellar scattering is shown (with ± 1 order of magnitude; thin dashed black) assuming the empirical scattering dependence on DM of Bhat et al. (2004). While this dependence is likely reasonable for estimating the scattering of Galactic sources, it is likely to grossly overestimate the scattering of extragalactic sources (e.g. FRBs). In all cases, the middle of the observing band is assumed (~1375 MHz). Discontinuities are due to down sampling. The horizontal lines (red) show the down sampled time resolution at various DMs.

Periodicity Searching

For every dedispersed time series, the discrete Fourier transform (DFT) is computed using `PRESTO`'s `realfft`. Prior to searching the DFT for peaks, it is normalized to have unit mean and variance. The normalization algorithm is designed mainly to suppress red noise (i.e. low-frequency trends in the time series; for more details see § 3.3.4). Also, Fourier bins likely to contain interference are replaced with the median-value of nearby bins. Details of the algorithm used to determine RFI-prone frequencies are described in § 3.3.4.

Two separate searches of the DFT are conducted using `PRESTO`'s `accelsearch`. Both searches identify peaks in the DFT down to a frequency of 0.125 Hz.

The first, *zero-acceleration*, search is tuned to identify isolated pulsars. The power spectrum of the signal from an isolated pulsar will consist of narrow peaks at the rotational frequency of the pulsar and at harmonically related frequencies. The number of significant harmonics depends on the width of the pulse profile, W, and the spin period, P, as $N_{\rm harm} \sim P/W$. To improve the significance of narrow signals, power from harmonics is summed with that of the fundamental frequency. The zero-acceleration search sums up to 16 harmonics, including the odd harmonics, in powers of 2 (i.e. 1, 2, 4, 8, 16 harmonics). For signals with significant higher harmonics, this harmonic summing procedure also improves the precision of the detected frequency.

The second, *high-acceleration*, search is optimized to find pulsars in binary systems. The time-varying line of sight velocity of such pulsars gives rise to a Doppler shift that varies over the course of an observation. This smears the signal over multiple bins in the Fourier domain. To recover sensitivity to binary pulsars we use the Fourier-domain acceleration search technique described in Ransom et al. (2002). In short, the high-acceleration search performs matched-filtering on the DFT using a series of templates each corresponding to a different constant acceleration. We search using templates up to 50 Fourier bins wide, which corresponds to a maximum acceleration of $\sim$1650 m/s^2 for a 5-minute observation of a 10-ms pulsar. Only up to 8 harmonics are summed in the high-acceleration case because of its larger computational requirements.

For each of the periodic signal candidates identified in both the zero- and high-acceleration searches we interpolate the frequency and frequency derivative (i.e. acceleration) to optimize the harmonics. We then normalize the harmonics, and compute the equivalent Gaussian significance of the candidate, σ_F, based on the probability of seeing a noise value with the same amount of incoherently summed power (see Ransom et al., 2002, for details). The zero- and high-acceleration candidate information is saved to separate lists for later post-processing. We record information candidates with $\sigma_F > 2$ for the zero-acceleration search. For the high-acceleration search we use a slightly larger threshold of $\sigma_F > 3$ to partially compensate for the increased number of trials. However, due to the large number of candidates resulting from searching all DM trials, we only consider those with $\sigma_F > 6$ for folding (see § 3.3.3 for details).

Typically, the zero-acceleration and high-acceleration searches make up between 2 % and 5 % and $\sim$30 % of the overall computation time, respectively.

Single Pulse Searching

Each dedispersed time series is also searched with `PRESTO`'s `single_pulse_search.py` for impulsive signals with a matched-filtering technique (e.g. Cordes & McLaughlin, 2003). Prior to searching, the time series is de-trended by subtracting the linear slope from each 1000-sample block. The standard deviation of each block, $\sigma_{\rm block}$ is estimated.[1] To identify single pulse candidates, multiple box-car templates corresponding to a range of durations up to 0.1 s are used.[2] Candidate single-pulse events at brighter than $5\,\sigma_{\rm block}$ are recorded. Diagnostic plots featuring only $>6\,\sigma_{\rm block}$ candidate events are generated and archived for later viewing. In addition to the basic diagnostic plots, all of the $>5\,\sigma_{\rm block}$ events are used in post-processing algorithms designed to distinguish astrophysical signals (e.g. from pulsars/RRATs and extragalactic FRBs) from RFI and noise. The algorithms employed by PALFA are described elsewhere (Spitler, 2013; Karako-Argaman et al., 2015).

The same searching and post-processing procedure is also applied to zero-DM filtered time series. To filter the data, we employ an enhanced version of what was originally described in Eatough et al. (2009). See § 3.3.4 for more details about the time-domain RFI-mitigation techniques used.

The single-pulse searching makes up approximately 20 % of the computing time.

---

[1] In `single_pulse_search.py`, the standard deviation calculation excludes the 2.5 % largest values and the 2.5 % smallest values in the block. The standard deviation is corrected for the discarded data assuming the remaining values are Gaussian distributed.

[2] The possible widths of the templates are 1, 2, 3, 4, 6, 9, 14, 20, 30, 45, 70, 100, 150, 220, 300 bins. The largest template used depends on the resolution of the time series and the <0.1 s restriction.

Sifting

As described above, the output of periodicity searching is a set of files, the zero- and high-acceleration candidate lists for each DM trial, containing the frequency of significant peaks found in the Fourier transformed time series, along with other information about the candidate. In total, for all DMs, there are typically $\sim 10^4$ period-DM pairs per beam. These signal candidates are *sifted* to identify the most promising pulsar candidates, match harmonically related signals, and reject RFI-like signals.

The first stage of the sifting process is to remove short-period candidate signals ($P < 0.5\,\mathrm{ms}$), which contribute a large number of false-positives, as well as to ensure no candidate signals with periods longer than the limit of our search ($P > 15\,\mathrm{s}$) are present. Weak candidates with Fourier-domain significances $\sigma_F < 6$ are also removed. Furthermore, candidates with weak or strange harmonic powers are rejected if they match one of the following cases: (1) the candidate has no harmonics whose power is at least 8 times larger than the local power spectrum level; (2) the candidate has $\gtrsim 8$ harmonics and is dominated by a high harmonic (fourth[1] or higher), having at least twice as much power as the next-strongest harmonic; (3) the candidate has 4 harmonics and is dominated by a high harmonic (third or higher), having at least three times as much power as the next-strongest harmonic.

The next stage of sifting is to group together candidates with similar periods (at most 1.1 Fourier bins apart) found in different DM trials. When a duplicate period is found, the less significant candidate is removed from the main list, and its DM is appended to a list of DMs where the stronger candidate was detected.

At this stage, for each periodic signal, there is a list of DMs at which it was detected. The next step is to purge candidates with suspect DM detections. Specifically, candidates not detected at multiple DMs, candidates that were most strongly detected at $\mathrm{DM} \leq 2\,\mathrm{pc\,cm^{-3}}$, and candidates that were not detected in consecutive DM trials are all removed from subsequent consideration.

The steps described above are applied separately to candidates found in the zero- and high-acceleration searches. At this point, the two candidate lists are merged, and signals harmonically related to a stronger candidate are removed from the list. This process checks for a conservative set of integer harmonics, and small integer ratios between the signal frequencies. As a result, some harmonically related signals are occasionally retained in the final candidate list.

The sifting process typically results in ~200 good candidates per beam, of which ~100 are above the significance threshold for folding. The fraction of time spent on candidate sifting is negligible ($< 0.1\,\%$) compared to the rest of the pipeline.

Folding

The raw data are folded for each periodicity candidate with $\sigma_F \geq 6$ remaining after the sifting procedure using `PRESTO`'s `prepfold`. At most 200 candidates are folded for each beam. In more than 99 % of cases this limit is sufficient to fold all $\sigma_F \geq 6$ candidates. If too many candidates have $\sigma_F \geq 6$, the candidates with largest σ_F are folded.

---

[1] We number harmonics such that the frequency of the Nth harmonic is N times larger than the fundamental frequency.

After folding, `prepfold` performs a limited search over period, period-derivative, and DM to maximize the significance of the candidate. However, for candidates with $P > 50\,\mathrm{ms}$ the search over DM is excluded because it is prone to selecting a strong RFI signal at low DM even if there is a pulsar signal present. Furthermore, the optimization of the period-derivative is also excluded for $P > 500\,\mathrm{ms}$ candidates.

For each folded candidate a diagnostic plot is generated (see Ransom, 2001, for examples). These plots, along with basic information about the candidate (optimized parameters, significance, etc.) are placed in the PALFA processing results database, hosted at the Cornell CAC. The `prepfold` binary output files generated for each fold are also archived at Cornell.

The binary output files created by `prepfold` are used by a candidate-ranking artificial intelligence (AI) system, as well as to calculate heuristics for candidate sorting algorithms. Details can be found in §3.3.5.

Folding the raw data for up to 200 candidates per beam is a considerable fraction (~25 %) of the overall computing time.

3.3.4 RFI-mitigation Components

The sensitivity of Arecibo and PALFA can only be fully realized if interference signals in the data are identified and removed. To work toward this goal, the PALFA pipeline includes multiple levels of RFI excision. Each algorithm is designed to detect and mitigate a different type of terrestrial signal. Because these interference signals are terrestrial they are not expected to show the $1/f^2$ frequency sweep characteristic of interstellar signals. Unfortunately, some terrestrial signals show broadband frequency sweeps that cannot be distinguished from astronomical signals by data analysis pipelines (e.g. "perytons" Burke-Spolaor et al., 2011; Petroff et al., 2015). Despite some non-astronomical signals remaining in the data, the suite of RFI-mitigation techniques described here are an essential part of the pipeline.

All of the algorithms described here are applied to non-dedispersed, topocentric data.

Removal of Site-specific RFI

Unfortunately, some of the electronics hardware at the Arecibo Observatory, specifically the ALFA bias monitoring system,[1] introduced strong periodic interference into our data. By the time the source of the interference was determined several months of observations had been affected. Fortunately, we were able to develop a finely tuned algorithm to excise the signal using our knowledge of the sub-pulse structure to identify and remove these intense bursts of interference. The removed sections of data are replaced with a running median, which is computed separately for each ~1 s block of data. Finely tuned algorithms such as this one have the advantage of more easily identifying specific RFI signals and only extracting the affected data. In this particular case, each 1-s burst of RFI is made up of a comb of ~10 ms-long sub-pulses repeated every ~50 ms. By removing these bursts, our algorithm largely eliminates the broad peaks in the Fourier domain that are introduced by the pernicious electronics, typically between 1 and 1000 Hz (i.e. exactly where we expect pulsars to be found). See Figure 3.4 for an example. Furthermore, by removing the interference pulses in the

---

[1] The ALFA bias monitoring system measures the amplifier bias voltages, as well as other systems in the dewars, including temperatures, currents and voltages.

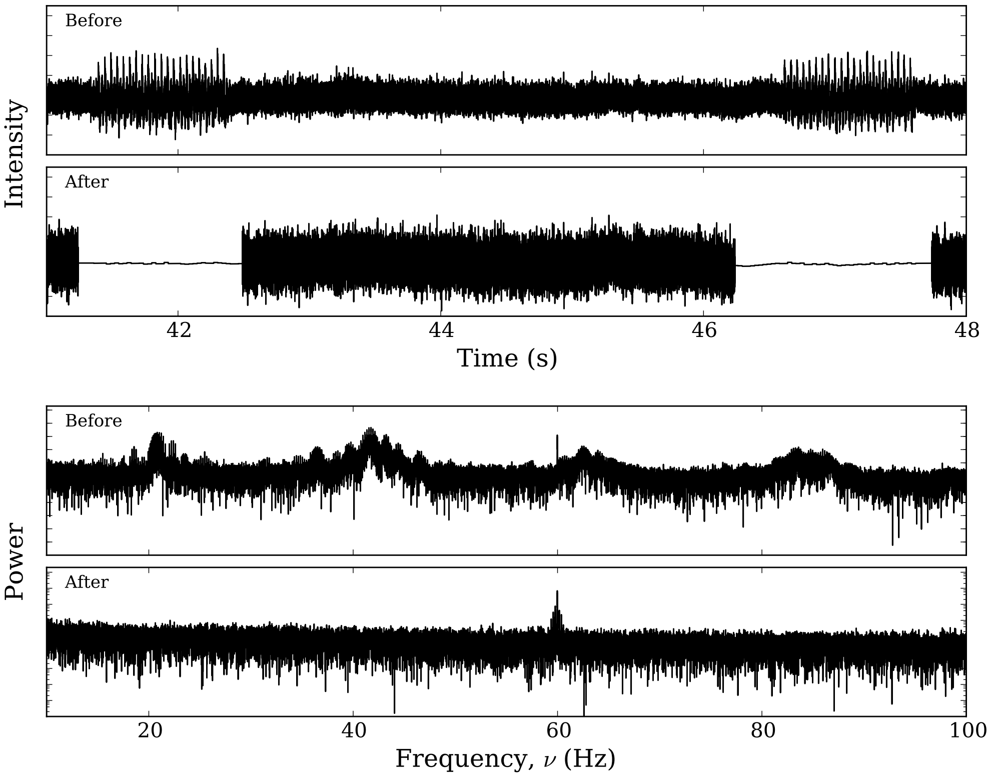

Figure 3.4: An example of the effect of the bursts of interference caused by some of the electronics equipment at the Arecibo Observatory on PALFA survey data in time and frequency domain (labelled "Before") and the same interval of time series and power spectrum after our finely tuned removal algorithm, described in § 3.3.4, is applied (labelled "After"). Part of the time series is sacrificed, but the broad features in the frequency domain are completely removed. The RFI peak at 60 Hz that remains in the bottom panel is caused by the electrical mains and is later removed by zapping intervals of the power spectrum (described in § 3.3.4). The source of this interference signal has been identified and can be dealt with by shutting it off during PALFA observations. The linear slope in the power spectrum is due to red noise in the PALFA data. The effect of red noise is discussed in §§ 3.6 and 3.7.

time domain, the power spectrum is cleaned without sacrificing any intervals of the Fourier domain, as would be the case with the zapping algorithm described in § 3.3.4.

Because the equipment causing the bursts of interference in our observations is not essential to data taking we have been able to shut it off during PALFA sessions.

Narrow-band Masking

Every observation is examined for narrow-band RFI signals using `PRESTO`'s `rfifind`, which considers 2-s long blocks of data in each frequency channel separately. For each block of data two time-domain statistics are computed: the mean of the block data value, and the standard deviation of the block data values. Also, one Fourier-domain statistic is computed for each block: the maximum value in the power spectrum. Blocks where the value of one or more of these three statistics is sufficiently far from the mean of its respective distribution are flagged as containing RFI. For the two time-domain metrics, in the PALFA survey the threshold for flagging a block is 10 standard deviations from the mean of the distribution, and for the Fourier-domain metric, the threshold is 4 standard deviations from the mean. The resulting list of flagged blocks is used to mask out RFI. Masked blocks are filled with constant data values chosen to match the median bandpass of that time interval. Sub-integrations that are at least 70 % masked are completely replaced. Similarly, channels that are more than 30 % masked are completely replaced with zeros.

On average, only ∼5.75 % of time-frequency space is masked by this algorithm, and ∼93 % of observations have mask-fractions less than 10 %. Having a mask-fraction larger than 15 % is one of the conditions used to identify observations that will be re-inserted into the list of sky positions to observe. Only ∼1.1 % of observations fall into this category.

The fraction of data masked for each beam, and a graphical representation of the mask are stored in the results database as diagnostics of the observation quality.

Generating the `rfifind` mask makes up only ∼1 % of the total pipeline running time.

Time-domain Clipping and Filtering

It is possible for broad-band impulsive interference signals to be missed by the masking procedure described above if the signals are not sufficiently strong to be detected in individual channels. Fortunately, the PALFA pipeline makes use of a complementary algorithm designed to remove such signals from the data: a list of bad time intervals is determined by identifying samples in the $\mathrm{DM} = 0\,\mathrm{pc\,cm^{-3}}$ time series that are significantly larger ($>6\,\sigma_{\mathrm{loc}}$) than the surrounding data samples. The spectra corresponding to the bad time intervals are replaced by the local median bandpass.

As previously mentioned, for single-pulse searching, the PALFA pipeline also applies the `PRESTO`-implementation of the zero-DM filtering technique described in Eatough et al. (2009). This implementation enhances the original prescription by using the bandpass shape as weights when removing the $\mathrm{DM} = 0\,\mathrm{pc\,cm^{-3}}$ signal. The zero-DM filter greatly reduces the impact of RFI on single-pulse searching, facilitating low-DM RRATs being distinguished from RFI. To illustrate the benefits of zero-DM filtering, Figure 3.5 shows a comparison of the single-pulse events identified by `single_pulse_search.py` in an observation of PSR J1908+0734 with and without filtering.

Red-noise Suppression

In order to properly normalize the power spectrum and compute more correct false-alarm probabilities (see Ransom et al., 2002), we use a power spectrum whitening technique to suppress frequency-dependent, and in particular “red” noise. The median power level is measured in blocks of Fourier frequency bins and then divided by $\log 2$ to convert the median level to an equivalent mean level assuming that the powers are distributed exponentially (i.e. χ^2 with 2 degrees-of-freedom).

The number of Fourier frequency bins per block is determined by the log of the starting Fourier frequency bin, beginning with 6 bins and increasing to approximately 40 bins by a frequency of 6 Hz. Above that frequency, where there is little to no “coloured” noise, block sizes of 100 bins are used. The resulting filtered power spectrum has unit mean and variance. This process is accomplished with `PRESTO`’s `rednoise` program.

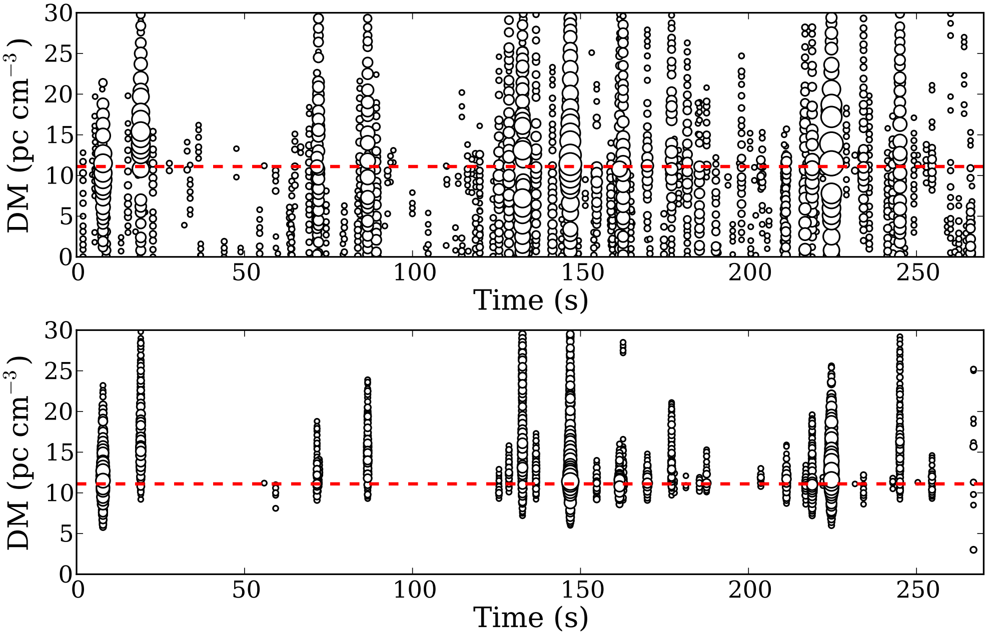

Figure 3.5: Comparison of single-pulse events detected in a PALFA observation of PSR J1908+0734 in a search of the un-filtered time series (top) and the zero-DM filtered time series (bottom). Each circle represents the time and DM of an impulsive signal found by `PRESTO`'s `single_pulse_search.py`. The size of the circle is proportional to the significance of the signal (up to a maximum radius). Most of the RFI is filtered out of the observation by the zero-DM algorithm while leaving the pulsar pulses, albeit with some loss of significance at the lower DMs (see Eatough et al., 2009, for a discussion). Thus, the zero-DM filtering technique makes it far easier to disentangle astrophysical signal at non-zero DMs from RFI at DM $= 0\,\mathrm{pc\,cm^{-3}}$ both by eye and algorithmically. The pulsar's DM $= 11\,\mathrm{pc\,cm^{-3}}$ is indicated with the dashed red line.

Fourier-domain Zapping

Sufficiently bright periodic sources of RFI can be mistakenly identified as pulsar candidates by our FFT search. To excise, or *zap*, these signals from our data we tabulate frequency ranges often contaminated by RFI. The Fourier bins contained in this *zap list* are replaced by the average of nearby bins prior to searching.

The RFI environment at Arecibo is variable. The number, location, and width of interference peaks in the Fourier transform of DM $= 0\,\mathrm{pc\,cm^{-3}}$ time series vary on a time scale of months to years. To demonstrate this, the fraction of Fourier bins occupied by RFI as a function of epoch is illustrated in Figure 3.6. The median fraction of the Fourier spectrum occupied by RFI for all Mock spectrometer data for various intervals is: 2.9 % (0 – 10 Hz), 5.1 % (10 – 100 Hz), and 0.5 % (100 – 1000 Hz). To account for this dynamic nature of the RFI, we compute zap lists for each MJD.

To compute zap lists we exploit the fact that RFI signals are typically detected by multiple feeds in a single 5 minute pointing, or persist for most of an observing session (typically 1 – 3 h). The strategy we employ here is similar to what was used in the Parkes Multibeam Pulsar Survey (Manchester et al., 2001). Fourier bins contaminated by RFI are determined by finding peaks in a *median power spectrum*, which is comprised of the bin-wise median of multiple DM $= 0\,\mathrm{pc\,cm^{-3}}$ power spectra. This is

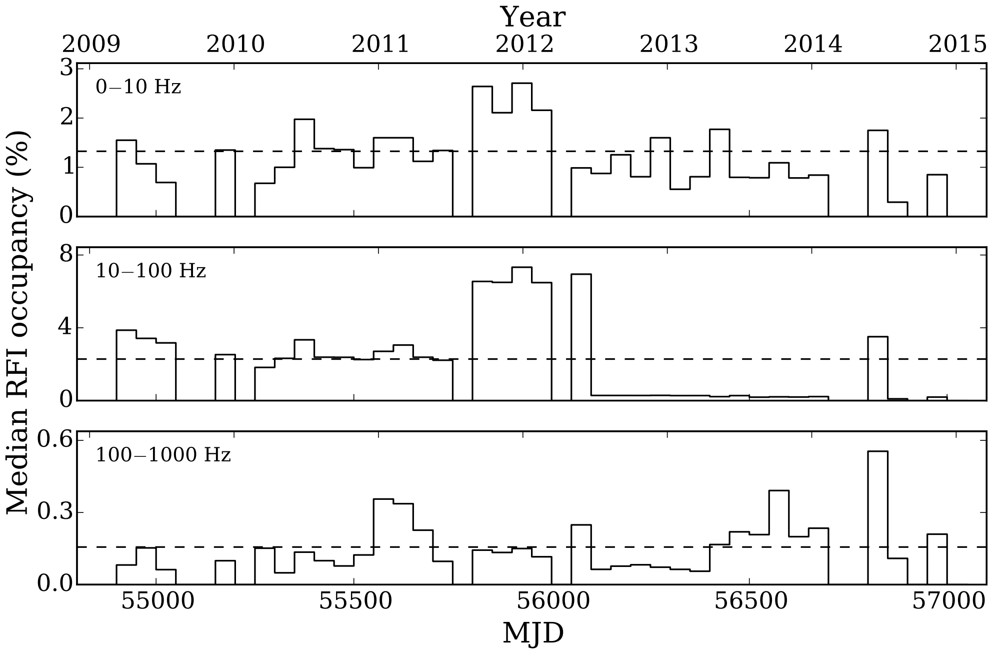

Figure 3.6: Median percentage of the Fourier domain occupied by RFI in three frequency ranges for 50-d intervals (solid lines) compared against the median percentage for all observations (dashed lines). Many periodic sources of RFI are found to vary on daily time scales. Thus, lists of RFI-contaminated Fourier frequencies to be removed from the power spectrum prior to searching are tailored to the RFI of each MJD. The increase in RFI in the middle panel between MJD 55750 and 56100 was due to on-site electronics at the telescope, which since being identified in 2012 June (MJD ≃56100) have nearly always been turned off during PALFA observations, significantly reducing the RFI in the 10 – 100 Hz interval.

done twice, using two different subsets of data: (a) all observations made with a given ALFA feed on a given day (to identify RFI signals that persist for multiple hours, or issues specific to the ALFA receiver), and (b) all seven observations from a given pointing (to identify shorter-duration periodic RFI signals that enter multiple feeds). The zap list for any given observation is the union of the lists for its pointing and its feed.

Observations whose power spectra are more than 8 % occupied by RFI are flagged for re-observation. Roughly 3 % of observations meet this criterion.

With the advent of sophisticated candidate ranking and candidate classifying machine-learning algorithms (see § 3.3.5), it is better to leave some RFI in the data than to remove large swaths of the Fourier domain. To avoid excessive zapping we remove at most 3 % from each frequency decade, up to a maximum of 1 % globally, preferentially zapping bins containing the brightest RFI.

In addition to being an essential part of the PALFA RFI-mitigation strategy, zap lists have also proven to be a useful diagnostic for monitoring the RFI environment at Arecibo.

3.3.5 Post-processing Components

Ratings

A series of 19 heuristic ratings are computed for each folded periodicity candidate produced by the data analysis pipeline. These ratings encapsulate information about the shape of the profile, the persistence and broadbandedness of the signal, whether the frequency of the signal is particularly RFI-prone, and whether the signal is stronger at DM $= 0\,\mathrm{pc\,cm^{-3}}$. Each of the ratings is uploaded to the results database, and is available for querying and sorting candidates (see § 3.3.6). The ratings and brief descriptions are presented in Table 3.4.

The ratings are incorporated into candidate-selection queries along with standard parameters such as period, DM, and various measures of time-domain and frequency-domain significance. Using ratings in this way allows users to constrain the candidates they view to have certain features they would require when selecting promising candidates by eye. Alternatively, the ratings have been used in a decision-tree-based AI algorithm, but this has since been supplanted by the more sophisticated "Pulsar Image-based Classification System (PICS)" algorithm described in § 3.3.5 (Zhu et al., 2014).

The code to compute the ratings[1] is compatible with the binary files produced by `PRESTO`'s `prepfold` for each periodicity candidate. For each candidate a text file is written containing the name, version, description, and value for all ratings being computed. This task is performed as part of the data analysis pipeline. The rating information is later uploaded to the results database. In cases where a new rating is devised, or an existing rating is modified, the `prepfold` binary files are fetched from the results archive, ratings are computed in a stand-alone process (i.e. independent of the pipeline), and the values are inserted into the database. The values of improved ratings are inserted alongside values from old versions to permit detailed comparisons.

Machine Learning Candidate Selection

All periodicity candidates are also assessed by the PICS (PICS; Zhu et al., 2014), an image-pattern-recognition-based machine-learning system for selecting pulsar-like candidates. The PICS deep neural network enables it to recognize and learn patterns directly from 2D diagnostic images produced for every periodicity pulsar candidate. The large variety of pulsar candidates used to train PICS has developed its ability to recognize both pulsars and their harmonics.

PICS can reduce the number of candidates to be inspected by human experts by a factor of ~100 while still identifying 100 % of pulsars and 94 % of harmonics to the top 1 % of all candidates (Zhu et al., 2014).

Since late 2013, PICS has been integrated directly into the PALFA processing pipeline. It produces a single rating for each candidate, which is uploaded into the results database as a rating (see § 3.3.5). So far, this has aided in the discovery of 8 pulsars (see § 3.4).

Coincidence Matching

While PALFA has been successful at finding moderately bright MSPs, the vast quantity of periodicity candidates close to the detection threshold at very short periods ($\lesssim 2\,\mathrm{ms}$) have made it more challenging to identify the *faint* MSPs in the PALFA

---

[1] Available at https://github.com/plazar/ratings2.0.

Table 3.4: Heuristic Candidate Ratings

Rating	Description
	Profile Ratings[a]
Duty Cycle	Fraction of profile bins larger than half the maximum value of the profile
Peak Over RMS	Maximum value of the profile divided by the RMS
	Profile Ratings (Gaussian Fitting)[a]
Amplitude	Amplitude of a single Gaussian component fit to the profile
Single Component GoF	Goodness of Fit of a single Gaussian component fit to the profile
FWHM	Full-width at half-maximum of a single Gaussian component fit to the profile
No. Components	Number of Gaussian components required to acceptably fit the profile (up to 5 components)
Multi-component GoF	Goodness of fit of the multiple Gaussian component fit (up to 5 components)
Pulse Width	Ratio of narrowest component of the multiple Gaussian fit compared to the pulse broadening (excluding scattering)
	Time vs. Phase Ratings
Period Stability	Fraction of good time intervals that deviate in phase by ≤ 0.02
Frac. of Good Sub-ints	Fraction of time intervals that contain the pulsar signal
Sub-int. S/N Variability	The standard deviation of sub-integration S/Ns
	Frequency vs. Phase Ratings
Frac. of Good Sub-bands	Fraction of sub-bands that contain the pulsar signal
Sub-band S/N Variability	The standard deviation of sub-band S/Ns
	DM Ratings
DM Comparison (standard deviation)	Ratio of the standard deviation of the profile at $\mathrm{DM} = 0\,\mathrm{pc\,cm^{-3}}$ and at the optimal DM
DM Comparison (χ^2)	Ratio of the χ^2 of the profile at $\mathrm{DM} = 0\,\mathrm{pc\,cm^{-3}}$ and at the optimal DM
DM Comparison (peak)	Ratio of the peak value of the profile at $\mathrm{DM} = 0\,\mathrm{pc\,cm^{-3}}$ and at the optimal DM
	Miscellaneous Ratings
Known Pulsar	A measure of how similar the candidate period and DM are to a nearby pulsar (also checks harmonic relationships)
Mains RFI	A measure of how close the topocentric frequency is to 60 Hz, or a harmonic
Beam Count	The number of beams from the same pointing containing another candidate with the same period

NOTES. — See § 3.3.5 for more details on how ratings are used to select candidates.

[a] Prior to computing ratings, the profile is normalized such that median level is 0 and the standard deviation is 1.

results database. To facilitate the process, a search for signals with compatible periods, DMs and sky positions has been performed on the periodicity candidates in the database. By applying our coincidence matching algorithm to the complete list of folded candidates we are able to reliably probe lower S/Ns than would be reasonable to do thoroughly by manual viewing. This algorithm is complementary to our machine learning technique that operates on each candidate individually. The software developed to find matching candidates is available on the web for general use.[1]

Large parts of the survey region have either been observed more than once or have been densely sampled (see Figure 3.1), making it possible to match the detection of a pulsar from multiple observations confidently. For each observation, a list of beams from other pointings that fall within $5'$ is generated. Candidates from the different beams are matched by their DMs and barycentric periods. Allowances are made for slightly different DMs and periods, as well as for harmonically related periods. Multiple matches that include the same candidate are consolidated to form groups of more than two candidates.

The results of this matching algorithm are examined with a dedicated, web-based interface. Many known pulsars, especially high harmonics of very bright slow pulsars, have already been identified.

As of 2015 January, our coincidence matching search has not yet resulted in the discovery of new pulsars, but it continues to be applied to the results database. This algorithm will be increasingly useful as more of the PALFA survey region becomes densely sampled, and as more Mock spectrometer observations cover positions previously observed with the WAPP spectrometers.

3.3.6 Collaborative Tools

The PALFA Consortium has created and made use of several online collaborative tools on the CyberSKA portal[2] (Kiddle et al., 2011), a website developed to help astronomers build tools and strategies for large-scale projects in the lead-up to the Square Kilometre Array (SKA).

The CyberSKA portal allows for third-party applications to be accessed directly without a need for separate user authentication. Within this framework several PALFA-specific applications were developed:

Candidate Viewer – The primary method for viewing and classifying PALFA candidates is by using the CyberSKA *Candidate Viewer* application. It allows users to access the Cornell-hosted results database using form-based, free-text, and saved queries. Queries include basic observation and candidate information (e.g. sky position, period, DM, significance), as well as ratings (§ 3.3.5), and the PICS classifications (§ 3.3.5). Users are presented with a series of `prepfold` diagnostic plots in sequence, one for each candidate matching the query. By inspecting the plots, as well as other relevant information provided, such as a histogram showing the number of occurrences of signals in the relevant frequency range as well as a summary plot showing all the beam's periodic signal candidates in a period-DM plot, the user can quickly classify candidates. Classifications are saved to the database and can be easily retrieved.

Top Candidates – Especially promising candidates found with the Candidate Viewer can be added to the *Top Candidates* application, which is designed to store the most

---

[1] https://github.com/smearedink/PALFA-coincidences

[2] http://www.cyberska.org

likely pulsar candidates. The application also allows collaboration members to view and vote on which candidates should be subject to confirmation observations, as well as help organize and track these observations and their outcomes.

Survey Diagnostics – Optimizing the use of telescope time and computing resources is extremely important for large-scale pulsar surveys such as PALFA. The *Survey Diagnostics* application automatically compiles a set of information and a set of plots from various sources to help the project run smoothly. This includes the status of data acquisition and reduction, the severity of the RFI environment, and the quality of the data.

3.4 Results

The PALFA survey has discovered 144 pulsars, including 19 MSPs and 11 RRATs, and one FRB, as of 2015 March. The `PRESTO`-based pipeline described in § 3.3 has discovered 40 pulsars from their periodic emission, 5 RRATs from their impulsive emission, and re-detected another 60 pulsars that were previously discovered with other PALFA data analysis pipelines. The other pulsars found in the PALFA survey were discovered with the different data analysis pipelines, such as the E@H and Quicklook pipelines (Allen et al., 2013; Stovall, 2013) which use complementary RFI-excision and search algorithms, with dedicated transient searches, or in earlier observations with the WAPP spectrometers using an earlier version of the pipeline described here. Not all sky positions observed with the WAPP spectrometers have been covered with the Mock spectrometers yet.

We report details for 40 of the periodicity-discovered pulsars found in Mock spectrometer data with the pipeline described above. All but one of these discoveries are in the inner Galaxy region. These pulsars were discovered by analyzing 85333 beams, covering a total of 134 sq. deg., which consists of 80 sq. deg. in the inner Galaxy region, and 54 sq. deg. in the outer Galaxy region (see Table 3.2). Basic parameters of the discoveries are in Table 3.5, and pulse profiles from the discovery observations are shown in Figure 3.7.

Eight of the 40 pulsars reported here are MSPs, including the most distant MSP (based on its DM) discovered to date, PSR J1850+0242. The distance estimated from the DM of PSR J1850+0242, assuming the NE2001 model (Cordes & Lazio, 2002), is 10.4 kpc, a testament to the ability of the PALFA survey to find highly dispersed, short period pulsars. PSR J1850+0242, along with three of the other MSPs discoveries reported here are described in detail in Scholz et al. (2015). Three more of the MSPs reported here will be included in Stovall et al. (in prep.).

Nine of the 40 pulsars reported here are in binary systems, including seven of the MSPs, and two slower pulsars, PSRs J1932+17 ($P \simeq 42\,\mathrm{ms}$) and J1933+1726 ($P \simeq 22\,\mathrm{ms}$), which have small spin-down rates, indicating they were spun-up by the accretion of mass and transfer of angular momentum, the so-called “recycling” process (Alpar et al., 1982). The timing analyses of PSRs J1932+17 and PSR J1933+1726 will be provided by Madsen et al. (in prep.) and Stovall et al. (in prep.), respectively.

Timing solutions for six of the slow pulsars presented in this work, including the young PSR J1925+1721, will be published in a forthcoming paper along with the timing of other PALFA-discovered pulsars (Lyne et al., in prep.).

In addition to the 40 pulsars detailed here that were discovered in periodicity searches, the `PRESTO`-based pipeline has found five RRATs. The beams containing

Table 3.5: Pulsars Discovered in Mock Spectrometer Data

Name	Disc. Period (ms)	Disc. DM ($\mathrm{pc\,cm^{-3}}$)	Disc. Significance (σ_F)	Flux Density [a] (mJy)
J0557+1550[b]	2.55	102.7	8.34	0.050(6)[c]
J1850+0242[b]	4.48	540.5	13.08	0.33
J1851+0232	344.02	605.4	10.82	0.09
J1853+03	585.53	290.2	14.28	–[d]
J1854+00[e]	767.33	532.9	10.44	–[d]
J1858+02	197.65	492.1	14.91	–[d]
J1901+0235[e]	885.24	403.0	26.7	–[d]
J1901+0300[b]	7.79	253.7	11.8	0.113(4)[c]
J1901+0459	877.06	1103.6	10.93	0.10
J1902+02[e]	415.32	281.2	7.58	–[d]
J1903+0415[e]	1151.39	473.5	12.48	–[d]
J1904+0451[b]	6.09	183.1	8.78	0.117(9)[c]
J1906+0055	2.79	126.9	16.47	0.12
J1906+0725	1536.51	480.4	7.13	0.05
J1907+0256	618.77	250.4	12.07	0.19
J1907+05	168.68	456.7	10.0	–[d]
J1909+1148	448.95	201.9	15.93	0.06
J1910+1027	531.47	705.7	9.29	0.06
J1911+09	273.71	334.7	7.13	–[d]
J1911+10	190.89	446.2	7.48	–[d]
J1913+0617	5.03	155.8	9.81	–[d]
J1913+1103	923.91	628.9	9.86	0.09
J1914+0659	18.51	224.7	12.66	0.33
J1915+1144	173.65	338.3	23.59	0.08
J1915+1149	100.04	702.1	7.58	–[d]
J1918+1310	856.74	247.4	6.56	–[d]
J1921+16	936.43	204.7	8.13	–[d]
J1924+1628[e]	375.09	542.9	21.12	0.09
J1924+17	758.43	527.4	10.66	–[d]
J1925+1721	75.66	223.7	16.06	0.09
J1926+1613[e]	308.30	32.9	14.9	–[d]
J1930+14[e]	425.71	209.2	12.15	0.04
J1931+1440	1779.23	239.3	23.63	0.12
J1932+17[e]	41.82	53.2	12.89	–[d]
J1933+1726	21.51	156.6	7.28	0.04
J1934+19	230.99	97.6	18.67	0.10
J1936+20	1390.88	205.1	6.6	–[d]
J1938+2012[e]	2.63	237.1	8.55	0.02
J1940+2246	258.89	218.1	14.47	0.09
J1957+2516	3.96	44.0	6.61	0.04

[a] Phase-averaged flux density. Determined using the radiometer equation (see § 3.4.1) unless otherwise noted.

[b] Pulsar was previously published by Scholz et al. (2015).

[c] Flux calibrated using noise diode. Value from Scholz et al. (2015).

[d] Refined position not available. Flux density could not be estimated.

[e] Pulsar was first identified using the PICS machine learning candidate selection system described in § 3.3.5.

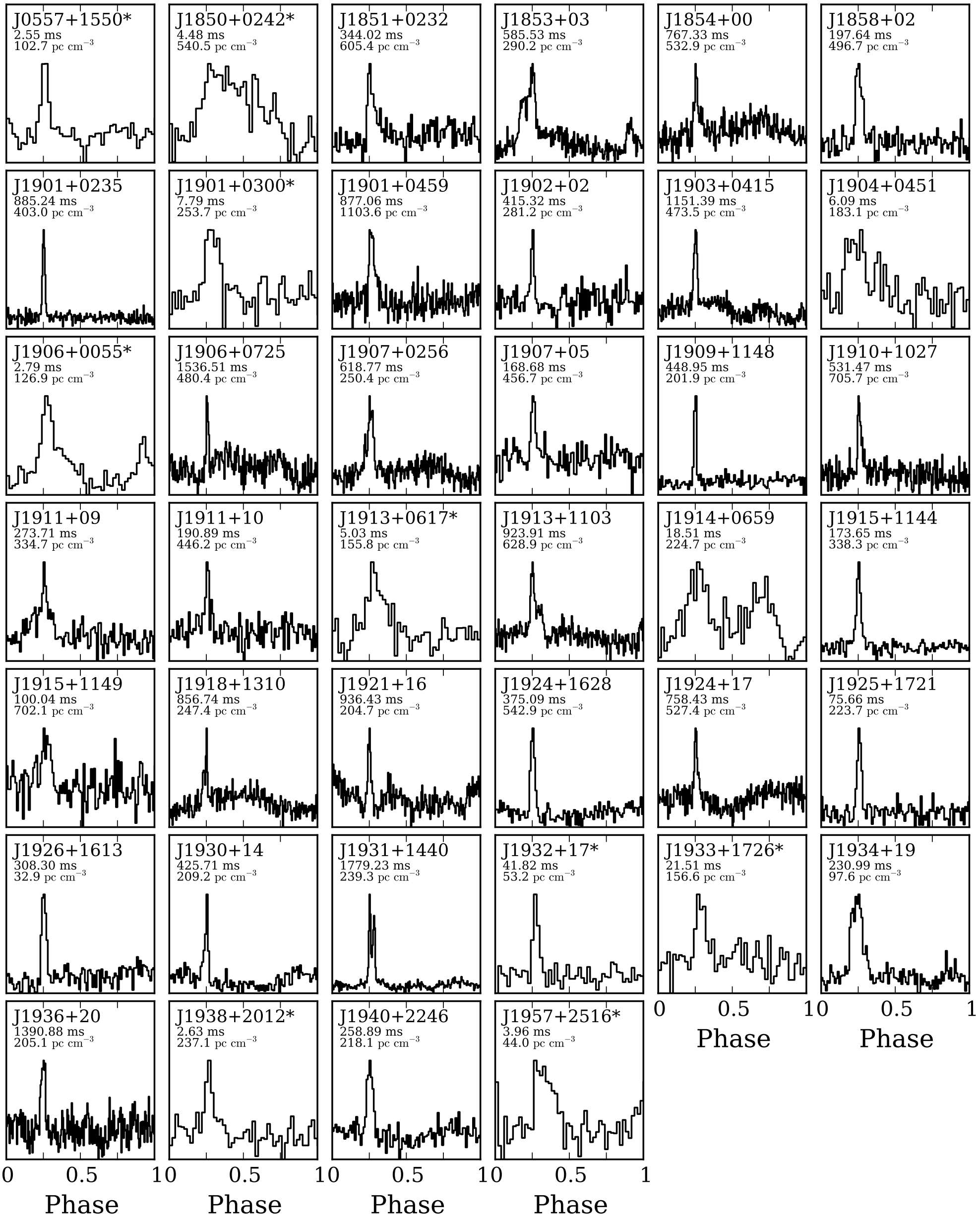

Figure 3.7: Pulse profiles at 1.4 GHz from the discovery observations of the 40 pulsars discovered with the `PRESTO`-based PALFA pipeline in Mock spectrometer data. The name of each pulsar is included above each profile along with the period, and dispersion measure. The names of binary pulsars are indicated with an asterisk (*). The number of bins across the profile is what was used by the pipeline, and is larger for longer period pulsars. These profiles also include intra-channel DM smearing, which is most significant for high-DM, short-period pulsars. The baselines of several profiles, predominantly of the long-period pulsars, show broad features due to interference and red noise in the data (for example, PSRs J1854+00, J1921+16, and J1924+17). The discovery profiles contaminated with RFI and red noise are shown here to highlight the ability of the PALFA pipeline to identify pulsars despite these conditions. Pulsars with truncated names do not yet have positions determined from timing campaigns.

these RRATs were identified using a post-processing algorithm originally developed for pulsar surveys at 350 MHz with the Green Bank Telescope (see Karako-Argaman et al., 2015, for details). Discovery parameters and detailed follow-up observations for these RRATs will be described elsewhere.

3.4.1 Estimating Flux Densities of New Discoveries

The flux densities of the new discoveries were estimated using the radiometer equation (Dewey et al., 1985),

$$S_{\rm est} = \frac{(S/N)_T\,(T_{\rm sys}+T_{\rm sky})}{G(\theta, ZA)\sqrt{n_p t_{\rm obs}\Delta f}}\sqrt{\frac{W}{P-W}}, \tag{3.3}$$

where relevant parameters are the pulse profile width, W, the telescope gain, $G(\theta, ZA)$, the number of polarization channels summed, n_p, the observation length, $t_{\rm obs}$, the observing bandwidth, Δf, the period of the pulsar, P, the system and sky temperatures, $T_{\rm sys}$ and $T_{\rm sky}$, respectively. The time-domain S/N, $(S/N)_T$, was measured from folded profiles using the area under the pulse and the off-pulse RMS.

In some cases, predominantly for long-period pulsars, the baseline of the pulse profile exhibited broad features, likely due to red noise. (See some examples in Figure 3.7.) To more robustly estimate flux densities, we fit Gaussian components to the pulse profile, including the broad off-pulse features. The integrated pulsar signal was determined from the on-pulse components, and the noise level of the profile was determined from the standard deviation of the residuals after subtracting all fitted components from the profile.

The gain was scaled according to the angular offset of the pulsar from the beam centre, θ, assuming an Airy disk beam pattern[1] with FWHM = $3\overset{\prime}{.}35$ (Cordes et al., 2006), as well as the dependence on the zenith angle, ZA. The gain also took into account the ALFA beam with which the pulsar was detected. We scaled the gain of the outer 6 beams to be 79 % of the gain of the central beam (Cordes et al., 2006).

Sky temperatures were scaled from the Haslam et al. (1982) 408-MHz survey to 1400 MHz using a spectral index of −2.76 for the Galactic synchrotron emission (Platania et al., 1998). The sky temperatures also include the 2.73 K cosmic microwave background.

The resulting phase-averaged flux density estimates (i.e. the integrated flux of the pulse divided by the pulse period) of the PALFA pulsars discovered with our pipeline range from 16 to 280 μJy (see Table 3.5), making them among the weakest detected pulsars in the Galactic field, along with other PALFA-discovered pulsars (see Figure 3.8).

3.4.2 Re-detections of Known Pulsars

In total, 83 pulsars for which 1400-MHz phase-averaged flux densities, S_{1400}, are reported in the ATNF catalogue were detected with the Mock spectrometers in 268 different PALFA observations (i.e. some known pulsars were re-detected multiple times).

---

[1] The FWHM of the ALFA beams varies by only ∼5 % over the ZA range of the telescope. Also, FWHM of all 7 beams are largely consistent with each other. Thus, we use a fixed FWHM for all beams and all ZA.

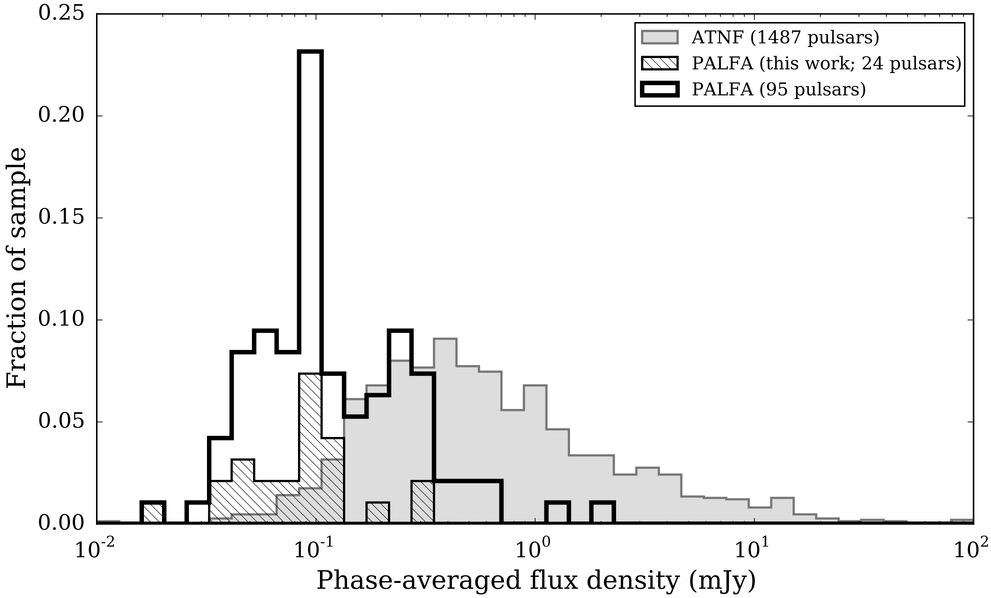

Figure 3.8: Distribution of phase-averaged flux densities of pulsars discovered in the PALFA survey, and the distribution of 1400-MHz phase-averaged flux densities from the ATNF pulsar catalogue of all non-PALFA, non-globular cluster discoveries. The sub-set of PALFA pulsars featured in this work is highlighted. Only PALFA-discovered pulsars with timing positions are included.

To confirm that our observing set-up is as sensitive as expected, we estimate the $(S/N)_T$ at which our pipeline should blindly re-detect known pulsars in our observations and compare with the $(S/N)_T$ measured from the profile of the corresponding candidate. The expected $(S/N)_T$ values were estimated by inverting Eq. 3.3 to solve for the signal-to-noise ratio using S_{1400} from the ATNF catalogue. As in § 3.4.1 the telescope gain is modelled as an Airy disk with FWHM = $3\overset{\prime}{.}35$.

By comparing expected and measured S/Ns against pulsar spin period we find that longer-period pulsars show an increase scatter in $(S/N)_T$ ratio as well as a bias toward larger ratios (see Figure 3.9). This is consistent with the reduced sensitivity to long-period pulsars due to red noise we find from our sensitivity analysis using synthetic pulsar signals (see § 3.5).

In addition to the 83 known pulsars with published S_{1400} detected with the PALFA `PRESTO` pipeline, there are 50 more that do not have values for S_{1400} listed in the ATNF catalogue. The complete list of 128 previously discovered pulsars blindly re-detected by the PALFA `PRESTO` pipeline is in Table 3.6.

Table 3.6: Known Pulsars Re-detected in Mock Spectrometer Data

Name	Period (ms)	DM ($\mathrm{pc\,cm^{-3}}$)	ATNF S_{1400} (mJy)	Measured S/N	Measured S_{1400} (mJy)
B1848+04	284.70	115.5	0.66(8)	36.9	–
B1849+00	2180.20	787.0	2.2(2)	64.1	–

Continued...

Table 3.6 (cont.): Known Pulsars Re-detected in Mock Spectrometer Data with the `PRESTO` Pipeline

Name	Period (ms)	DM (pc cm^{-3})	ATNF S_{1400} (mJy)	Measured S/N	Measured S_{1400} (mJy)
B1853+01	267.44	96.7	0.19(3)	99.7	0.323
B1854+00	356.93	82.4	0.9(1)	267.9	1.048
B1855+02	415.82	506.8	1.6(2)	470.2	2.288
B1859+01	288.22	105.4	0.38(5)	74.7	0.531
B1859+03	655.45	402.1	4.2(4)	1061.3	3.498
B1859+07	644.00	252.8	0.9(1)	339.1	1.830
B1900+01	729.30	245.2	5.5(6)	106.5	–
B1900+05	746.58	177.5	1.2(1)	283.2	1.228
B1900+06	673.50	502.9	1.1(1)	21.5	–
B1901+10	1856.57	135.0	0.58(7)	212.1	0.568
B1903+07	648.04	245.3	1.8(2)	91.2	1.892
B1904+06	267.28	472.8	1.7(2)	33.9	–
B1906+09	830.27	249.8	0.23(3)	17.7	0.127
B1907+02	989.83	171.7	0.63(7)	37.7	–
B1907+10	283.64	150.0	1.9(2)	365.2	2.591
B1907+12	1441.74	258.6	0.28(4)	28.2	0.196
B1910+10	409.35	147.0	0.22(3)	47.1	0.196
B1911+09	1241.96	157.0	0.14(2)	18.9	0.228
B1911+11	601.00	100.0	0.55(7)	85.4	0.301
B1911+13	521.47	145.1	1.2(1)	85.5	1.221
B1913+10	404.55	241.7	1.30(14)	416.8	0.905
B1913+105	628.97	387.2	0.22(3)	46.2	0.507
B1913+167	1616.23	62.6	–	16.1	–
B1914+09	270.25	61.0	0.9(1)	298.6	0.721
B1914+13	281.84	237.0	1.2(1)	616.7	2.043
B1915+13	194.63	94.5	1.9(2)	1453.2	4.477
B1916+14	1181.02	27.2	1.0(1)	14.3	0.362
B1919+14	618.18	91.6	0.68(8)	217.6	1.060
B1921+17	547.21	142.5	–	126.6	0.408
B1924+14	1324.92	211.4	0.48(6)	126.6	0.860
B1924+16	579.82	176.9	1.3(2)	179.1	0.735
B1925+18	482.77	254.0	–	156.0	0.441
B1925+188	298.31	99.0	–	77.3	0.385
B1929+15	314.36	140.0	–	69.4	0.360
B1929+20	268.22	211.2	1.2(4)	457.9	1.099
B1933+16	358.74	158.5	42(6)	73.0	–
B1933+17	654.41	214.6	–	62.8	0.176
B1937+21	1.56	71.0	13(5)	349.1	12.572
B1937+24	645.30	142.9	–	39.4	–
B1944+22	1334.45	140.0	–	55.0	0.173
B2002+31	2111.26	234.8	1.8(1)	68.2	–
J0621+1002	28.85	36.6	1.9(3)	11.4	–
J0625+10	498.40	78.0	–	14.5	0.086
J0631+1036	287.80	125.4	–	175.3	0.941
J1829+0000	199.15	114.0	–	52.4	0.370
J1843−0000	880.33	101.5	2.9(3)	38.5	–
J1844+00	460.50	345.5	8.6(9)	1226.8	4.616
J1849+0127	542.16	207.3	0.46(9)	143.2	0.444
J1849+0409	761.19	56.1	–	29.0	0.312
J1851+0118	906.98	418.0	0.10(2)	27.9	0.118
J1852+0305	1326.15	320.0	0.8(2)	37.7	0.214
J1853+0056	275.58	180.9	0.21(4)	55.3	0.281
J1853+0545	126.40	198.7	1.6(1.7)	5.3	–
J1854+0317	1366.45	404.0	0.12(1)	34.9	0.153
J1855+0307	845.35	402.5	1.0(1)	129.7	0.393
J1855+0422	1678.11	438.0	0.45(9)	104.0	0.245

Continued...

Table 3.6 (cont.): Known Pulsars Re-detected in Mock Spectrometer Data with the `PRESTO` Pipeline

Name	Period (ms)	DM ($\mathrm{pc\,cm^{-3}}$)	ATNF S_{1400} (mJy)	Measured S/N	Measured S_{1400} (mJy)
J1856+0102	620.22	554.0	0.4(1)	66.3	0.195
J1856+0404	420.25	341.3	0.48(1)	40.4	0.276
J1857+0143	139.76	249.0	0.7(2)	37.2	0.486
J1857+0210	630.98	783.0	0.30(6)	40.2	0.236
J1857+0526	349.95	466.4	0.66(8)	145.5	0.645
J1858+0215	745.83	702.0	0.22(4)	42.8	0.280
J1859+00	559.63	420.0	4.8(5)	581.9	24.461
J1859+0601	1044.31	276.0	0.30(4)	15.9	0.126
J1900+0227	374.26	201.1	0.33(7)	111.6	0.414
J1901+00	777.66	345.5	0.35(4)	32.4	–
J1901+0254	1299.69	185.0	0.58(7)	102.1	0.911
J1901+0320	636.58	393.0	0.9(1)	67.3	0.301
J1901+0355	554.76	547.0	0.15(3)	40.9	0.185
J1901+0413	2663.08	352.0	1.1(2)	161.9	0.521
J1901+0435	690.58	1042.6	–	106.9	4.244
J1901+0510	614.76	429.0	0.66(8)	47.6	0.498
J1902+0248	1223.78	272.0	0.17(3)	60.6	0.169
J1903+0601	374.12	388.0	0.26(4)	9.7	–
J1904+0412	71.09	185.9	0.23(5)	68.4	0.271
J1904+0800	263.34	438.8	0.36(5)	11.2	0.285
J1905+0600	441.21	730.1	0.42(5)	85.6	0.401
J1905+0616	989.71	256.1	0.51(6)	43.5	0.236
J1906+0912	775.34	265.0	0.32(6)	34.0	0.149
J1907+0249	351.88	261.0	0.5(1)	124.3	0.478
J1907+0345	240.15	311.7	0.17(3)	21.5	0.133
J1907+0534	1138.40	524.0	0.36(7)	24.6	0.096
J1907+0731	363.68	239.8	0.35(4)	68.8	0.571
J1907+0740	574.70	332.0	0.41(8)	121.4	0.327
J1907+0918	226.11	357.9	0.29(4)	133.4	0.263
J1907+1149	1420.16	202.8	–	30.4	0.156
J1908+0457	846.79	360.0	0.9(1)	274.4	0.958
J1908+0500	291.02	201.4	0.79(9)	48.5	–
J1908+0734	212.35	11.1	0.54(6)	36.0	0.205
J1908+0839	185.40	512.1	0.49(1)	114.4	0.403
J1908+0909	336.55	467.5	0.22(4)	110.7	0.340
J1909+0616	755.99	352.0	0.33(7)	10.3	–
J1909+0912	222.95	421.5	0.35(7)	125.8	0.533
J1910+0534	452.87	484.0	0.41(8)	62.4	0.444
J1910+0714	2712.42	124.1	0.36(5)	137.3	0.287
J1910+0728	325.42	283.7	0.8(1)	189.8	0.887
J1910+1256	4.98	38.1	0.5(1)	139.7	0.497
J1913+0832	134.41	355.2	0.6(1)	187.9	0.999
J1913+0904	163.25	95.3	–	96.7	0.224
J1913+1000	837.15	422.0	0.53(6)	28.8	0.522
J1913+1011	35.91	178.8	0.5(1)	111.0	0.434
J1913+1145	306.07	637.0	0.43(9)	126.5	0.403
J1913+1330	923.39	175.6	–	213.6	–
J1914+0631	693.81	58.0	0.3(1)	36.9	0.140
J1915+0738	1542.70	39.0	0.34(4)	109.1	0.254
J1915+0752	2058.31	105.3	0.21(3)	18.2	0.238
J1915+0838	342.78	358.0	0.29(4)	12.3	–
J1915+1410	297.49	273.7	–	11.6	0.134
J1916+0748	541.75	304.0	2.8(3)	66.8	–
J1916+0844	440.00	339.4	0.44(5)	89.9	0.526
J1916+0852	2182.75	295.0	0.13(2)	36.6	0.148
J1920+1040	2215.80	304.0	0.57(7)	24.5	0.092

Continued...

Table 3.6 (cont.): Known Pulsars Re-detected in Mock Spectrometer Data with the `PRESTO` Pipeline

Name	Period (ms)	DM ($\mathrm{pc\,cm^{-3}}$)	ATNF S_{1400} (mJy)	Measured S/N	Measured S_{1400} (mJy)
J1920+1110	509.89	182.0	0.39(8)	22.9	0.288
J1921+1544	143.58	385.0	–	65.5	0.211
J1922+1733	236.17	238.0	–	435.6	1.157
J1924+1639	158.04	208.0	–	73.6	0.207
J1926+2016	299.07	247.0	–	12.0	0.122
J1928+1923	817.33	476.0	–	221.7	0.639
J1929+1955	257.83	281.0	–	25.1	0.421
J1930+17	1609.69	201.0	–	30.9	–
J1931+1952	501.12	441.0	–	71.9	0.126
J1935+2025	80.12	182.0	–	79.6	0.527
J1936+21	642.93	264.0	–	13.6	–
J1938+2213	166.12	91.0	–	20.4	–
J1946+2611	435.06	165.0	–	232.0	0.697
J1957+2831	307.68	139.0	1.0(2)	34.4	–

Note. — Values for period, DM, and "ATNF S_{1400}" are taken from the ATNF Catalogue (Manchester et al., 2005)

3.4.3 Known Pulsars Missed

In addition to the 268 detections of 128 separate known pulsars mentioned in § 3.4.2, there were seven instances in which a known pulsar was not detected by the search pipeline, despite being detected when subsequently folding the search data with the most recently published ephemeris. In all cases the data were badly affected by RFI; there are strong signals within one Fourier bin of the pulsar period. Furthermore, these are long-period pulsars, which are more difficult to detect than expected due to red noise in the data. It is therefore not entirely surprising that these observations did not result in detections. A thorough analysis of the effects of RFI and red noise on the sensitivity to long period pulsars is therefore crucial, and forms the discussion of the following section.

3.5 Assessing the Survey Sensitivity

The sensitivity of pulsar observations is typically estimated using the radiometer equation (Eq. 3.3). In principle, the effects of DM, period, and pulse width on sensitivity are adequately described by the radiometer equation. The expression derived by Cordes & Chernoff (1997, see their Appendix A), includes a more complete description of pulse shape and the effect of DM, which causes distortions of the pulse profile. However, neither of these equations includes the effect of RFI nor red noise. In this section, we describe a prescription for accurately modelling the sensitivity of pulsar search observations including the effect of RFI, as well as its dependence on period, DM, and pulse width.

To estimate the survey sensitivity we injected synthetic pulsar signals into actual survey data, and attempted to recover the period and DM of the input signal using our pipeline. By using synthetic signals we can also better determine the selection effects imposed by our pipeline.

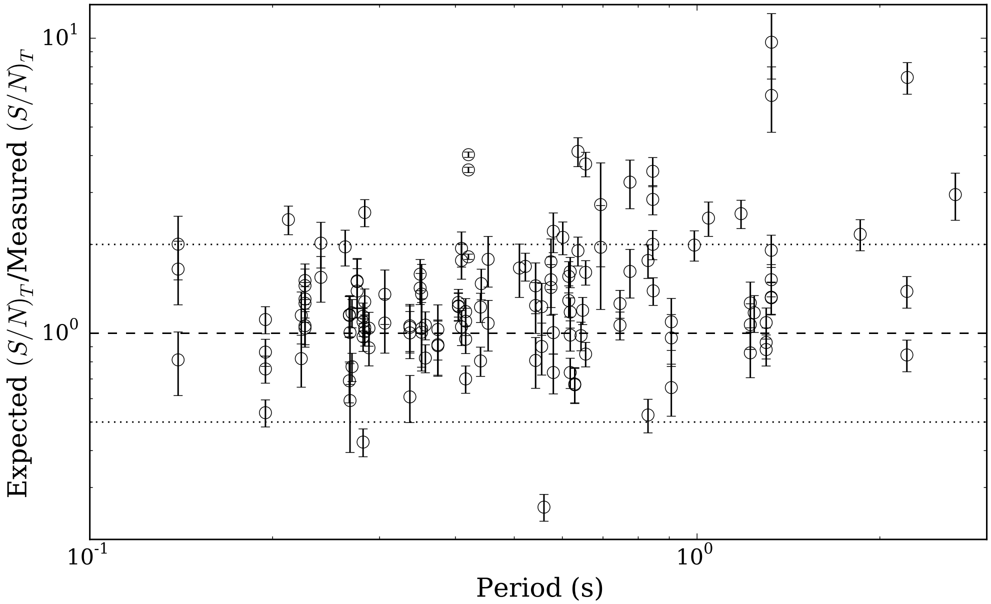

Figure 3.9: Ratio of expected and measured $(S/N)_T$ as a function of pulsar period. Expected $(S/N)_T$ values are calculated using the radiometer equation and measured flux densities at 1400 MHz from the ATNF catalogue. Measured $(S/N)_T$ values are computed from detections of known pulsars in PALFA observations. The increased scatter and bias toward higher S/N ratios of longer-period pulsars are consistent with reduced sensitivity to these pulses due to red noise (see § 3.5.4 and Figure 3.11). Known pulsars without reported flux densities and uncertainties are excluded, as are pulsars that have reported flux densities consistent with 0 mJy. Also excluded from the plot are 15 known pulsars with published flux densities that were detected in observations pointed more than $3'$ from the position of the pulsar. This is because the actual beam pattern differs considerably from the theoretical Airy disk beam pattern beyond $\sim 3'$, making it difficult to reliably estimate the expected $(S/N)_T$. The dashed line indicates equality of the expected and measured $(S/N)_T$ values, and the dotted lines are at a factor of two above and below equality.

3.5.1 Constructing a Synthetic Pulsar Signal

For this work, a simple synthetic pulsar signal was constructed for a given combination of period, DM, phase-averaged flux density, and profile shape. Once the relevant parameters were chosen (see § 3.5.3 and Table 3.7), a two-dimensional pulse profile (intensity vs. spin phase and observing frequency) was generated.

The pulse profile of each frequency channel was smeared by convolving with a boxcar whose phase width corresponded to the dispersion delay within the channel, as well

Table 3.7: Synthetic pulsar signal parameters

Parameter	Possible Values					
	0.766	1.102	2.218	5.218	10.870	18.505
Period (ms)	26.965	61.631	126.175	286.555	533.320	850.158
	1657.496	2643.410	3927.013	5580.899	10964.532	
DM ($\mathrm{pc\,cm^{-3}}$)	10	40	150	325	400	600
	1000					
FWHM (% Phase)	1.5	2.6	5.9	11.9	24.3	

as scattered by convolving with a one-sided exponential function with a characteristic phase width corresponding to the pulse broadening time scale. We determined the scattering time scale using version of Eq. 3.1 from Cordes (2002). Care was taken to conserve the area under the profile during the convolutions. The scaling factor applied to the synthetic signals was determined by flux-calibrating the PALFA observing system (see §3.5.2).

3.5.2 Calibration

On 2013 December 21, we observed the radio galaxy 3C 138 in order to calibrate the central beam of ALFA. Three observations using the standard survey set-up described in § 3.2 were conducted, but with 5 minute integrations, and with the calibration diode being pulsed on and off at 40 Hz. The on-source scan of 3C 138 was preceded by an off-source scan 0.5° to the north of 3C 138 and followed by a similar off-source scan 0.5° to the south.

The calibration observation data were converted to 4-bit samples, and the Mock spectrometer sub-bands were combined (see § 3.3.2). The data were folded at the modulation frequency of the calibrator diode using `fold_psrfits` of `psrfits_utils`. Next, the on-cal and off-cal levels in the on-source and off-source observations were used to relate the flux density of the calibration diode with the catalogued flux density of 3C 138 (for details, see e.g. Lorimer & Kramer, 2004). The result is the flux density of the calibration diode as a function of observing frequency. In practice, this was done using `fluxcal` of `psrchive`.[1]

The per-channel scaling factors between flux density and the observation data units were determined by applying the calibration solution along with the calibration diode signal. This procedure determines the absolute level of the injected signal corresponding to a target phase-averaged flux density, as well as the shape of the bandpass, which was retained thanks to the `PSRFITS` scales and offsets (see § 3.2).

3.5.3 Injection Trials

Artificial pulsar signals were injected into the data by summing the two-dimensional, smeared, scattered, and scaled synthetic pulse profile with the data at regular intervals corresponding to the period of the synthetic pulsar. The scaling was determined using the calibration procedure described in § 3.5.2. The resulting data file, including the injected signal, was written out with 32-bit floating-point samples in `SIGPROC` "filterbank" format[2] for simplicity, without re-quantizing the data. Neither using 32-bit floating-point samples nor filterbank format data should significantly influence the results.

Many synthetic signals with a broad range of parameters were required to build a comprehensive picture of the survey sensitivity (see Table 3.7). In total, 17 periods were selected between 0.77 ms and 11 s along with six DMs ranging from 10 to 1000 $\mathrm{pc\,cm^{-3}}$. In all cases, the profile of the synthetic signal was chosen to have a single centred von Mises component with a FWHM selected from 5 possible values between ∼1.5 and 24 % of the period. The example profile in Figure 3.10 shows the case where FWHM = 2.6 %. The synthetic signals were injected into 12 different observations to determine the survey sensitivity in a variety of RFI conditions. All

---

[1] http://psrchive.sourceforge.net/

[2] http://sigproc.sourceforge.net/

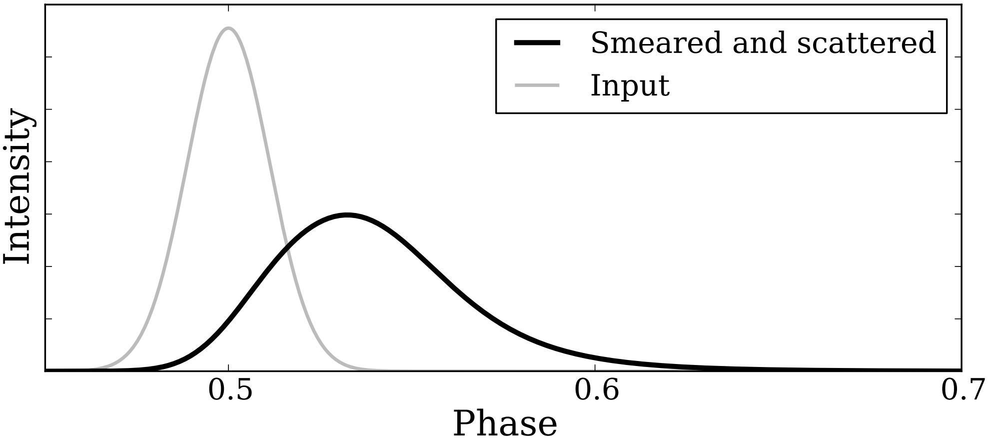

Figure 3.10: The profile of a synthetic $P = 5\,\mathrm{ms}$ pulsar consisting of a single von Mises component with FWHM $= 2.6\,\%$ (grey), and the same profile broadened according to DM $= 250\,\mathrm{pc\,cm^{-3}}$. The broadening is caused by dispersive smearing within each channel and scattering according to Eq. 3.1. Note that the plot is zoomed into the region: $0.45 < \phi < 0.7$.

12 observations used in this analysis are from late 2013 and from the central beam of ALFA. Although the gains of the outer beams are lower than that of the central beam, the response of the observing system and pulsar search pipeline to RFI and red noise derived for the central beam should also apply to the outer beams.

The total number of combinations of synthetic signals and observations is > 7000. Multiple trials, each with a different amplitude, were constructed, injected, and searched to determine the sensitivity limit at each point in (period, DM, pulse FWHM) phase-space. To reduce the computational burden, not all possible combinations of parameters were used. In particular, only the profile with FWHM $\sim 2.6\,\%$ was injected into all 12 observations. The remaining four profiles shapes were only injected into a single observation. This still permits the determination of the dependence of the minimum detectable flux density, S_{min}, on pulse width.

In addition to injecting synthetic pulsars into the 12 survey observations, we also conducted a series of trials where we injected the FWHM $\sim 2.6\,\%$ signal into five independently simulated observations consisting of pure white noise.

3.5.4 Realistic Survey Sensitivity

It is well known (Dewey et al., 1985) that the S_{min} of a pulsar depends on the intrinsic width of its profile, as well as the DM, because dispersive smearing and scattering broaden the profile. It is also reasonable to expect a reduction of sensitivity due to RFI and red noise, even with the red noise suppression algorithms employed (see § 3.3.4). By recovering injected signals using the pipeline described in § 3.3, we have determined the true sensitivity of the PALFA survey, and its dependence on spin period and DM (see Figure 3.11). We found the commonly used version of the radiometer equation (Eq. 3.3; Dewey et al., 1985) overestimates the survey sensitivity to long-period pulsars. For example, for $P = 0.1 - 2.0\,\mathrm{s}$ pulsars with DM $> 150\,\mathrm{pc\,cm^{-3}}$ (the majority of the pulsars we expect to find with PALFA), the degradation in sensitivity compared with the ideal case is a factor of $\sim 1.1 - 2$.

We have also confirmed the claim by Cordes & Chernoff (1997) that the Dewey et al. (1985) radiometer equation underestimates the sensitivity to high-DM MSPs, by not correctly modelling the distortion of the profile due to smearing and scattering. The more accurate variant of the radiometer equation from Cordes & Chernoff (1997) better matches our measured sensitivity curves in the MSP regime, thanks to its inclusion of the profile shape and distortions. However, the degraded sensitivity we find at long periods is still not properly modelled with these adjustments.

Red noise present in pulsar search data due to RFI, receiver gain fluctuations, and opacity variations of the atmosphere makes it difficult to detect long-period radio pulsars. Our analysis has shown that for the PALFA survey, at low DMs, the reduction in sensitivity already affects pulsars with periods of ~100 ms. Fortunately, the effect is slightly less significant for pulsars with higher DMs. This is evident in Figure 3.11.

We have parameterized the sensitivity curves by fitting $\log S_{\rm min}$ vs. DM with a cubic function and modelling how these curves depend on period. To estimate $S_{\rm min}$ at an arbitrary profile width, we first estimate $S_{\rm min}$ at each of the five trial widths, then fit a quadratic function in $\log S_{\rm min}$ vs. width, and use the parameters of the fit to calculate $S_{\rm min}$ at the desired width. This empirical scheme provides reliable estimates of $S_{\rm min}$ within the intervals used for trial values of period, DM, and width. Sensitivity maps for each of the five profile widths used are shown in Figure 3.12.

3.6 Population Synthesis Analysis

We have used the sensitivity curves determined above (see § 3.5.4) to re-evaluate the expected yield of the PALFA survey by performing a population synthesis analysis with `PsrPopPy`[1] (Bates et al., 2014).

Galactic populations of non-recycled pulsars were simulated using the radial distribution from Lorimer et al. (2006b) and a Gaussian distribution of heights above/below the plane with a scale height of 330 pc. The pulsar periods were described by a log-normal distribution with $\langle \log P \rangle = 2.7$ and $\sigma_{\log P} = -0.34$ (Lorimer et al., 2006b). The pulse-width-to-period relationship was also taken from Lorimer et al. (2006b). We used a log-normal luminosity distribution described by the best-fit parameters found by Faucher-Giguère & Kaspi (2006), $\langle \log L \rangle = -1.1$ and $\sigma_{\log L} = 0.9$.

We created 5000 simulated pulsar populations, each containing enough pulsars such that a simulated version of the Parkes multi-beam surveys detected 1038 pulsars, the number of non-recycled pulsars detected by the actual surveys. We then compared the pulsars in each of these populations against a list of PALFA observations,[2] and estimated their significance using the radiometer equation. Pulsars with $(S/N)_{\rm expect} > 11.3$ were considered "detectable."[3] Next, we compared the flux-density for each "detectable" pulsar against the parameterized PALFA sensitivity curves to determine if the pulsar also has a sufficiently large flux density to lie above the measured sensitivity curves. For each pulsar, the measured sensitivity curves are

---

[1] https://github.com/samb8s/PsrPopPy

[2] For each observation we used the sky position, integration time, zenith angle and beam number. We used the model of gain and system temperature dependence on zenith angle provided by the observatory. We assumed the six outer beams have a gain of ~80 % of the central beam, consistent with the gains reported by Cordes et al. (2006).

[3] The value of $(S/N)_{\rm expect}$ was chosen such that the minimum detectable flux density coincided with the measured sensitivity curves for a duty cycle of 2.6 %.

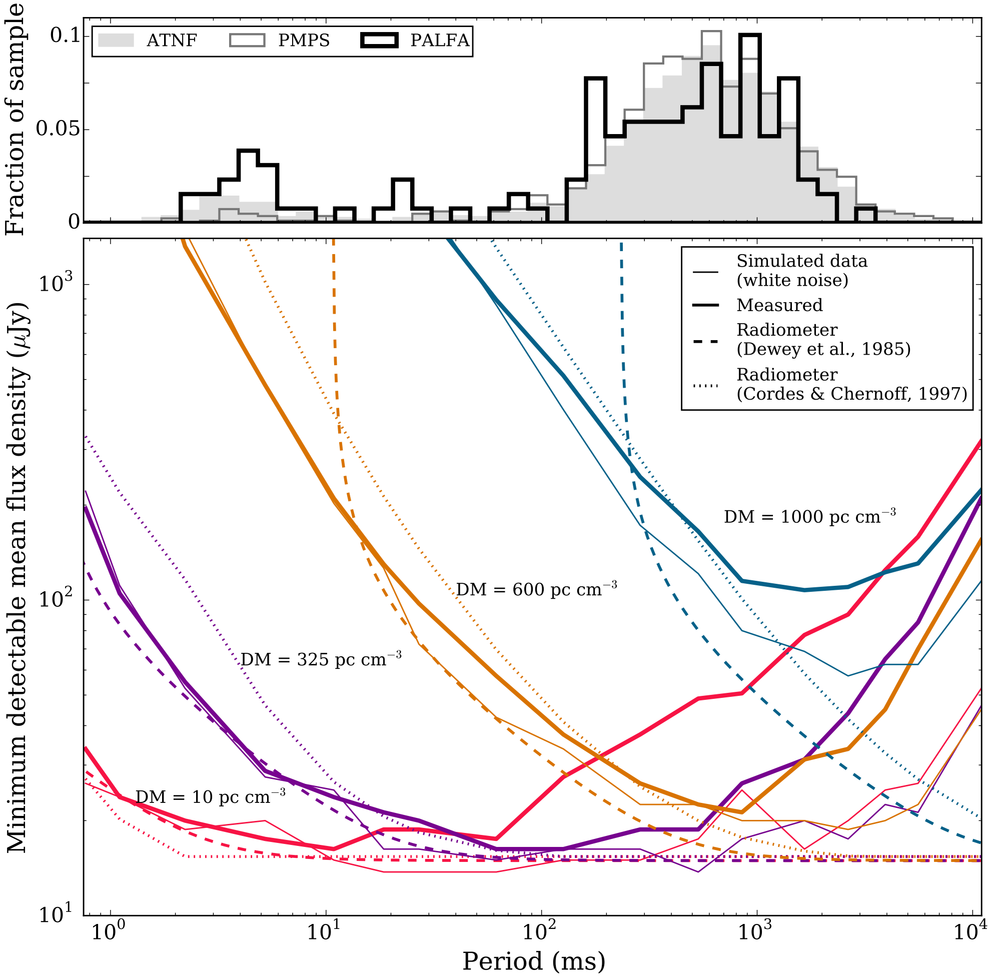

Figure 3.11: *Top* – Period distribution of all Galactic radio pulsars, excluding RRATs, listed in the ATNF catalogue. Pulsars discovered in the Parkes Multibeam Pulsar Survey of the Galactic Plane (PMPS) are highlighted, as are as those found in PALFA.
Bottom – Minimum detectable phase-averaged flux density curves for the PALFA survey as measured using synthetic pulsar signals with FWHM=2.6 % (thick solid lines). Only four of the seven trial DM values are shown here for clarity; these are DM = 10 pc cm^{-3} (dark blue), 325 pc cm^{-3} (green), 600 pc cm^{-3} (purple), and 1000 pc cm^{-3} (light blue). The omitted trials (DM = 40, 150, and 400 pc cm^{-3}) exhibit similar behaviour. The majority of the reduction in sensitivity at long periods is due to RFI and red noise in the data. This is especially clear when comparing against the pipeline sensitivity we determined by injecting synthetic pulsar signals into simulated purely Gaussian distributed noise (thin lines). Furthermore, we see clear discrepancies when comparing the measured curves with the analogous sensitivity limits derived with the commonly used radiometer equation (Dewey et al., 1985) (dashed lines). Sensitivity to long-period pulsars is overestimated, and sensitivity to MSPs is underestimated. However, the formulation of the radiometer equation by Cordes & Chernoff (1997, dotted lines) is more complete – albeit less frequently used – and better models the sensitivity in the short-period regime. See § 3.5.4 for details.

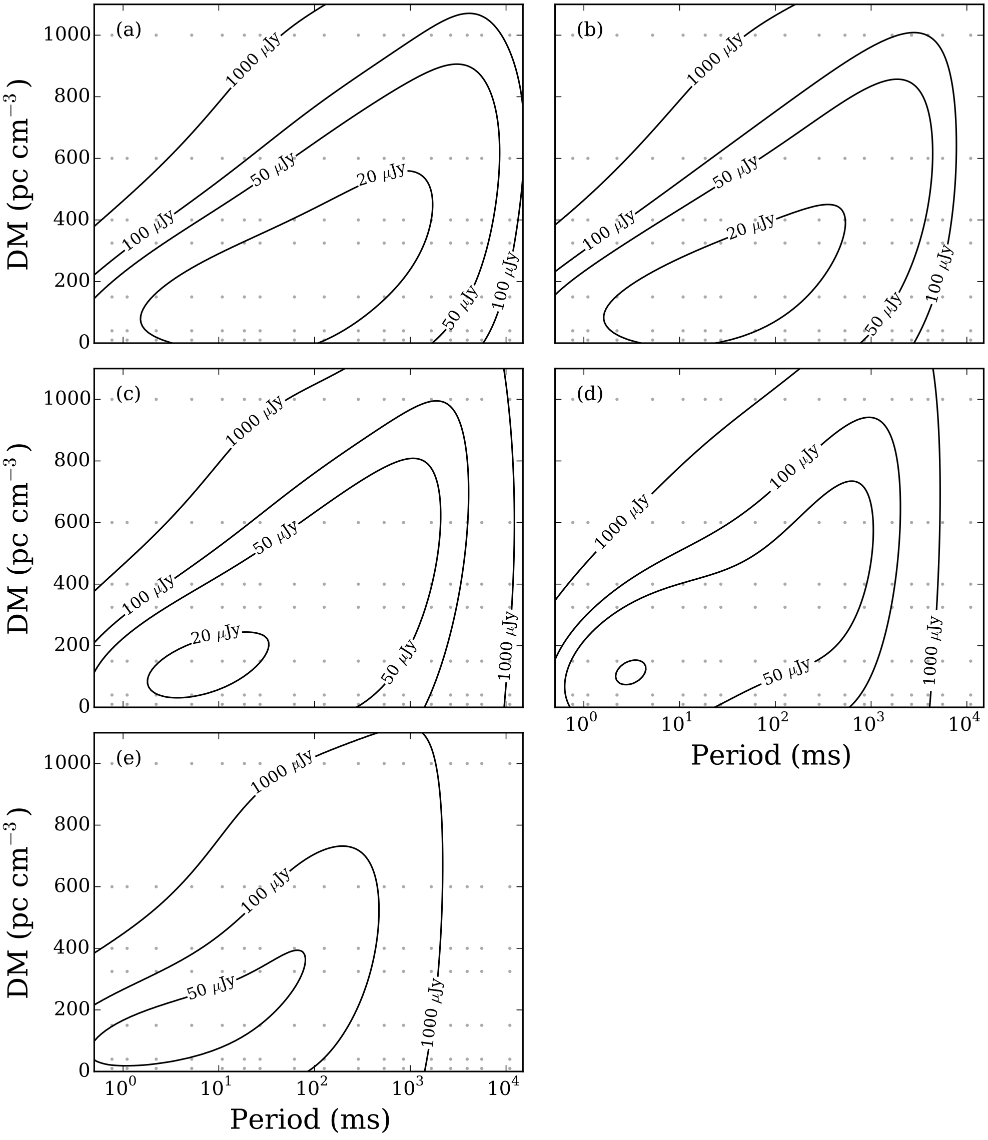

Figure 3.12: PALFA survey sensitivity as a function of DM and spin period. The maps are determined using synthetic pulsar signals injected into observations and recovered using the pipeline. Contours correspond to minimum detectable phase-averaged flux densities of 20, 50, 100, 1000 μJy. The five panels (a)–(e) correspond to profile FWHMs of 1.5 %, 2.6 %, 5.9 %, 11.9 %, and 24.3 %, respectively. In all cases, the profile consists of a single centred von Mises component (see Figure 3.10 for an example). The period, DM combinations used in the sensitivity analysis are shown with the small dots.

shifted according to the zenith angle of the observation, the gain of the beam used, the sky temperature and the angular offset between the pulsar position and the beam centre.

We found $33 \pm 3\,\%$ of the simulated pulsars having fluxes above the theoretical sensitivity threshold derived from the radiometer equation (Eq. 3.3) are not sufficiently bright to also be "detected" by our measured sensitivity limits for the PALFA survey (e.g. Figure 3.12) due to the residual effect of red noise and RFI following the extensive mitigation procedures described in § 3.3.4. The median period of the pulsars missed is $P_{\rm miss} \simeq 585\,{\rm ms}$, which is considerably longer than the median period of the potentially detectable pulsars brighter than the radiometer-equation-based threshold, $P_{\rm det.} \simeq 440\,{\rm ms}$ (see Figure 3.13).

Our 5000 realizations of simulated Galactic pulsar populations, adjusted for the reduced sensitivity to long-period pulsars, suggest 224 ± 16 un-recycled pulsars should be detected in PALFA Mock spectrometer observations, given the current processed pointing list. As of 2015 January, 241 un-recycled pulsars have been discovered (or re-detected) in PALFA observations with the Mock spectrometers.

The number of un-recycled pulsar detections predicted for the PALFA survey by Swiggum et al. (2014) is an overestimate for two reasons. First, their analysis used a threshold $S/N = 9$. Given the observing parameters assumed, a more appropriate threshold of $S/N = 11.3$ should have been used to correspond to the minimum detectable flux density we find ($S_{\rm min} = 0.015\,{\rm mJy}$). Second, the analysis by Swiggum et al. (2014) did not include the effect of red noise, which we have shown reduces the number of pulsars expected to be found in the PALFA survey by 33 %.

3.7 Discussion

The detailed sensitivity analysis of § 3.5.4 confirms that, on average, the PALFA survey is as sensitive to MSPs and mildly recycled pulsars as expected from the radiometer equation. However, the survey is less sensitive to long-period pulsars than predicted. The degradation in sensitivity is between 10 % and a factor of 2 for the majority of pulsars we expect to find in the PALFA survey (spin periods between 0.1 s and 2 s and $\mathrm{DM} > 150\,{\rm pc\,cm^{-3}}$), and up to a factor of $\sim$10 in the worst case ($\mathrm{DM} < 100\,{\rm pc\,cm^{-3}}$ and $P > 2\,{\rm s}$; this fortunately corresponds to a parameter space that contains far fewer expected pulsars). The reduction of sensitivity is mostly caused by red noise present in the observations (see Figure 3.11).

The empirical sensitivity curves we determined apply specifically to the PALFA survey, its observing set-up, and the search algorithms used. Because the effects of red noise on radio pulsar survey sensitivity have the potential to be significant, as in the case of PALFA, we strongly suggest measuring the impact of red noise on other surveys by performing similar analyses to what we described in § 3.5. Also, future population analyses should include these measured effects of red noise rather than assuming the theoretical radiometer equation (e.g. Faucher-Giguère & Kaspi, 2006; Lorimer et al., 2006b) when deriving spatial, spin, and luminosity distributions for the underlying Galactic population of pulsars.

What are the potential ramifications of reduced sensitivity to long-period pulsars being unaccounted for in population synthesis analyses? First, the existence of radio-loud pulsars beyond the "death line" is important to our understanding of the radio emission mechanism in pulsars. For example, the existence of the 8.5-s

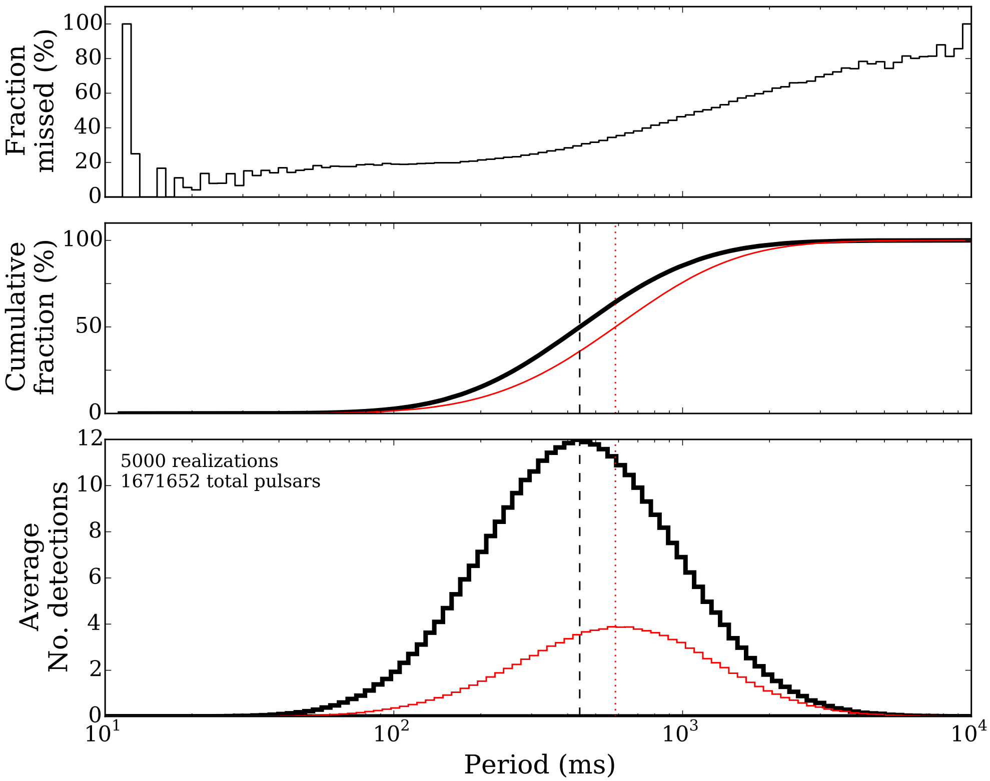

Figure 3.13: *Top* – Fraction of potentially detectable pulsars missed by PALFA due to red noise as a function of spin period, assuming the underlying pulsar population is accurately modelled by our input distributions (i.e. the distributions in Lorimer et al. (2006b), see § 3.6).
Middle – Cumulative fraction of simulated pulsars (thick black line), and pulsars missed (thin red line) as a function of pulse period.
Bottom – Period distribution of potentially detectable simulated population of un-recycled pulsars averaged over 5000 realizations (thick black line) compared with the period distribution of pulsars expected to be missed due to red noise (thin red line). The median spin period of the potential detectable pulsars ($P \simeq 440\,\mathrm{ms}$) is shown by the dashed black line, and the median spin period ($P \simeq 585\,\mathrm{ms}$) of the missed pulsars is shown by the dotted red line.

PSR J2144−3933 contradicted several existing emission theories (Young et al., 1999; Zhang et al., 2000). The existence of a larger population of slowly rotating pulsars, particularly the discovery of pulsars so slow that existing theories cannot explain their radio emission, would further constrain models.

It is also possible there is a larger population of highly magnetized rotation-powered pulsars and quiescent radio-loud magnetars that have been missed by the lower than predicted sensitivity of pulsar surveys. Radio emission from three of the four known radio-loud magnetars was detected following high-energy radiative events (Camilo et al., 2006, 2007a; Eatough et al., 2013b; Shannon & Johnston, 2013). However, the other radio-loud magnetar PSR J1622−4950 was discovered from its radio emission (Levin et al., 2010; Olausen & Kaspi, 2014). There is no evidence that the turn-on of PSR J1622−4950 at radio wavelengths was preceded by a high-energy event. The possibility that radio emission from magnetars is not always accompanied by X-ray or γ-ray emission means it is crucial to understand the biases against finding such long-period pulsars. Characterizing, and hopefully uncovering a hidden population of radio-loud magnetars, as well as highly magnetized-rotation powered pulsars, will help clarify the relationship between these two classes of pulsars, as well as the influence of strong magnetic fields on emission properties (e.g flux and spectral index variability).

It may be possible to address the reduced sensitivity to long-period pulsars by using algorithms that perform better in the presence of red noise, as well as algorithms that remove red noise without suppressing the pulsar signal.

Long-period pulsars may be found via their harmonics even if red noise obscures the signal in the Fourier domain at the fundamental frequency of the pulsar, or if the power of the fundamental is suppressed by the red noise removal algorithm. As a result, the total summed power of the pulsar signal will not include the power of the fundamental and possibly even low harmonic frequencies, which can contain large amounts of power, especially in the case of pulsars with wide profiles. Furthermore, by not being based at the fundamental frequency of the pulsar, the total summed power will not include the power of slower, more significant harmonics in favour of weaker harmonics at higher frequencies. Despite the reduction in sensitivity several pulsars have been found in the PALFA survey thanks to their higher harmonic content.

One suggested method of improving sensitivity to long-period pulsars is by using the Fast-folding algorithm (FFA; see e.g. Lorimer & Kramer, 2004; Kondratiev et al., 2009, and references therein). The periodograms produced by the FFA, a time-domain algorithm, are generated from computing a significance metric from pulse profiles. Thus, the broad profile features caused by red noise pose a problem for FFA-based searches. In short, the FFA is not immune to the degradation of sensitivity to long-period pulsars described above. However it does have the advantage of coherently summing *all* harmonics of a given period and greater period resolution than the DFT. These two factors should make the FFA slightly more sensitive to long-period pulsars, especially those with narrow profiles, than the Fourier Transform techniques described in § 3.3.3, which is limited in the number of harmonics that can be summed (typically incoherently; Kondratiev et al., 2009). The FFA has only been used sparingly in large-scale pulsar searches (e.g. Kondratiev et al., 2009). A more systematic investigation and application of the FFA is warranted.

Another algorithm that might have better performance in the presence of red noise is the single-pulse search technique described in § 3.3.3. Single-pulse search algorithms are known to be more sensitive than standard FFT techniques to long-period pulsars in short observations (Deneva et al., 2009; Karako-Argaman et al., 2015). This is because of the natural variability of pulsar pulses and small number of pulses. Pulse-to-pulse variability was not included in the synthetic pulsar signals used in our sensitivity analysis and no single pulse searching was performed. It is likely that the sensitivity curves determined in this work are partially compensated by the single-pulse search techniques already in place, especially considering the recent suggestion that pulsars with $P > 200\,\mathrm{ms}$ have a greater likelihood of being detected in single-pulse searches than faster pulsars (Karako-Argaman et al., 2015), at least in short integrations like the ones employed in PALFA observations. However, the extent of this compensation depends on the pulse-energy distributions of pulsars and the relative significances of their detections in periodicity and single-pulse searches.

3.8 Conclusions

We described the `PRESTO`-based PALFA pipeline, the primary data analysis pipeline used to search PALFA observations made with the Mock spectrometers. This pipeline has led to the discovery of 40 pulsars in periodicity searches and 5 RRATs, the re-detection of 60 pulsars previously discovered in the survey (using other pipelines), and the detection of 128 previously known pulsars. The `PRESTO`-based pipeline described here consists of several complementary search algorithms and RFI-mitigation strategies. The performance of the pipeline was determined by injecting synthetic pulses into actual survey observations and recovering the signals.

We have found that the PALFA survey is as sensitive to fast-spinning pulsars as expected by the theoretical radiometer equation. However, in the case of long-period pulsars, we have found that there is a reduction in the sensitivity due to RFI and red noise in the observations. The actual detection threshold for pulsars with $P > 4\,\mathrm{s}$ at $\mathrm{DM} < 150\,\mathrm{pc\,cm^{-3}}$ is up to $\sim$10 times higher than predicted by the theoretical radiometer equation. We have performed a population synthesis analysis using this empirical model of the survey sensitivity. Our analysis indicates that $33 \pm 3\,\%$ of pulsars, with predominantly long periods, are missed by PALFA, compared to expectations based on theoretical sensitivity curves derived using the radiometer equation.

The magnitude of the effect of red noise on the PALFA survey's sensitivity to long-period pulsars is surprising and should be taken into account in future population synthesis analyses. Furthermore, the effect of red noise on other radio pulsar surveys should be quantified in a similar manner and be included in population synthesis analyses to ensure the distributions determined for the underlying pulsar population are robust. The presence of more long-period pulsars could have implications on the location of the pulsar death line, the structure of pulsar magnetospheres and radio emission mechanism, as well as the relationship between canonical pulsars, highly magnetized rotation-powered pulsars, radio-loud magnetars, and RRATs.

PART II

TIMING PULSARS

4

PULSAR TIMING

The rotation of pulsars is so extremely stable that it is possible to develop models capable of predicting the stars' *every* revolution. Such a model is commonly referred to as a timing solution or as an ephemeris.[1] A timing solution is said to be *phase-connected* or *phase-coherent* if it can be used to predict the times-of-arrival (TOAs) of pulses accurate to within a fraction of a phase rotation. At first, a pulsar's discovery parameters (e.g. spin period, DM, position) must be used as a rough timing solution. This model is then iteratively refined by observing the pulsar, measuring TOAs, computing the difference between the TOAs and the predictions made by the timing model, and adjusting the model parameters to minimize these differences until the timing solution is phase connected. This process is called *pulsar timing.* Even after a phase-connected timing solution is determined, this timing process is sometimes continued in order to further refine the model.

The parameters of the timing model are attributed to various physical processes that influence the TOAs. These processes may be intrinsic to the pulsar system, for example, its spin and spin-down rates or irregularities in its rotation. Alternatively, TOAs may be affected by the pulsar's motion, either through the Galaxy, or, if it is in a binary system, due to its motion around the companion star. Factors extrinsic to the pulsar also impact TOAs. Examples include dispersive delays[2] due to the interstellar medium (ISM) and the motion of the Earth around the Solar System barycentre. The Earth's orbital motion introduces advances and delays in TOAs as a function of the day of year (see § 4.3 for details). Furthermore, the passage of gravitational waves (GWs) through the Solar System also affects TOAs. Recall from § 1.6 that detecting the signature of GWs on pulsars' TOAs is the main goal of Pulsar Timing Array (PTA) projects.

The high precision to which TOAs can be measured and the accuracy to which they can be modelled enables detailed studies of the physical processes that affect the TOAs. Many of the applications of pulsar research discussed in § 1.6 leverage pulsar timing analyses.

This chapter describes the theoretical concepts and practical aspects of pulsar timing. Important factors to consider when setting up and scheduling timing observations are discussed in § 4.1. Then, the steps required to reduce the observations and compute TOAs are outlined in § 4.2. Finally, the process of determining and refining timing solutions is covered in § 4.3.

4.1 Timing Observations

When planning timing observations, two important factors must be considered: the observing set-up, and the observing cadence. The choices made, along with the properties of the pulsar observed, dictate how sensitive the timing campaign will be to

---

[1] Any model of the motion of an astronomical object is also commonly referred to as an *ephemeris.*

[2] This is the same effect as what was detailed in § 2.3.

various parameters.

Observing Set-Up

The durations of timing observations are chosen based on the sensitivity of the telescope and observing-system performance (i.e. gain, bandwidth, etc.), the flux density of the pulsar, the number of pulses that must be summed to provide a stable profile, the desired S/N of the detection, and the available telescope time.

Most timing observations are performed between ∼350 and 3100 MHz (e.g. Manchester et al., 2013; Arzoumanian et al., 2015; Desvignes et al., 2016). Choosing which frequency band to use depends on the radio spectrum of the pulsar, the performance of the observing systems available, the RFI environment, and magnitude of the ISM effects, which are weaker at higher frequencies. Broad frequency coverage must be used to better measure the ISM, which is necessary either if it is of interest or if strong ISM variations are a significant source of noise that must be mitigated. Many of the large PTA projects use a core set of observations at ∼1400 MHz complemented by observations at other frequencies (Manchester et al., 2013; Arzoumanian et al., 2015; Desvignes et al., 2016, also, see Chapter 6 for a discussion).

Observations

Some observing systems (e.g. the PSRIX backend at Effelsberg 100-m radio telescope in Germany, see Chapter 6) support multiple modes that can be used for timing. Conducting timing observations in *search mode* (the same mode as is used in pulsar surveys), is useful for timing newly discovered pulsars, especially binary pulsars that do not yet have phase-coherent timing solutions. Alternatively, when *baseband mode* is used, the raw voltage values are recorded. This mode requires large amounts of disk storage, but is by far the most flexible. Software like `dspsr`[1] can be used to convert the saved voltage data into many other refined data formats (van Straten & Bailes, 2011). Most commonly, however, timing observations are conducted in on-line *coherently dedispersed folding mode*.

Coherent dedispersion completely removes the frequency-dependent delay *within* each frequency channel.[2] This capitalizes on the fact that the effect of the dispersion delay caused by the ISM can be represented by a linear filter applied to the pulsar signal. Thus, by applying the inverse filter to the raw voltage signal the data can be dedispersed (Hankins, 1971). To coherently dedisperse an observation in real-time, the DM of the pulsar must already be known, but this is not a problem when monitoring known pulsars. Furthermore, because the dispersive delay is completely removed, recording data files with high frequency resolution is no longer required as it is in the case of search-mode data. However, some frequency resolution is retained; this is done to reduce the fraction of the observing band that must be discarded when the observation is affected by narrow-band interference. Maintaining frequency resolution also allows the DM to be refined, to correct for DM variations. Finally, by completely removing the intra-channel dispersive smearing coherent dedispersion makes it possible to resolve fine structures in the pulse profile that would otherwise be obscured. Unfortunately, dedispersion cannot correct for interstellar scattering,

---

[1] http://dspsr.sourceforge.net

[2] This should be contrasted with the incoherent dedispersion technique described in § 2.3, which only removes the delay *between* frequency channels.

which still acts to broaden the pulse profiles, and thus limits the precision of TOA measurements.

Only pulsars for which a timing solution is available can be reliably folded in real time. By using a phase-coherent ephemeris, it is possible to phase-align and average together all the pulses in a coherently dedispersed observation. This is exactly the same as what is done for candidates found in pulsar surveys (recall § 2.4), except here folding is done *while* recording the data. As in the case of folding survey data, the end result is a data cube consisting of pulse phase, observation time, and radio frequency along its axes. In practice, individual pulses are not only phase-aligned, but also summed together to generate sub-integrations. Typically, these sub-integrations are $\sim 10 - 120\,\mathrm{s}$ in duration. Retaining some time resolution allows the pulse summation to be refined if an improved timing model is determined in the future. Also, using shorter sub-integrations limits the contamination of the data by RFI, allowing smaller portions of the observation to be discarded. In general, saving a folded data cube significantly reduces the volume of data recorded compared to search-mode and baseband-mode observations,[1] making it easier to archive and process the data sets from large, long-term monitoring campaigns. The modest disk space requirements of folded data also make it reasonable to record many phase bins (using between 1024 and 4096 is common; see e.g. Demorest et al., 2013, and Chapter 6), which enables finer structures in the pulse profile to be resolved. This improves the precision of the determination of pulse TOAs, but comes at the expense of S/N, so a balance is often required.

Observing Cadence

Pulsars are observed repeatedly over long time spans to maintain and improve the phase-connected timing solutions describing their rotation. The longest possible interval between subsequent observations is determined by the precision of the timing parameters such that the phase-error incurred between observations is a significant fraction of a rotation. When this occurs, there is an ambiguity in the number of pulsar revolutions in the intervening time. This is commonly referred to as *losing phase-connection.*

The parameters describing the spin of newly discovered pulsars are not precisely known. Generally, for isolated pulsars, the discovery parameters are sufficient for a first guess at a timing solution. In contrast, this is not the case for binary pulsars, which require additional parameters to describe their observed TOAs. In these cases, densely-spaced observations are required to determine the orbital parameters from measurements of the Doppler-shifted spin period (e.g. Freire et al., 2001). This initial model of the binary motion can then be used construct a phase-connected timing solution.

Once a phase-connected timing solution is available, most pulsars can be observed relatively infrequently. Many pulsars are observed roughly monthly, as is the case for the Effelsberg observations described in Chapter 6. On the other hand, desiring to measure a particular phenomenon might require irregularly-spaced observations, or dense orbital campaigns. An example of such an orbital campaign is described

---

[1] A 5-min observation with 200 MHz of bandwidth recorded in coherently dedispersed folding mode is only ~50 MB, whereas the same observation would be ~5 GB if recorded in search mode, and ~240 GB if recorded in baseband mode.

in Chapter 5, where my collaborators and I use dedicated observations covering all orbital phases of PSR J1952+2630 in an attempt to detect the signature of Shapiro delay, a relativistic TOA delay caused when the emission of a binary pulsar passes through the gravitational well of its companion.

Once the timing observations are conducted, the data acquired need to be distilled into TOAs.

4.2 Data Reduction

The process of reducing folded timing data into TOAs consists of several steps. At each stage, care must be taken to reduce systematics that adversely impact the resulting TOAs and subsequent analysis. This is especially true when conducting high-precision PTA analyses, in which TOAs from multiple pulsars are jointly analyzed for correlated signals. Mature, well-maintained software suites (e.g. `psrchive`;[1] Hotan et al., 2004b) can be used to perform all of the required steps. Nevertheless, custom software is occasionally used to augment the analysis (for example, see § 6.3.1).

RFI Excision

RFI signals introduce artifacts into integrated pulse profiles. These artifacts cause deviations in the measured TOAs with respect to the true TOA, as well as an increase in the uncertainty of the TOA. Thus, once timing observations have been folded[2] they must be cleaned of RFI. An example of the effect of RFI on an observation with Effelsberg is shown in Figure 4.1.

RFI excision can be done manually, although this is quite time-consuming when reducing large numbers of observations. It is therefore generally more efficient to use an algorithmic approach. Several different algorithms have been developed to deal with the diversity of RFI signals. In Chapter 6, I describe a custom algorithm that I developed to remove RFI from observations recorded with the PSRIX instrument at Effelsberg.

Automated algorithms typically split the observation into multiple parts and summarize each block of data using one or more metrics. The resulting values for each block are compared to one another in order to identify outliers that exceed some user-defined threshold. These outlier blocks are flagged as RFI and are either ignored in the subsequent analysis, set to some constant value (possibly 0), or replaced with appropriately levelled random noise.

Polarization Calibration

The profiles of pulsars are polarized. Thus, slight systematic differences in the observed profiles can be introduced by the polarization properties of the telescope, receiver, etc., as well as the relative orientation of the receiver and the pulsar/sky (i.e. the *parallactic angle*). As a result of this dependence on the parallactic angle, uncalibrated profiles can introduce trends in pulsar timing data that depend on the time of day and/or day of year of the observations. Such long-term trends will cause errors in the determination of timing parameters.

---

[1] http://psrchive.sourceforge.net

[2] As described above this can be done on-line, or alternatively, the data can be recorded in search-mode or base-band mode and folded after the observations are finished.

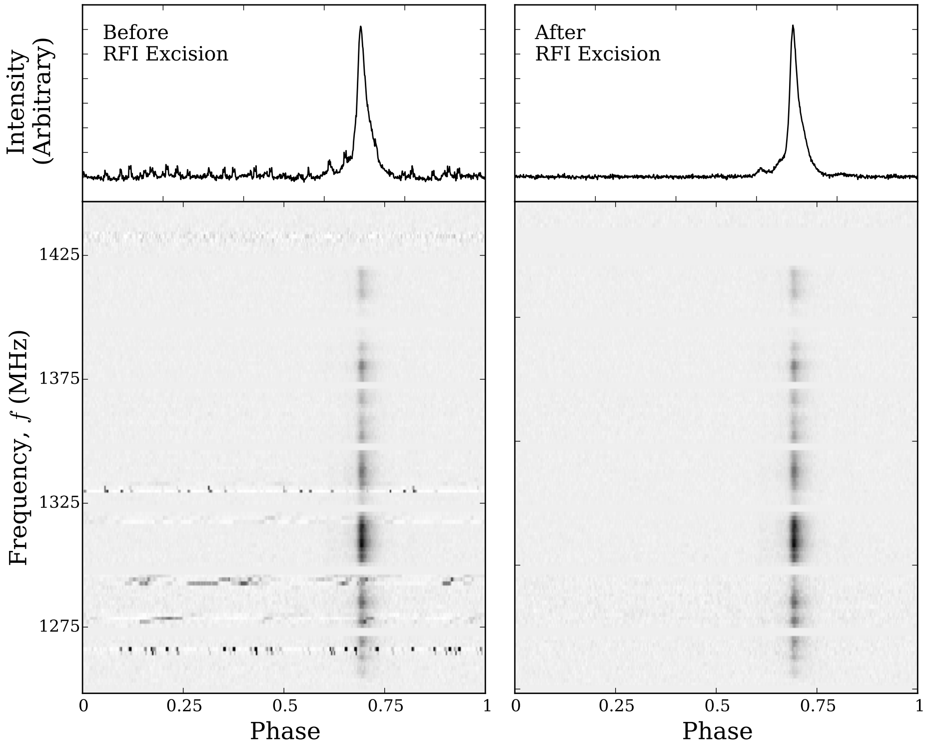

Figure 4.1: *Top Left* – The fully time and frequency-integrated profile for a ∼30-min observation of the MSP PSR J1713+0747 made with the Effelsberg radio telescope. The small spikes throughout the profile are caused by RFI.
Bottom Left – A frequency vs. phase plot of the uncleaned observation showing that these particular RFI signals are narrow-band, and thus can be easily removed from the observation by discarding the affected channels.
Right – The same observation after the RFI has been excised by the automated procedure described in § 6.3.1.

Therefore, it is important to record individual orthogonal polarizations. These individual polarizations must then be separately calibrated before combining them. The receiver may use either dual linear feeds or dual circular feeds. The basic polarization calibration procedure is the same in the case of both linear and circular feeds.

The simplest form of polarization calibration involves observing a polarized noise diode[1] just prior to, or immediately following, the pulsar scan. The relative gain and phase of the two polarization feeds are then adjusted following the formalism of Britton (2000) assuming they both measure the same diode intensity and that they are orthogonal. Other, more complete polarization calibration methods make use of additional information such as a flux calibration observation or a model of the receiver response (e.g. Ord et al., 2004).

---

[1] In the case of dual linear feeds, the diode is oriented at 45° with respect to the dipoles such that they are both expected to receive the same signal.

In any case, the ultimate goal of polarization calibration is to reliably determine pulse profiles and compute accurate TOAs that are free of systematics, such that the observations can be used for polarimetric studies (e.g. Everett & Weisberg, 2001; Manchester et al., 2010; Dai et al., 2015).

Flux Calibration

The pulsar profiles measured from timing observations are scaled to arbitrary units. Dedicated observations of an astronomical source with a known flux density (i.e. a *standard candle* source), must be used to determine the flux densities of pulsars. The difference in mean data levels between a scan pointed directly at the standard candle and another nearby off-source scan is assumed to be entirely due to the standard candle. This comparison makes it possible to determine the conversion factor between the arbitrary observation units and physical flux density units.

The conversion factor between the arbitrary data units and physical units depends on the attenuation of the telescope signal applied in the receiver/data recorder chain. Additionally, telescopes have sensitivities that depend on their orientation.[1] To overcome these complications a noise diode is pulsed during the on and off-source flux calibration scans of the standard candle, permitting the intensity of the diode to be expressed in physical units. Then, before each pulsar observation, the diode is again pulsed. By comparing the diode level with the pulsar level, the flux density of the pulsar can be determined in physical units, regardless if the telescope position and attenuation settings have changed since the observation of the standard candle.

Flux calibration is of limited importance to pulsar timing. However, a recent study of the MSP PSR J0437−4715 has found a correlation between pulse intensities and their shape (Osłowski et al., 2014). Thus, it might be possible to use information about the flux densities of individual pulses to correct for their variations, as well as the associated deviations in their TOAs. This could help reduce the amount of associated noise affecting the resulting timing analysis (see § 4.3 for more details about the noise affecting pulsar timing). In any case, flux-calibrating regular timing observations provides an excellent opportunity to monitor pulsar flux densities over time.

Determining the Time-Of-Arrival

It is common to report a TOA as the *Modified Julian Date* (MJD)[2] that corresponds to the chosen reference point of the pulse profile, the *fiducial point*. A TOA is calculated by determining the phase offset between the observed pulse profile and a reference profile[3] (see Figure 4.2). The phase offset of the fiducial point of the observed pulse is converted to a time offset, τ, by multiplying by the pulse period, and then added to the MJD at the start of the profile, thus yielding the MJD of the fiducial point (i.e. the TOA). The phase offset is typically computed by cross-correlating the observed profile against the reference profile. This is typically performed in the Fourier domain. Taylor (1992) describe details of how to compute a TOA and estimate its uncertainty in the Fourier domain. By using this technique, it is possible to accurately determine the phase offset within a fraction of a profile bin.

---

[1] In most cases this is caused by to deformations of the reflector due to gravity as the telescope is moved.

[2] The MJD is the time since midnight UT on Nov 17, 1858, reported in units of days.

[3] Commonly known as a “template” or “standard profile”.

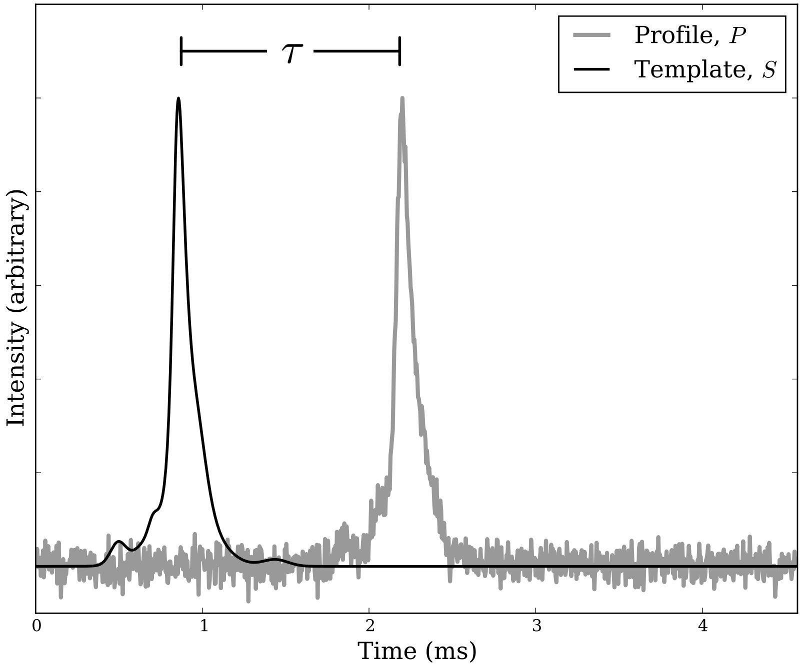

Figure 4.2: TOAs are commonly determined by cross-correlating a high-S/N or noise-free template, S, with pulse profiles, P. The cross-correlation provides a measurement of the phase offset of the observed profile, which is converted to a time offset, τ, and added to the MJD of the start of the profile. See text for details.

In practice, TOAs are generated from *integrated profiles*, generated from summing together many pulses (recall from § 4.1 that most timing observations already consist of sub-integrations). The main reasons for summarizing a collection of pulses into a single TOA is that integrated profiles have greater S/Ns than individual pulses, allowing for a more precise determination of the pulse phase, and that individual pulses show significant shape and amplitude variability, so-called *jitter noise* (e.g. Cordes & Shannon, 2010; Liu et al., 2012), but the profiles resulting from integrating $\gtrsim 10^4$ pulses together are remarkably stable. Sources of noise are discussed further in § 4.3.

When computing a single TOA from an interval of data containing many pulses, the phase-shift corresponding to the position of the fiducial point is added to the MJD corresponding to the start of the pulse closest to the mid-point of the interval. This choice minimizes the effects of systematic errors present (e.g. phase-drifts over time caused by using an incorrect period when folding).

Recently, sophisticated techniques have been developed for reducing the systematic errors occasionally introduced when computing TOAs. These algorithms include using the full frequency information of the folded data to reduce the effect of profile shape evolution with frequency, scintillation, and frequency-dependent pulse broadening by the ISM (Pennucci et al., 2014; Liu et al., 2014b). Another advanced algorithm uses the full polarization information rather than simply using the total intensity profile (van Straten, 2006).

4.3 Timing Analysis

Once the observation data are reduced and TOAs are available, the next step is to perform the timing analysis. This process requires an initial timing model that can be used to predict the phase of each TOA. These predictions are then compared to the measured phases. Model parameters are iteratively refined to provide improved predictions, that is, to minimize the difference between the measured and predicted phases. Fortunately, publicly available software has been developed to analyze timing data using the techniques described below. The two most commonly used timing programs are `TEMPO` and `TEMPO2`, both of which follow the same basic procedure. The ultimate goal of pulsar timing is to use the resulting parameters to infer information about the pulsar and its environment.

Timing Model

The *timing model* is used to transform the observed TOAs of a pulsar, as measured at a telescope, to the proper time of the pulsar. Thus, a timing model consists of parameters describing a pulsar's spin, astrometry, DM, and binary motion. Following the notation of Taylor (1992), the conversion of a measured TOA, $t_{\rm obs}$, to the pulsar's proper time, T, can be generically summarized as

$$T = t_{\rm obs} - t_0 + \Delta_C - D/f^2 + [\Delta_{R\odot} + \Delta_{E\odot} - \Delta_{S\odot}] - [\Delta_R + \Delta_E + \Delta_S + \Delta_A]\,, \quad (4.1)$$

where t_0 is a reference TOA, Δ_C corrects the observatory clock relative to terrestrial time standards, D/f^2 is the dispersion delay (D is related to the DM of the pulsar). The trio of terms, $\Delta_{R\odot}$, $\Delta_{E\odot}$, and $\Delta_{S\odot}$ are the Roemer, Einstein, and Shapiro delays of the Solar System, respectively. These terms remove the effect of the Solar System from the TOAs (see below). The terms Δ_R, Δ_E, and Δ_S are the equivalent corrections for binary pulsars. Fully removing the effect of binarity from the TOAs requires an additional correction related to aberration effects, Δ_A. These four corrections for binary pulsars are computed using a model of the binary motion (see below). The proper time of the pulsar can then be related to the rotational phase of the pulsar, $\phi(T)$. This is typically done by expressing the pulsar phase as a Taylor expansion of T,

$$\phi(T) = \nu T + \frac{\dot{\nu} T^2}{2} + \frac{\ddot{\nu} T^3}{6} + ... + \epsilon(T), \quad (4.2)$$

where ν is the spin frequency of the pulsar, $\dot{\nu}$, $\ddot{\nu}$, etc. are time derivatives of the pulsar's spin, and $\epsilon(T)$ is an error term representing spin irregularities of the pulsar (i.e. spin noise).

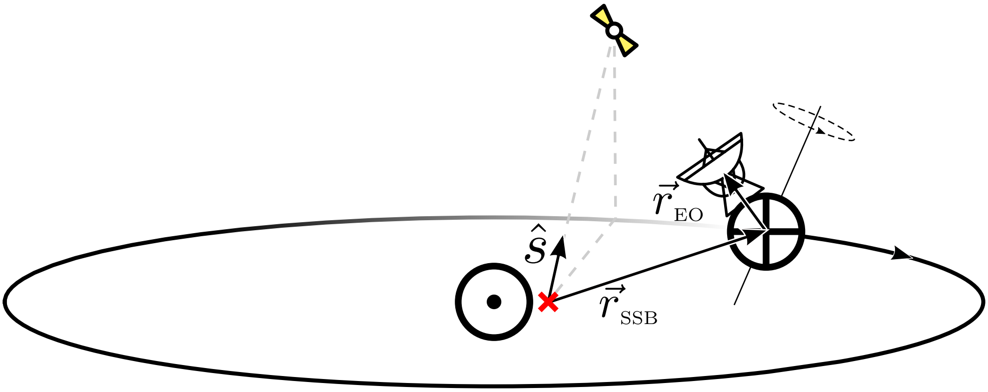

Figure 4.3: A schematic showing the quantities relevant for correcting TOAs for the Roemer delay, $\Delta_{R\odot}$. That is, removing the effect of the Earth's orbit, as well as its daily spin. The vector $\vec{r}_{\rm SSB}$ connects the SSB (the red '**X**') with the centre of the Earth, '$\bigoplus$', and the vector $\vec{r}_{\rm EO}$ connects the centre of the Earth with the phase centre of the telescope. The unit vector $\hat{s}$ points in the direction of the pulsar. The expression for $\Delta_{R\odot}$ with respect to these quantities is given by Eq. 4.3. Note that the SSB does not coincide with the centre of the Sun, '$\odot$'.

Barycentric Corrections

The *topocentric* TOAs measured at the telescopes need to be corrected for Earth and Solar System effects. In particular, the Roemer delay, $\Delta_{R\odot}$, is the geometric delay caused by the annual motion of the Earth around the Sun and the daily spin of the Earth. In short, TOAs arrive earlier when the telescope approaches the pulsar, and similarly, TOAs arrive later when the telescope recedes away from the pulsar. This can be summarized by (e.g Lorimer & Kramer, 2004)

$$\Delta_{R\odot} = -\left[(\vec{r}_{\rm SSB} + \vec{r}_{\rm EO}) \cdot \hat{s}\right]/c, \tag{4.3}$$

where $\vec{r}_{\rm SSB}$ is the position vector of the centre of the Earth relative to the Solar System barycentre (SSB), $\vec{r}_{\rm EO}$ is the position of the phase centre of the telescope with respect to the centre of the Earth, $\hat{s}$ is a unit vector pointing in the direction of the pulsar, and c is the speed of light. This set-up is shown graphically in Figure 4.3. The Roemer delay can contribute deviations in the TOAs of up to ∼500 s, depending on the ecliptic latitude of the pulsar. Since this correction is much larger than the periods of known pulsars, phase-connected pulsar timing would be impossible without first correcting for the motion of the Earth. Fortunately, accurate models of the motion of the Earth and the other Solar System bodies (i.e. *Solar System ephemerides*; SSEs) are regularly published, as are models of the rotation and orientation of the Earth. `TEMPO` and `TEMPO2` typically use SSEs from the "DE" family of models produced by NASA's Jet Propulsion Laboratory (JPL).

Topocentric TOAs must also be corrected for General and Special Relativistic effects that induce predictable variations on the rates of the atomic clocks used to time-tag the observations. These variable rates are caused by the Earth's elliptical orbit about the Sun. Collectively, these relativistic effects are referred to as the Einstein delay, $\Delta_{E\odot}$.

Furthermore, pulsar signals are also delayed slightly as they pass near to a Solar

System body. This delay is caused by the emission passing through the body's gravitational potential well. This General Relativistic effect is called the Shapiro delay, $\Delta_{S\odot}$. The Shapiro delay of the Solar System is analogous to the Shapiro delay effect occasionally observed in binary pulsars.

The process of applying these three corrections is referred to as *barycentering.* Applying $\Delta_{R\odot}$, $\Delta_{E\odot}$, and $\Delta_{S\odot}$ to a topocentric TOA results in a *barycentric* TOA, which is the time at which the pulse would arrive at the Solar System barycentre (SSB), if it was not for the motion of the Earth and the influence of the other Solar System bodies. Barycentering is a necessary step that converts the TOAs measured in a moving reference frame (i.e. the Earth) to an inertial reference frame (i.e. the SSB). Errors in the SSE would result in systematic trends in the pulsar timing data. A detailed search for the signature of SSE errors using data from the International Pulsar Timing Array (IPTA) is presented in Chapter 7.

Lastly, because the radio frequencies of the pulsar emission are Doppler shifted by the Earth's motion, the *barycentric frequencies* of each TOA must be computed to accurately measure and remove the effect of the ISM. This is accomplished by using the SSE to compute the velocity of the telescope along the line-of-sight to the pulsar and using it to un-Doppler shift the observed frequencies.

Binary Pulsars

Accounting for the effect of binarity on TOAs is done with a model of the pulsar's binary motion. The basic principle is analogous to the case of removing Solar System effects described above. That is, pulsar-centric times are referred to the binary system's barycentre. Fortunately, pulsar binary systems can be summarized by a relatively small number of models that require only a few parameters.

One of the most commonly used binary models is the `BT` model (Blandford & Teukolsky, 1976), which approximates the binary motion of the pulsar by assuming Newtonian gravity and using the five Keplerian parameters: the orbital period, P_b, the time of periastron passage, T_0, the projected semi-major axis, $x = (a \sin i)/c$, the eccentricity, e, and the longitude of periastron, ω. The `BT` model also supports the ad-hoc inclusion of the post-Keplerian parameters $\dot{P}_b$, $\dot{x}$, $\dot{\omega}$, and $\dot{e}$. A more consistent description of the binary motion in post-Newtonian gravity is provided by the `DD` model, which also includes the Shapiro delay range, r, and shape, $s = \sin i$, parameters (Damour & Deruelle, 1986). The `DD` model is formulated such that it is applicable to GR, as well as alternative theories of gravity. There exist other, more specialized, binary models such as the `ELL1` model (Lange et al., 2001). This model parameterizes the pulsar's binary motion in such a way that is particularly well suited to describe orbits with small eccentricities. The `ELL1` model is used in Chapter 5 to analyze the timing data of PSR J1952+2630. A summary of these and other binary models can be found in the literature (e.g. Weisberg & Taylor, 1981; Damour & Taylor, 1992; Edwards et al., 2006, and references therein).

As mentioned in § 1.6, studying binary pulsars has proven to be extremely useful in constraining relativistic gravity, measuring neutron star masses, and studying the equation-of-state of ultra-dense matter.

Residuals

The *timing residuals* of a pulsar are the differences between the phases of the measured TOAs,[1] $\{\phi\left(T_i\right)\}$, computed using Eqs 4.1 and 4.2, and the phases predicted by a timing model, $\{n_i\}$. The quality of a timing model is usually measured by the reduced χ^2 of the timing residuals, that is the χ^2 (e.g. Taylor & Weisberg, 1989),

$$\chi^2 = \sum_{i=1}^{N} \left(\frac{\phi(T_i) - n_i}{\sigma_i} \right)^2 , \tag{4.4}$$

divided by the number of degrees of freedom, $N_{\rm dof} = N_{\rm TOA} - N_{\rm params}$, where $N_{\rm TOA}$ is the number of TOAs fit, and $N_{\rm params}$ is the number of parameters included in the fit. In Eq. 4.4, σ_i is the uncertainty of TOA i in terms of the pulsar's spin phase.

TOA uncertainties are often underestimated. This may occur due to biases of the algorithm used to estimate the uncertainties when it is used in the low or high-S/N regime, the presence of RFI, or pulse jitter, to list a few. Incorrectly estimated TOA uncertainties cause the reduced χ^2 to deviate from 1 and introduce biases in the timing parameter uncertainties. The effect of these biases on the parameter uncertainty estimates can be eased by artificially adjusting the TOA uncertainties such that $\chi^2 \approx 1$. This is commonly done with a multiplicative factor, "EFAC", which accounts for incorrect scaling of the measurement uncertainties, and "EQUAD", which is added in quadrature to the measured TOA uncertainty to account for additional unmodelled noise processes. These two parameters typically depend on the pulsar and the observing system, and thus are different for different observing set-ups.

If a timing model accurately predicts the TOAs of a pulsar, then the residuals will be small and Gaussian-distributed (i.e. "white" noise). In this case, the root-mean-square (RMS) of the residuals is a small fraction of the period of the pulsar. On the other hand, deficiencies in the timing model will manifest themselves as systematic trends in the timing residuals, and cause the RMS to be inflated.

Signatures of Unmodelled Timing Parameters

As the time span over which a pulsar is monitored increases, or as the timing precision improves (e.g. by modifying the observing set-up or refining the pointing position), deficiencies in the timing model become apparent. These generally manifest themselves as systematic trends in the timing residuals, resulting in a non-Gaussian distribution of residuals.

These deviations might be caused by an inaccurate timing model (e.g. an unmodelled proper motion or a slightly inaccurate spin frequency), and thus are deterministic. Figure 4.4 shows an example of the residuals formed when using a timing solution that correctly models the data (i.e. white timing residuals) and the residuals resulting from an incorrect timing solution, which show clear systematic trends.

Alternatively, the deviations in the timing residuals might be caused by inherently unpredictable processes (e.g. intrinsic spin irregularities of the pulsar or variations of the ISM), which are broadly categorized as *noise sources*, and will be briefly discussed below.

---

[1] Here we give expressions for the residuals in terms of the pulsar's spin phase. However, it is also common to express residuals in units of time.

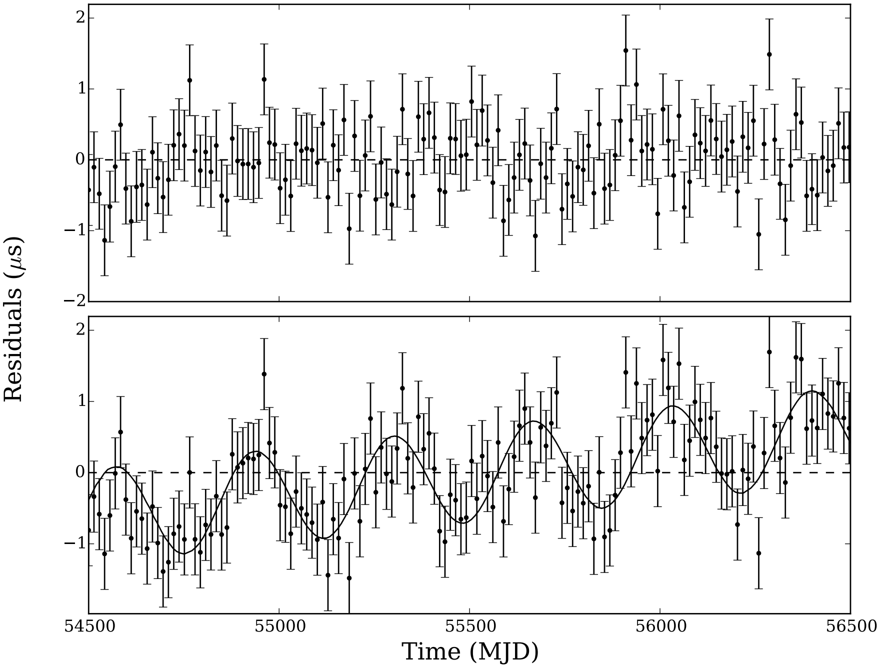

Figure 4.4: *Top* – Simulated Gaussian-distributed timing residuals.
Bottom – The same simulated TOAs analyzed with an incorrect timing solution. There are small deviations in both the spin frequency, giving rise to a linear trend, and the pulsar position, giving rise to a sinusoidal trend. The result of the compounded systematic trend is show with the solid line.

The timing model can be improved by fitting its parameters to the measured TOAs to provide better predictions, and when possible, by mitigating for sources of noise.

Fitting

In order to facilitate the process of fitting model parameters to TOAs, timing programs such as `TEMPO` and `TEMPO2` first linearize the timing model by taking partial derivatives with respect to the fit parameters (see e.g. Taylor & Weisberg, 1989; Hobbs et al., 2006). These parameters are then optimized to reduce the χ^2 by applying a linear least-squares fitting algorithm to the linearized timing model. It is common to take into account the TOA uncertainties by performing a *weighted* least-squares fit (Hobbs et al., 2006; Coles et al., 2011).

Occasionally, some timing model parameters are covariant with each other. One strategy for understanding these covariances is to compute a χ^2 map. This is usually done by specifying a uniformly-spaced grid of values containing each of the offending parameters. Then, for each grid point, the χ^2 is computed while holding offending parameters fixed and allowing the other timing parameters to be optimized. This brute-force approach helps to understand the nature of the covariance and allows the uncertainties to be properly propagated in further analyses. A χ^2 map is used in Chapter 5 to determine constraints on the mass and orbital inclination of PSR J1952+2630 given the lack of detection of the Shapiro delay.

Unmodelled long-timescale trends (i.e. red noise) in the timing residuals can have a similar effect. Such trends arise from closely-spaced TOAs that are correlated due to intrinsic spin irregularities of the pulsar or slow variations of the ISM. These red noise processes may be covariant with timing parameters, and thus result in inaccurate parameter estimations and incorrect uncertainty determinations. Dealing with these covariances requires special care. Fortunately, several algorithms have been developed to manage these issues. Some options include artificially whitening the residuals with higher-order spin derivatives (Hobbs et al., 2006) or explicitly including the correlation between data points in a generalized least-squares fit (Coles et al., 2011) by measuring the spectral properties of the red noise. I use this latter strategy in Chapter 7 when measuring the masses of the Solar System planets by using pulsar timing techniques.

The pulsar timing program `TempoNest` uses a Bayesian approach to map the timing parameter space even in the presence of parameter covariances, red noise, and DM variations (Lentati et al., 2014). Furthermore, `TempoNest` uses the full timing model, as opposed to the linearized version used in `TEMPO` and `TEMPO2`, to better estimate the uncertainties of the timing parameters. These techniques have been applied to derive robust limits on the gravitational wave background (GWB) using high-precision pulsar timing data from the European Pulsar Timing Array (EPTA; Lentati et al., 2015).

Sources of Noise

As alluded to earlier, several sources of noise adversely influence TOAs and timing residuals. Despite the origins of the noise not being fully understood, it is possible to broadly characterize them. Following the discussion by Cordes & Shannon (2010), noise processes influencing timing residuals can be partly characterized by their spectral behaviour. For instance, radiometer noise from the background of Galactic radio emission and subtle profile shape variations caused by summing a finite number of jittering pulses both produce an excess of white noise (i.e. uncorrelated deviations in the TOAs). The timing residuals of some pulsars also exhibit red noise (i.e. correlated deviations in the TOAs). Examples of processes that introduce red noise include intrinsic pulsar spin irregularities and ISM variations which may give rise to variations in DM and the degree of profile broadening due to multi-path scattering. Cordes & Shannon (2010) also characterize noise sources as either achromatic (i.e. independent of observing frequency) or chromatic (i.e. dependent on observing frequency). Figure 4.5 shows an example of both of these varieties of noise.

Fortunately, it is possible to partially mitigate several of these sources of noise (see e.g. Cordes & Shannon, 2010). Radiometer noise can be reduced by using more sensitive telescopes, larger bandwidths, and longer integration times. Summing more pulses is required to reduce the noise caused by pulse jitter (e.g. Liu et al., 2012). Also, it is possible to compensate for ISM-induced chromatic noise by conducting multi-frequency observations or by using larger bandwidths (e.g. Keith et al., 2013; Lee et al., 2014). The degree to which the noise can be corrected relative to the required timing precision is an important factor when determining if a pulsar is useful for a

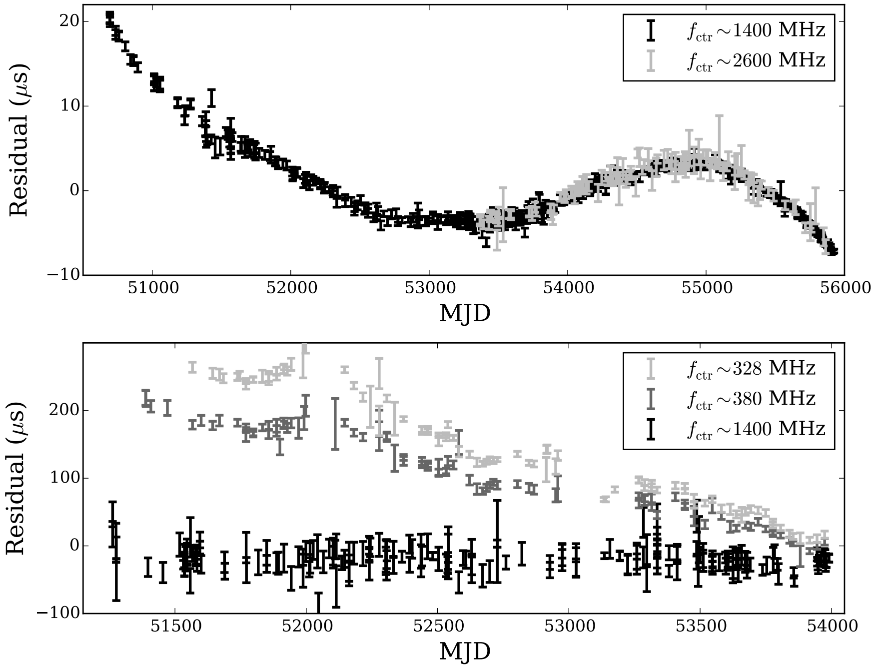

Figure 4.5: *Top* – Timing residuals for PSR B1937+21 from the EPTA (Desvignes et al., 2016), exhibiting achromatic red noise due to irregularities in the pulsar's spin. The amplitude of the noise does not depend on the central frequency of the observing band, $f_{\rm ctr}$. This type of noise cannot be mitigated, thus limiting the usefulness of B1937+21 to searches for weak long-time scale signals in timing data, such as the effect of the stochastic GWB or errors in SSE models (see Chapter 7).
Bottom – Timing residuals for PSR J0218+4232, also from the EPTA. The ISM along the line-of-sight to this pulsar varies, giving rise to fluctuations of the observed DM. This is a chromatic effect that more strongly affects observations centred at lower frequencies. Fortunately, DM variations can be modelled from multi-frequency observations, allowing much of the excess systematic noise to be removed (e.g. Keith et al., 2013; Lee et al., 2014).

particular purpose. This is especially true for the high precision required by PTAs to detect GWs.

Science

Once the timing parameters have converged and the limitations of the data have been carefully considered, the next step is to make physically meaningful inferences about the pulsar. In many cases, timing models are designed such that their parameters are directly related to interesting properties of the pulsar or the intervening ISM. In other cases, additional modelling or calculations are required. For example, in Chapter 5 we use the timing parameters of PSR J1952+2630, a binary pulsar, along with detailed simulations of stellar evolution, to infer the nature of its binary companion, as well as the history and ultimate fate of the binary system.

5

PSR J1952+2630:
A MILDLY RECYCLED PULSAR WITH A MASSIVE WHITE DWARF COMPANION

This chapter is based on an article published in the Monthly Notices of the Royal Astronomical Society (Lazarus et al., 2014). Information about the article can be found online at:
http://adsabs.harvard.edu/abs/2014MNRAS.437.1485L

The text, figures, and tables have only been modified to match the style, spelling and format of the rest of this thesis.

I am the lead author of the article. My main contributions include performing the observations, the data reduction, and the timing analysis.

The full list of authors is:
P. Lazarus, T. M. Tauris, B. Knispel, P. C. C. Freire, J. S. Deneva, V. M. Kaspi, B. Allen, S. Bogdanov, S. Chatterjee, I. H. Stairs, and W. W. Zhu

Abstract

We report on timing observations of PSR J1952+2630, a binary pulsar discovered in the PALFA survey using the Arecibo Observatory. The mildly recycled 20.7-ms pulsar is in a 9.4-h orbit with a massive, $M_{WD} > 0.93\ M_{\odot}$, white dwarf (WD) companion. We present, for the first time, a phase-coherent timing solution, with precise spin, astrometric, and Keplerian orbital parameters. This shows that the characteristic age of PSR J1952+2630 is 77 Myr, younger by one order of magnitude than any other recycled pulsar–massive WD system. We derive an upper limit on the true age of the system of 150 Myr. We investigate the formation of PSR J1952+2630 using detailed modelling of the mass-transfer process from a naked helium star on to the neutron star following a common-envelope phase (Case BB Roche-lobe overflow). From our modelling of the progenitor system, we constrain the accretion efficiency of the neutron star, which suggests a value between 100 and 300 % of the Eddington accretion limit. We present numerical models of the chemical structure of a possible oxygen-neon-magnesium WD companion. Furthermore, we calculate the past and the future spin evolution of PSR J1952+2630, until the system merges in about 3.4 Gyr due to gravitational wave emission. Although we detect no relativistic effects in our timing analysis, we show that several such effects will become measurable with continued observations over the next 10 years; thus PSR J1952+2630 has potential as a testbed for gravitational theories.

5.1 *Introduction*

Since 2004, the Arecibo L-band Feed Array (ALFA), a 7-beam receiver at the focus of the 305-m William E. Gordon radio telescope at the Arecibo Observatory, has been used to carry out the Pulsar–ALFA (PALFA) survey, a deep pulsar survey of low Galactic latitudes (Chapter 3; Cordes et al., 2006). Given its short pointings, the PALFA survey is especially sensitive to binary pulsars in tight orbits, as demonstrated by the discovery of the relativistic binary pulsar PSR J1906+0746, which did not require any acceleration search techniques (Lorimer et al., 2006a). Another aspect of this and other modern Galactic plane surveys is the high time and frequency resolution, which allow the detection of millisecond pulsars (MSPs) at high dispersion measures (DMs) (Champion et al., 2008; Deneva et al., 2012; Crawford et al., 2012) and therefore greatly expand the volume in which these can be discovered.

One of the innovative aspects of this survey is the use of distributed, volunteer computing. One of the main motivations is the detection of extremely tight (down to $P_b \sim 10$ min) binaries, for which acceleration and jerk searches become computationally challenging tasks. The analysis of survey data is distributed through the Einstein@Home (E@H) infrastructure (Knispel et al., 2010; Allen et al., 2013). Thus far, the E@H pipeline has discovered 24 new pulsars in the PALFA survey data alone, complementing the other data analysis pipelines the PALFA survey employs (Quicklook, and PRESTO; Stovall, 2013, and Chapter 3, respectively).

PSR J1952+2630 was the first binary pulsar discovered with the E@H pipeline (Knispel et al., 2011). At that time the few observations available allowed only a rough estimate of the orbital parameters of this MSP based on Doppler measurements of the spin period. These already showed that PSR J1952+2630 has a massive WD companion ($M_{WD} > 0.945\mathrm{M}_\odot$ assuming $M_p = 1.4\mathrm{M}_\odot$), and may have evolved from an intermediate-mass X-ray binary (IMXB). Building on the analysis by Knispel et al. (2011), we present in this chapter the phase-coherent timing solution of PSR J1952+2630 resulting from dedicated follow-up observations with the Arecibo telescope, which provides orbital parameters far more precise than those previously determined. Our timing solution also shows the system is relatively young ($\tau_c = 77\,\mathrm{Myr}$).

It is commonly accepted that MSPs are spun up to their high spin frequencies via accretion of mass and angular momentum from a companion star (Alpar et al., 1982; Radhakrishnan & Srinivasan, 1982; Bhattacharya & van den Heuvel, 1991). In this recycling phase, the system is observable as a X-ray binary (e.g. Hayakawa, 1985; Nagase, 1989; Bildsten et al., 1997) and towards the end of this phase as a X-ray MSP (Wijnands & van der Klis, 1998; Papitto et al., 2013).

The majority of MSPs have helium WD companions and their formation is mainly channelled through low-mass X-ray binaries (LMXBs) which have been well investigated in previous studies (e.g. Webbink et al., 1983; Pylyser & Savonije, 1988, 1989; Rappaport et al., 1995; Ergma et al., 1998; Tauris & Savonije, 1999; Podsiadlowski et al., 2002; Nelson et al., 2004; van der Sluys et al., 2005). In contrast, binary pulsars, such as PSR J1952+2630, with relatively heavy WDs (CO or ONeMg WDs) are less common in nature. Their formation and recycling process involves a more massive WD progenitor star in an IMXB (see Tauris et al., 2011, and references therein, for a discussion of their suggested formation channels). Here we distinguish IMXBs from other X-ray binaries as systems that leave behind a massive WD companion rather than a neutron star (NS). Some of these IMXB systems with donor stars of $6 - 7$ $M_\odot$ could also be classified observationally as Be/X-ray binaries since these stars are of spectral class B3-4 with emission lines. Recently, Tauris et al. (2012) presented a detailed study of the recycling process of pulsars via both LMXBs and

IMXBs and highlighted their similarities and differences. These authors also presented the first calculations of mild recycling in post-common envelope (CE) systems where mass transfer proceeds via so-called Case BB Roche-lobe overflow (RLO; see § 5.4 for details).

PSR J1952+2630's combination of a young, massive WD in a close orbit with a recycled pulsar poses interesting questions about its formation and future evolution. Binary MSPs represent the advanced stage of stellar evolution in close, interacting binaries. Their observed orbital and stellar properties are thus fossil records of their evolutionary history. Therefore, by using the precise description of a pulsar binary system determined from phase-coherent timing, and binary evolution modelling, we use PSR J1952+2630 as a probe of stellar astrophysics.

We also demonstrate that PSR J1952+2630 is an interesting test case for modelling Case BB RLO, enabling interesting constraints on the accretion physics from the combined modelling of binary stellar evolution and the spin kinematics of this young, mildly recycled pulsar.

The rest of this chapter is presented as follows. § 5.2 describes the observations of PSR J1952+2630, and details of the data reduction and timing analysis. Results from this analysis are presented in § 5.3. The binary evolution of the system is detailed in § 5.4. The implications of our results and future prospects are described in §§ 5.5 and 5.6, respectively. Finally, § 5.7 summarizes the chapter.

5.2 Observations and Data Analysis

Following its discovery in 2010 July, PSR J1952+2630 was observed during PALFA survey observing sessions using the usual survey observing set-up: the 7-beam ALFA receiver with the Mock spectrometers.[1] In this set-up, ∼322 MHz ALFA observing band was split into two overlapping sub-bands centred at 1300.168 and 1450.168 MHz, each with a bandwidth of 172.0625 MHz. All timing observations using this set-up were performed with ALFA's central beam, and were typically 5-10 min in duration.

A dedicated timing programme at the Arecibo Observatory started in 2011 November. The dedicated timing observations took data using the 'L-wide' receiver. These data were divided into four non-overlapping, contiguous sub-bands recorded by the Mock spectrometers in search mode. Each sub-band has 172 MHz of bandwidth divided into 2048 channels, sampled every ∼83.3 μs. Together the four sub-bands cover slightly more than the maximum bandwidth of the receiver, 580 MHz, and are centred at 1444 MHz.

At the start of the dedicated timing campaign, three 3-h observing sessions on consecutive days were conducted to obtain nearly complete orbital coverage, with the goal of detecting, or constraining a Shapiro delay signature caused by the pulsar's signal passing through its companion's gravitational potential well.

Subsequently, monthly observations of 1 h each were used for the next 11 months to monitor the pulsar, and refine our timing solution.

For analysis, each observation was divided into segments no longer than 15 min for each of the separate sub-bands. Each segment was folded offline using the appropriate topocentric spin period through the `prepfold` program from `PRESTO`.[2] The resulting

---

[1] http://www.naic.edu/∼astro/mock.shtml

[2] http://www.cv.nrao.edu/∼sransom/presto/

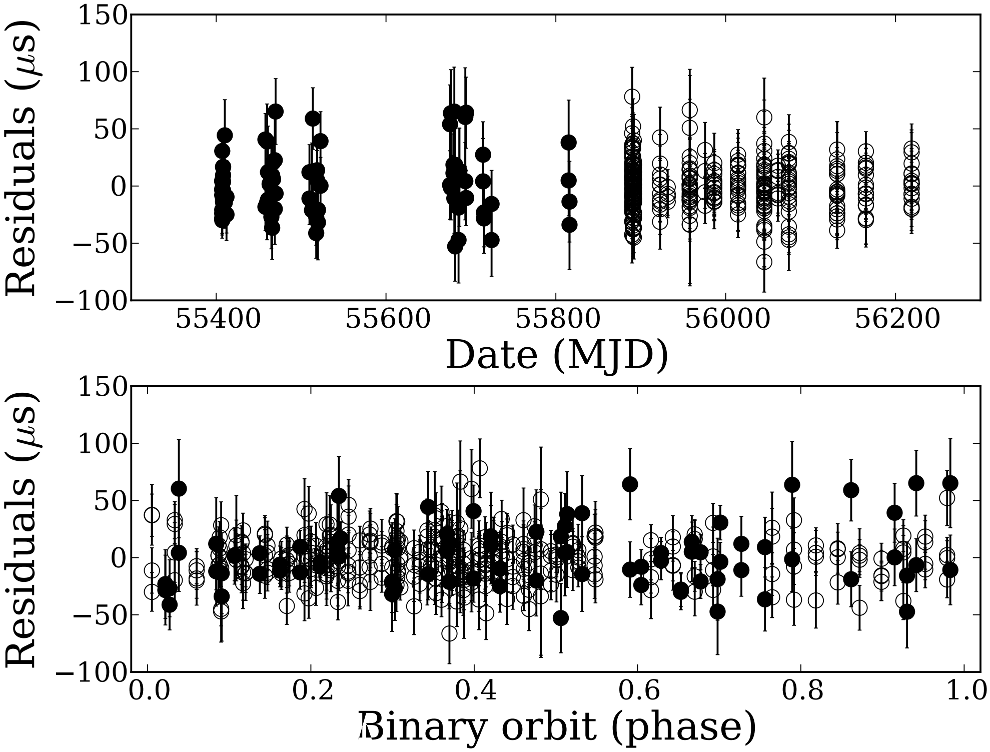

Figure 5.1: The difference between our pulse TOAs and our timing solution. The filled circles are TOAs from data taken with the ALFA receiver and the unfilled circles TOAs from data taken with the L-wide receiver. No systematic trends are visible as a function of epoch or orbital phase.

folded data files were converted to PSRFITS format (Hotan et al., 2004b) with `pam` from the `psrchive` suite of pulsar analysis tools.[1] Data files were fully time and frequency integrated, and times of arrival (TOAs) were computed using `pat` from `psrchive`. The result was a single TOA for each ∼15 min of observing for each sub-band.

TOAs for the different sub-bands were computed using a separate analytic template produced by fitting von Mises functions to the sum of profiles from the closely spaced 3-d observing campaign. Profiles from different observations were aligned using the pulsar ephemeris.

Timing analysis was performed with the `TEMPO2` software (Hobbs et al., 2006). The phase-coherent timing solution determined fits the 418 pulse TOAs. Our timing solution accurately models the timing data, leaving no systematic trends as a function of epoch or orbital phase (see Figure 5.1).

5.3 Results

The timing analysis of PSR J1952+2630 has resulted in the determination of astrometric, spin, and Keplerian orbital parameters. The fitted timing parameters, as well

---

[1] http://psrchive.sourceforge.net/

as some derived parameters, can be found in Table 5.1. The timing solution also includes a marginal detection of the proper motion of the pulsar.

5.3.1 The Nature of the Binary Companion Star

Given the combination of a relatively large observed mass function, $f_m = 0.153\ M_\odot$ (see Table 5.1), and a small orbital eccentricity, $e = 4.1 \times 10^{-5}$, it is clear that PSR J1952+2630 has a massive WD companion. The minimum companion mass is $M_{\rm WD}^{\rm min} \approx 0.93\ M_\odot$, obtained for an orbital inclination angle of $i = 90°$ and an assumed NS mass, $M_{\rm NS} = 1.35\ M_\odot$. The small eccentricity excludes a NS companion star since the release of the gravitational binding energy alone, during the core collapse, would make the post-SN eccentricity much larger ($e \gg 0.01$; Bhattacharya & van den Heuvel, 1991), in contrast with the observed value. Furthermore, no known double-NS system has $e < 0.01$, according to the ATNF Pulsar Catalogue[1] (Manchester et al., 2005). Thus a double-NS system is not possible and PSR J1952+2630 must have a massive WD companion, i.e. a carbon-oxygen (CO) or an oxygen-neon-magnesium (ONeMg) WD. The upper (Chandrasekhar) mass limit for a rigidly rotating WD is $\sim$1.48 $M_\odot$ (e.g. Yoon & Langer, 2005) and therefore we conclude that the WD companion star is in the mass interval $0.93 \lesssim M_{\rm WD}/M_\odot \lesssim 1.48$.

The distance to PSR J1952+2630, estimated using the observed DM, and the `NE2001` model of Galactic free electrons, is $d \simeq 9.6$ kpc (Cordes & Lazio, 2002). The uncertainty in DM-derived distances using the `NE2001` model can, in some cases, be up to a factor of $\sim$2 off from the true distance. Unfortunately, this places the binary system too far away to hope to optically detect the WD companion with current telescopes. As expected, a search of optical and infrared catalogues yielded no counterpart.

5.3.2 The Age of PSR J1952+2630

PSR J1952+2630 has a spin period of $P = 20.7$ ms and one of the highest values of the spin period derivative, $\dot{P} = 4.27 \times 10^{-18}\,{\rm s\,s^{-1}}$, for any known recycled pulsar[2] and by far the highest value for a mildly recycled pulsar with a massive WD companion. The observed value of $\dot{P}$ is contaminated by kinematic effects (see § 5.6). However, the contamination is only $\sim$0.01 %, assuming our current value of the proper motion. The combination of P and $\dot{P}$ of PSR J1952+2630 yields a small characteristic age, $\tau \equiv P/2\dot{P} \simeq 77$ Myr. The characteristic age of a pulsar should only be considered a rough order-of-magnitude estimate of the true age of the pulsar (i.e. time since recycling terminated). Thus the *true* ages are quite uncertain for recycled pulsars with large τ values of several Gyr (Tauris, 2012; Tauris et al., 2012), unless a cooling age of their WD companion can be determined. However, the true ages of recycled pulsars with small values of τ (less than a few 100 Myr) are relatively close to the characteristic age. Hence, we conclude that PSR J1952+2630 is young, for a recycled pulsar, and in §§ 5.5.1 and 5.5.1 we discuss its true age (i.e. its actual age since it switched on as a recycled radio pulsar) and also constrain its spin evolution in the past and in the future.

---

[1] http://www.atnf.csiro.au/people/pulsar/psrcat/

[2] This comparison was made using the ATNF Pulsar Catalogue.

Table 5.1: Fitted and derived parameters for PSR J1952+2630

Parameter	Value [a]
General Information	
MJD Range	55407 – 56219
Number of TOAs	418
Weighted RMS of Timing Residuals (μs)	19
Reduced-χ^2 value[b]	1.03
MJD of Period Determination	55813
Binary Model Used	ELL1
Fitted Parameters	
R.A., α (J2000)	19:52:36.8401(1)
Dec., δ (J2000)	26:30:28.073(2)
Proper motion in R.A., μ_α (mas/yr)	-6(2)
Proper motion in Dec., μ_δ (mas/yr)	0(3)
Spin Frequency, ν (Hz)	48.233774295845(7)
Spin Frequency derivative, $\dot{\nu}$ ($\times 10^{-15}$ Hz/s)	-9.9390(5)
Dispersion Measure, DM (pc cm^{-3})	315.338(2)
Projected Semi-Major Axis, $a \sin i$ (lt-s)	2.798196(2)
Orbital Period, P_b (d)	0.39187863896(7)
Time of Ascending Node, T_{asc} (MJD)	55812.89716459(4)
ϵ_1	-0.000038(1)
ϵ_2	0.000015(1)
Derived Parameters	
Spin Period, P (ms)	20.732360562672(3)
Spin Period Derivative $\dot{P}$ ($\times 10^{-18}$s s^{-1})	4.2721(2)
Galactic longitude, l (°)	63.254
Galactic latitude, b (°)	-0.376
Distance (NE2001, kpc)	9.6
Orbital Eccentricity, e ($\times 10^{-5}$)	4.1(1)
Longitude of Periastron, ω (°)	291(2)
Mass Function, f_m ($M_\odot$)	0.153184(1)
Characteristic Age, $\tau_c = P/(2\dot{P})$ (Myr)	77
Inferred Surface Magnetic Field Strength, B_S ($\times 10^9$ G)	9.5
Spin-down Luminosity, $\dot{E}$ ($\times 10^{35}$ ergs/s)	0.19

[a] The numbers in parentheses are the $1\,\sigma$, `TEMPO2`-reported uncertainties on the last digit.

[b] The uncertainties of the ALFA and L-wide data sets were individually scaled such that the reduced χ^2 of the data sets are 1.

5.3.3 Constraints on the Binary System from Timing

Given the current timing data, the binary motion of PSR J1952+2630 can be accurately modelled without requiring any relativistic, post-Keplerian parameters. Unfortunately, this means that the masses of the pulsar and its WD companion cannot be precisely determined by the current timing model.

Nevertheless, a χ^2 analysis was performed to investigate what constraints the lack of a Shapiro delay detection imposes on the make-up and geometry of the binary system (i.e. the mass of the pulsar, $M_{\rm NS}$, and that of its companion, $M_{\rm WD}$, as well as the binary system inclination, i, by using the mass function). A χ^2-map was computed using the `ChiSqCube` plug-in[1] for `TEMPO2` (see Figure 5.2). The χ^2-map was computed for $M_{\rm WD}$ between 0 and $1.5\,M_\odot$, in steps of $0.001\,M_\odot$, and $\cos i$ from 0 to 1 in steps of 0.001.

For each point in the χ^2 map, the timing model was refitted, holding the values of $M_{\rm WD}$ and $\cos i$ fixed. The resulting χ^2 values were converted to probabilities by following Splaver et al. (2002), and then normalized. The 1, 2, and $3\,\sigma$ contours were chosen such that they contain ~68.3, ~95.5, and ~99.7 % of the allowed binary system configurations. Based on this analysis we know the binary system cannot be edge-on ($i = 90^\circ$). The inclination angle is constrained to be be $i \leq 75^\circ$ for $M_{\rm NS} \geq 1.35 M_\odot$, at the $3\,\sigma$ level.

However, based on the massive companion, and small, but significantly non-zero eccentricity, we expect that with our current timing precision we will measure two (or possibly three) post-Keplerian parameters precisely enough to provide a stringent test of relativistic gravity, within the next 10 yr (see § 5.6).

5.4 Binary Evolution of the Progenitor

In general, binary pulsars with a CO WD companion[2] can form via different formation channels (see Tauris et al., 2012, and references therein).

Pulsars with CO WDs in orbits of $P_{\rm orb} \leq 2-3\,{\rm d}$, like PSR J1952+2630 ($P_{\rm orb} = 9.4\,{\rm h}$), are believed to have formed via a CE scenario. Such systems originate from IMXBs which have very large values of $P_{\rm orb}$ prior to the onset of the mass transfer. These systems are characterized by donor stars with masses in the range $2 < M_2/M_\odot < 7$, and very wide orbits up to $P_{\rm orb} \simeq 10^3\,{\rm d}$. Donor stars near the tip of the red giant branch or on the asymptotic giant branch evolve via late Case B RLO or Case C RLO, respectively. As a result, these donor stars develop a deep convective envelope as they enter the giant phase, before filling their Roche lobe. These stars respond to mass-loss by expanding, which causes them to overfill their Roche lobe even more. Binaries where mass transfer occurs from a more massive donor star to a less massive accreting NS shrink in size, causing further overfilling of the donor star's Roche lobe, which further enhances mass-loss. This process leads to a dynamically unstable, runaway mass transfer and the formation of a CE (Paczyński, 1976; Iben & Livio, 1993; Ivanova et al., 2013). However, the wide orbit prior to the RLO is also the reason why these systems survive the CE and spiral-in phase, since the binding energy

---

[1] The `ChiSqCube` plug-in populates a three-dimensional χ^2 space. For the purpose of the analysis presented here, the third dimension was not used.

[2] Here, and in the following, we simply write 'CO WD' for any massive WD whose exact chemical composition (CO or ONeMg) is unknown.

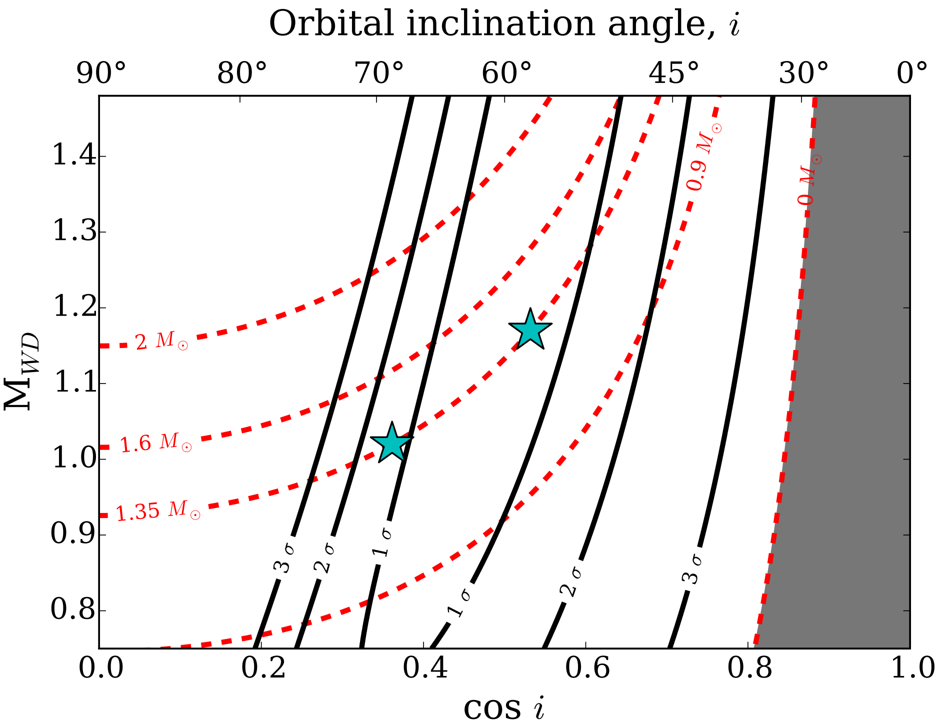

Figure 5.2: Map of companion-mass and inclination combinations allowed by the current timing data. The 1, 2, and $3\,\sigma$ contours, shown in black, enclose ~68.3, 95.5, and 99.7 % of the allowed binary system configurations, respectively, given the current timing data, and requiring the companion's mass to lie in the range $0.75 \leq M_{\rm WD} \leq 1.48\ M_\odot$. The red dashed lines trace constant pulsar mass. The grey region on the right-hand side is excluded because the pulsar mass must be larger than 0. The two stars are the results from the two simulations of the binary system's evolution (see § 5.4.1).

of donor star's envelope becomes weaker with advanced stellar age, and therefore the envelope is easier to eject, thereby avoiding a merger event.

Given that the duration of the CE and spiral-in phase is quite short ($< 10^3$ yr; e.g. Podsiadlowski, 2001; Passy et al., 2012; Ivanova et al., 2013), the NS can only accrete $\sim 10^{-5}\ M_\odot$ during this phase, assuming that its accretion is limited by the Eddington accretion rate (a few $10^{-8}\ M_\odot\,{\rm yr}^{-1}$). This small amount is not enough to even mildly recycle the pulsar. Instead, the NS is thought to be recycled during the subsequent so-called Case BB RLO (Tauris et al., 2012). This post-CE mass-transfer phase is a result of the naked helium star (the stripped core of the original IMXB donor star) filling its Roche lobe when it expands to become a giant during helium shell burning. Hence, for the purpose of understanding the recycling of PSR J1952+2630 we only have to consider this epoch of evolution in detail. A complete overview the full progenitor evolution of the system is illustrated in Figure 5.3.

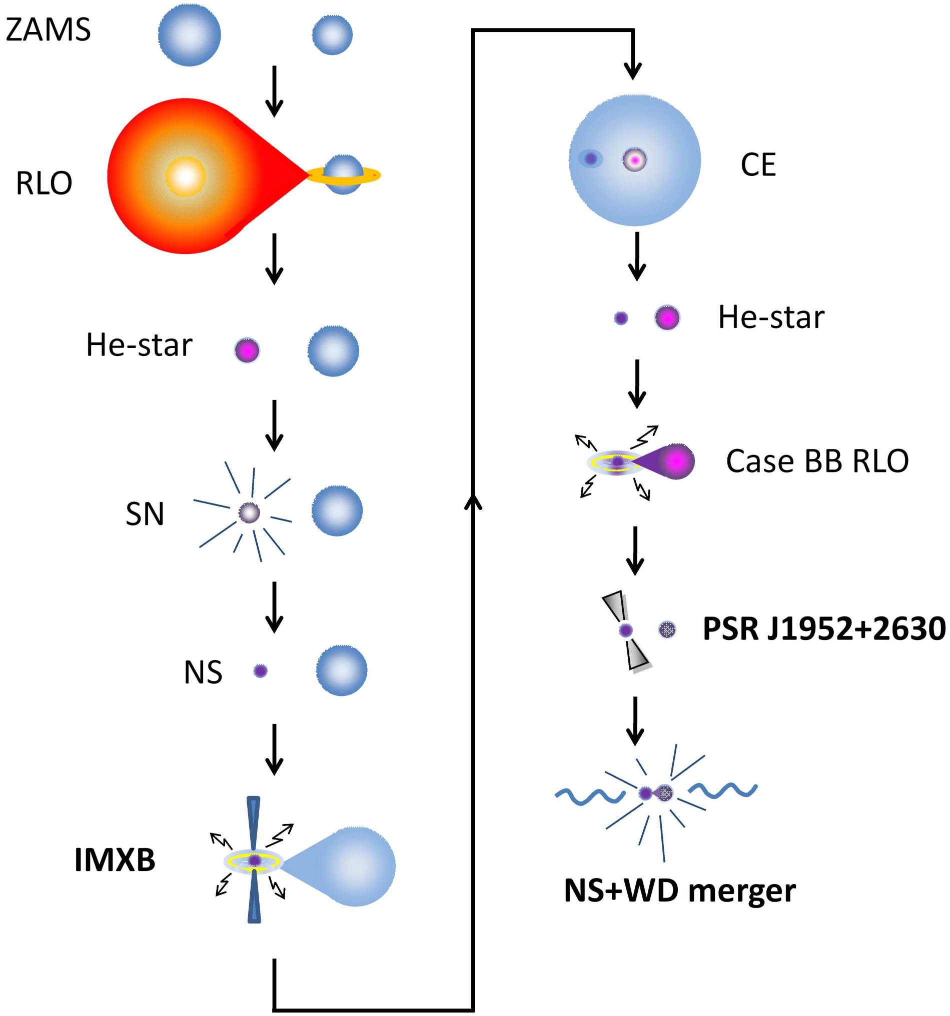

Figure 5.3: An illustration of the full binary stellar evolution from the zero-age main sequence (ZAMS) to the final merger stage. The initially more massive star evolves to initiate RLO, leaving behind a naked helium core which collapses into an NS remnant, following a supernova (SN) explosion. Thereafter, the system becomes a wide-orbit IMXB, leading to dynamically unstable mass transfer and the formation of a CE, when the $6-7\,M_{\odot}$ donor star initiates RLO. The post-CE evolution, calculated in detail in this work, is responsible for recycling the NS via Case BB RLO when the helium star companion expands to initiate a final mass-transfer episode. PSR J1952+2630 is currently observed as a mildly recycled radio pulsar orbiting a massive WD. The system will merge in $\sim$3.4 Gyr, possibly leading to a γ-ray burst-like event and the formation of a single black hole.

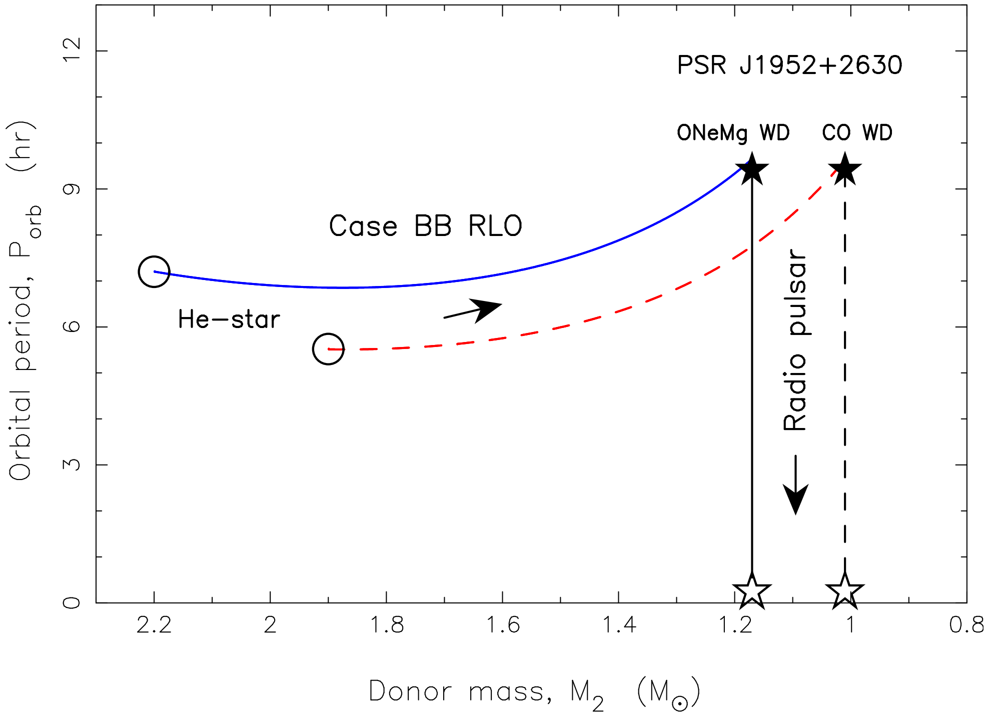

Figure 5.4: Progenitor evolution of the PSR J1952+2630 system in the $(M_2, P_{\rm orb})$ plane during mass transfer via Case BB RLO. The blue solid line is the evolutionary track for a 2.2 $M_\odot$ helium star leaving a 1.17 $M_\odot$ ONeMg WD remnant. The red dashed line is for a 1.9 $M_\odot$ helium star leaving a 1.02 $M_\odot$ CO WD remnant. The open circles show the location of the helium star donors at the onset of the RLO. The solid stars indicate the termination of the RLO when the radio pulsar turns on. In about 3.4 Gyr, the system will merge (open stars).

5.4.1 Calculations of Case BB RLO Leading to Recycling of PSR J1952+2630

Binary evolution for NS–massive WD systems have been studied using detailed calculations of the Case BB RLO by applying the Langer stellar evolution code (e.g. Tauris et al., 2011, 2012). However, none of the previously computed models produced systems sufficiently similar to that of PSR J1952+2630. We used the same code to study what progenitor systems can result in PSR J1952+2630 like binaries, the Case BB RLO of these systems, and the nature of the WD companion.

The masses of the WD and the NS ($M_{\rm WD}$ and $M_{\rm NS}$, respectively) are not known from timing at this stage (see § 5.3.3). In order to limit the number of trial computations, we assumed $M_{\rm NS} = 1.35\ M_\odot$ and performed various calculations with different values of initial orbital period and initial mass of the helium donor star, M_2.

The young age of PSR J1952+2630 implies that $P_{\rm orb}$ (now 9.4 h) has not changed much by gravitational wave radiation since the termination of the mass transfer (it was at most ∼9.6 h; see § 5.5). Therefore, we only select progenitor solutions of our modelling that have similar orbital periods. We also impose the criterion $M_{\rm WD}$ =0.93 − 1.48 $M_\odot$, to be consistent with the minimum companion mass derived from our timing solution.

Two solutions satisfying our selection criteria are shown in Figure 5.4. The first solution (blue solid line) is for a 2.2 $M_\odot$ helium star leading to formation of a 1.17 $M_\odot$ ONeMg WD. The second solution (red dashed line) is for a 1.9 $M_\odot$ helium star leading to a 1.02 $M_\odot$ CO WD. In both cases, we assumed a helium star metallicity of $Z = 0.02$ (solar metallicity), a reasonable assumption given that their $\sim$6 – 7 $M_\odot$ progenitors had short lifetimes of $\sim$100 Myr and thus belong to Galactic Population I stars. The second solution predicts a shorter pulsar spin period at the termination of accretion, and therefore imposes a less strict limit on the mass-accretion efficiency; see § 5.5.1 for a discussion.

Unfortunately, given the current timing data, it is not possible to place sufficiently stringent constraints on the binary system to be used to select either of the two simulated scenarios as the actual evolution of the binary (see § 5.3.3, and Figure 5.2).

For the remainder of § 5.4, we will consider only the ONeMg WD solution to our modelling. In particular, we will highlight some of the more interesting characteristics of the WD.

The mass-transfer rate, $|\dot{M}_2|$, for the solution leading to the 1.17 $M_\odot$ ONeMg WD is shown in Figure 5.5 as a function of time. The duration of the Case BB RLO is seen to last for about $\Delta t = 60$ kyr, which causes the NS to accrete an amount $\Delta M_{\rm NS} \approx 0.7 - 6.4 \times 10^{-3}$ $M_\odot$, depending on the assumed accretion efficiency and the exact value of the Eddington accretion limit, $\dot{M}_{\rm Edd}$. Here we assumed $\dot{M}_{\rm Edd} = 3.9 \times 10^{-8}$ $M_\odot$ yr^{-1} (a typical value for accretion of helium-rich matter, Bhattacharya & van den Heuvel, 1991) and allowed for the actual accretion rate to be somewhere in the interval 30 – 300 % of this value. This is to account for the fact that the value of $\dot{M}_{\rm Edd}$ is derived under idealized assumptions of spherical symmetry, steady-state accretion, Thomson scattering opacity and Newtonian gravity. As we shall see, the accretion efficiency, and thus $\Delta M_{\rm NS}$, is important for the spin period obtained by the NS during its spin-up phase.

The mass-transfer rate from the helium star is highly super-Eddington ($|\dot{M}_2| \sim 10^3\ \dot{M}_{\rm Edd}$). The excess material (99.9 %) is assumed to be ejected from the vicinity of the NS, in the form of a disc wind or a jet, with the specific orbital angular momentum of the NS following the so-called isotropic re-emission model (see Tauris et al., 2000, and references therein).

5.4.2 Detailed WD Structure

The calculated interior structure and evolution of a likely progenitor of PSR J1952+2630, a 2.2 $M_\odot$ helium star which undergoes Case BB RLO and leaves behind an ONeMg WD, is illustrated in the “Kippenhahn diagram” (Kippenhahn & Weigert, 1990) in Figure 5.6. The plot shows the last 10 kyr of the mass-transfer phase (t = 2.85 – 2.86 Myr), followed by 32 kyr of evolution (t = 2.860 – 2.892 Myr) during which carbon is ignited in the detached donor star.

In our modelling of the companion star, there are four instances of off-centred carbon burning shells. These shells are the four blue regions underneath the green-hatched convection zones in Figure 5.6. The ignition points are off-centre because these surrounding layers are hotter than the interior due to more efficient neutrino cooling in the higher density inner core. The maximum temperature is near a mass coordinate of $m/M_\odot \simeq 0.4$.

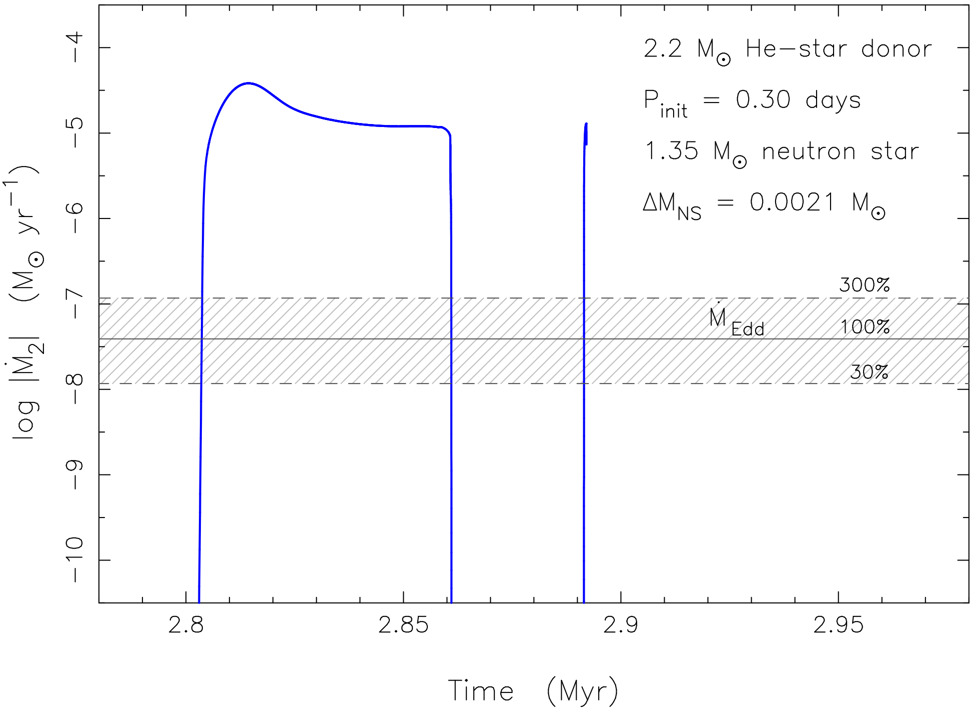

Figure 5.5: Mass-transfer rate as a function of stellar age for the progenitor evolution plotted in Figure 5.4 leading to an ONeMg WD. The initial configuration is a 2.2 $M_\odot$ helium star orbiting a 1.35 $M_\odot$ NS with $P_{\rm orb} = 0.30$ d. The Case BB RLO lasts for about 60 000 yr, then terminates for about 30 000 yr until a final vigorous helium shell flash is launched (the spike). The mass-transfer rate is seen to be highly super-Eddington ($\sim 10^3\ \dot{M}_{\rm Edd}$). The horizontal lines mark different values for the accretion efficiency in units of the Eddington accretion rate, $\dot{M}_{\rm Edd}$. Depending on the exact value of $\dot{M}_{\rm Edd}$, and the accretion efficiency, the NS accretes $(0.7-6.4)\times 10^{-3}\ M_\odot$, which is sufficient to recycle PSR J1952+2630 – see text.

The second carbon-burning shell penetrates to the centre of the proto-WD. However, at no point in the modelled evolution of the companion do the carbon burning shells, or the associated convection zones on top of these shells, reach the surface layers of the proto-WD. Therefore, the resulting WD structure is a hybrid, with a large ONeMg core engulfed by a thick CO mantle. The chemical abundance profile of the WD companion at the end of our modelling ($t = 2.892$ Myr) is demonstrated in Figure 5.7. Notice the tiny layer ($2.7 \times 10^{-2}\ M_\odot$) of helium at the surface which gives rise to a vigorous helium shell flash at $t = 2.892$ Myr. This shell flash can also be seen in Figures 5.5 and 5.6 and gives rise to numerical problems for our code. We therefore end our calculations without resolving this flash. However, since the NS is only expected to accrete of the order $\sim 10^{-5}\ M_\odot$ as a result of this flash (based on modelling of similar binaries where we managed to calculate through such a helium shell flash), its impact on the final binary and spin parameters will be completely negligible.

As far as we are aware, this is the first presentation in the literature of detailed calculations leading to an ONeMg WD orbiting a recycled pulsar.

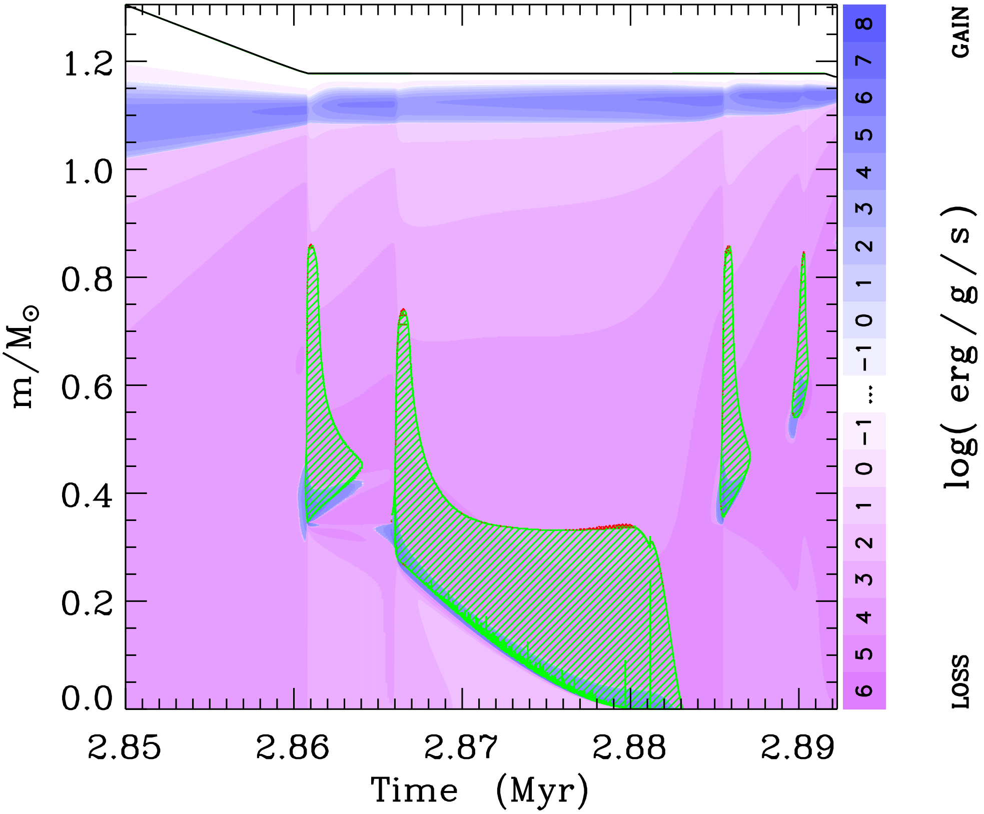

Figure 5.6: The Kippenhahn diagram showing the formation of an ONeMg WD companion to PSR J1952+2630. The plot shows cross-sections of the progenitor star in mass coordinates from the centre to the surface, along the y-axis, as a function of stellar age (since the helium star ZAMS) on the x-axis. Only the last 42 kyr of our calculations are plotted. The Case BB RLO is terminated at time $t = 2.86$ Myr when the progenitor star has reduced its mass to 1.17 $M_{\odot}$. The green hatched areas denote zones with convection. The intensity of the blue/purple colour indicates the net energy production rate; the helium burning shell near the surface is clearly seen at $m/M_{\odot} \simeq 1.1$ as well the off-centred carbon ignition in shells, starting at $m/M_{\odot} \simeq 0.4$, defining the subsequent inner boundaries of the convection zones. The mixing of elements due to convection expands the ONeMg core out to a mass coordinate of about $m/M_{\odot} \simeq 0.85$ (see Figure 5.7). Energy losses due to neutrino emission are quite dominant outside of the nuclear burning shells.

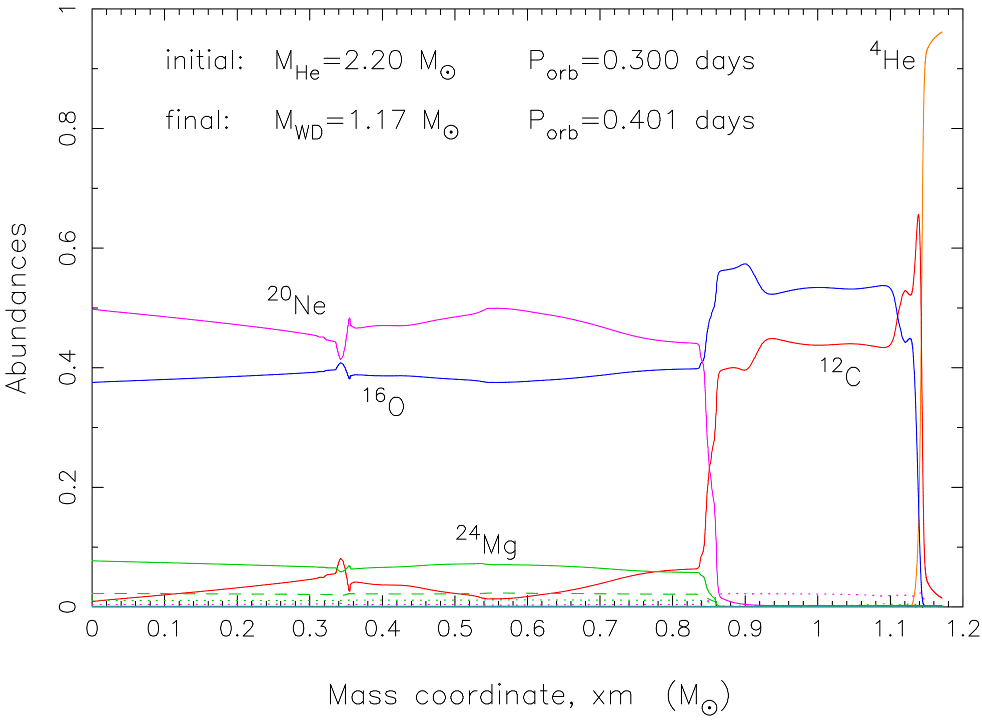

Figure 5.7: The chemical abundance structure of the ONeMg WD remnant (from our last calculated model at t = 2.892 Myr) of the Case BB RLO calculation shown in Figures 5.4–5.6, one of the plausible solutions for PSR J1952+2630's companion found in our modelling. This 1.17 $M_\odot$ WD has a hybrid structure with an ONeMg core enclosed by a CO mantle and a tiny (0.027 $M_\odot$) surface layer of helium.

5.5 *Discussion*

The future and past spin evolution of PSR J1952+2630 can be computed from the measured values of P and $\dot{P}$ and assuming a (constant) braking index, n, which, recalling Eq. 1.3, is defined by $\dot{\nu} = -K\nu^n$, where $\nu = P^{-1}$ and K is a scaling factor. The resulting future and the past spin evolution of PSR J1952+2630 are shown in Figure 5.8, top and bottom panels, respectively.

Given our modelling, the true age of PSR J1952+2630 is $\lesssim$150 Myr. If a cooling age of the WD companion of a pulsar in a similar system were accurately determined (for which the WD mass is needed), it would be possible to constrain the braking index of a recycled pulsar. Although this is not likely possible in the case of PSR J1952+2630 due to its large (DM) distance of 9.6 kpc, it may be feasible for other systems in the future.

The orbital decay due to gravitational wave radiation has also been computed (see Figure 5.8, top panel). It is evident that $P_{\rm orb}$ has hardly decayed since the formation of PSR J1952+2630. § 5.5.1 describes the implication for our binary stellar evolution modelling.

Table 5.2: Equilibrium spin obtained via Case BB RLO

Acc. eff.	$\Delta t_{\rm RLO}$ (kyr)	$\Delta M_{\rm NS}$ ($M_\odot$)	P (ms)
2.2 $M_\odot$ *He star* $\longrightarrow$ 1.17 $M_\odot$ *ONeMg WD*			
30 %	57	0.7×10^{-3}	80
100 %	61	2.1×10^{-3}	35
300 %	61	6.4×10^{-3}	15
1.9 $M_\odot$ *He star* $\longrightarrow$ 1.02 $M_\odot$ *CO WD*			
30 %	113	1.5×10^{-3}	45
100 %	119	4.4×10^{-3}	20
300 %	113	12.4×10^{-3}	9.3

5.5.1 On the Age and Spin Evolution of PSR J1952+2630

Our modelling of binary stellar evolution and accretion physics provides initial conditions for the spin of PSR J1952+2630, which must be consistent with current measurements. In particular, the spin period of PSR J1952+2630 predicted at the termination of accretion must be smaller than the observed spin period.

The minimum equilibrium spin period can be estimated, given the amount of mass accreted by the NS, $\Delta M_{\rm NS}$. This quantity depends on our binary evolution models and the assumed accretion efficiency (in units of $\dot{M}_{\rm Edd}$, see Figure 5.5). Following Eq. 14 of Tauris et al. (2012),

$$P_{\rm ms} = \frac{(M_{\rm NS}/M_\odot)^{1/4}}{(\Delta M_{\rm NS}/0.22\ M_\odot)^{3/4}}, \tag{5.1}$$

where $P_{\rm ms}$ is the equilibrium spin period in units of ms, we estimate the minimum equilibrium spin period of PSR J1952+2630. These results are tabulated in Table 5.2, and compared with PSR J1952+2630's current spin period in Figure 5.8 (bottom panel). It is interesting to notice that we only obtain solutions for an accretion efficiency of 100 or 300 % of $\dot{M}_{\rm Edd}$.[1] If the accretion efficiency is smaller, the equilibrium spin period becomes larger than the present spin period of P = 20.7 ms, which is impossible.

The reason for the possibility of a lower initial spin period in case PSR J1952+2630 has a CO WD companion, is simply that the helium star progenitor of a CO WD has a lower mass and therefore evolves on a longer time-scale, thereby increasing $\Delta M_{\rm NS}$. Hence, a cooling age estimate of the WD companion could, in principle, also help constrain the accretion physics, because it puts limitations on the possible values of the initial spin period.

This is the first time an accretion efficiency has been constrained for a recycled pulsar which evolved via Case BB RLO. In contrast, the accretion efficiency of MSPs formed in LMXBs has been shown to be much lower, about 30 % in some cases (Tauris & Savonije, 1999; Jacoby et al., 2005; Antoniadis et al., 2012). The reason for this difference in accretion efficiencies may be related to the extremely high mass-transfer

---

[1] Solutions requiring larger-than-$\dot{M}_{\rm Edd}$ accretion efficiencies are in fact physically viable because assumptions made during the calculation of $\dot{M}_{\rm Edd}$ mean it is only a rough measure of the true limiting accretion rate.

rates during Case BB RLO which could influence the accretion flow geometry and thus $\dot{M}_{\rm Edd}$. Furthermore, accretion disc instabilities (Lasota, 2001; Coriat et al., 2012), which act to decrease the accretion efficiency in LMXBs, do not operate in Case BB RLO binaries, due to the high value of $|\dot{M}_2|$.

Evolution in the P–$\dot{P}$ Diagram

By integrating the pulsar spin deceleration equation: $\dot{\nu} = -K\nu^n$, assuming a constant braking index, n, we obtain isochrones (i.e. lines of constant pulsar age). The kinematic solution at time t (positive in the future, negative in the past) is given by

$$P = P_0 \left[1 + (n-1)\frac{\dot{P}_0}{P_0}\, t \right]^{1/(n-1)} , \tag{5.2}$$

$$\dot{P} = \dot{P}_0 \left(\frac{P}{P_0} \right)^{2-n} , \tag{5.3}$$

where $P_0 = 20.7$ ms and $\dot{P}_0 = 4.27 \times 10^{-18} \rm s\, s^{-1}$ are approximately the present-day values of the spin period and its derivative. The past and future spin evolution of PSR J1952+2630 in the P–$\dot{P}$ diagram are plotted in Figure 5.9. The isochrones are calculated using Eqs 5.2 and 5.3 where n varies from 2 to 5, for different fixed values of t in the future (rainbow colours) and past (brown). For each isochrone, the time is given by the well-known expression (recall § 1.3 and Eq. 1.4)

$$t = \frac{P}{(n-1)\dot{P}} \left[1 - \left(\frac{P_0}{P} \right)^{n-1} \right] . \tag{5.4}$$

These solutions, however, are purely based on rotational kinematics. As already discussed above, one must take the constraints obtained from binary evolution and accretion physics into account. Therefore, if the Case BB RLO is not able to spin up the pulsar to a value smaller than, for example, 15 ms, then the true age of PSR J1952+2630 cannot be much more than 40 Myr for all values of $2 \leq n \leq 5$. For closer binary systems similar to PSR J1952+2630 where a cooling age determination of the WD is possible, such a measurement could be useful for constraining the birth period of the pulsar, as well as the system's accretion efficiency.

Also shown in Figure 5.9 is the future spin evolution of PSR J1952+2630 until the system merges in about 3.4 Gyr. It is interesting to notice that a system like PSR J1952+2630 should be observable as a radio pulsar binary until it merges, suggesting the existence of similar NS–massive WD binaries with much shorter orbital periods, to which PALFA is sensitive (Chapter 3; Allen et al., 2013). The unique location of PSR J1952+2630 with respect to other known recycled pulsars with a massive WD companion (marked with blue diamonds) is also clear from this figure. It is seen that only three other systems may share a past location in the P–$\dot{P}$ diagram similar to that of PSR J1952+2630 (if $2 \leq n \leq 5$). This could suggest that such surviving post-CE systems are often formed with small values of $P_{\rm orb}$ which cause them to merge rapidly – either during the Case BB RLO or shortly thereafter due to gravitational wave radiation.

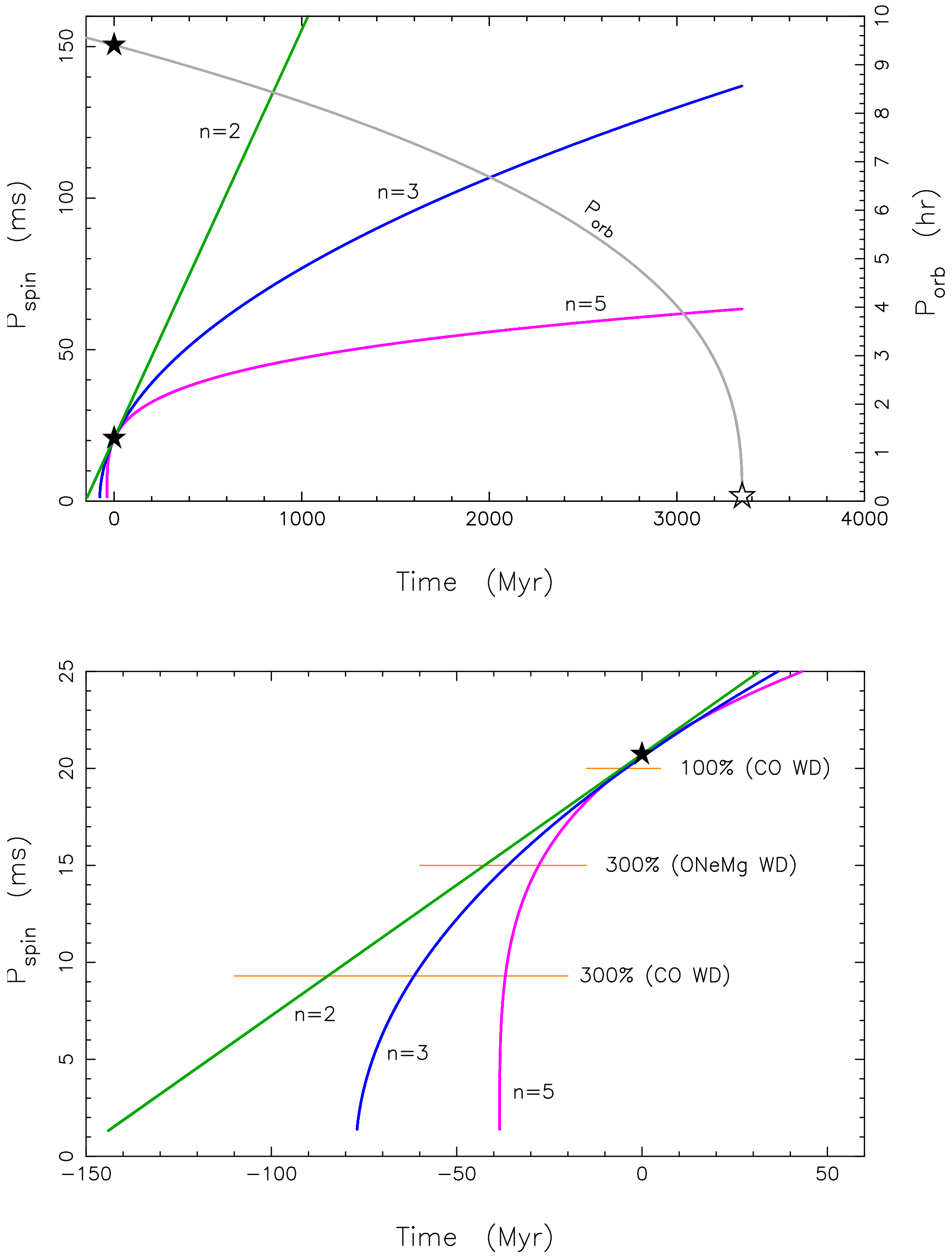

Figure 5.8: The future (top panel) and the past (bottom panel) spin evolution of PSR J1952+2630 for different values of the braking index, n. The location of PSR J1952+2630 at present is marked by a solid star. In the top panel, the grey curve shows the calculated orbital decay due to gravitational wave radiation until the system merges in about 3.4 Gyr (marked by an unfilled star). The lower panel is a zoom-in on the past spin evolution. Depending on n, the WD companion mass and the accretion efficiency of the NS during Case BB RLO, the pulsar could have been spun up to the initial spin periods indicated by the orange horizontal lines – see text for a discussion.

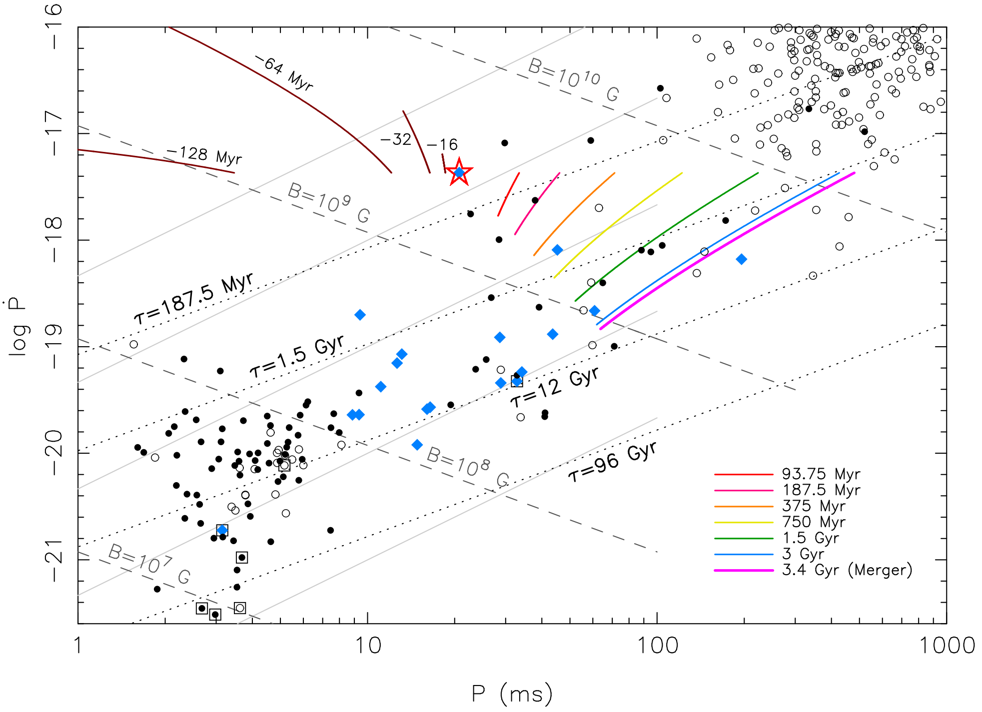

Figure 5.9: Isochrones of past (brown colour) and future evolution (rainbow colours) of PSR J1952+2630 in the P–$\dot{P}$ diagram. The present location is marked by the open red star. All isochrones were calculated for braking indices in the interval $2 \leq n \leq 5$. Also plotted are inferred constant values of B-fields (dashed lines) and characteristic ages, τ (dotted lines). The thin grey lines are spin-up lines with $\dot{M}/\dot{M}_{\rm Edd} = 1$, 10^{-1}, 10^{-2}, 10^{-3} and 10^{-4} (top to bottom), assuming a pulsar mass of $1.4\,M_{\odot}$. Observational data of the plotted Galactic field pulsars are taken from the ATNF Pulsar Catalogue in 2013 March. Binary pulsars are marked with solid circles and isolated pulsars are marked with open circles. For further explanations of the calculations, and corrections to $\dot{P}$ values see Tauris et al. (2012). Binary pulsars with a massive (CO or ONeMg) WD companion are marked with a blue diamond. The past spin evolution of PSR J1952+2630 is particularly interesting as it constrains both the binary evolution and the recycling process leading to its formation – see text.

5.6 Future Prospects for PSR J1952+2630

We now investigate the future use of PSR J1952+2630 as a gravitational laboratory. Looking at Table 5.1, we can see that the eccentricity, e, and longitude of periastron, ω, can be measured quite precisely, in the latter case to within 1.2°, despite the small absolute value of the eccentricity, $4.1(1) \times 10^{-5}$. If we assume a mass of 1.35 $M_{\odot}$ for the pulsar and 1.1 $M_{\odot}$ for the WD, then general relativity (GR) predicts that ω should increase at a rate $\dot{\omega} = 1.72^{\circ}\,{\rm yr}^{-1}$, which, given the precision of ω implies that the effect should be detectable in the next few years. Measuring it will eventually give us an estimate of the total mass of the system (Weisberg & Taylor, 1981).

Furthermore, thanks to PSR J1952+2630's rather short orbital period, the shortest among recycled pulsar–massive WD systems, the rate of gravitational wave emission is much higher than for any other such system. This emission will cause the orbit to

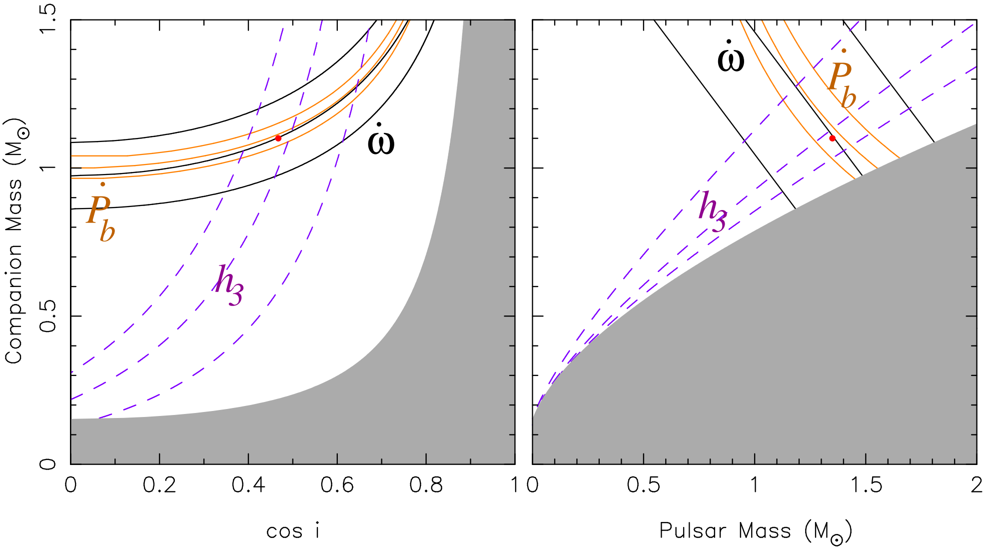

Figure 5.10: Constraints on system masses and orbital inclination from simulated radio timing of PSR J1952+2630. Each triplet of curves corresponds to the most likely value and standard deviations of the respective parameters; the region limited by it is the "$1\,\sigma$" band for that parameter. The masses and inclination used in the simulation are indicated by the red points. Left-hand side: $\cos i$–$M_{\rm WD}$ plane. The grey region is excluded by the condition $M_{\rm NS} > 0$. Right-hand side: $M_{\rm NS}$–$M_{\rm WD}$ plane. The grey region is excluded by the condition $\sin i \leq 1$.

decay. For the same assumptions as above, the orbital period should change at a rate $\dot{P}_{b,\rm pred} = -1.14 \times 10^{-13}\,{\rm s\,s^{-1}}$. As previously mentioned, this will cause the system to merge within about 3.4 Gyr.

The orbital decay due to the emission of gravitational waves is not measurable at present, but it should be detectable in the near future. In order to verify this, we made simulations of future timing of this pulsar that assume similar timing precision to that at present (a single 18-μs TOA every 15 min for each of two 300-MHz bands centred around 1400 MHz). We assume two campaigns in 2015 and 2020, where the full orbit is sampled a total of eight times, spread evenly for each of those years. The total observing time of 72 h for each of those years is a realistic target. These simulations indicate that by the year 2020 $\dot{P}_b$ should be detectable with $12\,\sigma$ significance and $\dot{\omega}$ to about $9\,\sigma$ significance.

The resulting constraints on the masses of the components and system inclination are depicted graphically in Figure 5.10. We plot the $1\,\sigma$ bands allowed by the 'measurement' of a particular parameter. The figure shows several interesting features. The first is that even with these measurements of $\dot{P}_b$ and $\dot{\omega}$, it is not possible to determine the two masses accurately from them, given the way their $1\,\sigma$ uncertainty bands intersect in the mass–mass diagram. The $1\,\sigma$ band of h_3 (the orthometric amplitude of the Shapiro delay, see Freire & Wex 2010) intersects the others at a rather sharp angle and can in principle be used to determine the masses more accurately. However, at the moment it is not clear whether h_3 is precisely measurable. A more massive companion in a less inclined orbit yields more pessimistic expectations, as depicted in Figure 5.10.

Fortunately, very precise masses are not required to perform a test of GR using $\dot{\omega}$ and $\dot{P}_b$. As illustrated in Figure 5.10, the bands allowed by $\dot{\omega}$ and $\dot{P}_b$ are nearly parallel. As the precision of these measurements improves, GR is tested by the requirement that the two bands still overlap. Figure 5.10 also shows that even if we could determine h_3 precisely, the precision of this $\dot{\omega}$-h_3-$\dot{P}_b$ test will be limited by the precision of the measurement of $\dot{\omega}$, because its uncertainty only decreases with $T^{-3/2}$ (where T is the timing baseline), while for $\dot{P}_b$ the measurement uncertainty decreases with $T^{-5/2}$.

Eventually, though, the uncertainty of the measurement of $\dot{\omega}$ will become very small. At that stage, the precision of this test will be limited by the precision of $\dot{P}_b$, which is limited by the lack of precise knowledge of the kinematic contributions (Damour & Taylor, 1991),

$$\left(\frac{\dot{P}_b}{P_b}\right) = \left(\frac{\dot{P}_b}{P_b}\right)_{\rm obs} - \frac{\mu^2 d}{c} - \frac{a(d)}{c}, \tag{5.5}$$

where the subscript ‘obs’ indicated the observed quantity, μ is the total proper motion, d is the distance to the pulsar and $a(d)$ is the (distance-dependent) difference between the Galactic acceleration of the system and that of the Solar System barycentre (SSB), projected along the direction from the SSB to the system. At present, these cannot be estimated because the proper motion has not yet been measured precisely. However, they likely represent the ultimate constraint to the precision of this GR test, as in the case of PSR B1913+16 (Weisberg et al., 2010). For that reason, we now estimate the magnitude of these kinematic effects.

If we assume that the final proper motion is of the same order of magnitude as what is observed now ($\sim$6 mas yr^{-1}), then at the assumed DM distance of 9.6 kpc the kinematic contribution to $\dot{P}_b$ will be about $3 \times 10^{-14}\,\mathrm{s\,s^{-1}}$. This is four times smaller than $\dot{P}_{b,\rm pred}$, as defined above, which means that if we cannot determine the distance accurately, then the real value for the intrinsic orbital decay, $\dot{P}_{b,\rm int}$, cannot be measured with a relative precision better than about 25 %. Things improve if the proper motion turns out to be smaller.

Is such a measurement useful? Surprisingly the answer is that it is likely to be so. For pulsar–WD systems, alternative theories of gravity, like scalar–tensor theories (see Damour & Esposito-Farèse, 1998, and references therein), predict the emission of dipolar gravitational waves, which would result in an increased rate of orbital decay. In the case of PSR J1738+0333, the orbital decay for that system was measured only with a significance of $8\,\sigma$. However, the absolute difference between the $\dot{P}_b$ predicted by GR and the observed value is so small that it introduces the most stringent constraints ever on these gravity theories (Freire et al., 2012). The implication is that for PSR J1952+2630, one should be able to derive similarly low limits. However, if the proper motion is significantly smaller, and/or if we are able to determine the distance independently, then this system can provide a much more stringent test of alternative theories of gravity. The main reason for this is that the limiting factor of the PSR J1738+0333 test is the limited precision in the measurement of the component masses (Antoniadis et al., 2012) which would not be an issue for PSR J1952+2630, given the tighter constraints on the total mass that will eventually be derived from $\dot{\omega}$.

5.7 Conclusions

We have presented phase-coherent timing of PSR J1952+2630. Our timing model includes precise determinations of parameters describing the pulsar spin-down, astrometry and binary motion. No post-Keplerian orbital parameters are required. However, detailed modelling suggests the current pulsar–massive WD binary system evolved via post-CE Case BB RLO with an accretion efficiency which exceeded the Eddington limit by a factor of $1-3$. We presented, for the first time, a detailed chemical abundance structure of an ONeMg WD orbiting a pulsar.

By projecting PSR J1952+2630's orbital evolution into the future, we estimate it will merge with its WD companion in $\sim$3.4 Gyr due to the orbital decay from gravitational wave emission. Unfortunately, PSR J1952+2630 is too distant to make a detection of the cooling age of the pulsar's WD companion. In the case of the discovery of a less distant analog of PSR J1952+2630, such a measurement could make it possible to constrain the braking index of the recycled pulsar, and/or the accretion efficiency during the Case BB RLO-phase. Also, timing observations over the next 10 yr will result in the detection of the advancement of periastron, and the orbital decay, enabling a test of GR. Finally, additional timing may also further elucidate the nature of the companion, and will permit PSR J1952+2630 to be used to perform gravitational tests.

6

PROSPECTS FOR HIGH-PRECISION PULSAR TIMING WITH THE NEW EFFELSBERG PSRIX BACKEND

This chapter is based on an article published in the Monthly Notices of the Royal Astronomical Society. Information about the article can be found online at:

http://adsabs.harvard.edu/abs/2016MNRAS.458..868L

The text, figures, and tables have only been modified to match the style, spelling and format of the rest of this thesis.

I am the lead author of the article. My main contributions include developing the data reduction pipeline, including `CoastGuard` *and most of* `TOASTER`*. I also reduced the PSRIX data, and compared the results with the reduced EBPP data. I conducted and reduced the high-frequency observations, and evaluated the potential of using various receivers and telescopes.*

The full list of authors is:

P. Lazarus, R. Karuppusamy, E. Graikou, R. N. Caballero, D. J. Champion, K. J. Lee, J. P. W. Verbiest, and M. Kramer

Abstract

The PSRIX backend is the primary pulsar timing instrument of the Effelsberg 100-m radio telescope since early 2011. This new ROACH-based system enables bandwidths up to 500 MHz to be recorded, significantly more than what was possible with its predecessor, the Effelsberg–Berkeley Pulsar Processor (EBPP). We review the first four years of PSRIX timing data for 33 pulsars collected as part of the monthly European Pulsar Timing Array (EPTA) observations. We describe the automated data analysis pipeline, `CoastGuard`, that we developed to reduce these observations. We also introduce `TOASTER`, the EPTA timing database used to store timing results, processing information and observation metadata. Using these new tools, we measure the phase-averaged flux densities at 1.4 GHz of all 33 pulsars. For seven of these pulsars, our flux density measurements are the first values ever reported. For the other 26 pulsars, we compare our flux density measurements with previously published values. By comparing PSRIX data with EBPP data, we find an improvement of $\sim 2-5$ times in signal-to-noise ratio, which translates to an increase of $\sim 2-5$ times in pulse time-of-arrival (TOA) precision. We show that such an improvement in TOA precision will improve the sensitivity to the stochastic gravitational wave background. Finally, we showcase the flexibility of the new PSRIX backend by observing several millisecond-period pulsars (MSPs) at 5 and 9 GHz. Motivated by our detections, we discuss the potential for complementing existing pulsar timing array data sets with MSP monitoring campaigns at these higher frequencies.

6.1 Introduction

Pulsars are extremely useful tools for studying various fields of astrophysics. Many important results are the product of regular timing campaigns that are used to determine models of pulsars' spin capable of accounting for every rotation of the star. High-precision timing observations of millisecond-period pulsars (MSPs) have proven to have a large number of diverse applications, such as testing of relativistic gravity (e.g. Kramer et al., 2006b), constraining the equation-of-state of ultra-dense matter (e.g. Demorest et al., 2010), and studying binary stellar evolution (e.g. Freire et al., 2011). In general, studies of radio pulsars have also been used to probe the interstellar medium (ISM; e.g. Bhat et al., 1998; Berkhuijsen & Müller, 2008; Eatough et al., 2013b). Furthermore, collections of MSPs are being observed regularly as part of so-called pulsar timing array (PTA) projects, which have the ultimate goal of detecting low-frequency gravitational waves (GW), possibly arising from the cosmic population of supermassive black hole binaries (e.g. Sesana, 2013b) or from cosmic strings (e.g. Sanidas et al., 2012).

To maximize the scientific potential of pulsar timing observations, high signal-to-noise ratio (S/N) observations are required to determine pulse times of arrival (TOAs) precisely. Given a telescope, the S/N can be improved either by increasing the integration time, which is limited by the total available telescope time and the number of pulsars to observe, or by using more sensitive and/or wider bandwidth receivers. In order to fully leverage wider bandwidths, instruments capable of processing the increased frequency range must be used.

The Effelsberg–Berkeley Pulsar Processor (EBPP) coherent dedispersion backend (Backer et al., 1997) has been running since 1995. Its long, uniform data sets for some MSPs have enabled unique studies. For example, Shao et al. (2013) used EBPP data to constrain profile variations in MSPs, and thus improve limits on the violation of local Lorentz invariance of gravity by several orders of magnitude relative to previously published limits (see Will, 1993, and references therein). The EBPP data set has also been a key component of several European Pulsar Timing Array (EPTA) projects, such as characterizing the noise properties of MSPs (Caballero et al., 2015), constraining the low-frequency gravitational wave background (GWB; Lentati et al., 2015), and searching for single sources of gravitational waves (GWs Babak et al., 2016).

The EBPP is beginning to show its age. For instance, the EBPP bandwidth is limited to only $\sim$64 – 128 MHz, depending on the integrated Galactic electron content along the line-of-sight to the pulsar (i.e. the pulsar's dispersion measure, DM), whereas most current receiver systems operating in the 1 – 3 GHz band can simultaneously observe bandwidths of 200 – 800 MHz (e.g. the Greenbank Ultimate Pulsar Processing Instrument – GUPPI – used at the Green Bank Telescope, and its similarly named clones PUPPI[1] at Puerto Rico's Arecibo Observatory and NUPPI[2] at the Nançay observatory in France; Ford et al., 2010), and in the case of the Ultra-Broadband (UBB) receiver at Effelsberg, $\sim$2600 MHz. Furthermore, the EBPP hardware is becoming increasingly unreliable, and replacement parts are increasingly difficult to come by.

For these reasons, the EBPP backend was replaced as the main data recorder for pulsar timing observations at Effelsberg by the PSRIX backend in 2011 March. PSRIX is built around a Reconfigurable Open Architecture Computing Hardware (ROACH) system, a programmable platform designed by the Collaboration for Astronomy Signal Processing and Electronics Research (CASPER).[3] The EBPP is still run in parallel with PSRIX whenever possible.

PSRIX was originally designed as part of the Large European Array for Pulsars (LEAP) project (Bassa et al., 2016), which has the objective of coherently combining signals from the five largest European radio telescopes.[4] To meet this goal, the primary mode of operation of PSRIX is to record baseband data; however, additional modes were implemented to record coherently dedispersed profiles folded in real time and coherently dedispersed single pulses. PSRIX's coherent-dedispersion modes support bandwidths up to 500 MHz and are flexible

---

[1] The Puerto Rico Ultimate Pulsar Processing Instrument.

[2] The Nançay Ultimate Pulsar Processing Instrument.

[3] https://casper.berkeley.edu/

[4] Specifically, the Lovell Telescope, the Westerbork Synthesis Radio Telescope, the Nançay Telescope, the Sardinia Radio Telescope, and Effelsberg.

enough to observe at different frequencies, taking advantage of Effelsberg's many receivers. Technical details of the backend design and the implementation of its various modes of operation will be described in a future paper.

Thanks to the increased bandwidth and more robust design of PSRIX compared to the EBPP, the timing campaigns undertaken at Effelsberg using PSRIX are producing data of superior quality, thus enabling even higher-precision timing studies than previously possible. Moreover, PSRIX may further improve the prospects of high-precision timing at Effelsberg by making it possible to conduct timing observations of MSPs at 5 GHz and higher, helping to mitigate noise arising from variations of the ISM along the line of sight towards the pulsar, a serious impediment to searches for GWs with Pulsar Timing Arrays (PTAs).

The EPTA has previously incorporated the ∼17-year-long EBPP data set into its timing analyses and GW searches (e.g. Janssen et al., 2008; Lazaridis et al., 2009, 2011; Lentati et al., 2015; Desvignes et al., 2016). Here we describe the PSRIX data and its analysis, which will be included in future EPTA projects and be shared with the International Pulsar Timing Array (IPTA) collaboration (Verbiest et al., 2016).

In addition to the monthly observing sessions of many binary pulsars and MSPs, several pulsars have been the target of dedicated observing campaigns with PSRIX over the past four years. In particular, PSRIX data were included in the IPTA effort to observe PSR J1713+0747 continuously for 24 h using the largest radio telescopes around the Earth (Dolch et al., 2014). Also, PSR J0348+0432, a $2\,M_\odot$ pulsar in a ∼2.5 h relativistic binary with a white-dwarf companion (Antoniadis et al., 2013; Lynch et al., 2013), has been regularly observed for full orbits using PSRIX. Several full-orbit observing campaigns of PSR J1518+4904, a 41 ms pulsar in an 8.6 d double-neutron-star binary, have been conducted with PSRIX to precisely measure the mass of the pulsar and its companion (Janssen et al., in prep.).

The remainder of this chapter is organized as follows. § 6.2 describes the monthly EPTA observations undertaken with the Effelsberg telescope using PSRIX. The analysis of these observations is detailed in § 6.3, and includes an overview of the automated data reduction suite `CoastGuard`, as well as the timing database `TOASTER`. Flux density measurements for 33 pulsars at 1.4 GHz and a comparison between PSRIX and the old EBPP backends are presented in § 6.4, as are the results of observations at 5 and 9 GHz. The results are discussed in § 6.5 and this work is finally summarized in § 6.6.

6.2 Observations

Every month, the Effelsberg radio telescope is used to observe bright, stable MSPs as part of the EPTA project. These observations are conducted with PSRIX in its coherent-dedispersion real-time folding mode, evenly dividing the pulse profiles into 1024 phase bins. Each session typically consists of observations at both 1.4 and 2.6 GHz (wavelengths of 21 and 11 cm, respectively). The 1.4-GHz observations use either the central feed of the 7-beam receiver (called "P217mm") or the single-feed 1.4 GHz receiver ("P200mm").[1] Both of these 1.4-GHz receivers are situated in the primary focus of the Effelsberg telescope. Only one of the 1.4-GHz receivers is installed for any given observing session. We use whichever receiver is available. The 2.6-GHz observations are done with the "S110mm" secondary-focus receiver. PSRIX is used to record a 200-MHz band, which is divided into eight 25-MHz sub-bands. In the case of P200mm and S110mm observations, this exceeds the available bandwidths of 140 MHz and 80 MHz, respectively. See Table 6.1 for details of the observing set-ups used. All of the receivers used in this work have circularly polarized feeds.

Whenever possible, we record data with the EBPP coherent-dedispersion pulsar timing backend in parallel with PSRIX. This enables for a more accurate determination of the time

---

[1] http://www.mpifr-bonn.mpg.de/effelsberg/astronomen

Table 6.1: Observing Set-Ups Used

Parameter	Receiver P200mm	 P217mm (Central beam)	 S110mm	 S60mm	 S36mm
Low freq. (MHz)	1290	1240	2599.5	4600	7900
High freq. (MHz)	1430	1480	2679.5	5100	9000
Recorded BW (MHz)[a]	200	200	200	500	500
Centre freq. (MHz)[b]	1347.5	1347.5	2627	4857.8	8357.8
System temp. (K)	21, 27[c]	23	17	27	22
Gain (K/Jy)	1.55	1.37	1.5	1.55	1.35
No. of sub-bands	8	8	8	32	32

Note. — All of these receivers have circularly polarized feeds. Also, in all cases, 1024 phase bins were recorded across each pulse profile.

[a] For receivers where the recorded bandwidth exceeds the available bandwidth, extra channels consisting of noise are included in the file. These are later removed (see § 6.3.1).

[b] The centre of the recorded band.

[c] The reported temperatures for the two polarization channels.

offset between the two instruments. We have also used these simultaneous observations to characterize the improvement of PSRIX over the EBPP (see § 6.4.3).

Our monthly EPTA observing sessions typically consist of 24 h at 1.4 GHz and 12 – 24 h at 2.6 GHz. Each observing session includes pulsar observations of ∼30 – 60 min in duration. Polarization calibration scans are conducted prior to each pulsar observation and each consist of a 2-min integration of the receiver noise diode offset by 0.5° from the pulsar position. The diode is pulsed with a 1-s repetition rate and a 50% duty cycle.

Since 2013, at 1.4 GHz, we also performed on- and off-source scans of a radio source with a stable, well-known flux density, usually 3C 218 (i.e. Hydra A). These flux calibration observations use the noise diode as described above.

Every month, we observe ∼45 pulsars at 1.4 GHz and ∼20 pulsars at 2.6 GHz. Pulsars that are never, or rarely, detected at 2.6 GHz during a 6 – 12 month probationary period are dropped from the regular observing schedule. Here we focus on the data sets of 33 MSPs and binary pulsars acquired between 2011 and 2015. Tables 6.2 and 6.3 show a summary of our 1.4 and 2.6 GHz observations of these pulsars, respectively.

As we will discuss in § 6.5.2, since ISM effects weaken with increasing radio frequency, high-frequency observations of pulsars may be extremely useful to avoid and mitigate the effects of variability in the ISM, which limit the sensitivity of attempts at detecting GWs with pulsars. In 2015 January, we conducted observations of 12 MSPs at 5 GHz (6 cm) using the "S60mm" secondary-focus receiver with the aim of assessing their utility to the PTAs. We used PSRIX in its 500-MHz coherent-dedispersion real-time folding mode for these observations. We also observed three of these pulsars at 9 GHz (3.6 cm) with the "S36mm", also a secondary-focus receiver, again with 500 MHz of bandwidth. Our high-frequency observations are listed in Table 6.5. We selected the pulsars for these exploratory high-frequency observations based on their 1.4 and 2.6 GHz detection significances, which we scaled to higher frequencies using the radiometer equation, the receiver performance, and published spectral indices.[1] Specifically, we required an estimated $S/N \gtrsim 10$ for a 30-min observation when selecting pulsars for the preliminary 5 and 9-GHz observations reported here. High-frequency observations of other (fainter) MSPs are being conducted and will be reported elsewhere.

---

[1] For pulsars without spectral indices available in the literature, we used a spectral index of $\alpha = -2$ for our estimates.

Table 6.2: Summary of monthly observations of EPTA pulsars at 1.4 GHz

Pulsar	Period (ms)	DM ($\mathrm{pc\,cm^{-3}}$)	Obs. Span (YYYY/MM)	$N_{\mathrm{obs.}}$	$N_{\mathrm{det.}}$	$\langle S/N \rangle$ [a]
J0023+0923	3.05	14.3	2012/03 – 2014/10	37	32	32
J0030+0451	4.87	4.3	2011/05 – 2015/02	46	46	48
J0218+4232	2.32	61.3	2011/04 – 2015/02	48	48	61
J0340+4129	3.30	49.6	2011/04 – 2015/02	44	44	34
J0348+0432	39.12	40.5	2011/07 – 2015/04	354	231	38
J0613−0200	3.06	38.8	2011/03 – 2015/02	62	61	133
J0621+1002	28.85	36.6	2011/03 – 2015/02	56	55	92
J0751+1807	3.48	30.2	2011/01 – 2015/02	89	81	106
J1012+5307	5.26	9.0	2011/03 – 2015/02	58	55	173
J1022+1001	16.45	10.3	2011/01 – 2015/02	119	114	308
J1024−0719	5.16	6.5	2011/03 – 2015/02	60	57	113
J1518+4904	40.93	11.6	2011/03 – 2014/10	226	190	379
J1600−3053	3.60	52.3	2011/03 – 2015/02	45	45	136
J1640+2224	3.16	18.4	2011/03 – 2015/02	83	72	66
J1643−1224	4.62	62.4	2011/03 – 2015/02	47	47	276
J1713+0747	4.57	16.0	2011/03 – 2015/02	105	96	746
J1730−2304	8.12	9.6	2011/03 – 2015/02	50	48	239
J1738+0333	5.85	33.8	2011/06 – 2015/02	37	36	44
J1741+1351	3.75	24.0	2011/10 – 2015/02	38	36	29
J1744−1134	4.07	3.1	2011/03 – 2014/12	49	48	193
J1853+1303	4.09	30.6	2013/05 – 2015/02	20	18	34
B1855+09	5.36	13.3	2011/03 – 2015/02	47	45	177
J1911+1347	4.63	31.0	2013/05 – 2015/02	22	21	57
J1918−0642	7.65	26.6	2011/03 – 2015/02	45	45	67
B1937+21	1.56	71.0	2011/03 – 2015/02	84	75	524
J2010−1323	5.22	22.2	2012/09 – 2015/02	25	24	70
J2017+0603	2.90	23.9	2011/04 – 2015/02	44	36	25
J2043+1711	2.38	20.7	2011/04 – 2015/02	44	19	15
J2145−0750	16.05	9.0	2011/03 – 2015/02	52	50	382
J2229+2643	2.98	23.0	2011/03 – 2015/02	48	40	98
J2234+0944	3.63	17.8	2011/11 – 2014/10	42	39	62
J2317+1439	3.45	21.9	2011/03 – 2015/02	52	46	54
J2322+2057	4.81	13.4	2013/07 – 2015/02	21	17	20

[a] Mean S/N, computed using S/N values only from observations longer than 20 minutes and scaled to a canonical integration time of 30 minutes.

6.3 Data Analysis

6.3.1 CoastGuard: An Automated Timing Data Reduction Pipeline

We developed an automated pipeline, `CoastGuard`,[1] to reduce PSRIX data. `CoastGuard` is written in python and is largely built around programs from the `psrchive` package[2] (Hotan et al., 2004a), using its python wrappers to read PSRIX data files, which are `psrchive`-compatible. `CoastGuard` contains components that are sufficiently general for use with `psrchive`-compatible data files from other observing systems despite that it was primarily designed for Effelsberg PSRIX data. In particular, the radio frequency interference (RFI) removal algorithm described below has been applied to data from the Parkes Telescope (Ng et al., 2014) and has also been adopted by the Low-Frequency Array (LOFAR) pulsar timing data reduction pipeline (Kondratiev et al., 2015).

`CoastGuard` contains considerable error checking, logging, logistics, and control logic required to automate large portions of the pipeline, which is marshalled by a control script

---

[1] Available at https://github.com/plazar/coast_guard

[2] http://psrchive.sourceforge.net/

Table 6.3: Summary of monthly observations of EPTA pulsars at 2.6 GHz

Pulsar	Period (ms)	DM ($\mathrm{pc\,cm^{-3}}$)	Obs. Span (YYYY/MM)	$N_{\mathrm{obs.}}$	$N_{\mathrm{det.}}$	$\langle S/N \rangle$ [a]
J0023+0923	3.05	14.3	2012/03 – 2014/10	28	3	14
J0030+0451	4.87	4.3	2011/05 – 2015/02	40	34	13
J0218+4232	2.32	61.3	2011/05 – 2015/02	17	0	–
J0340+4129	3.30	49.6	2011/05 – 2015/02	36	13	10
J0613−0200	3.06	38.8	2011/03 – 2015/02	42	37	20
J0621+1002	28.85	36.6	2011/03 – 2015/02	39	29	15
J0751+1807	3.48	30.2	2011/03 – 2015/02	49	35	30
J1012+5307	5.26	9.0	2011/03 – 2015/02	48	46	39
J1022+1001	16.45	10.3	2011/03 – 2015/02	60	54	109
J1024−0719	5.16	6.5	2011/05 – 2015/02	46	39	20
J1518+4904	40.93	11.6	2011/03 – 2014/06	7	6	63
J1600−3053	3.60	52.3	2011/05 – 2014/12	31	29	25
J1640+2224	3.16	18.4	2011/06 – 2015/02	48	32	13
J1643−1224	4.62	62.4	2011/05 – 2015/01	36	36	57
J1713+0747	4.57	16.0	2011/05 – 2015/02	46	44	258
J1730−2304	8.12	9.6	2011/05 – 2015/02	35	24	48
J1738+0333	5.85	33.8	2011/06 – 2015/01	9	2	32
J1741+1351	3.75	24.0	2012/01 – 2015/02	35	15	17
J1744−1134	4.07	3.1	2011/05 – 2015/01	39	37	27
J1853+1303	4.09	30.6	2013/05 – 2015/02	24	6	10
B1855+09	5.36	13.3	2011/03 – 2015/02	43	35	46
J1911+1347	4.63	31.0	2013/05 – 2015/02	22	17	14
J1918−0642	7.65	26.6	2011/05 – 2015/02	41	24	22
B1937+21	1.56	71.0	2011/03 – 2015/02	54	48	87
J2010−1323	5.22	22.2	2012/09 – 2015/02	26	18	17
J2017+0603	2.90	23.9	2011/07 – 2015/02	16	1	11
J2043+1711	2.38	20.7	2011/05 – 2015/02	17	1	6
J2145−0750	16.05	9.0	2011/03 – 2015/02	47	45	70
J2229+2643	2.98	23.0	2011/03 – 2015/02	46	35	25
J2234+0944	3.63	17.8	2011/11 – 2014/10	36	28	21
J2317+1439	3.45	21.9	2011/03 – 2015/02	43	28	14
J2322+2057	4.81	13.4	2013/07 – 2015/02	16	3	8

[a] Mean S/N, computed using S/N values only from observations longer than 20 minutes and scaled to a canonical integration time of 30 minutes.

and a MySQL database.

In its coherent-dedispersion real-time folding mode the PSRIX backend writes data files every 10 s for each 25-MHz sub-band. These fragments are then grouped together and combined using `psradd`. At this stage, the data are re-aligned using an up-to-date pulsar ephemeris, if necessary, and 6.25 % of the channels at the edge of each sub-band are zero-weighted to reduce the effect of aliasing.

Next, the metadata stored in these consolidated files are cross-checked against telescope observing logs and all discrepancies are corrected. This is primarily to repair issues with the observation metadata that were common during the commissioning of PSRIX. These issues have since been resolved.

The data files are then cleaned of RFI. In the pipeline, our cleaning process excludes RFI by setting the weights of individual profiles to zero. That is, the data from RFI-affected sub-integration/channel combinations are ignored in the rest of the analysis without altering the data values. Therefore, it is possible to reverse the automated RFI masking.

`CoastGuard`'s RFI-excision script, `clean.py`, includes four distinct algorithms that can be chained together to clean corrupted data. Each algorithm has several parameters that can be used to optimize its performance. In our automated data analysis, we use two of the four available cleaning algorithms, namely `rcvrstd` and `surgical`. The other two algorithms, `bandwagon` and `hotbins`, are occasionally applied manually to observations requiring special attention. Our standard RFI-excision algorithm proceeds as follows:

First, `clean.py`'s `rcvrstd` algorithm is used to zero-weight frequency channels beyond the receiver response and channels falling within a list of receiver-dependent bad frequency intervals.

Second, the `surgical` algorithm is used to find profiles corrupted by RFI in the folded data cube. To avoid being biased by the presence of the pulsar signal, the amplitude and phase of the integrated pulse profile is fit using a least-squares algorithm to individual profiles containing a significant detection and the difference is computed. It is these pulsar-free residuals that are treated in the remainder of the algorithm. Next, RFI-contaminated data are identified with a set of four metrics, which are computed for each sub-integration/channel pair (i.e. each total-intensity profile stored in the data file). These metrics are: (1) the standard deviation, (2) the mean, (3) the range, and (4) the maximum power of the Fourier transform of the mean-subtracted residuals. These four metrics were selected due to their sensitivity to the RFI signals present in Effelsberg data, which include, but are not limited to: excess noise, occasional data drop-outs, and infrequently, rapid (sub-ms) periodic bursts. For each metric, a $N_{\rm sub} \times N_{\rm chan}$-sized matrix of values is produced. Trends in the rows and columns of these matrices are removed by subtracting piece-wise quadratic functions that were fit to the data. The subtraction of these trends account for slow variations in time, as well as the shape of the bandpass. These rescaled matrices are then searched for outliers, which are defined as being $>5\,\sigma$ from the median of either their sub-integration or channel. Finally, profiles that are identified as an outlier by at least two of the four metrics are zero-weighted.

The `bandwagon` algorithm completely removes sub-integrations and channels that already have a sufficiently large fraction of data masked, and the `hotbins` algorithms replaces outlier off-pulse profile phase-bins with locally sourced noise.[1] Neither of these two algorithms are part of our standard automated data reduction.

Once the observations are cleaned, they are reviewed before proceeding with the rest of the automated analysis. This is to identify observations that still need to be cleaned manually. In practice, only a small fraction of observations require additional RFI zapping. This quality-control stage also provides an opportunity to identify observations where the pulsar is not detected or where the data are contaminated by RFI beyond repair. Observations falling into these two categories do not continue further in the data reduction process.

The above data reduction process (combine, correct, clean, quality control) is also applied to polarization calibration scans of the noise diode. The cleaned and vetted calibration scans are fully time-integrated, and then loaded into the appropriate `psrchive pac`-compatible "database" files. The pipeline maintains one calibration database file for each pulsar.

Polarization calibration of the cleaned pulsar data files is performed with `psrchive`'s `pac` program,[2] using its "SingleAxis" algorithm, which appropriately adjusts the relative gain and phase difference of the two polarization channels by applying the technique of Britton (2000). These calibrated observations are manually reviewed a second time to verify that no artifacts have been introduced.

Flux calibration has not been incorporated into the automated data analysis pipeline. Nevertheless, we have manually performed flux calibration wherever possible. In our analysis, we used `psrchive`'s `fluxcal` and `pac` programs. `fluxcal` compares the power levels of on- and off-source observations of a standard candle target to determine the system equivalent flux density over the observing band. This information is used to determine the flux density scale of the polarization-calibrated pulsar observations.

---

[1] Because the `hotbins` algorithm replaces data, it is irreversible.

[2] http://psrchive.sourceforge.net/manuals/pac/

For this work, we refolded all data with up-to-date ephemerides.

6.3.2 TOASTER: The TOAs Tracker Database

We have developed a python package, TOAS TrackER (`TOASTER`),[1] for computing and storing TOAs in a fully described and reproducible way. At its core, `TOASTER` consists of an SQL database and full-featured python toolkit for reliably interacting with the data and database.

Beyond simply storing TOA information, `TOASTER`'s database also records information about telescopes and observing systems, observation information (e.g. frequency, epoch, integration time, the ephemeris used for folding), the standard profile used to determine each TOA, as well as version numbers of relevant software, such as `psrchive` and `TEMPO2` (Hobbs et al., 2006).

Once the database is populated, `TOASTER` can also launch TOA generation processes that use a variety of "manipulators" to prepare the data prior to automatically computing TOAs using standard `psrchive` tools. The most basic manipulator fully integrates data in frequency and time. However, more sophisticated manipulations can be included to adjust the data according to an updated, possibly time-varying DM, integrate a fixed number of pulses or variable number of pulses depending on the resulting S/N. Manipulators can also be used to scale the measured profiles to have uniform off-pulse variance, as was done by (Arzoumanian et al., 2015). Typically these types of manipulations are included in the data reduction pipelines that prepare observations prior to determining TOAs. By performing these data reduction steps in `TOASTER`, the details of the manipulations performed on the data and the resulting TOAs are logged in the database, making it easy to store the resulting TOAs, as well as systematically compare the effect of different manipulations on the eventual timing analysis. Furthermore, the `TOASTER` database includes a reference to the template used to compute each TOA. The end result is a completely described and reproducible TOA-generation procedure. This makes `TOASTER` a useful tool for high-precision timing projects like the EPTA and IPTA that are constantly adding new data, as well as developing new data reduction algorithms.

The `TOASTER` toolkit scripts can be used to easily query the information stored in its database. For example, `TOASTER` provides scripts to list and summarize the TOAs in the database. These scripts can also be used to generate TOA files in multiple formats, including a `TEMPO2` format that includes all the annotations ("TOA flags") requested by the IPTA.

`TOASTER` can be used to load TOAs directly into the database (i.e. without information concerning the observations, templates, etc.). This feature is useful for including previously computed, and finalized, data sets, such as the EPTA legacy TOAs (Desvignes et al., 2016).

We set up the `TOASTER` software and database to manage the reduced (i.e. cleaned and calibrated) PSRIX data, which are automatically loaded into the `TOASTER` database by the data reduction pipeline described in § 6.3.1.

6.4 Results

Over the past four years, we have collected timing data on 45 pulsars at 1.4 and 2.6 GHz using the PSRIX backend with the 100-m Effelsberg radio telescope. Here we report on a selection of 33 pulsars. Most of these pulsars have been monitored monthly in both bands for the entire four-year period. An overview of our 1.4 and 2.6 GHz observations can be found in Tables 6.2 and 6.3, respectively.

6.4.1 Flux Density Measurements

We measured flux densities for all 33 pulsars at 1.4 GHz. For each pulsar, we report the mean flux density, $\langle S \rangle$, and the median flux density, S_{med}, to account for observed modulation due

---

[1] `TOASTER` and its documentation are publicly available at https://github.com/plazar/toaster

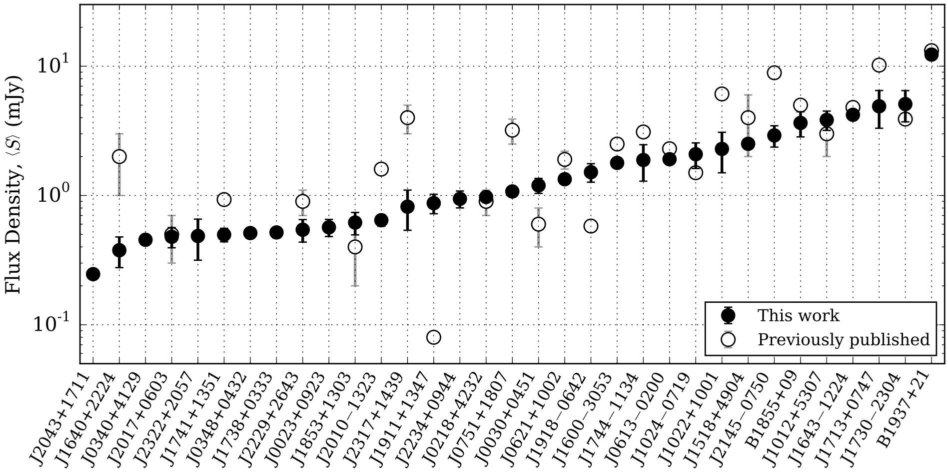

Figure 6.1: Measured 1.4 GHz flux densities of 33 pulsars estimated from averaging over multiple PSRIX observations (filled circles). The uncertainties are estimated as the standard error on the mean (see Eq. 6.1). Additional details of the calibration process can be found in §§ 6.3 and 6.4.1. The previously published flux densities (unfilled circles) do not all have properly measured uncertainties. See Table 6.4 for notes and references.

to interstellar scintillation. We estimate the precision of the mean flux densities as the standard error on the mean, that is,

$$\delta \langle S \rangle = \sigma_S / \sqrt{N_{\rm cal}}, \tag{6.1}$$

where σ_S is the standard deviation of the individual flux measurements and $N_{\rm cal}$ is the number of calibrated observations.

The flux densities we measure are reported in Table 6.4, along with previously measured values at 1.4 GHz. Seven of the pulsars we report flux densities for do not have previously published measurements, and three other pulsars have previously published measurements that were not calibrated against observations of standard candle sources. Most of the rest of our flux density measurements are consistent with previously reported values (see Figure 6.1). Inconsistencies may arise from scintillation, which impacts both the observed flux density as well as the apparent uncertainty. The effect of scintillation is most apparent when only a small number of observations are used to estimate the flux density and is further exacerbated when observations make use of short integrations and/or small bandwidths.

Data from 2013 November to 2014 August could not be calibrated due to saturation and/or non-linearities in the data resulting from insufficient attenuation of the telescope signal. Fortunately, this was only an issue when observing extremely strong sources (e.g. flux calibrators with the noise diode). We find no anomalies in the observed pulse profiles, allowing these observations from late-2013 to mid-2014 to be used for timing.

6.4.2 Clock Stability

The PSRIX system suffered four clock offsets over its first four years of operation. The first offset occurred between 2012 October 27 and November 10, and was due to switching clock sources without measuring the phase difference between their signals. The second offset, which occurred on 2013 July 27, was caused by cutting the power to the clock signal generator and not re-syncing the phase of the signal after the system was restarted. The third

Table 6.4: Measured flux densities of EPTA pulsars at 1.4 GHz

Pulsar	N_{cal}	$\langle S \rangle$[a] (mJy)	S_{med} (mJy)	S_{pub}[b] (mJy)	Ref.[c]
J0023+0923	13	0.57(9)	0.47	–	–
J0030+0451	11	1.20(16)	1.08	0.6(2)	(1)
J0218+4232	11	0.97(6)	1.01	0.9(2)	(2)
J0340+4129	10	0.45(4)	0.43	–	–
J0348+0432	80	0.51(2)	0.48	–	–
J0613−0200	13	1.91(9)	1.87	2.3[d]	(3)
J0621+1002	14	1.34(7)	1.31	1.9(3)	(2)
J0751+1807	23	1.07(7)	1.02	3.2(7)	(2)
J1012+5307	12	3.8(7)	3.3	3(1)	(2)
J1022+1001	16	2.3(8)	1.0	6.1[d]	(3)
J1024−0719	15	2.1(5)	1.1	1.5[d]	(3)
J1518+4904	149	2.5(2)	1.7	4(2)	(2)
J1600−3053	9	1.79(5)	1.78	2.5[d]	(3)
J1640+2224	11	0.4(1)	0.3	2(1)	(2)
J1643−1224	13	4.2(1)	4.3	4.8[d]	(3)
J1713+0747	21	4.9(1.6)	2.4	10.2[d]	(3)
J1730−2304	10	5.1(1.4)	3.6	3.9[d]	(3)
J1738+0333	7	0.52(5)	0.50	–	–
J1741+1351	9	0.50(6)	0.56	0.93[e]	(4)
J1744−1134	10	1.9(6)	1.1	3.1[d]	(3)
J1853+1303	7	0.6(1)	0.5	0.4(2)	(5)
B1855+09	10	3.6(8)	2.3	5.0[d]	(3)
J1911+1347	7	0.87(15)	0.71	0.08[e]	(6)
J1918−0642	10	1.5(3)	1.2	0.58(2)[f]	(7)
B1937+21	11	12(1)	12	13.2[d]	(3)
J2010−1323	8	0.64(7)	0.58	1.6[e]	(4)
J2017+0603	10	0.48(9)	0.40	0.5(2)	(8)
J2043+1711	7	0.246(16)	0.237	–	–
J2145−0750	10	2.9(5)	2.6	8.9[d]	(3)
J2229+2643	9	0.5(1)	0.5	0.9(2)	(2)
J2234+0944	15	0.94(14)	0.93	–	–
J2317+1439	11	0.8(3)	0.3	4(1)	(2)
J2322+2057	6	0.5(2)	0.3	–	–

[a] Mean phase-averaged flux density. The uncertainty reported is the standard error on the mean (i.e. $\sigma_{S_{\mathrm{mean}}}/\sqrt{N_{\mathrm{cal}}}$).

[b] Previously published phase-averaged flux density.

[c] References for S_{pub} – (1): Lommen et al. (2000), (2): Kramer et al. (1998), (3): Manchester et al. (2013), (4): Jacoby et al. (2007), (5): Stairs et al. (2005), (6): Lorimer et al. (2006b), (7): Janssen et al. (2010), (8): Cognard et al. (2011)

[d] Manchester et al. (2013) report the RMS of multiple flux density measurements. This does not represent the uncertainty on the mean, but rather how much scintillation can modulate the observed flux density.

[e] No uncertainty reported.

[f] The flux density of PSR J1918−0642 reported by Janssen et al. (2010) is for a single observation. Thus, the value is likely affected by scintillation, but the uncertainty does not take scintillation into account.

offset was deliberately introduced on 2014 March 4 when the clock signal was synchronized to the original clock phase. Finally, the fourth offset on 2014 November 20 was also deliberately introduced by installing a new clock signal generator.

The first two clock offsets were initially measured by fitting timing data for the orbital phase of PSR J0348+0432. These measurements were sufficiently precise to determine the offsets to within one phase rotation of PSR J0348+0432 ($P \simeq 39\,\mathrm{ms}$), allowing the values to be further refined by fitting arbitrary time offsets ("JUMPs") to the timing residuals of PSR J0348+0432 and then with PSR J1744−1134 ($P \simeq 4.1\,\mathrm{ms}$). The final values of the clock offsets have been measured by fitting JUMPs individually to the timing data of four pulsars, namely PSRs J0613−0200, J1643−1224, J1713+0747, and J1744−1134. These were selected on the basis of being of the most precisely timed pulsars in the PSRIX data set. The JUMPs were fit simultaneously with pulsar parameters and noise models using `TempoNest` (Lentati et al., 2014). The resulting JUMP values, all of which were measured relative to the original clock signal, were averaged together resulting in measurements of $\Delta T_A = 97.2851(6)\,\mathrm{ms}$ and $\Delta T_B = 409.2691(8)\,\mathrm{ms}$. These measurements have been confirmed with data from LEAP by measuring and comparing the phase delays between the signals of simultaneous observations with several European radio telescopes before and after the epochs of the PSRIX clock offsets (see Bassa et al., 2016, for an overview of the project).[1] The third and fourth offsets were directly measured at the telescope by comparing clock signals with an oscilloscope. The results are high-precision measurements of $\Delta T_C = 0.000612(1)\,\mathrm{ms}$ and $\Delta T_D = 0.000127(1)\,\mathrm{ms}$, which are consistent with offset values derived from fitting JUMPs to pulsar timing data.

A schematic of the PSRIX clock offsets is shown in Fig. 6.2. The timing residuals of PSR J1713+0747 after the JUMPs are removed show no evidence of the clock offsets, as shown in the bottom panel of Fig. 6.2. Similarly, the residuals of all other pulsars are also free of the effect of the clock offsets after applying the offsets listed above.

Note that the EBPP uses an independent reference clock, and thus was not affected by any of the four offsets seen in the PSRIX data.

6.4.3 Comparison With the EBPP Backend

We have compared the S/N derived from data recorded simultaneously with PSRIX and the old EBPP backend (see Figures 6.3). In particular, we used multiple observations of four MSPs, PSRs J0613−0200, J1643−1224, J1713+0747, and J1744−1134. We have found that PSRIX provides significantly stronger detections, roughly 2–5 times higher S/N, than the simultaneously recorded EBPP data. A similar comparison of TOA uncertainties derived for simultaneous PSRIX and EBPP data also shows improvements of a factor of 2–5.

There are several reasons why PSRIX outperforms the EBPP:

1) The 200-MHz bandwidth of PSRIX is considerably larger than the EBPP's usable bandwidth ($\sim$40 – 50 MHz for most pulsars, and $\sim$95 MHz for pulsars with DM $\lesssim 10\,\mathrm{pc\,cm^{-3}}$). A comparison of the observing bands from both backends is shown in Figure 6.4. PSRIX's larger bandwidth allows more signal to be integrated, reducing radiometer noise, and also increases the chance of observing constructive scintels.

2) The PSRIX data are recorded with 8 bits, making them even more resilient in the presence of strong RFI than the EBPP with its 4-bit data.

3) The 10-s sub-integrations of PSRIX are much shorter than the 2-min sub-integrations of the EBPP. Thus, the expense of removing impulsive RFI is diminished. Also, the shorter

---

[1] The precision of the LEAP-based measurements is expected to surpass what is possible with timing-based JUMP measurements. However, the uncertainties of the LEAP-based measurements are not yet well determined, so here we report the values and uncertainties derived from the more standard and conservative JUMP measurements.

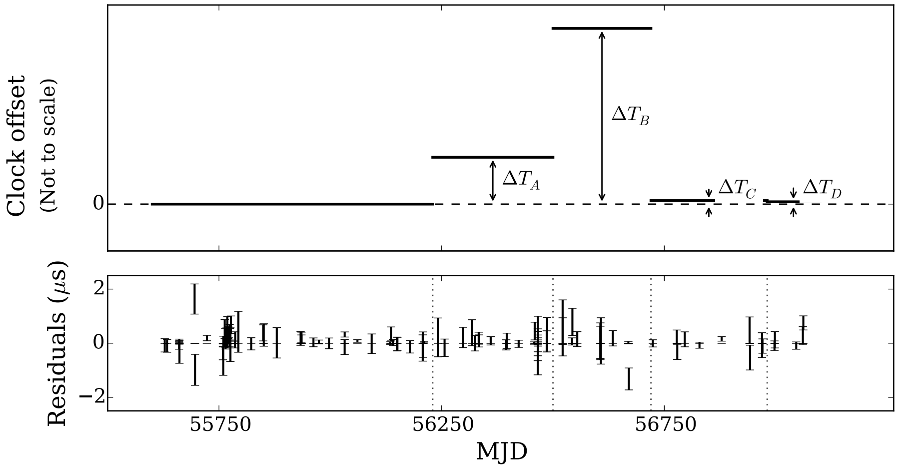

Figure 6.2: *Top* – A schematic of the four clock offsets suffered by the PSRIX system. The offset values are: $\Delta T_A = 97.2851(6)\,\mathrm{ms}$, $\Delta T_B = 409.2691(8)\,\mathrm{ms}$, $\Delta T_C = 0.000612(1)\,\mathrm{ms}$, and $\Delta T_D = 0.000127(1)\,\mathrm{ms}$. Offsets A and B are larger than the spin periods of the pulsars reported here ($P \sim 1-50\,\mathrm{ms}$), thus resulting in phase ambiguities and different apparent offsets in residuals for different pulsars. See § 6.4.2 for the origins of the clock offsets and how their magnitudes were determined.
Bottom – Timing residuals from PSRIX observations at 1.4 GHz of PSR J1713+0747 after accounting for the clock offsets, showing that no significant offsets remain.

sub-integrations make re-aligning the pulse profiles with an updated timing model more accurate.
4) PSRIX is a more robust instrument than the EBPP. This is especially true now that the latter is nearly 20 years old, and hardware and networking issues occasionally preclude it of recording data. In these instances, data files are cut short, or not written at all.

The increase in bandwidth of PSRIX over the EBPP is even more apparent when full polarization information is recorded. Polarization observations with the EBPP are limited to only 28 MHz, whereas with PSRIX full polarization information can be recorded for up to 500 MHz of bandwidth. Moreover, because recording polarization information required the EBPP to be set up in a special mode prior to commencing observations, it is much less flexible than PSRIX, which always provides full Stokes parameters for timing-mode observations.

In addition to investigating individual observations, we also examined the timing data of several pulsars to compare the timing stability achievable with PSRIX vs. the EBPP. Depending on the pulsar, we found the weighted root-mean-square (RMS) of the PSRIX timing residuals is a factor of ∼1.3 – 3 times better than that of the EBPP over the same time interval. In our analysis, we whitened the timing residuals with three frequency derivatives and two DM derivatives to not be biased by the effects of pulsar spin noise and DM variations.[1] We also removed the four clock offsets affecting PSRIX data mentioned in § 6.4.2. The smallest improvement factor we found (1.3×) was for PSR J1744−1134. This is because the pulsar's particularly low DM of $3.1\,\mathrm{pc\,cm^{-3}}$ made it possible for the EBPP to coherently dedisperse ∼95 MHz of usable bandwidth.

Despite PSRIX providing better detections than the EBPP, we still observe with both backends in parallel whenever possible to extend the latter's nearly 20-year long data set.

---

[1] The timing residuals from PSRIX and the EBPP closely trace the residuals from other EPTA telescopes, so we are confident that the systematic trends we are removing are not instrumental.

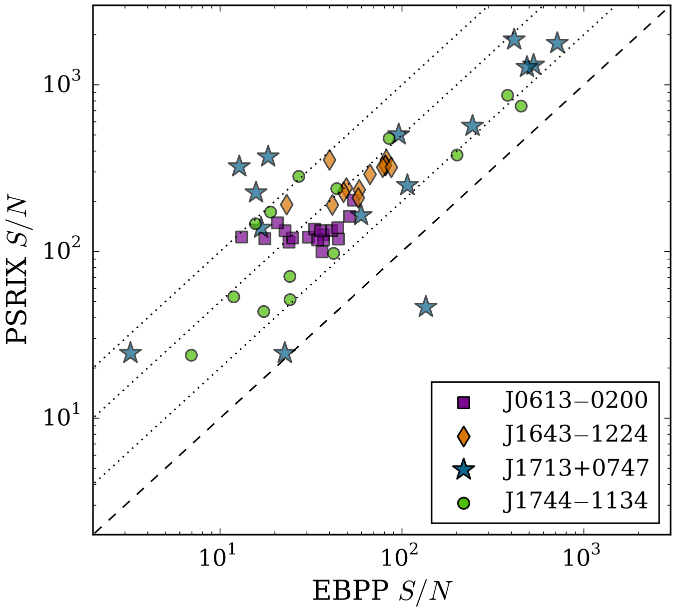

Figure 6.3: Comparison of S/N for simultaneous observations with the PSRIX and EBPP backends. Equal S/N is shown with the dashed line. The dotted lines represent 2×, 5×, and 10× improvements. The one observation of PSR J1713+0747 where the S/N is larger in the EBPP observation is due to there being a single scintillation maximum within the 200-MHz PSRIX band that falls inside the smaller EBPP observing window. Note that we did not weight the frequency channels by S/N when integrating the band.

6.4.4 *High-Frequency Observations*

Our 5 and 9-GHz observations of 12 EPTA pulsars all resulted in detections. The integrated pulse profiles from individual high-frequency observations are shown in Figure 6.5. PSRs J1012+5307, J1713+0747, B1937+21, and PSR J2145−0750 were observed twice at 5 GHz. PSR J2145−0750 was also observed twice at 9 GHz. Details of the 5 and 9-GHz observations presented in Table 6.5.

To flux calibrate our observations, we observed 3C 48 at both 5 and 9 GHz on 2015 January 7 and again on 2015 January 24. These observations were used to derive calibrated flux densities of our observations at these frequencies. We observed the pulsars to have flux densities ranging from 0.2 to 1.5 mJy at 5 GHz, and from 0.2 to 0.3 mJy at 9 GHz (see Table 6.5). We found some variation in the measured flux densities of the pulsars observed multiple times. However, these variations are consistent with amplitude modulations expected from weak scintillation at these frequencies (e.g. Lorimer & Kramer, 2004).

For each of our high-frequency observations, we computed TOA uncertainties using an analytic template, which was generated by fitting von Mises-shaped pulse components to the summed profile. TOA uncertainties we determined range from 0.1 to 7.5 μs at 5 GHz and from 5 to 30 μs at 9 GHz (see Table 6.5).

Our 5 and 9-GHz detections show that it is feasible to monitor some MSPs at these observing frequencies, which are higher than those typically employed for long-term monitoring projects (350 – 3100 MHz; e.g. Manchester et al., 2013; Arzoumanian et al., 2015; Shannon et al., 2015; Desvignes et al., 2016). It is important to note that observing campaigns will only benefit from high-frequency detections of pulsars that are sufficiently bright to be able

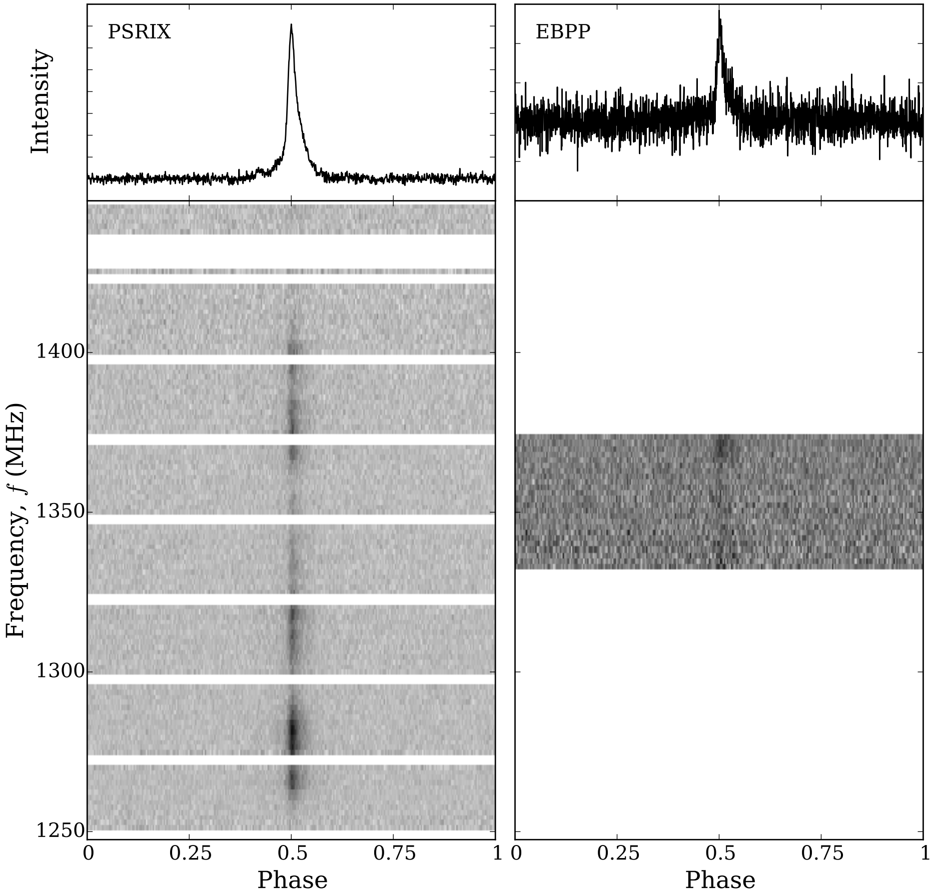

Figure 6.4: *Left* – The integrated pulse profile and frequency vs. phase plot for a 28-min observation with PSRIX of PSR J1713+0747 on 2013 January 6. This detection has a $S/N = 225$ thanks to its 200-MHz bandwidth. The frequency channels missing are removed due to interference and roll-off at the edges of the sub-bands (see §6.3).
Right – The integrated pulse profile and frequency vs. phase plot for the same observation of PSR J1713+0747 using data from the EBPP, which was recording in parallel. The EBPP provides a significantly weaker detection with $S/N = 20$, owing to its limited ~40 MHz bandwidth.

Table 6.5: High-frequency observations

Pulsar	Obs. Start (UTC)	Integ. Time (s)	S/N	Flux Dens. (mJy)	TOA Uncert. (μs)
5-GHz Observations					
J0751+1807	2015/01/28 02:12	2960	47.05	0.375	2.890
J1012+5307	2015/01/24 20:03 [a]	3740	15.96	0.209	7.278
	2015/01/28 03:11	2060	26.22	0.385	4.866
J1022+1001	2015/01/24 21:01	1780	39.47	0.562	3.552
J1518+4904	2015/01/28 03:59	1770	25.51	0.441	5.87
J1600−3053	2015/01/28 06:38	1770	10.49	0.318	6.657
J1643−1224	2015/01/26 07:14	1780	22.78	0.343	4.920
J1713+0747	2015/01/26 06:13	1200	133.87	1.463	0.470
	2015/01/28 04:38	1780	110.45	1.102	0.541
J1730−2304	2015/01/26 07:51	1770	27.10	0.503	5.892
J1744−1134	2015/01/28 06:09	1280	14.40	0.389	1.421
B1855+09	2015/01/26 08:29	1780	52.50	0.895	1.482
B1937+21	2015/01/07 15:13	2310	86.56	1.234	0.101
	2015/01/28 05:26	1780	35.91	0.639	0.211
J2145−0750	2015/01/07 15:59	1780	52.70	0.702	3.812
	2015/01/25 15:20	1780	54.00	0.797	3.883
9-GHz Observations					
J1022+1001	2015/01/24 22:09	2610	10.06	0.233	18.237
J1713+0747	2015/01/26 06:38	1780	15.74	0.258	5.297
J2145−0750	2015/01/07 17:11	2950	16.90	0.251	12.269
	2015/01/26 13:37	2680	16.43	0.218	10.631

[a] Two closely spaced observations added together.

to take advantage of the reduced ISM effects. See § 6.5.2 for a more detailed discussion.

6.5 Discussion

The new PSRIX data set already contains roughly monthly observations of 45 MSPs, black widow pulsars and relativistic binaries at 1.4 and 2.6 GHz spanning at least two years, including the 33 pulsars summarized in Tables 6.2 and 6.3. This data set is the successor of the venerable EBPP data set, and includes stronger detections and more precise TOAs thanks to the larger bandwidth and more robust design of PSRIX.

6.5.1 Improved Sensitivity to a GW Background

One of the primary goals of our monthly observations with PSRIX is to contribute to the EPTA and IPTA objective of detecting the GWB. To this end, we will be combining our observations with the EPTA and IPTA data sets.

We have estimated the improvement to GWB sensitivity made possible by switching from the EBPP to PSRIX for two separate scenarios: first, assuming all pulsars exhibit only pure white noise (e.g. radiometer noise or from pulse jitter), and second, assuming the pulsars also suffer from red noise following a power-law spectrum (e.g. from intrinsic spin noise or uncorrected DM variations). In both cases, we considered a 7-pulsar[1] hybrid data set that combines the higher timing precision of the PSRIX TOAs with the longevity of the existing EBPP data set. We then compared our results for this hybrid data set to a hypothetical extension of the current EBPP data set without having switched to PSRIX.

---

[1] We used the positions of PSRs J0218+4232, J0613−0200, J1022+1001, J1600−3053, J1713+0747, B1855+09, and J2145−0750. Because we are computing improvement factors, we find there is no significant difference in the results as the number of pulsars is increased.

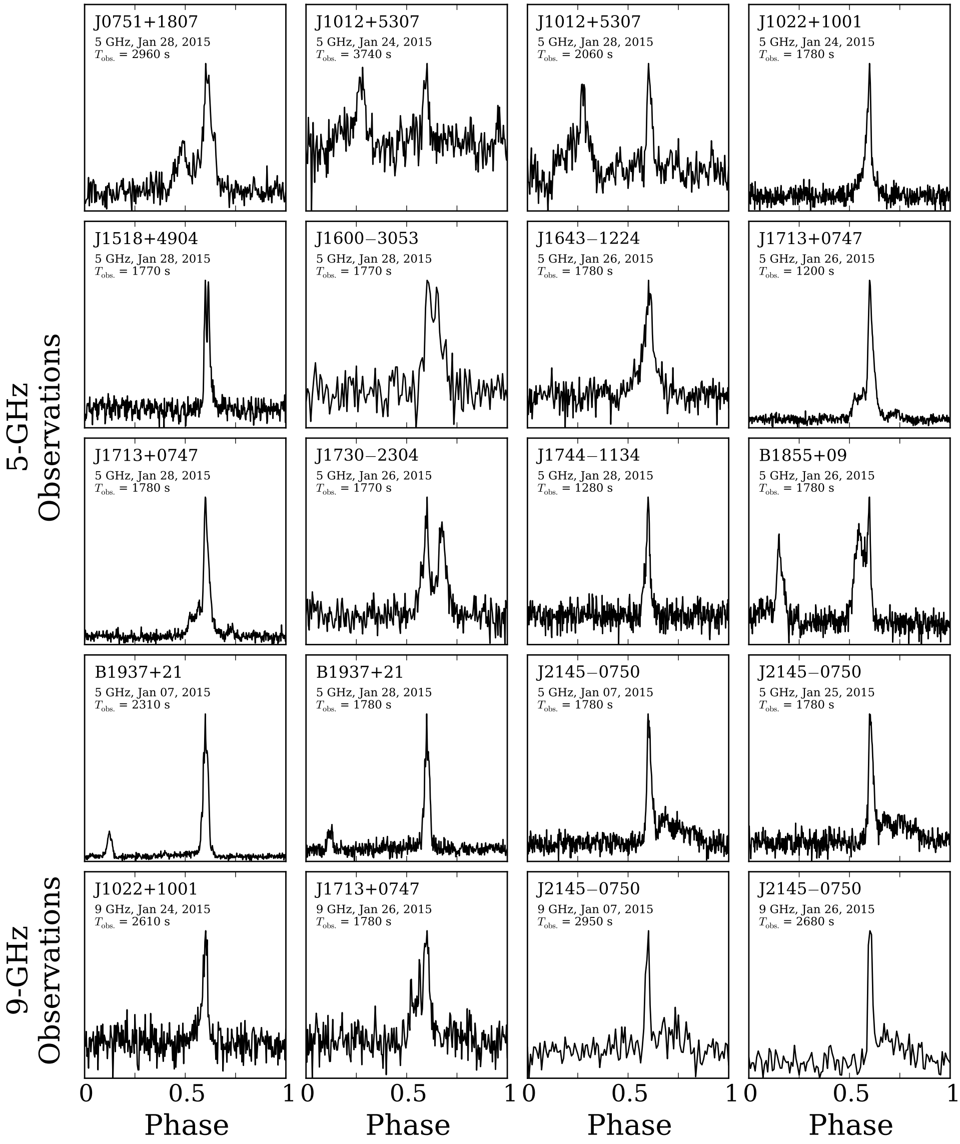

Figure 6.5: Integrated pulse profiles from PSRIX observations at 5 and 9 GHz. In all cases, a bandwidth of 500 MHz was used. These detections were cleaned of RFI and polarization calibrated. See Table 6.5 for observation details.

In our first set of estimates, we assumed pulsars with pure white noise timing residuals. We assumed the timing residuals RMS in EBPP data is $\mathrm{RMS_E} = 1\,\mu\mathrm{s}$, and the RMS of PSRIX residuals is improved by a factor η (i.e. $\mathrm{RMS_P} = \mathrm{RMS_E}/\eta$). We performed separate estimates for $\eta = 2$, 3, and 5. For simplicity, we also assumed that the phase offset between the EBPP-era data and the PSRIX-era data is perfectly determined. We then used the Cramér-Rao Bound (e.g. Fisz, 1963) to compute the minimum GWB amplitude required to reject the null hypothesis, which was that there is no GWB (i.e. a zero-amplitude GWB) at the $1\,\sigma$ level. A more complete description of the use of the Cramér-Rao Bound in the context of estimating PTA sensitivity to the GWB can be found in Caballero et al. (2015). In making our estimates, we assumed that the GWB signal has a power-law strain spectrum with an index of $-2/3$, appropriate for an isotropic stochastic background of super-massive black hole binaries. Improvement factors were determined by comparing the GWB amplitude derived for the hybrid data set with the analogous value computed for the pure EBPP-style data set. Our estimated improvement factors for $\eta = 2$, 3, and 5 as a function of date are shown in Figure 6.6.

Our second set of estimates are determined following the same procedure described above, but assuming an additional red noise contribution to the timing residuals. We used a red noise spectrum with an amplitude corresponding to $\mathrm{RMS_{red}} = 100\,\mathrm{ns}$ and a spectral index of $\alpha_{\mathrm{red}} = -1.5$ for all pulsars. This optimistically flat value of α is within the measured range for MSPs, $-7 \lesssim \alpha \lesssim -1$ (e.g. Arzoumanian et al., 2015; Caballero et al., 2015).[1] Even when assuming this nearly best-case red noise spectrum, we find the overall improvement in sensitivity to the GWB is considerably reduced. This is because only the power of the white noise is reduced by switching to PSRIX. It is, therefore, the red noise that restricts the sensitivity to the GWB. We also find that the improvement factor saturates earlier because the low frequencies probed as the data set is extended are dominated by red noise. Thus, in the red-noise case, these lowest frequencies contribute little sensitivity to the GWB. The improvement factors for GWB sensitivity found for these red noise cases are indicated with the red curves in Figure 6.6.

The difference between the black and red curves in Figure 6.6 is caused by the presence of red noise, which can arise from a variety of sources (see e.g. Cordes & Shannon, 2010). While it may not be possible to fully remove the deleterious effect of red noise from pulsar timing data, some of these noise processes (e.g. from the ISM – see § 6.5.2) can be mitigated, further improving the prospects for the detection of the GWB.

As suggested by Siemens et al. (2013), another way to counter the loss of sensitivity to the GWB due to pulsars' red timing noise is to include other, possibly newly discovered MSPs in PTAs. This exemplifies the importance of on-going high time and frequency radio pulsar surveys such as the Pulsar Arecibo L-Band Feed Array (PALFA) survey (Chapter 3 and Lazarus et al., 2015), the High-Time Resolution Universe (HTRU) surveys (Keith et al., 2010a; Barr et al., 2013b), and the Greenbank North Celestial Cap (GBNCC) survey (Stovall et al., 2014).

6.5.2 PTA Monitoring of MSPs at High Frequencies

ISM variations, primarily DM variations, can introduce a significant amount of red noise into the timing residuals of some MSPs (e.g. Cordes & Shannon, 2010; Keith et al., 2013; Lee et al., 2014; Lentati et al., 2016). This can be a major hindrance to reliably detecting long-time-scale signals in the data (e.g. the nHz GWB spectrum being searched for with PTAs). Thus, mitigating ISM variations is of great importance. In general, this can be accomplished in two ways: (1) by avoiding ISM variations, either by discarding data sets contaminated

---

[1] MSPs with very steep spectral indices (e.g. B1937+21) are not typically used in searches for the GWB.

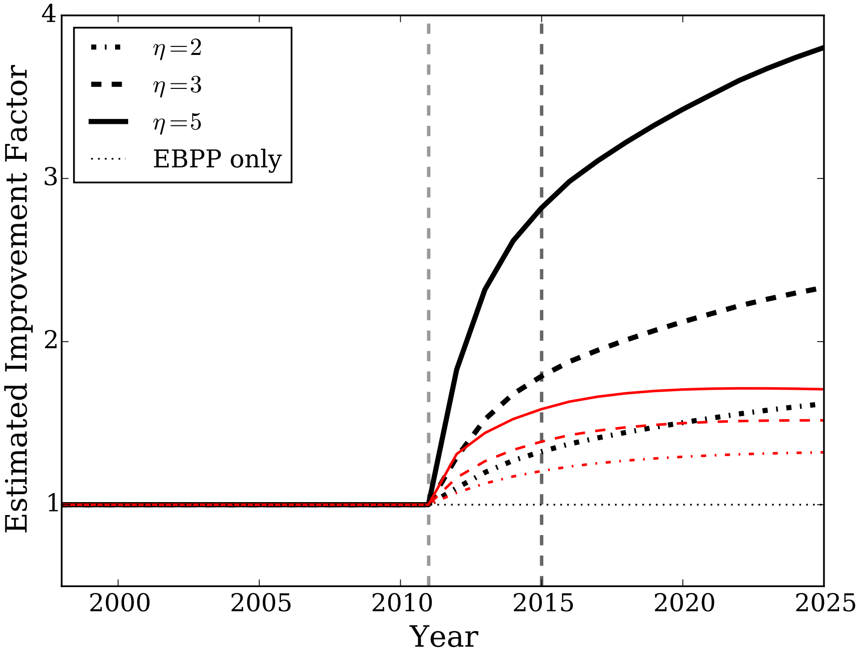

Figure 6.6: Estimated improvement in sensitivity to the GWB as a function of date provided by including PSRIX data compared to a hypothetical extended EBPP-only data set. We have assumed white noise with $\mathrm{RMS_E} = 1\,\mu\mathrm{s}$ for EBPP-era data (1997 to 2011), and $\mathrm{RMS_P} = \mathrm{RMS_E}/\eta$ for PSRIX data. The baseline of our comparison assumed EBPP data only. By using the Cramér-Rao Bound we calculated the GWB amplitude at which the data would show a $1\,\sigma$ inconsistency with the no-GWB null hypothesis. The three black curves correspond to pure white noise and improvement factors of $\eta = 2$, 3, and 5. The red curves include an additional source of red noise with an amplitude corresponding to $\mathrm{RMS_{red}} = 100\,\mathrm{ns}$ and a conservatively flat spectral index of $\alpha_{\mathrm{red}} = -1.5$ for all pulsars. See text for additional discussion.

by ISM variations or by observing at frequencies high enough that the amplitude of ISM-induced noise is sufficiently small (e.g. as was done by Shannon et al., 2015), and (2) by removing the ISM effects, either by leveraging multi-frequency and wide-band observations to measure DM variations (e.g. Keith et al., 2013; Demorest et al., 2013; Arzoumanian et al., 2015).

The effect of the ISM diminishes with increasing observing frequency: DM delays scale as $\tau_d \propto f^{-2}$ (e.g. Lorimer & Kramer, 2004) and pulse broadening caused by interstellar scattering scales as $\tau_s \propto f^{-3.86\pm0.16}$ (Bhat et al., 2004). Therefore, pulsar timing data from high-frequency observations will contain less significant red ISM noise. Unfortunately, the radio spectra of pulsars, which are generally described by a simple power law, $S \propto f^{\alpha}$, are rather steep, with spectral indices of $-1 \lesssim \alpha \lesssim -2$ (Maron et al., 2000; Bates et al., 2013), making it difficult to completely avoid ISM variations while maintaining the S/N required for high-precision timing. Thus, in practice, ISM effects cannot be completely ignored by observing at arbitrarily high frequencies. Some effort to remove these effects is necessary.

When removing DM variations the key resulting quantity is the infinite-frequency TOA, T_∞ (i.e. the DM-corrected TOA). Estimates of T_∞ can be made by combining multi-frequency observations or by splitting a single wide-band observation into multiple sub-bands (see e.g. Lee et al., 2014). The uncertainty on T_∞ is $\sigma_\infty = \sqrt{\langle \delta T_\infty^2 \rangle}$, and in the two-band case, is given by (Eq. 12 of Lee et al., 2014)

$$\left\langle \delta T_\infty^2 \right\rangle = \frac{f_1^4 \sigma_1^2 + f_2^4 \sigma_2^2}{\left(f_1^2 - f_2^2\right)^2}, \tag{6.2}$$

where the f_i and σ_i terms are the centre frequencies and TOA uncertainties of the two bands, respectively.

To measure and remove DM variations, timing data at $1-3$ GHz are typically complemented by low-frequency observations (e.g. $\lesssim 350$ MHz). To illustrate the precision on T_∞ attainable, we have estimated the relative improvement in σ_∞ from combining observations with the LOFAR international station at Effelsberg,[1] with 1.4 GHz PSRIX data. Note that we have neglected the differences in propagation paths through Galaxy of the lower and higher-frequency radio emission due to scattering (see Cordes et al., 2015, for a discussion of this effect). We estimated the ratio of TOA uncertainties derived from observations of the same duration with different observing systems, “A” and “B”, using

$$\begin{aligned} \frac{\sigma_{t_A}}{\sigma_{t_B}} &= \frac{(S/N)_B}{(S/N)_A} \\ &= \frac{S_{\rm sys,A}}{S_{\rm sys,B}} \sqrt{\frac{\Delta f_A}{\Delta f_B}} \left(\frac{{f_{{\rm hi},B}}^{(\alpha+1)} - {f_{{\rm lo},B}}^{(\alpha+1)}}{{f_{{\rm hi},A}}^{(\alpha+1)} - {f_{{\rm lo},A}}^{(\alpha+1)}} \right), \end{aligned} \tag{6.3}$$

where $S_{\rm sys}$ is the system-equivalent flux density, Δf is the recorded bandwidth, $f_{\rm lo}$ and $f_{\rm hi}$ are the low and high-frequency edges of the recorded band, respectively, and α is the spectral index. In deriving Eq. 6.3, we have ignored the effect of profile evolution across the band, which is minimal for MSPs (Kramer et al., 1999), as well as pulse broadening, which can be significant at 150 MHz. We have also assumed that $S_{\rm sys}$ is constant across the individual bands. Our estimates are plotted in Figure 6.7 for $-3 \le \alpha \le -1$.

For simplicity, in Figure 6.7 we have assumed the entire recorded bandwidth is summed to form a single TOA. This is a reasonable assumption given recent work on wide-band template matching (Pennucci et al., 2014; Liu et al., 2014b). In fact, by using these new wide-band TOA determination algorithms, it is possible to simultaneously account for profile evolution, DM variations, scattering, and scintillation while summarizing wide-band observations into a single TOA.

Clearly, complementing PSRIX TOAs with observations using the Effelsberg LOFAR station, provides precise DM-corrected TOAs. However, there are some complications with using low-frequency data to remove DM variations. First, the background of Galactic synchrotron emission is strong and line-of-sight dependent (Haslam et al., 1982). Thus, MSPs in unfortunate directions may be too weak to use low-frequency observations to make DM measurements. Another possible complication, not included in our estimates, is spectral turnover, which occurs in a significant fraction of MSPs (Kuniyoshi et al., 2015). This also conspires to weaken detections at low frequencies. Finally, there is concern that the DMs measured at low frequencies are different than those measured at higher frequencies due to differences in the ISM probed as a result of interstellar scattering (Cordes et al., 2015).

Our 5 and 9-GHz detections of several MSPs indicate that complementing timing campaigns at $1-3$ GHz with observations at higher frequencies might be a viable alternative for mitigating ISM effects. Figure 6.7 includes estimates of σ_∞ attainable by complementing 1.4 GHz PSRIX data with observations from current and planned receiver systems. Using

---

[1] The international LOFAR station at Effelsberg is also known as “DE601”.

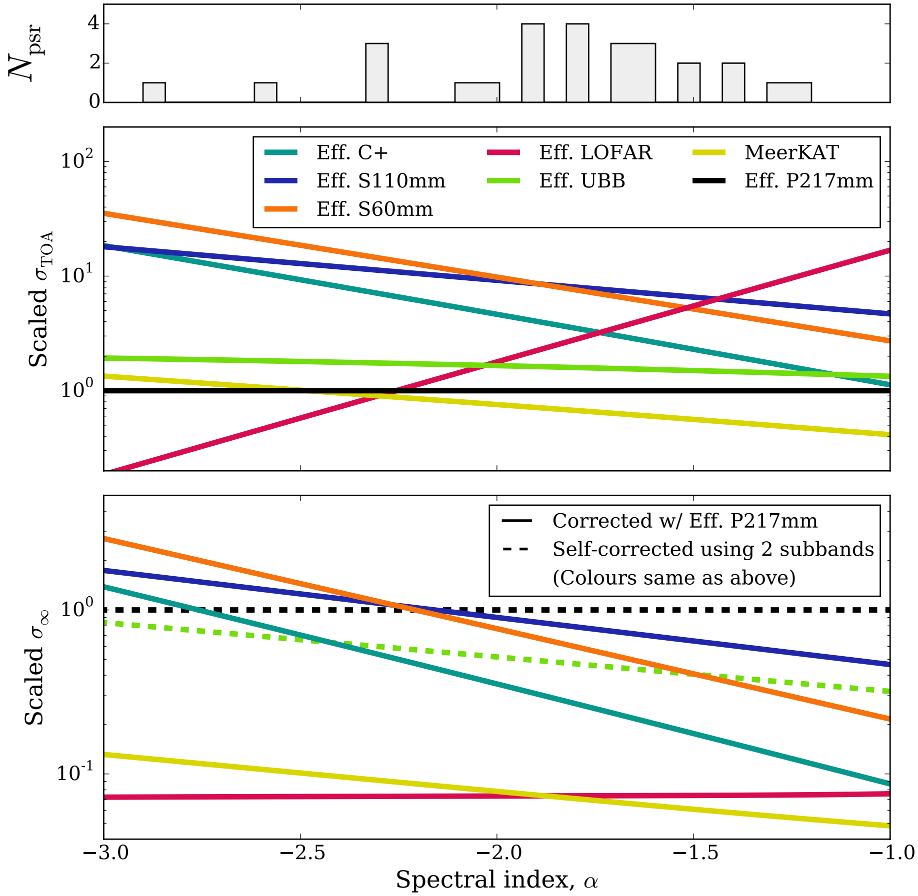

Figure 6.7: *Top* – Distribution of spectral indices from the ATNF Pulsar Catalogue (Manchester et al., 2005) for the pulsars in Table 6.2.
Middle – TOA uncertainties for various existing and future observing systems scaled to what is achievable with PSRIX using the P217mm receiver as a function of pulsar radio spectral index. Lower values indicate more precise (i.e. better) TOAs. Note that the estimated TOA precision of the UBB receiver is worse than the P217mm receiver because of the former's high SEFD, which will be reduced when a high-pass filter is installed.
Bottom – The uncertainty of the infinite frequency TOA (i.e. the uncertainty of the DM-corrected TOA), σ_∞, obtained from combining Effelsberg 1.4-GHz (P217mm) detections with data from another observing system relative to the uncertainty of the self-corrected P217mm observation. The σ_∞ values for the self-corrected observations are estimated assuming the band is divided evenly into two parts. Note that doubling the integration time only improves σ_∞ by $\sqrt{2}$.

Table 6.6: Parameters for selected available and planned observing set-ups

	Observing Set-Up			
Telescope	Effelsberg	Effelsberg	MeerKAT	LOFAR
Receiver	UBB	S45mm (“C+”)	S-band	DE601[a]
Receiver band (MHz)	600 – 2700[b]	4000 – 9300	1600 – 3500	111.5 – 186.5
Recorded band (MHz)	1100 – 2700	4000 – 6000	1600 – 2300	111.5 – 186.5
System Temperature (K)	25/(55)[c]	$\sim$25[d]	<25[e]	–[f]
Gain (K/Jy)	1.25	$\sim$1.35[d]	2.5	–[f]
SEFD (Jy)	45	18.5	10	1500[f]

[a] DE601 is the international LOFAR station located at Effelsberg.

[b] The observing band of the UBB receiver currently goes as low as 600 MHz. However, strong interference from digital television broadcasts at $\sim$500 – 800 MHz and GSM emission at $\sim$900 MHz greatly deteriorates the quality of the observations. There are plans to insert a high-pass filter at $\sim$1100 MHz. We use this planned frequency band for our estimates.

[c] The strong interference in the UBB band causes the system temperature to be on the order of $\sim$55 K, significantly higher than the value of $T_{\mathrm{sys}} = 25$ K measured in the lab. A high-pass filter will be installed around 1100 MHz and should lower T_{sys} to $\sim$25 K. Nevertheless, in our estimates of the system performance, we use the current, higher, measured value to be conservative.

[d] Preliminary estimate.

[e] This is the target system temperature. In our estimates we use $T_{\mathrm{sys}} = 25$ K.

[f] We estimated the SEFD Effelsberg LOFAR station by scaling the SEFD of the LOFAR core published by van Haarlem et al. (2013).

the current 5-GHz set-up with PSRIX should provide better TOA precision than the 2.6-GHz set-up described in § 6.2 for $\alpha \gtrsim -1.9$, as well as better σ_∞ for $\alpha \gtrsim -2.25$, thanks to the larger frequency separation between the bands.

We also examined new wide-bandwidth receivers coming online, such as the 0.6 – 2.7-GHz UBB receiver at Effelsberg,[1] as well as the new 4 – 9-GHz “C+” receiver currently being commissioned at Effelsberg, and the 1.8 – 3.5-GHz receivers being designed at the Max-Planck-Institut für Radioastronomie for MeerKAT. The assumed receiver parameters are shown Table 6.6.

Effelsberg’s C+ receiver and the MeerKAT 1.8 – 3.5-GHz observing systems present significant improvements in the bandwidths currently available for pulsar timing at these frequencies, and thus provide compelling cases for using high-frequency observations to mitigate ISM-related noise. Furthermore, other sensitive high-frequency observing systems (e.g. the 3.85 – 6 GHz “C-band” receiver at the Arecibo Observatory, the 2 – 4 GHz “S-band” system at the Jansky Very Large Array (JVLA), and the 4 – 8 GHz “C-band” system at the JVLA) should be considered for regular PTA monitoring of MSPs. Furthermore, the potential high-frequency capabilities of the SKA could also be important for PTA-studies.

Note that, at $\sim$5 GHz, we expect slow, roughly hourly, intensity variations of only $\sim$10 – 30 %. Also, the attenuation of the transmission of radio waves through the atmosphere due to water vapour only becomes a concern at $f \gtrsim 10$ GHz.

When formulating observing strategies for high-precision, multi-frequency timing campaigns, deciding what observing systems to use should depend on the spectral index of the pulsar, the magnitude of the noise introduced by ISM effects, and the shape of the pulse profile, including the degree of profile broadening. Furthermore, deciding how often multi-frequency observations are necessary for a particular pulsar depends on the time-scale of the DM variations affecting the pulsar (see e.g. Keith et al., 2013). At Effelsberg, because the secondary-focus receivers are always available, and can be switched to within minutes, issues arising from the non-simultaneity of multi-frequency observations described by Lam et al.

---

[1] Currently, the UBB receiver at Effelsberg can observe frequencies as low as 0.6 GHz. However, since the RFI is particularly strong below 1 GHz, a high-pass filter will be installed around 1.1 GHz to improve the overall performance of the receiver.

(2015) are not a concern, as they may be at other telescopes.

6.6 Conclusions

We have described how the PSRIX backend is being used at the Effelsberg radio telescope for monthly EPTA observations. The coherently dedispersed data from PSRIX have a larger bandwidth than what is possible with its predecessor, the EBPP. As a result, the now four-year-old PSRIX data set has stronger detections, more precise TOAs, and will improve the sensitivity to the GWB compared to the EBPP data.

We have also shown how bright, highly stable MSPs being monitored by the EPTA can be detected at 5 and 9 GHz. Given the reduced ISM effects at these frequencies compared to 1.4 GHz and the ability to more precisely correct DM variations, there could be advantages to complementing existing data sets (typically $1 \lesssim f \lesssim 3\,\mathrm{GHz}$) with observations at these higher frequencies. This is especially true considering the new wide-bandwidth, high-frequency receivers currently being commissioned, and those expected to come online in the next few years.

7

STUDYING THE SOLAR SYSTEM WITH PULSARS

The work described in this chapter is part of an on-going official project of the International Pulsar Timing Array (IPTA) collaboration, "Studying the Solar System with IPTA Data."

I am the principal investigator of the project. I have performed all of the analysis presented in this chapter.

The ultimate goals of this project include using new and existing methods to measure deviations in planetary masses from the values assumed when constructing Solar System ephemerides (SSEs), which are models of the motion of the Earth and other Solar System bodies. Another aspect of this project is to search for unknown, unmodelled Solar System bodies. In short, this project is designed to verify that the SSEs used in pulsar timing are sufficiently accurate, and if not, to determine why and study the implications.

Pulsars can be used as probes of other physical systems, enabling studies in a wide variety of fields (see § 1.6 and Chapter 5 for examples). This is especially true of pulsar timing analyses, in which a pulsar's regular and extremely predictable pulses allow the star to be used as a precise clock.

Arguably, the most exciting applications of pulsar timing are studies of relativistic gravity, and in particular, gravitational waves (GWs). In fact, in 1993 the Nobel Prize in Physics was awarded to Russell A. Hulse and Joseph H. Taylor, Jr. for their studies of relativistic gravity, including the indirect detection of the emission of GWs from PSR B1913+16, a binary pulsar in a double-neutron-star system.[1] One of the most ambitious and concerted efforts to use pulsars to study gravity is to jointly analyze the timing data from a collection of the most stably rotating millisecond pulsars (MSPs) with the ultimate goal of detecting the stochastic GW background (GWB) that permeates the Universe.

To maximize the probability of detecting the minuscule signal of the GWB in the pulsar timing residuals, a data set of unmatched size, length, and quality has been assembled, the International Pulsar Timing Array (IPTA) data set (see § 7.2). In addition to requiring the best data possible, GWB searches also require accurate pulsar ephemerides, SSEs, and terrestrial time standards. Predictions of the GWB amplitude suggest that pulsars with timing precisions of $\lesssim$100 ns will be required (Jenet et al., 2005). This, for example, imposes stringent constraints on the SSE. An error of the position of the Earth with respect to the Solar System barycentre (SSB) of only $\sim$30 m can introduce systematic errors of $\sim$100 ns in the timing residuals of a pulsar.

Fortunately, satisfying these strong requirements upon the data set, SSEs, and time standards enables other high-precision "spin-off" science. In this chapter, we describe how the Solar System can be studied using pulsars, one of the many applications that take advantage of the exquisite MSP timing data set assembled for GW searches. Specifically, we used the IPTA data set to constrain the Solar System planet masses,[2] and compared these to the well-measured masses. Furthermore, this serves as an indirect test that the SSEs,

---

[1] Officially the prize was awarded for "the discovery of a new type of pulsar, a discovery that has opened up new possibilities for the study of gravitation." (http://www.nobelprize.org/nobel_prizes/physics/laureates/1993/)

[2] Throughout this work, we use the term "planet masses" to refer to the total mass of the entire planetary system. That is, the sum of the masses of the planet and any moons or rings around it.

as well as the dispersion measure models and spin noise models of individual pulsars, are sufficiently accurate for searches for GWs, the main objective of the IPTA.

7.1 Solar System Ephemeris Errors and Pulsar Timing

As described in § 4.3, the motion of the Earth about the SSB, and other smaller effects, influence the measured topocentric TOAs, and thus must be corrected for. The resulting barycentric TOAs are referred to the SSB, and thus assumed to be fixed to an inertial reference frame. However, barycentering TOAs requires a SSE, and if that model is not sufficiently accurate, small but significant trends will remain in the TOAs, since they were incorrectly barycentred. For example, Kaspi et al. (1994) repeated their timing analysis of PSR B1937+21 with different SSEs and found a clear dependence of the timing residuals on the SSE used. Also, Splaver et al. (2005) compared timing residuals from PSR J1713+0747 computed with both the DE200 and DE405 SSEs produced by the NASA Jet Propulsion Laboratory (JPL). They found that using the newer, more complete DE405 ephemeris resulted in an improved fit, with fewer systematic trends in the pulsar's residuals.

It is possible to parameterize some likely sources of SSE errors, enabling these errors to be attributed to a particular body. The simplest parameterization is accomplished by allowing for perturbations in the planet masses, δM_i, where i refers to the planet, in order, from Mercury ($i = 1$) to Neptune ($i = 8$). If the mass of a Solar System planet is incorrect, the assumed position of the SSB will be offset from the true SSB in the direction of that planet. As a result, the timing analysis will refer TOAs to a point that is not in an inertial reference frame, in other words, a point that is not fixed with respect to the pulsar. Such an error would give rise to anomalous trends in the residuals. The offset of the SSB is (Champion et al., 2010)

$$\delta\vec{s} \approx \sum_{i=1}^{8} \vec{r}_i \frac{\delta M_i}{M_T}, \tag{7.1}$$

where the $\vec{r}_i$ are the positions of the planets and $M_T \simeq M_\odot + \sum_{i=1}^{8} M_i \simeq M_\odot$ is the total mass of the Solar System. This expression assumes that the mass errors are small (i.e. $\delta M_i \ll M_i$) and that the change in the total mass of the Solar System is negligible.

Since all timing analyses use a SSE to barycentre TOAs, any errors will affect all pulsars. This gives rise to residuals that have an angular correlation with a dipolar signature.

As explained in Champion et al. (2010), the effect of planet-mass errors on the residuals can be described with increasing levels of completeness:

To first order, an error in the mass of a Solar System planet induces a roughly sinusoidal signal in the residuals of pulsars caused by incorrectly barycentering TOAs. In this first-order approximation, the orbit of the Earth is assumed to be unchanged, that is, it is assumed to be centred on the true SSB, and not the incorrect SSB used. The period of the signal induced in the residuals matches the orbital period of the planet. The phase of this signal depends on the position of the planet, the sign of the mass offset, and the ecliptic longitude of the pulsar. The amplitude of the signal depends on the magnitude of the error, the ecliptic latitude of the pulsar, and the distance of the planet from the SSB. The top panel of Figure 7.1 shows the residuals induced by an error of $\delta M_5 = 7 \times 10^{-11}\,M_\odot$ in the mass of Jupiter in this first-order approximation.

A slightly more complete, second-order description of the residuals caused by an error in the mass of a Solar System planet is shown in the middle panel of Figure 7.1. In this case, there are two superposed signals: there is a long-term modulation which is identical to what was described above for the first-order approximation, as well as an annual modulation arising from the Earth's orbit being centred on the incorrect SSB position. This latter signal can be explained by the assumed position of the Earth being occasionally closer to, and at other times farther from, the true SSB, depending on the time of year. To generate the residuals in the middle panel of Figure 7.1, simulated TOAs were barycentred using a SSE that was computed while assuming an incorrect mass of Jupiter of $\delta M_5 = 7 \times 10^{-11}\, M_\odot$ (Champion et al., 2010).

Moreover, the residuals introduced by SSE-errors can become severely distorted both when the pulsar parameters are fit to the data, and when the SSE is constructed. In both cases, the fit causes the wrong parameters to assume inaccurate values as they compensate for the incorrectly parameterized differences between the data and the model. The SSE fitting process is extremely complex (e.g. Newhall et al., 1983; Fienga et al., 2008; Folkner et al., 2009), and unavailable, so it is difficult to simulate its effect. However, the bottom panel of Figure 7.1 shows the effect of fitting the pulsar parameters in the presence of the second-order signal described above ($\delta M_5 = 7 \times 10^{-11}\, M_\odot$). Note that the annual variations are nearly completely absorbed when fitting for the pulsar's position and that the long-term sinusoid is distorted when fitting for the frequency and frequency-derivative of the pulsar.

When the pulsar timing data set only covers part of a planet's orbit, the signature of the error in the planet mass will be considerably absorbed into the parameters describing the frequency and frequency-derivative of the pulsar. In other words, a fraction of the long-period sinusoid resembles a linear or quadratic trend, and thus can be absorbed by the frequency and frequency-derivative parameters, respectively (see Figure 7.2). As the observation time span is increased, the degeneracy between planet-mass errors and pulsar spin parameters is broken, allowing the signal of the mass offsets to be recovered. However, until the data span enough time for that to happen, pulsar timing techniques are not sensitive to bodies with orbits longer than roughly twice the span of the data sets used (i.e. bodies with $P_{\mathrm{orb}} \gtrsim 40-50\,\mathrm{yr}$, Uranus, Neptune, Pluto).

Champion et al. (2010) devised a technique for simultaneously fitting timing residuals from multiple pulsars to constrain the masses of the planets of the Solar System in the first-order approximation. They included additional fit parameters describing errors in the masses of Mercury, Venus, Mars, Jupiter, and Saturn,[1] and optimized each of these parameters independently to simultaneously minimize the reduced χ^2 of the residuals of multiple MSPs.

Champion et al. (2010) implemented their algorithm into `TEMPO2`, making it available for others to use and enhance. In § 7.2, we describe a new, improved data set that we use in § 7.3 to measure the masses of the Solar System planets. The results of this analysis are described in § 7.4, and discussed in § 7.5. We conclude this chapter by summarizing additional, related analyses to be undertaken in the future in § 7.6.

7.2 The Data Set

The International Pulsar Timing Array (IPTA) data set is the combination of the long, high-precision, multi-frequency data sets assembled by the European Pulsar Timing Array (EPTA), the North-American Nanohertz Observatory for Gravitational Waves (NANOGrav), and the Parkes Pulsar Timing Array (PPTA) projects. In all, the combined IPTA data set[2] includes 68 324 TOAs from 49 pulsars (Verbiest et al., 2016). The individual pulsar data sets span ∼5 – 25 yr and include observing frequencies in the range 0.3 – 3.1 GHz. The IPTA data set was carefully and uniformly combined. Special care was taken to model the red noise arising from DM variations and spin irregularities, to account for phase offsets between different telescopes and observing systems, and to identify issues arising from incomplete

---

[1] As described earlier, the orbital periods of the even more distant planets are so long that any errors in their masses would induce linear or quadratic trends in the residuals. These trends would be tracelessly absorbed into pulsars' frequency and frequency derivative parameters when fitting. See Figure 7.2.

[2] Specifically, this analysis uses version 1.05 of the IPTA data set. Each incremental version improves the data combination and/or fixes minor issues uncovered.

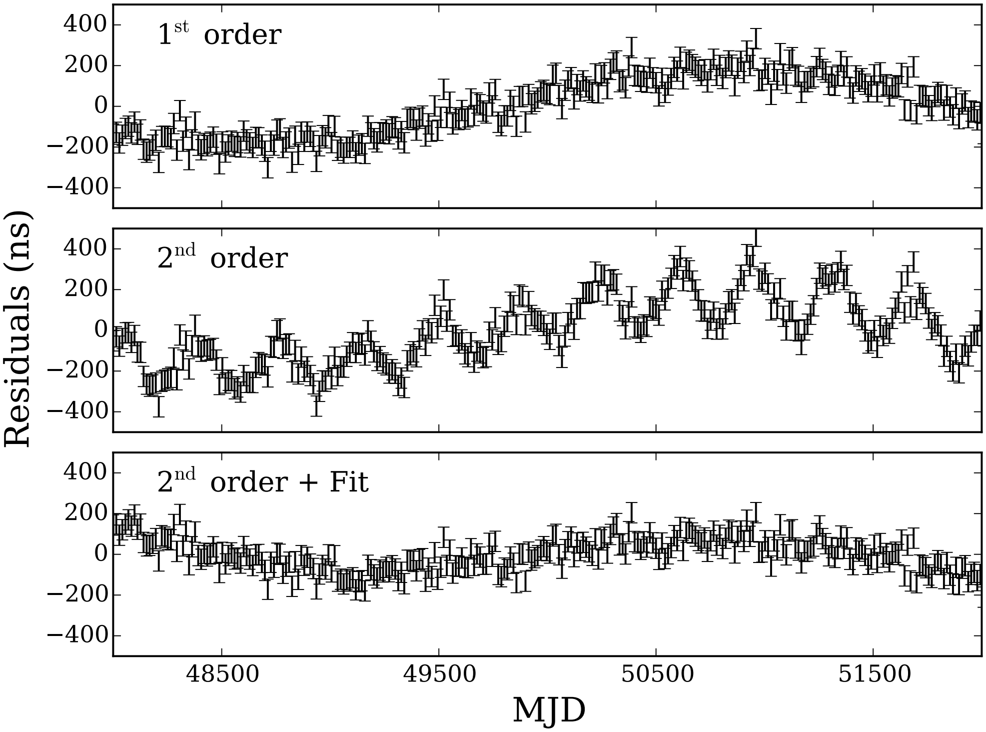

Figure 7.1: *Top* – Simulated timing residuals showing the first-order approximation of the error introduced by an (incorrect) offset in the mass of Jupiter of $\delta M_5 = 7 \times 10^{-11}\ M_{\odot}$. In this approximation, the orbit of the Earth is computed relative to the true SSB and the pulsar timing parameters are assumed to be known exactly. The long-term sinusoidal modulation is due to the SSB being offset in the direction of Jupiter.
Middle – Simulated timing residuals showing the second-order approximation of the error introduced by assuming $\delta M_5 = 7 \times 10^{-11}\ M_{\odot}$. In this case, the orbit of the Earth is computed relative to the assumed SSB. This induces the annual modulations. The pulsar parameters are still assumed to be known exactly.
Bottom – The same second-order approximation of the timing residuals as shown in the middle panel, but after the pulsar parameters have been fit to the data. The annual modulations have been almost entirely absorbed into the parameters describing the pulsar's position and most of the long-term sinusoidal signal have been absorbed into the pulsar's spin frequency and frequency derivative parameters. See Figure 7.2 for more details about the covariance between planet mass errors and pulsar spin parameters.

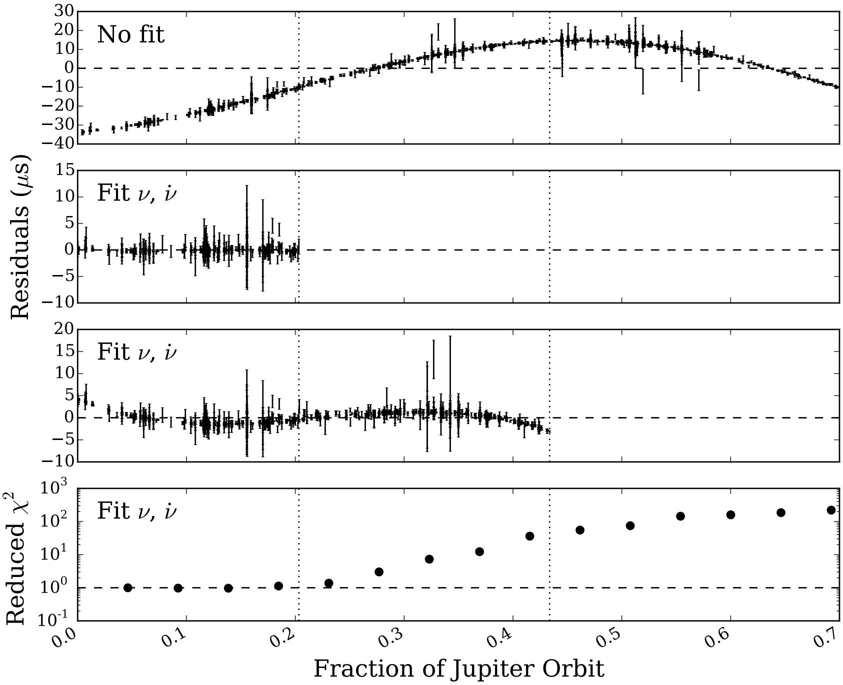

Figure 7.2: *Top* – Timing residuals for PSR J1909−3744 assuming an error in the mass of Jupiter of $\delta M_5 = 10^{-8}\,M_\odot$. No fitting is performed. That is, the values of all timing parameters are kept fixed at their best-known values.
Second from top – Timing residuals from only ~20 % of Jovian orbit, still assuming $\delta M_5 = 10^{-8}\,M_\odot$, but after fitting for the pulsar spin frequency and frequency-derivative, ν and $\dot{\nu}$, respectively. The Jupiter-mass-error signal is almost entirely absorbed. This shows that the mass-error signal is co-variant with the pulsar spin when only a fraction of a planet's orbit is observed.
Third from top – Timing residuals from ~45 % of Jovian orbit, still assuming $\delta M_5 = 10^{-8}\,M_\odot$, but after fitting for ν and $\dot{\nu}$. The Jupiter-mass-error signal can no longer be completely absorbed by the pulsar spin parameters, allowing it to be identified and measured.
Bottom – The reduced χ^2 of the residuals resulting from fitting ν and $\dot{\nu}$ over sub-sets of the data of different lengths. A satisfactory fit results in post-fit residuals that are flat and follow a Gaussian distribution, and reduced $\chi^2 \approx 1$. That is, by fitting the pulsar parameters the signal induced by $\delta M_5 = 10^{-8}\,M_\odot$ has been absorbed. As the time span of the residual being fit increases, the degeneracy between mass-error and spin parameters is broken, giving rise to systematic trends in the residuals with larger amplitudes, and thus resulting in larger reduced χ^2 values.

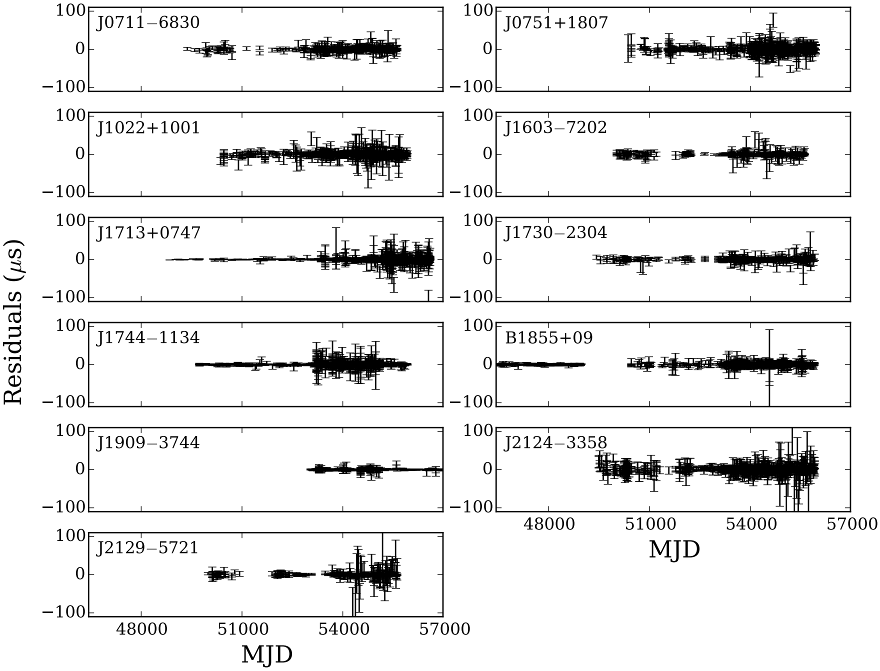

Figure 7.3: Timing residuals of the 11 pulsars used in the analysis of the Solar System presented here. These data were prepared for the IPTA community by Verbiest et al. (2016).

or incorrect observation metadata. The result is the largest, longest, and highest-precision pulsar timing data set ever assembled.

In order to derive stringent constraints on the planet masses, there are important factors to consider when choosing which pulsars of the IPTA data set to include. First, using pulsars with high-precision TOAs allows small signals in their timing residuals to be uncovered. Second, pulsars with observations spanning many years are required to be sensitive to planets with long orbital periods, such as Jupiter ($P_{\mathrm{orb}} \sim 12\,\mathrm{yr}$) and Saturn ($P_{\mathrm{orb}} \sim 29\,\mathrm{yr}$; recall § 7.1 and Figure 7.2). Third, because the signature of a SSE error is correlated between all pulsars, it is beneficial for the data set to include pulsars whose data sets overlap in time. Also, the distribution of the pulsars should be considered. In particular, pulsars closer to the ecliptic plane will be more sensitive to planet-mass offsets and pulsars at different ecliptic longitudes will be sensitive to different phases of the planet orbits. Finally, because red noise contaminates the same part of the pulsar timing spectrum which is searched for planet-mass errors, it is preferable to use pulsars that do not show evidence for strong red noise. While taking these factors into account, we selected an 11-pulsar sub-set of the IPTA data set to use for the analysis of the Solar System presented here. In particular, we chose pulsars with high precision TOAs, long time spans, and low-to-moderate contamination from red noise. The timing residuals and spatial distribution of these 11 pulsars are highlighted in Figures 7.3 and 7.4, respectively. Details about the individual pulsar data sets are listed in Table 7.1.

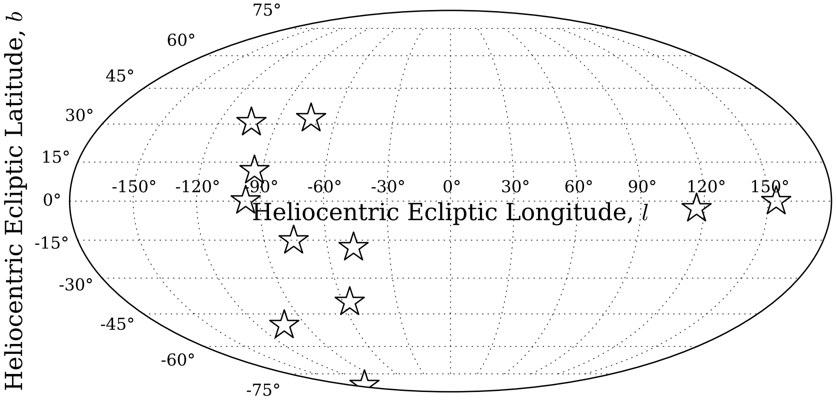

Figure 7.4: Spatial distribution, in ecliptic coordinates, of the 11 pulsars used in the analysis of the Solar System. The residuals of pulsars which are closer to the plane of the Solar System ($b = 0°$) will be more strongly affected by erroneous planet masses.

Table 7.1: Summary of the data set used for planet mass measurements

Pulsar	MJD Range	Time Span (yr)	No. TOAs	Cadence [a] (d)	Residual RMS (μs)
J0711−6830	49373–55619	17.1	549	18.3	2.064
J0751+1807	50363–55948	15.3	1129	11.4	3.704
J1022+1001	50361–55923	15.2	1375	6.5	2.424
J1603−7202	50026–55618	15.3	483	19.3	2.160
J1713+0747	48850–56598	21.2	19983	5.1	0.286
J1730−2304	49421–55920	17.8	563	16.0	2.256
J1744−1134	49729–55925	17.0	2589	8.4	1.052
J1857+0943	46436–55916	26.0	1641	13.4	0.540
J1909−3744	53041–56980	10.8	2623	4.4	0.205
J2124−3358	49489–55924	17.6	1115	7.7	3.138
J2129−5721	49987–55618	15.4	447	19.2	1.656

NOTE. — The data set used here is a subset of the IPTA data setpresented in Verbiest et al. (2016).
[a] The average interval between days on which the pulsar is observed.

7.3 Analysis

We analyzed the 11-pulsar sub-set of the IPTA data set described in § 7.2 with `TEMPO2` using the technique developed by Champion et al. (2010).

Modelling the Red Noise

The pulsars of our data set suffer from varying degrees of red noise. This red noise, be it from intrinsic spin instabilities of the pulsar, unmodelled DM variations, or instrumental effects, indicates that residuals from TOAs closely spaced in time are correlated. This breaks one of the assumptions underlying both the ordinary and weighted least-squares fitting algorithms. Namely, that all measurement errors are uncorrelated (see e.g. Press et al., 2007; Coles et al., 2011). Therefore, in our analysis, we use the generalized least-squares algorithm. This algorithm uses a data covariance matrix to improve the accuracy of the best-fit parameters and their uncertainties.

In `TEMPO2`, the data covariance matrices can be constructed from models of the spectra of the individual pulsars' residuals. The functional form of the power spectrum model used is a power law that flattens at low frequencies (Coles et al., 2011),

$$P(\xi; A, \alpha, \xi_c) = \frac{A}{\left[1 + (\xi/\xi_c)^2\right]^{\alpha/2}} \tag{7.2}$$

where ξ is the frequency, and the three model parameters are the amplitude, A, the spectral index, α, and the corner frequency, ξ_c. The corner frequency, which limits the model power at $\xi < \xi_c$, is used to empirically account for the effect of fitting the pulsar's spin frequency and frequency derivative.

The IPTA data set includes spectral models for pulsars that were found to have significant red noise. However, these models were fit using a two-parameter power-law functional form that does not include a corner frequency. These models were adapted to the form defined in Eq. 7.2 by introducing a corner frequency set to $\xi_c = T_{\rm span}^{-1}$, where $T_{\rm span}$ is the total time span of the observations. This disparity between the functional forms used by the IPTA and `TEMPO2` is a source of concern, so in addition to performing the analysis with the models provided with the IPTA data set, we repeated the analysis using fits of the flattened power-law model (Eq. 7.2) to the residuals' power spectra that were determined with the `spectralModel` plug-in of `TEMPO2`.

Because fitting for the pulsar's frequency and frequency derivative absorbs the power of the red noise at $\xi \lesssim \xi_c$, the true amount of low-frequency noise is unknown. It is possible to create noise models that estimate the underlying covariances in the data by assuming that the power law spectrum observed at $\xi > \xi_c$ can be extended to even lower frequencies. In practice, to avoid modifying `TEMPO2`, we accomplished this by setting $\xi_c' = 0.01\,\mathrm{yr}^{-1}$ and adjusting the amplitude, A', such that the updated noise model matches the original flattened power law spectrum at $\xi \gg \xi_c$. Specifically, we set the amplitude to

$$A' = A\left(\frac{\xi_c}{\xi_c'}\right)^{\alpha}, \tag{7.3}$$

where the primed variables refer to the new (roughly) turn-over-free noise model. When creating these new noise models the spectral index, α, was left unchanged.

To select noise models, for each pulsar, we constructed a uniformly spaced grid of spectral indices from $1.0 \leq \alpha \leq 4.0$ in steps of 0.1 and corner frequencies from $0.1 \leq \xi_c \leq 1.0\,\mathrm{yr}^{-1}$ in steps of $0.1\,\mathrm{yr}^{-1}$. For each point on the grid (i.e. for each α, ξ_c pair) the amplitude, A, that best fit the power spectrum of the pulsar's timing residuals was determined while holding α and ξ_c fixed. Then, for each of the resulting power-law models, the corner frequency was shifted to $\xi_c = 0.01\,\mathrm{yr}^{-1}$ using Eq. 7.3. For each of these shifted models, we computed the whitened power spectrum using the Cholesky decomposition implemented in `spectralModel` (see Coles et al., 2011). Spectral models that produced a non-white whitened power spectrum were discarded. To determine the sensitivity of the planet-mass measurements on our choice of spectral parameters, we compiled three families of noise models. The noise models were selected based on the power they predict at the orbital frequency of Jupiter. This particular frequency was chosen because it is in a regime that is relevant to planet mass measurements, but likely contains significant red noise and is also severely affected by absorption due to fitting the pulsar's frequency and frequency derivative. In one case, for each pulsar, we selected the models that predicted the least power. In another case, we selected the models that predicted the most power. In the final case, we selected models that predicted roughly the mean power predicted by the collection viable models.

Finally, to verify the necessity of modelling the red noise, we performed yet another analysis using a weighted least-squares fitting algorithm (i.e. foregoing covariance matrices altogether).

To summarize, the five sets of analyses and the noise models they used are:

Case A No noise models
Case B IPTA noise models, translated from two-parameter power law to three-parameter power law by introducing a corner frequency at $\xi_c = T_{\mathrm{span}}^{-1}$
Case C Re-computed noise models (with $\xi_c = 0.01\,\mathrm{yr}^{-1}$) chosen to have a low noise power level at the orbital frequency of Jupiter
Case D Re-computed noise models (with $\xi_c = 0.01\,\mathrm{yr}^{-1}$) chosen to have an average noise power level at the orbital frequency of Jupiter
Case E Re-computed noise models (with $\xi_c = 0.01\,\mathrm{yr}^{-1}$) chosen to have a high noise power level at the orbital frequency of Jupiter

A graphical comparison of the noise models for PSR J1713+0747 used in cases B–E is shown in Figure 7.5.

The results of all of five analyses are presented in § 7.4.

Constraining the Masses of the Solar System Planets

For each of the cases defined above, we used the 11-pulsar sub-set of the IPTA data set described in § 7.2 to constrain the masses of Mercury, Venus, Mars, Jupiter and Saturn by fitting for the appropriate δM_i parameters. These parameters, along with those describing the 11 pulsars, were simultaneously optimized using the generalized least-squares algorithm implemented in `TEMPO2`. Each analysis incorporated data covariance matrices determined from the power-law noise models described above to more accurately estimate the fit parameters and their uncertainties.

All analyses used the JPL DE421 SSE. Therefore, all of the resulting mass-offset measurements are relative to the planet masses assumed by this model.

7.4 Results

The planet-mass offsets determined in each of the five analyses are presented in Table 7.3 along with the planet masses assumed in the JPL DE421 SSE. Table 7.3 includes the measured mass differences, δM_i, the resulting mass measurements, M_i, and the significance of the measurements, computed by dividing δM_i by the corresponding uncertainties, σ_i. These results are shown graphically in Figure 7.6, as are the best-known planet mass measurements and the results of Champion et al. (2010), which were derived using a four-pulsar data set.

In the results of case A, we found significant offsets in the masses of Jupiter and Saturn of $\sim$30 and 60 σ, respectively. Such significant deviations were not reproduced in any of the other cases despite the δM_i being of similar magnitudes. This implies that the uncertainties in case A are underestimated, a conclusion consistent with the general findings of Coles et al. (2011) about least-squares fitting in the presence of red noise.

Table 7.2: Spectral noise models used

Pulsar	Amplitude, A	Spectral Index, α	Corner Freq., ξ_c (yr^{-1})
Case B: IPTA noise models			
J0711−6830[a]	–	–	–
J0751+1807	2.64439×10^{-26}	1.92753	0.065402
J1022+1001	1.95808×10^{-40}	2	0.065669
J1603−7202	1.97974×10^{-40}	2	0.065308
J1713+0747	4.98610×10^{-27}	2.77167	0.047136
J1730−2304	2.67297×10^{-40}	2	0.056205
J1744−1134	4.55463×10^{-27}	4.09572	0.058945
J1857+0943[a]	–	–	–
J1909−3744[a]	–	–	–
J2124−3358[a]	–	–	–
J2129−5721[a]	–	–	–
Case C: Re-computed models assuming low noise level			
J0711−6830	6.78523×10^{-23}	2.6	0.01
J0751+1807	9.56082×10^{-26}	1	0.01
J1022+1001	2.58857×10^{-23}	2.1	0.01
J1603−7202	4.43965×10^{-22}	2.8	0.01
J1713+0747	9.34829×10^{-27}	1.2	0.01
J1730−2304	2.38466×10^{-26}	1	0.01
J1744−1134	8.49188×10^{-27}	1	0.01
J1857+0943	4.71076×10^{-27}	1	0.01
J1909−3744	1.03648×10^{-27}	1	0.01
J2124−3358	9.40287×10^{-25}	1.5	0.01
J2129−5721	7.62549×10^{-23}	2.7	0.01
Case D: Re-computed models assuming mean noise level			
J0711−6830	5.87546×10^{-21}	3.8	0.01
J0751+1807	1.21220×10^{-24}	1.5	0.01
J1022+1001	1.31641×10^{-20}	3.7	0.01
J1603−7202	8.04673×10^{-21}	3.4	0.01
J1713+0747	2.61872×10^{-25}	1.7	0.01
J1730−2304	1.86957×10^{-25}	1.3	0.01
J1744−1134	4.10445×10^{-26}	1.2	0.01
J1857+0943	1.63994×10^{-26}	1	0.01
J1909−3744	2.54436×10^{-27}	1.1	0.01
J2124−3358	2.73633×10^{-24}	1.7	0.01
J2129−5721	7.95832×10^{-22}	3.2	0.01
Case E: Re-computed models assuming high noise level			
J0711−6830	2.48894×10^{-20}	3.8	0.01
J0751+1807	8.28700×10^{-20}	4	0.01
J1022+1001	2.88929×10^{-19}	4	0.01
J1603−7202	8.75180×10^{-20}	4	0.01
J1713+0747	1.16542×10^{-23}	2.5	0.01
J1730−2304	3.49654×10^{-22}	2.9	0.01
J1744−1134	2.63474×10^{-21}	3.7	0.01
J1857+0943	7.32943×10^{-25}	1.8	0.01
J1909−3744	7.06797×10^{-24}	2.7	0.01
J2124−3358	7.54315×10^{-24}	1.9	0.01
J2129−5721	3.02419×10^{-21}	3.5	0.01

[a] Red noise model was not considered necessary, no model was created.

Table 7.3: Planet-mass measurements using an 11-pulsar data set

Planet	Mass difference [a] δM_i ($M_\odot$)	Mass [a] (M_i $M_\odot$)	Significance [b] $\delta M_i/\sigma_i$
Case A: No noise models			
Mercury	$-6.0(1.3) \times 10^{-11}$	$1.65954(15) \times 10^{-7}$	4.53
Venus	$-6.1(7) \times 10^{-11}$	$2.447777(7) \times 10^{-6}$	8.86
Mars	$-1.4(4) \times 10^{-11}$	$3.22702(4) \times 10^{-7}$	3.74
Jupiter	$-9.51(32) \times 10^{-11}$	$9.54791821(16) \times 10^{-4}$	29.91
Saturn	$-3.51(6) \times 10^{-10}$	$2.85885322(10) \times 10^{-4}$	61.36
Case B: IPTA noise models			
Mercury	$-0.4(2.1) \times 10^{-11}$	$1.66010(22) \times 10^{-7}$	0.20
Venus	$8.5(1.5) \times 10^{-11}$	$2.447923(15) \times 10^{-6}$	5.65
Mars	$6.1(9) \times 10^{-11}$	$3.22777(9) \times 10^{-7}$	6.67
Jupiter	$-6.5(1.8) \times 10^{-11}$	$9.54791851(24) \times 10^{-4}$	3.64
Saturn	$0.7(6.6) \times 10^{-11}$	$2.8588568(7) \times 10^{-4}$	0.10
Case C: Re-computed models assuming low noise level			
Mercury	$0.6(1.0) \times 10^{-10}$	$1.6607(10) \times 10^{-7}$	0.58
Venus	$0.9(7.6) \times 10^{-11}$	$2.44785(8) \times 10^{-6}$	0.12
Mars	$2.1(5.9) \times 10^{-11}$	$3.2274(6) \times 10^{-7}$	0.35
Jupiter	$-1.0(6) \times 10^{-10}$	$9.5479182(6) \times 10^{-4}$	1.70
Saturn	$-2.0(1.5) \times 10^{-10}$	$2.8588547(15) \times 10^{-4}$	1.32
Case D: Re-computed models assuming mean noise level			
Mercury	$0.4(1.1) \times 10^{-10}$	$1.6605(11) \times 10^{-7}$	0.35
Venus	$-0.5(9.3) \times 10^{-11}$	$2.44783(9) \times 10^{-6}$	0.05
Mars	$1.3(8.3) \times 10^{-11}$	$3.2273(8) \times 10^{-7}$	0.16
Jupiter	$-0.8(1.0) \times 10^{-10}$	$9.5479183(10) \times 10^{-4}$	0.82
Saturn	$-1.7(2.5) \times 10^{-10}$	$2.8588550(25) \times 10^{-4}$	0.68
Case E: Re-computed models assuming high noise level			
Mercury	$-5.3(5.8) \times 10^{-11}$	$1.6596(6) \times 10^{-7}$	0.91
Venus	$7.1(7.7) \times 10^{-11}$	$2.44791(8) \times 10^{-6}$	0.92
Mars	$0.1(1.5) \times 10^{-10}$	$3.2273(15) \times 10^{-7}$	0.10
Jupiter	$-2.3(4.0) \times 10^{-10}$	$9.547917(4) \times 10^{-4}$	0.58
Saturn	$-1.4(7.3) \times 10^{-10}$	$2.858855(7) \times 10^{-4}$	0.19

Masses assumed in the JPL DE421 ephemeris

Planet	Mass [a] (M_i $M_\odot$)	Reference
Mercury	$1.66014(7) \times 10^{-7}$	(1)
Venus	$2.44783829(6) \times 10^{-6}$	(2)
Mars	$3.22715604(20) \times 10^{-7}$	(3)
Jupiter	$9.54791916(16) \times 10^{-4}$	(4)
Saturn	$2.85885673(8) \times 10^{-4}$	(5)

References – (1): Anderson et al. (1987), (2): Konopliv et al. (1999), (3): Konopliv et al. (2006), (4): Folkner et al. (2009), (5): Jacobson et al. (2006)

[a] The numbers in parentheses are the ($1\,\sigma$) uncertainties on the last digit.

[b] Mass difference divided by its uncertainty.

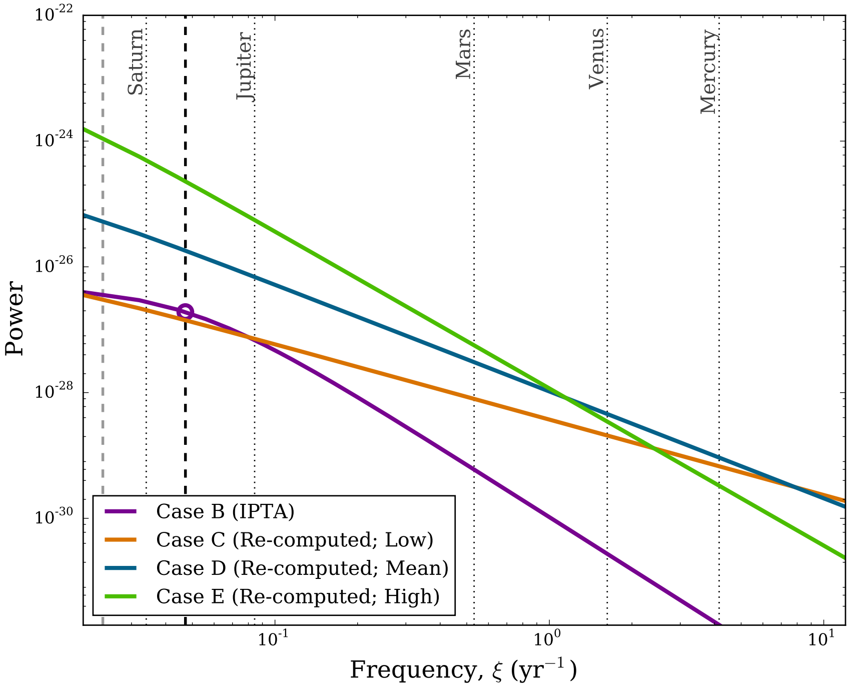

Figure 7.5: A comparison of the spectral noise models of PSR J1713+0747 from cases B–E. (Recall, case A does not include noise models). The parameter values of all three models are given in Table 7.2, and follow the functional form of Eq. 7.2. The corner frequency, ξ_c, of case B is indicated with a coloured circle. The values of ξ_c for cases C, D, and E are all at $0.01\,\mathrm{yr}^{-1}$. The dotted lines indicate the orbital frequencies of the planets studied. The black dashed line indicates T_{span}^{-1}, where T_{span} is the length of the data set, and the light grey dashed line marks $0.5\,T_{\mathrm{span}}^{-1}$, which is roughly the lowest frequency of a planetary orbit that the data sets have sensitivity to. See the text for a description of the different cases.

In the cases where noise models were used, the resulting mass measurements are more consistent with the best-known values. However, there are still somewhat large deviations of up to $\sim 7\,\sigma$ in case B, and modest deviations of up to $\sim 2\,\sigma$ in case C. The results of cases D and E are entirely consistent with the best-known values within the $1\,\sigma$ uncertainties.

Clearly, the results of our analyses depend strongly on the noise models used. Hence, appropriately modelling the red noise in pulsar timing data is essential for making accurate parameter estimations, and determining robust uncertainties.

7.5 Discussion

The best planet mass measurements not using pulsars have precisions $\sim 1-2$ orders of magnitude better than what can currently be obtained with pulsar-based analyses (see Table 7.3). Nevertheless, it is possible to use the results presented here to assess the quality of our subset of the IPTA data given the various noise models of each case. To do this, the best-known values are assumed to be correct, and the consistency between the results of the individual

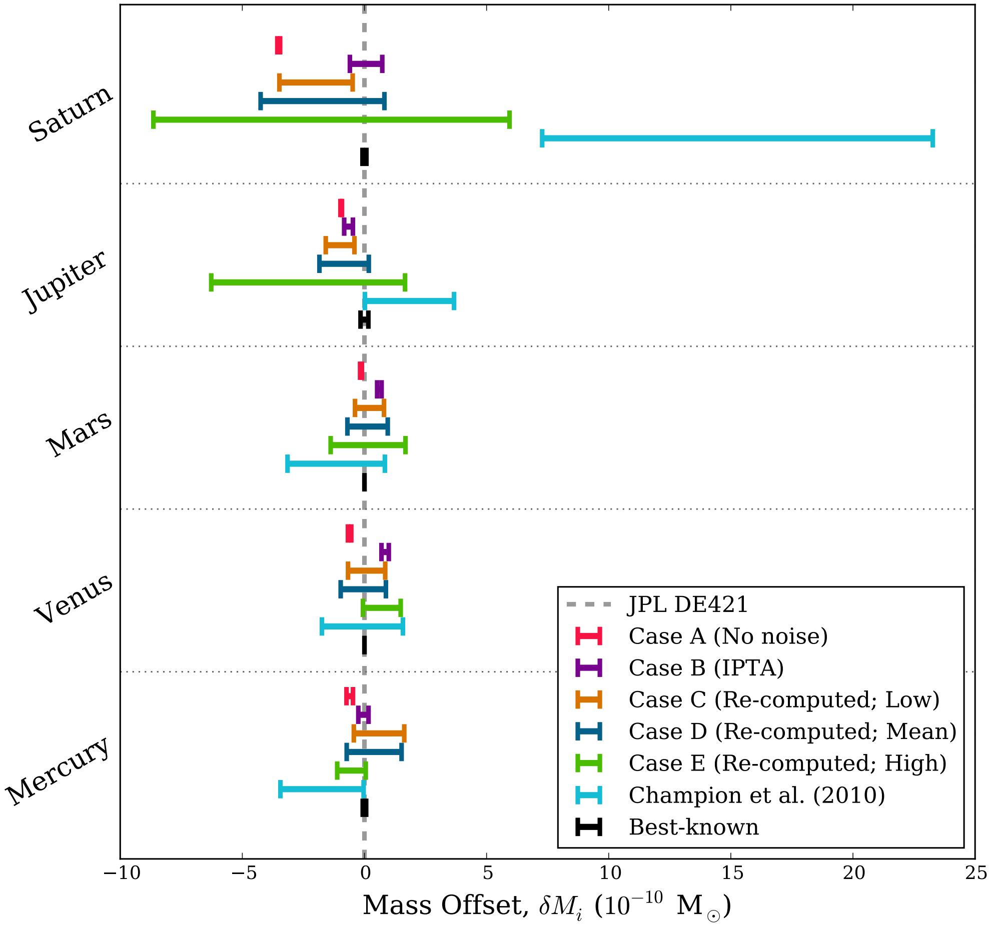

Figure 7.6: Planet-mass offsets, δM_i, with respect to the masses assumed in the JPL DE421 Solar System ephemeris as determined with an 11-pulsar sub-set of the IPTA data set. The five cases correspond to different choices of noise models (see § 7.3 and Table 7.2 for details). The previously published pulsar-based mass measurements of Champion et al. (2010) are also shown. The results based on the analysis presented here are more precise than those of Champion et al. (2010), but the degree of this improvement depends on the noise models used. References for the best-known measurements can be found in Table 7.3.

cases and the best-known values is evaluated.

As mentioned above, the results of case A are highly inconsistent with the best-known planet masses. This demonstrates the necessity of accounting for data covariances when fitting for planet masses. It is important to note that the same is probably also true when fitting for other long-timescale parameters, such as those describing the GWB.

The significant δM_i found in cases B and C might be due to underestimating the amount of red noise in the IPTA data, and thus, likely results in slightly underestimated uncertainties. In contrast, by assuming high levels of noise, case E likely provides the most conservative (i.e. largest) uncertainties. The results of case D are entirely consistent with the masses assumed in the JPL DE421 SSE and provide more precise mass measurements than what was previously published by Champion et al. (2010), who used a 4-pulsar data set with a shorter overall time span.

The analysis presented here can likely be improved upon. In particular, including more pulsars, with a more uniform distribution of ecliptic longitudes, should provide more precise results. Furthermore, the single power-law noise models we used are satisfactory, but can be more complete. In particular, by analyzing the IPTA data set, Lentati et al. (2016) found evidence for different noise processes operating in distinct observing systems and/or observing bands. Moreover, because multi-frequency observations are not available throughout the entire IPTA data set, limiting the effectiveness of modelling DM variations is limited. In particular, epochs where DM measurements were not available will have excess DM noise compared to epochs for which DM variations are well-measured and can be corrected for. The presence of multiple noise sources indicates that the simplistic, single-power-law models used here are sub-optimal. Therefore, allowing for multiple noise processes, each described by a different power law, will likely produce more robust results mass measurements and smaller, more reliable uncertainties.

Properly modelling covariances in the timing data is crucial to measuring the Solar System planet masses. The same will be true for pulsar-based GW searches. The GWB signal is expected to be a red power law, thus estimations of the data covariances will also be important for constraining and/or reliably detecting the GWB. Based on the analysis conducted here, one possible method of verifying a given set of noise models is to measure the masses of Jupiter and Saturn, and check that the resulting masses are consistent with the best-known measurements, as was done here. In this regard, the noise models of case A are woefully inadequate, those of cases B and C are better, but still slightly incomplete or inaccurate, and the models of cases D and E are likely sufficient for GWB searches. Future noise models should also be verified against the planet-mass analysis in this way.

Finally, given the reasonable noise models of cases D and E, we find no offsets in the masses of the Solar System planets and no systematics in the timing residuals. This indicates that the JPL DE421 SSE is sufficient for high-precision PTA experiments, as expected. Another possible technique for assessing the accuracy of SSEs is described below.

7.6 Future work

As we have shown in § 7.4, the details of the noise models used can significantly impact planet-mass estimates. Thus, a natural follow-up to our work is to repeat the analysis using more complete descriptions of the noise and data covariances, as described in § 7.5. Recently, there has been significant progress in implementing efficient samplers of the pulsar-parameter phase space that may help with this task (Lentati et al., 2016). In particular, with these new sampling techniques, it may even be possible to simultaneously constrain the planet masses, determine the optimal pulsar noise models, and optimize the pulsar parameters. In principle, this would provide the most reliable measurements and uncertainty estimates possible with the IPTA data, although at considerable additional computational complexity. An even more computationally demanding alternative is to directly including pulsar data when constructing SSEs. This ambitious option would require merging the timing analysis procedure with the process of constructing a SSE.

Future extensions of the IPTA data set, both in terms of the number of pulsars included and the time span of observations, will help to improve the quality of planet-mass measurements. To estimate the potential for improvement, we have repeated our analysis on simulated data sets to determine the dependence of the planet mass measurement uncertainties, σ_i, on number of pulsars and the observation span. To determine the scaling of σ_i with the number of pulsars, we simulated TOAs for the IPTA pulsars. The resulting TOAs were spaced every 14 d and spanned a total of 6000 d (~55 % of Saturnian orbit). Optimistically, the timing residuals of each pulsar had an RMS of 100 ns, and contained no red noise. We measured σ_i for planets out to Saturn (excluding the Earth) using between 3 and 20 pulsars. The results of this idealized simulation are shown in the top panel of Figure 7.7. To measure how σ_i depends on T_{span}, we also simulated data consisting of 4 pulsars with TOAs every 10 d, again with white-noise-only residuals with an RMS of 100 ns. We measured the corresponding σ_i for data spans between 20 and 17500 d (i.e. up to ~45 yr). The resulting σ_i as a function of the number of orbits observed is presented in the bottom panel of Figure 7.7.

Additional studies of the Solar System are possible with the IPTA data set. In preparation for some of these projects, we have added flexible SSE-reading code to `TEMPO2`. It is now possible to read SSE files in the format used by the NASA SPICE toolkit,[1] as well as the format expected by the CALCEPH library. These modifications allow `TEMPO2` to use the INPOP models produced by the French "institut de mécanique céleste et de calcul des éphémérides" (IMCEE), as well as the EPM models produced by the Russian Laboratory of Ephemeris Astronomy, in addition to the JPL SSEs it can currently read. Therefore, it will be possible to compare the three families of SSEs (JPL, INPOP, EPM). This will help with the important task of verifying that none of the modern SSEs available introduce excess systematic noise into pulsar timing analyses.

Furthermore, the IPTA data set should have enough sensitivity to constrain the mass of Ceres ($M_{\mathrm{Ceres}} = 4.75(3) \times 10^{-10}\,M_{\odot}$), the most massive asteroid (Baer & Chesley, 2008). Thus, we have also extended `TEMPO2` to include mass-error parameters for arbitrary bodies listed in the SPICE-format JPL SSEs, including the major asteroids. With this modification, it is now possible to use the IPTA data set to compute constraints on the mass of Ceres, as well as other large asteroids that are close to the limit of our sensitivity, such as Pallas and Vesta ($M_{\mathrm{Pallas}} = 1.06(16) \times 10^{-10}\,M_{\odot}$ and $M_{\mathrm{Vesta}} = 1.3 \times 10^{-10}\,M_{\odot}$, respectively; Baer & Chesley 2008).

Finally, another more ambitious application of the IPTA data is to search for unknown bodies. A new technique described by Hobbs (2013a) simultaneously fits the timing data from multiple pulsars to compute the offset of the SSB relative to the position of the SSB assumed by the SSE. This eliminates the need to know the exact position of a body to predict its affect on the SSB, as is the case for the Champion et al. (2010) algorithm. Thus, in principle, this new technique can be used to identify the presence of unknown massive bodies, including objects lying outside the ecliptic plane. However, fitting pulsar parameters could greatly distort the signal of such a body, making it hard to study in detail. A firm understanding of how the signal of an offset in the position of the SSB is masked by pulsar fitting is required to do a complete and thorough analysis with the Hobbs (2013a) technique. Such studies would be complementary to the work presented here, and would allow further verification that the SSEs used for high-precision PTA studies are sufficiently accurate.

---

[1] http://naif.jpl.nasa.gov/naif/toolkit.html

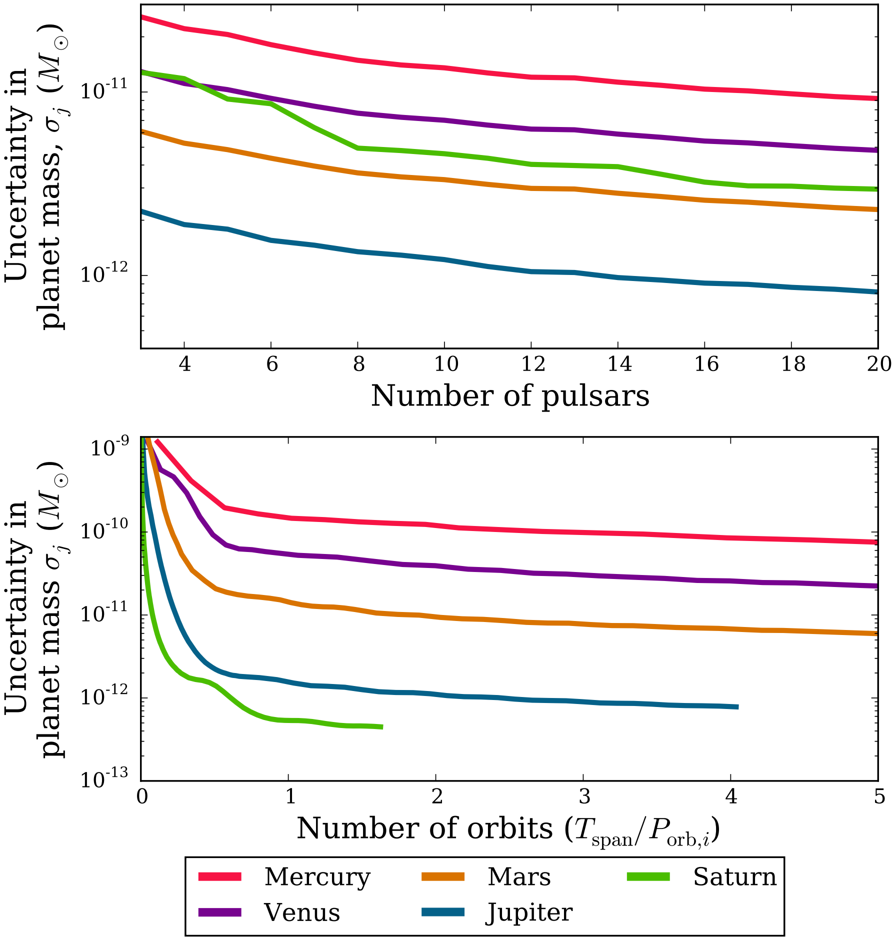

Figure 7.7: *Top* – Simulated improvement in planet mass precision as a function of the number of pulsars included in the fit.
Bottom – Simulated improvement in planet mass precision as as function of the number of orbits spanned by the observations (i.e. the observation time span, T_{span} divided by the planet's orbital period, $P_{\mathrm{orb},i}$).
See the text for details about how the data sets were simulated.

8

CONCLUSIONS

Pulsars are remarkable astrophysical objects. Their extreme properties have made them indispensable tools for a broad range of applications, including the study of ultra-dense matter, the tests of relativistic theories of gravity, the census of the Galactic population of pulsars, and the search for low-frequency gravitational waves.

Of the roughly 2500 pulsars known to date, the majority were found in large-scale, non-targeted searches with the largest, most sensitive radio telescopes. Many different algorithms have been developed to thoroughly search radio observations for the presence of unknown periodic and impulsive signals, as well as to excise the deleterious effect of radio frequency interference (RFI). The detailed implementations of these algorithms depends on the parameter space to be searched and the characteristics of the data.

I described the analysis of Mock spectrometer observations from the on-going PALFA survey at the Arecibo Observatory in Puerto Rico using the `PRESTO` software suite. The fully-automated analysis pipeline I developed was used to find 40 pulsars, bringing the total number of pulsars found in the survey to 144. I devised and applied a novel technique for robustly determining the sensitivity of survey observations, including the effect of biases on the data analysis procedure, as well as the effect of red noise and RFI. Simulations using the results of my realistic sensitivity analysis suggest that $33 \pm 3\%$ of pulsars were missed despite being brighter than previous, idealized predictions of the survey's sensitivity threshold. By accounting for this fraction of missed pulsars, I estimated that the PALFA survey should have detected 224 ± 16 pulsars to date, which is consistent with the 241 actual detections.

Most of the scientific studies that exploit pulsars require a so-called pulsar timing analysis of many monitoring observations, which are often spread over many years. The resulting phase-coherent timing models are capable of accounting for every rotation of the pulsar. This is possible only by including the effects of the spin of the pulsar, its motion through the Galaxy, propagation delays in the interstellar medium, the motion of the Earth, and if applicable, the pulsar's binary dynamics.

I derived a phase-coherent timing model for PSR J1952+2630, a 26.7 ms pulsar in a binary system with a massive white dwarf companion and which was found in the PALFA survey. My collaborators and I combined information about the pulsar's binary motion with models of binary stellar evolution to determine that the system underwent Case BB Roche-lobe overflow. We used simulations of stellar evolution to hypothesize the composition of the pulsar's companion and constrain the accretion episode that spun-up the pulsar to its fast rotation rate. We predict that with additional observations spread over the next ~10 years, this pulsar might enable useful constraints on relativistic gravity.

To capitalize on the high-precision timing analyses possible for extremely stably rotating millisecond-period pulsars (MSPs), long-running, multi-frequency observing campaigns such as those of the European Pulsar Timing Array (EPTA) were instituted at several radio telescopes, including the Effelsberg 100-m radio telescope. The ultimate goal of the EPTA is to use pulsar timing data to detect low-frequency gravitational waves (GWs). The most likely source being the GW background (GWB) from the cosmic population of super-massive black-hole binaries. I provided an overview of the new PSRIX instrument installed at Effelsberg, a data recording system providing improved sensitivity for pulsar timing observations. PSRIX is flexible, and can be used in conjunction with receivers operating at different frequencies. I also evaluated the prospects of complementing Effelsberg's existing monitoring campaigns at

1.4 and 2.6 GHz with observations at 5 and 9 GHz. These high-frequency data could reduce the effect of variations in the ISM that result in low-frequency noise that interferes with searches for GWs.

By combining EPTA data with similar projects based in Australia and North America as part of the International Pulsar Timing Array (IPTA) project, the community has assembled the longest, largest, highest-precision pulsar timing data set to date. This data set will undoubtedly provide the most stringent constraints on the amplitude of the GWB, and potentially be used to detect it. The IPTA data set is of unmatched quality, making it suitable for many other research projects. I have begun conducting an official IPTA project to study the Solar System. In particular, I used a subset of the IPTA data to measure the masses of Mercury, Venus, Mars, Jupiter and Saturn. Part of this analysis involved modelling of the low-frequency noise affecting the pulsars. I found that the resulting planet masses and uncertainties are significantly impacted when the noise models are varied. Focusing on the conservative estimates, I find that my results are more precise and more accurate than the previous pulsar-based measurements. This improvement is owing to the exceptional quality of the IPTA data set. Moreover, the IPTA data set will likely yield even better mass measurements in the future if the analysis is repeated with noise models that incorporate additional details about the multiple noise processes affecting the pulsars. Furthermore, given the strong dependence of the planet mass measurements on the choice of noise models and that the orbital frequencies of Jupiter and Saturn are in the same regime as the expected GWB signal, the analysis I performed here can be used as an example of how to verify that noise models are sufficient for use in searches for the GWB. Other pulsar noise models should be verified in the same manner.

By continuing to conduct sensitive pulsar surveys, refining data analysis methods, studying interesting discoveries, and compiling large, high-precision timing data sets, as I have presented here, it is possible to exploit the vast scientific potential of pulsars.

BIBLIOGRAPHY

Allen, B., Knispel, B., Cordes, J. M., et al. 2013, ApJ, 773, 91

Alpar, M. A., Cheng, A. F., Ruderman, M. A., & Shaham, J. 1982, Nat., 300, 728

Anderson, J. D., Colombo, G., Espsitio, P. B., Lau, E. L., & Trager, G. B. 1987, Icarus, 71, 337

Antoniadis, J., van Kerkwijk, M. H., Koester, D., et al. 2012, MNRAS, 423, 3316

Antoniadis, J., Freire, P. C. C., Wex, N., et al. 2013, Science, 340, 448

Archibald, A. M., Stairs, I. H., Ransom, S. M., et al. 2009, Science, 324, 1411

Arnett, D. 1996, Supernovae and Nucleosynthesis

Arzoumanian, Z., Brazier, A., Burke-Spolaor, S., et al. 2015, ArXiv e-prints, arXiv:1505.07540

Babak, S., Petiteau, A., Sesana, A., et al. 2016, MNRAS, 455, 1665

Backer, D. C., Dexter, M. R., Zepka, A., et al. 1997, PASP, 109, 61

Baer, J., & Chesley, S. R. 2008, Celestial Mechanics and Dynamical Astronomy, 100, 27

Barr, E. D., Guillemot, L., Champion, D. J., et al. 2013a, MNRAS, 429, 1633

Barr, E. D., Champion, D. J., Kramer, M., et al. 2013b, MNRAS, 435, 2234

Bassa, C. G., Janssen, G. H., Karuppusamy, R., et al. 2016, MNRAS, 456, 2196

Bates, S. D., Lorimer, D. R., Rane, A., & Swiggum, J. 2014, MNRAS, 439, 2893

Bates, S. D., Lorimer, D. R., & Verbiest, J. P. W. 2013, MNRAS, 431, 1352

Berkhuijsen, E. M., & Müller, P. 2008, A&A, 490, 179

Bhat, N. D. R., Cordes, J. M., Camilo, F., Nice, D. J., & Lorimer, D. R. 2004, ApJ, 605, 759

Bhat, N. D. R., Gupta, Y., & Rao, A. P. 1998, ApJ, 500, 262

Bhattacharya, D., & van den Heuvel, E. P. J. 1991, Phys. Rep., 203, 1

Bildsten, L., Chakrabarty, D., Chiu, J., et al. 1997, ApJ Supp., 113, 367

Blandford, R., & Teukolsky, S. A. 1976, ApJ, 205, 580

Breton, R. P., Kaspi, V. M., Kramer, M., et al. 2008, Science, 321, 104

Britton, M. C. 2000, ApJ, 532, 1240

Bruck, Y. M., & Ustimenko, B. Y. 1973, Nature Physical Science, 242, 58

Burbidge, G. R., & Strittmatter, P. A. 1968, Nat., 218, 433

Burgay, M., Rea, N., Israel, G. L., et al. 2006, MNRAS, 372, 410

Burke-Spolaor, S., & Bailes, M. 2010, MNRAS, 402, 855

Burke-Spolaor, S., Bailes, M., Ekers, R., Macquart, J.-P., & Crawford, III, F. 2011, ApJ, 727, 18

Burke-Spolaor, S., Johnston, S., Bailes, M., et al. 2012, MNRAS, 423, 1351

Caballero, R. N., Lee, K. J., Lentati, L., et al. 2015, ArXiv e-prints, arXiv:1510.09194

Camilo, F., Ransom, S. M., Halpern, J. P., & Reynolds, J. 2007a, ApJL, 666, L93

Camilo, F., Ransom, S. M., Halpern, J. P., et al. 2006, Nat., 442, 892

Camilo, F., Reynolds, J., Johnston, S., Halpern, J. P., & Ransom, S. M. 2008, ApJ, 679, 681

Camilo, F., Cognard, I., Ransom, S. M., et al. 2007b, ApJ, 663, 497

Camilo, F., Ransom, S. M., Peñalver, J., et al. 2007c, ApJ, 669, 561

Carroll, B. W., & Ostlie, D. A. 2006, *An Introduction to Modern Astrophysics and*

Cosmology, 2nd ed. (Addison-Wesley)

Champion, D. J., Ransom, S. M., Lazarus, P., et al. 2008, Science, 320, 1309

Champion, D. J., Hobbs, G. B., Manchester, R. N., et al. 2010, ApJL, 720, L201

Coenen, T., van Leeuwen, J., Hessels, J. W. T., et al. 2014, A&A, 570, A60

Cognard, I., Guillemot, L., Johnson, T. J., et al. 2011, ApJ, 732, 47

Cole, T. W. 1969, Nat., 221, 29

Coles, W., Hobbs, G., Champion, D. J., Manchester, R. N., & Verbiest, J. P. W. 2011, MNRAS, 418, 561

Comella, J. M., Craft, H. D., Lovelace, R. V. E., & Sutton, J. M. 1969, Nat., 221, 453

Cook, G. B., Shapiro, S. L., & Teukolsky, S. A. 1994, ApJ, 424, 823

Cordes, J. M. 2002, in Astronomical Society of the Pacific Conference Series, Vol. 278, Single-Dish Radio Astronomy: Techniques and Applications, ed. S. Stanimirovic, D. Altschuler, P. Goldsmith, & C. Salter, 227–250

Cordes, J. M., & Chernoff, D. F. 1997, ApJ, 482, 971

Cordes, J. M., & Lazio, T. J. W. 2002, ArXiv Astrophysics e-prints, arXiv:astro-ph/0207156

Cordes, J. M., & McLaughlin, M. A. 2003, ApJ, 596, 1142

Cordes, J. M., & Shannon, R. M. 2010, ArXiv e-prints, arXiv:1010.3785

Cordes, J. M., Shannon, R. M., & Stinebring, D. R. 2015, ArXiv e-prints, arXiv:1503.08491

Cordes, J. M., Freire, P. C. C., Lorimer, D. R., et al. 2006, ApJ, 637, 446

Coriat, M., Fender, R. P., & Dubus, G. 2012, MNRAS, 424, 1991

Crawford, F., Hessels, J. W. T., & Kaspi, V. M. 2007, ApJ, 662, 1183

Crawford, F., Stovall, K., Lyne, A. G., et al. 2012, ApJ, 757, 90

Dai, S., Hobbs, G., Manchester, R. N., et al. 2015, MNRAS, 449, 3223

Damour, T., & Deruelle, N. 1986, Ann. Inst. Henri Poincaré Phys. Théor., Vol. 44, No. 3, p. 263 - 292, 44, 263

Damour, T., & Esposito-Farèse, G. 1998, Phys. Rev. D, 58, 042001

Damour, T., & Taylor, J. H. 1991, ApJ, 366, 501

—. 1992, Phys. Rev. D, 45, 1840

Davies, J. G., Hunt, G. C., & Smith, F. G. 1969, Nat., 221, 27

Demorest, P. B., Pennucci, T., Ransom, S. M., Roberts, M. S. E., & Hessels, J. W. T. 2010, Nat., 467, 1081

Demorest, P. B., Ferdman, R. D., Gonzalez, M. E., et al. 2013, ApJ, 762, 94

Deneva, J. S., Stovall, K., McLaughlin, M. A., et al. 2013, ApJ, 775, 51

Deneva, J. S., Cordes, J. M., McLaughlin, M. A., et al. 2009, ApJ, 703, 2259

Deneva, J. S., Freire, P. C. C., Cordes, J. M., et al. 2012, ApJ, 757, 89

Desvignes, G., Cognard, I., Champion, D., et al. 2013, in IAU Symposium, Vol. 291, IAU Symposium, ed. J. van Leeuwen, 375–377

Desvignes, G., Caballero, R. N., Lentati, L., et al. 2016, ArXiv e-prints, arXiv:1602.08511

Detweiler, S. 1979, ApJ, 234, 1100

Dewey, R. J., Taylor, J. H., Weisberg, J. M., & Stokes, G. H. 1985, ApJL, 294, L25

Dolch, T., Lam, M. T., Cordes, J., et al. 2014, ApJ, 794, 21

Dowd, A., Sisk, W., & Hagen, J. 2000, in Astronomical Society of the Pacific Conference Series, Vol. 202, IAU Colloq. 177: Pulsar Astronomy - 2000 and Beyond, ed. M. Kramer, N. Wex, & R. Wielebinski, 275

Durney, B. R., Faulkner, J., Gribbin, J. R., & Roxburgh, I. W. 1968, Nat., 219, 20

Eatough, R. P., Keane, E. F., & Lyne, A. G. 2009, MNRAS, 395, 410

Eatough, R. P., Kramer, M., Lyne, A. G., & Keith, M. J. 2013a, MNRAS, 431, 292

Eatough, R. P., Molkenthin, N., Kramer, M., et al. 2010, MNRAS, 407, 2443

Eatough, R. P., Falcke, H., Karuppusamy, R., et al. 2013b, Nat., 501, 391

Edwards, R. T., Hobbs, G. B., & Manchester, R. N. 2006, MNRAS, 372, 1549

Ergma, E., Sarna, M. J., & Antipova, J. 1998, MNRAS, 300, 352

Everett, J. E., & Weisberg, J. M. 2001, ApJ, 553, 341

Faucher-Giguère, C.-A., & Kaspi, V. M. 2006, ApJ, 643, 332

Faulkner, J., & Gribbin, J. R. 1968, Nat., 218, 734

Fienga, A., Manche, H., Laskar, J., & Gastineau, M. 2008, A&A, 477, 315

Fisz, M. 1963, Probability theory and mathematical statistics (Polish Scientifique)

Folkner, W. M., Williams, J. G., & Boggs, D. H. 2009, Interplanetary Network Progress Report, 178, C1

Ford, J. M., Demorest, P., & Ransom, S. 2010, in Society of Photo-Optical Instrumentation Engineers (SPIE) Conference Series, Vol. 7740, Society of Photo-Optical Instrumentation Engineers (SPIE) Conference Series, 0

Freire, P. C., Kramer, M., & Lyne, A. G. 2001, MNRAS, 322, 885

Freire, P. C. C., & Tauris, T. M. 2014, MNRAS, 438, L86

Freire, P. C. C., & Wex, N. 2010, MNRAS, 409, 199

Freire, P. C. C., Bassa, C. G., Wex, N., et al. 2011, MNRAS, 412, 2763

Freire, P. C. C., Wex, N., Esposito-Farèse, G., et al. 2012, MNRAS, 423, 3328

Gold, T. 1968, Nat., 218, 731

—. 1969, Nat., 221, 25

Goldreich, P., & Julian, W. H. 1969, ApJ, 157, 869

Gonzalez, M. E., Stairs, I. H., Ferdman, R. D., et al. 2011, ApJ, 743, 102

Halpern, J. P., Gotthelf, E. V., Becker, R. H., Helfand, D. J., & White, R. L. 2005, ApJL, 632, L29

Hankins, T. H. 1971, ApJ, 169, 487

Hankins, T. H., Kern, J. S., Weatherall, J. C., & Eilek, J. A. 2003, Nat., 422, 141

Haslam, C. G. T., Salter, C. J., Stoffel, H., & Wilson, W. E. 1982, A&A Supp., 47, 1

Hayakawa, S. 1985, Phys. Rep., 121, 317

Helfand, D. J., Manchester, R. N., & Taylor, J. H. 1975, ApJ, 198, 661

Hellings, R. W., & Downs, G. S. 1983, ApJL, 265, L39

Henning, P. A., Springob, C. M., Minchin, R. F., et al. 2010, AJ, 139, 2130

Hermsen, W., Hessels, J. W. T., Kuiper, L., et al. 2013, Science, 339, 436

Hessels, J. W. T., Ransom, S. M., Stairs, I. H., et al. 2006, Science, 311, 1901

Hessels, J. W. T., Nice, D. J., Gaensler, B. M., et al. 2008, ApJL, 682, L41

Hewish, A., Bell, S. J., Pilkington, J. D. H., Scott, P. F., & Collins, R. A. 1968, Nat., 217, 709

Hobbs, G. 2013a, in IAU Symposium, Vol. 291, IAU Symposium, ed. J. van Leeuwen, 165–170

Hobbs, G. 2013b, Classical and Quantum Gravity, 30, 224007

Hobbs, G. B., Edwards, R. T., & Manchester, R. N. 2006, MNRAS, 369, 655

Hotan, A. W., van Straten, W., & Manchester, R. N. 2004a, PASA, 21, 302

—. 2004b, PASA, 21, 302

Iben, Jr., I., & Livio, M. 1993, PASP, 105, 1373

Ivanova, N., Justham, S., Chen, X., et al. 2013, A&A Rev., 21, 59

Jacobson, R. A., Antreasian, P. G., Bordi, J. J., et al. 2006, AJ, 132, 2520

Jacoby, B. A., Bailes, M., Ord, S. M., Knight, H. S., & Hotan, A. W. 2007, ApJ, 656, 408

Jacoby, B. A., Hotan, A., Bailes, M., Ord, S., & Kulkarni, S. R. 2005, ApJL, 629, L113

Janssen, G. H., Stappers, B. W., Bassa, C. G., et al. 2010, A&A, 514, A74

Janssen, G. H., Stappers, B. W., Kramer, M., et al. 2008, A&A, 490, 753

Jenet, F. A., Hobbs, G. B., Lee, K. J., & Manchester, R. N. 2005, ApJL, 625, L123

Jenet, F. A., Lommen, A., Larson, S. L., & Wen, L. 2004, ApJ, 606, 799

Johnston, H. M., & Kulkarni, S. R. 1991, ApJ, 368, 504

Karako-Argaman, C., Kaspi, V. M., Lynch, R. S., et al. 2015, ApJ, 809, 67

Kaspi, V. M., Manchester, R. N., Johnston, S., Lyne, A. G., & D'Amico, N. 1996, AJ, 111, 2028

Kaspi, V. M., Taylor, J. H., & Ryba, M. F. 1994, ApJ, 428, 713

Keane, E. F. 2010, PhD thesis, University of Manchester

Keane, E. F., & Kramer, M. 2008, MNRAS, 391, 2009

Keith, M. J., Eatough, R. P., Lyne, A. G., et al. 2009, MNRAS, 395, 837

Keith, M. J., Jameson, A., van Straten, W., et al. 2010a, MNRAS, 409, 619

—. 2010b, MNRAS, 409, 619

Keith, M. J., Johnston, S., Ray, P. S., et al. 2011, MNRAS, 414, 1292

Keith, M. J., Coles, W., Shannon, R. M., et al. 2013, MNRAS, 429, 2161

Kiddle, C., Andrecut, M., Brazier, A., et al. 2011, in Astronomical Society of the Pacific Conference Series, Vol. 442, Astronomical Data Analysis Software and Systems XX, ed. I. N. Evans, A. Accomazzi, D. J. Mink, & A. H. Rots, 669

Kippenhahn, R., & Weigert, A. 1990, Stellar Structure and Evolution (Springer, Berlin)

Knispel, B., Allen, B., Cordes, J. M., et al. 2010, Science, 329, 1305

Knispel, B., Lazarus, P., Allen, B., et al. 2011, ApJL, 732, L1

Knispel, B., Eatough, R. P., Kim, H., et al. 2013, ApJ, 774, 93

Kondratiev, V. I., McLaughlin, M. A., Lorimer, D. R., et al. 2009, ApJ, 702, 692

Kondratiev, V. I., Verbiest, J. P. W., Hessels, J. W. T., et al. 2015, ArXiv e-prints, arXiv:1508.02948

Konopliv, A. S., Banerdt, W. B., & Sjogren, W. L. 1999, Icarus, 139, 3

Konopliv, A. S., Yoder, C. F., Standish, E. M., Yuan, D.-N., & Sjogren, W. L. 2006, Icarus, 182, 23

Kouwenhoven, M. L. A., & Voûte, J. L. L. 2001, A&A, 378, 700

Kramer, M. 1998, ApJ, 509, 856

Kramer, M., & Champion, D. J. 2013, Classical and Quantum Gravity, 30, 224009

Kramer, M., Lange, C., Lorimer, D. R., et al. 1999, ApJ, 526, 957

Kramer, M., Lyne, A. G., O'Brien, J. T., Jordan, C. A., & Lorimer, D. R. 2006a, Science, 312, 549

Kramer, M., Xilouris, K. M., Lorimer, D. R., et al. 1998, ApJ, 501, 270

Kramer, M., Stairs, I. H., Manchester, R. N., et al. 2006b, Science, 314, 97

Kuniyoshi, M., Verbiest, J. P. W., Lee, K. J., et al. 2015, ArXiv e-prints, arXiv:1507.03732

Lam, M. T., Cordes, J. M., Chatterjee, S., & Dolch, T. 2015, ApJ, 801, 130

Lange, C., Camilo, F., Wex, N., et al. 2001, MNRAS, 326, 274

Large, M. I., Vaughan, A. E., & Mills, B. Y. 1968, Nat., 220, 340

Lasota, J.-P. 2001, New Astron. Rev., 45, 449

Lattimer, J. M., & Prakash, M. 2004, Science, 304, 536

Lazaridis, K., Wex, N., Jessner, A., et al. 2009, MNRAS, 400, 805

Lazaridis, K., Verbiest, J. P. W., Tauris, T. M., et al. 2011, MNRAS, 584

Lazarus, P., Kaspi, V. M., Champion, D. J., Hessels, J. W. T., & Dib, R. 2012, ApJ, 744, 97

Lazarus, P., Tauris, T. M., Knispel, B., et al. 2014, MNRAS, 437, 1485

Lazarus, P., Brazier, A., Hessels, J. W. T., et al. 2015, ApJ, 812, 81

Lee, K. J., Stovall, K., Jenet, F. A., et al. 2013, MNRAS, 433, 688

Lee, K. J., Bassa, C. G., Janssen, G. H., et al. 2014, MNRAS, 441, 2831

Lentati, L., Alexander, P., Hobson, M. P., et al. 2014, MNRAS, 437, 3004

Lentati, L., Taylor, S. R., Mingarelli, C. M. F., et al. 2015, ArXiv e-prints, arXiv:1504.03692

Lentati, L., Shannon, R. M., Coles, W. A., et al. 2016, MNRAS, arXiv:1602.05570

Levin, L., Bailes, M., Bates, S., et al. 2010, arXiv:1007.1052v1, arXiv:1007.1052

Lewin, W. H. G., van Paradijs, J., & van den Heuvel, E. P. J. 1997, X-ray Binaries

Liu, B., McIntyre, T., Terzian, Y., et al. 2013, AJ, 146, 80

Liu, K., Eatough, R. P., Wex, N., & Kramer, M. 2014a, MNRAS, 445, 3115

Liu, K., Keane, E. F., Lee, K. J., et al. 2012, MNRAS, 420, 361

Liu, K., Desvignes, G., Cognard, I., et al. 2014b, MNRAS, 443, 3752

Lommen, A. N., Zepka, A., Backer, D. C., et al. 2000, ApJ, 545, 1007

Lorimer, D. R. 2011, SIGPROC: Pulsar Signal Processing Programs, Astrophysics Source Code Library, ascl:1107.016

Lorimer, D. R., & Kramer, M. 2004, *Handbook of Pulsar Astronomy* (Cambridge University Press)

Lorimer, D. R., Lyne, A. G., & Camilo, F. 1998, A&A, 331, 1002

Lorimer, D. R., Stairs, I. H., Freire, P. C., et al. 2006a, ApJ, 640, 428

Lorimer, D. R., Faulkner, A. J., Lyne, A. G., et al. 2006b, MNRAS, 372, 777

Lorimer, D. R., Esposito, P., Manchester, R. N., et al. 2015, MNRAS, 450, 2185

Lynch, R. S., Boyles, J., Ransom, S. M., et al. 2013, ApJ, 763, 81

Lyne, A., & Graham-Smith, F. 2012, Pulsar Astronomy

Lyne, A., Graham-Smith, F., Weltevrede, P., et al. 2013, Science, 342, 598

Lyne, A., Hobbs, G., Kramer, M., Stairs, I., & Stappers, B. 2010, Science, 329, 408

Lyne, A. G., Biggs, J. D., Brinklow, A., McKenna, J., & Ashworth, M. 1988, Nat., 332, 45

Lyne, A. G., & Manchester, R. N. 1988, MNRAS, 234, 477

Lyne, A. G., McLaughlin, M. A., Keane, E. F., et al. 2009, MNRAS, 400, 1439

Lyne, A. G., Burgay, M., Kramer, M., et al. 2004, Science, 303, 1153

MacKay, C. D., Elsmore, B., & A., B. J. 1968, Nature, 219, 2123, 10.1038/219021a0

Maggiore, M. 2000, Phys. Rep., 331, 283

Maitia, V., Lestrade, J.-F., & Cognard, I. 2003, ApJ, 582, 972

Manchester, R. N. 1988, Proceedings of the Astronomical Society of Australia, 7, 548

—. 2013, Classical and Quantum Gravity, 30, 224010

Manchester, R. N., Hobbs, G. B., Teoh, A., & Hobbs, M. 2005, AJ, 129, 1993

Manchester, R. N., Lyne, A. G., Robinson, C., Bailes, M., & D'Amico, N. 1991, Nat., 352, 219

Manchester, R. N., Lyne, A. G., Camilo, F., et al. 2001, MNRAS, 328, 17

Manchester, R. N., Kramer, M., Stairs, I. H., et al. 2010, ApJ, 710, 1694

Manchester, R. N., Hobbs, G., Bailes, M., et al. 2013, PASA, 30, 17

Maron, O., Kijak, J., Kramer, M., & Wielebinski, R. 2000, A&A Supp., 147, 195

McLaughlin, M. A. 2013, Classical and Quantum Gravity, 30, 224008

McLaughlin, M. A., Lyne, A. G., Lorimer, D. R., et al. 2006, Nat., 439, 817

Nagase, F. 1989, PASJ, 41, 1

Nelson, L. A., Dubeau, E., & MacCannell, K. A. 2004, ApJ, 616, 1124

Newhall, X. X., Standish, E. M., & Williams, J. G. 1983, A&A, 125, 150

Ng, C., Bailes, M., Bates, S. D., et al. 2014, MNRAS, 439, 1865

Ng, C., Champion, D. J., Bailes, M., et al. 2015, MNRAS, 450, 2922

Noutsos, A., Johnston, S., Kramer, M., & Karastergiou, A. 2008, MNRAS, 386, 1881

Olausen, S. A., & Kaspi, V. M. 2014, ApJ Supp., 212, 6

Ord, S. M., van Straten, W., Hotan, A. W., & Bailes, M. 2004, MNRAS, 352, 804

Osłowski, S., van Straten, W., Bailes, M., Jameson, A., & Hobbs, G. 2014, MNRAS, 441, 3148

Ostriker, J. 1968, Nat., 217, 1227

Pacini, F., & Salpeter, E. E. 1968, Nat., 218, 733

Paczyński, B. 1976, in IAU Symposium, Vol. 73, Structure and Evolution of Close Binary Systems, ed. P. Eggleton, S. Mitton, & J. Whelan (Dordrecht, Holland), 75–+

Papitto, A., Ferrigno, C., Bozzo, E., et al. 2013, ArXiv e-prints, arXiv:1305.3884

Passy, J.-C., De Marco, O., Fryer, C. L., et al. 2012, ApJ, 744, 52

Pennucci, T. T., Demorest, P. B., & Ransom, S. M. 2014, ApJ, 790, 93

Petroff, E., Keane, E. F., Barr, E. D., et al. 2015, ArXiv e-prints, arXiv:1504.02165

Pilkington, J. D. H., Hewish, A., Bell, S. J., & Cole, T. W. 1968, Nat., 218, 126

Platania, P., Bensadoun, M., Bersanelli, M., et al. 1998, ApJ, 505, 473

Pletsch, H. J., Guillemot, L., Fehrmann, H., & et al. 2012, Science, 338, 1314

Podsiadlowski, P. 2001, in Astronomical Society of the Pacific Conference Series, Vol. 229, Evolution of Binary and Multiple Star Systems, ed. P. Podsiadlowski, S. Rappaport, A. R. King, F. D'Antona, & L. Burderi , 239–+

Podsiadlowski, P., Rappaport, S., & Pfahl, E. D. 2002, ApJ, 565, 1107

Press, W. H., Teukolsky, S. A., Vetterling, W. T., & Flannery, B. P. 2007, Numerical Recipes 3rd Edition: The Art of Scientific Computing, 3rd edn. (New York, NY, USA: Cambridge University Press)

Pylyser, E., & Savonije, G. J. 1988, A&A, 191, 57

Pylyser, E. H. P., & Savonije, G. J. 1989, A&A, 208, 52

Radhakrishnan, V., & Srinivasan, G. 1982, Current Science, 51, 1096

Ransom, S. M. 2001, PhD thesis, Harvard University

Ransom, S. M., Cordes, J. M., & Eikenberry, S. S. 2003, ApJ, 589, 911

Ransom, S. M., Eikenberry, S. S., & Middleditch, J. 2002, AJ, 124, 1788

Ransom, S. M., Hessels, J. W. T., Stairs, I. H., et al. 2005, Science, 307, 892

Ransom, S. M., Ray, P. S., Camilo, F., et al. 2011, ApJL, 727, L16

Ransom, S. M., Stairs, I. H., Archibald, A. M., et al. 2014, Nat., 505, 520

Rappaport, S., Podsiadlowski, P., Joss, P. C., Di Stefano, R., & Han, Z. 1995, MNRAS, 273, 731

Ray, P. S., Ransom, S. M., Cheung, C. C., et al. 2013, ApJL, 763, L13

Romani, R. W. 2012, ApJL, 754, L25

Ruderman, M. A., & Sutherland, P. G. 1975, ApJ, 196, 51

Sanidas, S. A., Battye, R. A., & Stappers, B. W. 2012, Phys. Rev. D, 85, 122003

Saslaw, W. C., Faulkner, J., & Strittmatter, P. A. 1968, Nat., 217, 1222

Scholz, P., Kaspi, V. M., Lyne, A. G., et al. 2015, ArXiv e-prints, arXiv:1501.03746

Sesana, A. 2013a, Classical and Quantum Gravity, 30, 244009

—. 2013b, MNRAS, 433, L1

Shannon, R. M., & Johnston, S. 2013, MNRAS, 435, L29

Shannon, R. M., Ravi, V., Coles, W. A., et al. 2013, Science, 342, 334

Shannon, R. M., Osłowski, S., Dai, S., et al. 2014, MNRAS, 443, 1463

Shannon, R. M., Ravi, V., Lentati, L. T., et al. 2015, Science, 349, 1522

Shao, L., Caballero, R. N., Kramer, M., et al. 2013, Classical and Quantum Gravity, 30, 165019

Shapiro, S. L., & Teukolsky, S. A. 1986, Black Holes, White Dwarfs and Neutron Stars: The Physics of Compact Objects (Wiley)

Siemens, X., Ellis, J., Jenet, F., & Romano, J. D. 2013, Classical and Quantum Gravity, 30, 224015

Spitler, L. G. 2013, PhD thesis, Cornell University

Spitler, L. G., Cordes, J. M., Hessels, J. W. T., et al. 2014, ApJ, 790, 101

Splaver, E. M., Nice, D. J., Arzoumanian, Z., et al. 2002, ApJ, 581, 509

Splaver, E. M., Nice, D. J., Stairs, I. H., Lommen, A. N., & Backer, D. C. 2005, ApJ, 620, 405

Staelin, D. H., & Reifenstein, III, E. C. 1968, Science, 162, 1481

Stairs, I. H. 2004, Science, 304, 547

Stairs, I. H., Faulkner, A. J., Lyne, A. G., et al. 2005, ApJ, 632, 1060

Stappers, B. W., Archibald, A. M., Hessels, J. W. T., et al. 2014, ApJ, 790, 39

Stovall, K. 2013, PhD thesis, The University of Texas at San Antonio

Stovall, K., Lynch, R. S., Ransom, S. M., et al. 2014, ApJ, 791, 67

Swiggum, J. K., Lorimer, D. R., McLaughlin, M. A., et al. 2014, ApJ, 787, 137

Tauris, T. M. 2012, Science, 335, 561

Tauris, T. M., Langer, N., & Kramer, M. 2011, MNRAS, 416, 2130

—. 2012, MNRAS, 425, 1601

Tauris, T. M., & Savonije, G. J. 1999, A&A, 350, 928

Tauris, T. M., & van den Heuvel, E. P. J. 2006, Formation and evolution of compact stellar X-ray sources (Cambridge University Press), 623–665

Tauris, T. M., van den Heuvel, E. P. J., & Savonije, G. J. 2000, ApJL, 530, L93

Taylor, J. H. 1992, Royal Society of London Philosophical Transactions Series A, 341, 117

Taylor, J. H., & Weisberg, J. M. 1989, ApJ, 345, 434

Thompson, C., & Duncan, R. C. 1995, MNRAS, 275, 255

—. 1996, ApJ, 473, 322

Thorne, K. S., & Ipser, J. R. 1968, ApJL, 152, L71

Thornton, D., Stappers, B., Bailes, M., et al. 2013, Science, 341, 53

Tiburzi, C., Johnston, S., Bailes, M., et al. 2013, MNRAS, 436, 3557

Torne, P., Eatough, R. P., Karuppusamy, R., et al. 2015, ArXiv e-prints, arXiv:1504.07241

Turtle, A. J., & Vaughan, A. E. 1968, Nat., 219, 845 van der Sluys, M. V., Verbunt, F., & Pols, O. R. 2005, A&A, 431, 647

van Haarlem, M. P., Wise, M. W., Gunst, A. W., et al. 2013, A&A, 556, A2

van Straten, W. 2006, ApJ, 642, 1004

van Straten, W., & Bailes, M. 2011, PASA, 28, 1

Verbiest, J. P. W., Weisberg, J. M., Chael, A. A., Lee, K. J., & Lorimer, D. R. 2012, ApJ, 755, 39

Verbiest, J. P. W., Bailes, M., Coles, W. A., et al. 2009, MNRAS, 400, 951

Verbiest, J. P. W., Lentati, L., Hobbs, G., et al. 2016, MNRAS, arXiv:1602.03640

Wang, N., Manchester, R. N., & Johnston, S. 2007, MNRAS, 377, 1383

Webbink, R. F., Rappaport, S., & Savonije, G. J. 1983, ApJ, 270, 678

Weisberg, J. M., Nice, D. J., & Taylor, J. H. 2010, ApJ, 722, 1030

Weisberg, J. M., & Taylor, J. H. 1981, General Relativity and Gravitation, 13, 1

Weltevrede, P., Edwards, R. T., & Stappers, B. W. 2006a, A&A, 445, 243

Weltevrede, P., Stappers, B. W., Rankin, J. M., & Wright, G. A. E. 2006b, ApJL, 645, L149

Wijnands, R., & van der Klis, M. 1998, Nat., 394, 344

Will, C. M. 1993, Theory and Experiment in Gravitational Physics

Woosley, S. E., & Weaver, T. A. 1986, Ann. Rev. A&A, 24, 205

Yoon, S.-C., & Langer, N. 2005, A&A, 435, 967

Young, M. D., Manchester, R. N., & Johnston, S. 1999, Nat., 400, 848

Zhang, B., Gil, J., & Dyks, J. 2007, MNRAS, 374, 1103

Zhang, B., Harding, A. K., & Muslimov, A. G. 2000, ApJL, 531, L135

Zhu, W. W., Berndsen, A., Madsen, E. C., et al. 2014, ApJ, 781, 117